

Development and analysis of novel light trapping schemes for silicon solar cells

Von der Fakultät für Mathematik und Physik
der Gottfried Wilhelm Leibniz Universität Hannover

zur Erlangung des akademischen Grades

Doktor der Naturwissenschaft

Dr. rer. nat.

genehmigte Dissertation von

Dipl.-Phys. Sören Schäfer

geboren am 11.12.1986 in Korbach

Erscheinungsjahr 2018

Referent: Prof. Dr. Rolf Brendel

Korreferent: Prof. Dr. Herbert Pfnür

Tag der Disputation: 04.09.2018

Kurzzusammenfassung

Siliziumsolarzellen bilden mit etwa 94 % Anteil den größten Posten an weltweit installierter Photovoltaik-Leistung. Der Anteil der reinen Waferkosten am fertigen Solarmodul beläuft sich auf etwa 40 %. Die Gründe sind einerseits die hohen Kosten der poly-Silizium Produktion mittels des Siemens-Prozesses sowie andererseits der Materialverlust beim Sägen des Si-Ingots oder Blocks in einzelne Wafer. Bestrebungen die Waferkosten zu senken zielen darauf ab, den Sägeverlust zu minimieren sowie die Waferdicke zu reduzieren. Ein dünnerer Wafer absorbiert jedoch weniger Licht, wodurch die Anwendung eines Lichteinfangkzeptes eine erhöhte Bedeutung erlangt. Das Thema der vorliegenden Dissertation ist die Entwicklung und Charakterisierung von verbesserten Lichteinfangkzepten für Siliziumsolarzellen mit dem langfristigen Ziel, die Stromgestehungskosten von Silizium-basierter Photovoltaik zu senken.

Im ersten Teil verwenden wir elektrochemisch geätzte Makroporen mit Strukturgrößen im Mikrometerbereich um einen Siliziumwafer ohne Sägeverlust in dünnere Absorberschichten zu zerteilen. Die Vorteile dieser Methode, bei der sich der Makroporendurchmesser durch geeignete Wahl der Ätzbedingungen verändern lässt, sind, dass i) die dünnen Schichten durch die durchgehenden Poren bereits über ein Lichteinfangkzept verfügen sowie ii) innerhalb eines Prozesses direkt mehrere Schichten vom Substratwafer abgelöst werden können. Wir demonstrieren das erfolgreiche Ablösen von 4 makroporösen Schichten mit einer Dicke von 18 μm und einer Größe von $(0.5 \times 0.5) \text{ cm}^2$. Diese Schichten wurden unter der Berücksichtigung der chemischen Auflösungsreaktionen und deren Auswirkungen auf die Porenmorphologie geätzt. Diese Anwendung geht über den Rahmen des in der Literatur bekannten Raumladungszonenmodells hinaus.

Als nächstes übertragen wir das Lichteinfangkzept der Makroporen auf dickere Wafer. Dies leitet den zweiten Teil der Arbeit ein, bei dem wir Lichteinfangstrukturen untersuchen, die eine höhere Effizienz im Vergleich zu einer Pyramidentextur ermöglichen. Wir entwickeln ein Vorderseitentextur aus nicht durchgehenden Makroporen und vergleichen diese mit einer pyramidalen Textur. Die Makroporentextur reflektiert lediglich 1 % des einfallenden Lichtes und zeigt, nach Passivierung mit atomlagenabgeschiedenem amorphem Aluminiumoxid (AlO_x) eine niedrige Oberflächenrekombinationsgeschwindigkeit von 8 cm/s . Wir erklären diesen niedrigen Rekombinationsparameter durch eine ungleichmäßige Ladungsträgerverteilung innerhalb der Porenwände der Textur. Die Kombination elektrischer und optischer Charakterisierung zeigt, dass die Makroporentextur einen relativen Effizienzgewinn von 2.0 – 5.3 %_{rel} auf einem 300 μm -dicken Absorber erlauben, wenn sie anstatt der Pyramiden verwendet wird.

Ein weiteres Lichteinfangkzept widmet sich der Rückseite von Si-Zellen. Dies ist relevant für Fälle, in denen die Vorderseite planar sein muss, etwa wenn Silizium als Absorber in einer Mehrschichtszelle fungiert, bei der der Absorber mit höherer Bandlücke auf die Vorderseite des Si aufgebracht werden. Wir tragen hierzu einen pigmentierten, diffusen Rückseitenreflektor (PDR) auf Siliziumwafer mit "Polysilizium auf Oxid"-Kontakten (POLO) auf. Die POLO-Kontakte ermöglichen eine räumliche Trennung des lichtstreuenden Reflektors von der elektrisch aktiven Grenzfläche, sodass im bzw. durch den PDR keine zusätzlichen Ladungsträger rekombinieren. Der PDR besteht aus Si-Nanopartikeln als lichtstreuendes Pigment, welche in einer Siliziumoxid-Matrix eingebettet sind. Zur Bestimmung des optischen Gewinns führen wir ein analytisches

optisches Modell ein, welches erlaubt, zwischen der Absorption im Silizium und der parasitären Absorption im PDR (bzw. den POLO-Kontakten) zu unterscheiden. Ein Vergleich des PDRs mit einer Pyramidentextur zeigt, dass letztere zwar ein besseres Lichteinfangkonzzept darstellen, dies jedoch durch eine erhöhte Ladungsträgerrekombination kompensiert wird. Der PDR erlaubt einen relativen Effizienzgewinn von $(2.7 \pm 0.7) \%_{\text{rel}}$ im Vergleich zu einer Rückseite ohne PDR, wohingegen die Pyramidentextur einen Wert von $(1.2 \pm 0.8) \%_{\text{rel}}$ zeigt. Den effizienzsteigernden Effekt des Rückreflektors weisen wir überdies auf Rückkontaktsolarzellen nach.

Im letzten Teil wird gezeigt, dass sich durch Anwendung der exakten Gleichung für Lambertschen Lichteinfang das Effizienzlimit von Si-Solarzellen um $0.12 \%_{\text{abs}}$ auf 29.56% erhöht.

Schlagnorte: elektrochemisches Ätzen, Anodisierung, Lichteinfang, Oberflächentextur, Silizium-Photovoltaik, Oberflächenpassivierung

Abstract

Silicon solar cells make up for 94 % of the worldwide installed photovoltaic power capacity. 40 % of the price of a finished solar module is incurred in the wafer. The reasons are on the one hand the costly production of poly-silicon with the Siemens process and on the other hand the loss of material when sawing the Si ingot or block into wafers, usually referred to as kerf-loss. Attempts to reduce the wafer costs aim to minimize the kerf-loss as well as reduce the thickness of the wafers themselves. However, a thinner wafer absorbs less light which gives the application of a light trapping scheme an increasing importance. The topic of the present thesis is to develop and characterize advanced light trapping schemes for silicon solar cells with the long-term goal to diminish the levelized cost of electricity of silicon-based photovoltaics.

In the first part, we use electrochemically etched macropores with structure sizes in the micrometer range to slice a Si wafer without kerf-loss into thinner absorber layers. The advantages of this method, where the macropore diameter can be tuned by the appropriate choice of the etch conditions, are that i) the penetrating pores already impart the layers with a light trapping scheme and ii) that multiple layers can be detached from the substrate wafer within one process. We successfully demonstrate the detachment of 4 macroporous layers with a thickness of 18 μm and a size of $(0.5 \times 0.5) \text{ cm}^2$. These layers are etched under consideration of the dissolution chemistry and its impact on the pore morphology. This application exceeds the scope of the space charge region model that is reported in literature.

Next, we transfer the light trapping scheme of the macropores to thicker wafers. This leads over to the second part of the thesis which deals with the analysis of light trapping schemes that allow for a higher efficiency than pyramidal textures. We develop a front side texture of non-penetrating blind holes and benchmark them against a pyramidal texture. The blind hole texture reflects only 1 % of the incoming light and exhibits, after passivation with atomic layer deposited amorphous aluminum oxide (AlO_x), a surface recombination velocity of 8 cm/s. We explain the low value of this recombination parameter by the interplay between the field effect passivation with the characteristic morphology of the texture. The combined analysis of optical and electrical properties yields that the blind hole texture allows for a relative gain in efficiency of 2.0 – 5.3 %_{rel} on a 300 μm -thick absorber if used instead of random pyramids.

Another light trapping scheme addresses the rear side of Si solar cells. This becomes relevant for cases in which the front side of the absorber must be planar, like when Si is used as absorber in a multijunction solar cell where wide band gap absorbers are deposited on top of the Si. Therefore we place a pigmented diffuse rear reflector (PDR) on a Si wafer with polysilicon on oxide (POLO) junctions. These POLO junctions allow the spatial separation of the light trapping region and the electronically active interface so that no additional recombination of charge carriers occurs in or due to the PDR. The PDR consists of Si nanopowder as scattering pigment that is embedded in a silicon oxide matrix. To determine the optical gain due to the PDR we derive an analytical model that allows for the separation of absorption in the wafer and parasitic absorption in the PDR (or POLO junctions). While the random pyramids allow for a higher photogeneration compared to the PDR, they have an enhanced surface recombination rate which overcompensates the optical benefit. The PDR allows for a relative efficiency gain of

$(2.7 \pm 0.7) \%_{\text{rel}}$ compared to a sample without PDR whereas the pyramidal texture shows a gain of $(1.2 \pm 0.8) \%_{\text{rel}}$. The beneficial effect of the PDR is demonstrated on back-contacted solar cells.

In the last part, we show that when applying the accurate expression for Lambertian light trapping, the theoretical efficiency limit of solar cells increases by $0.12 \%_{\text{abs}}$ to 29.56% .

Key words: electrochemical etching, anodization, light trapping, surface texture, silicon photovoltaics, surface passivation

Contents

1	Introduction	1
2	Theoretical background	5
2.1	Solar spectrum	5
2.2	Absorption in silicon	6
2.3	J_{sc}^* – A metric for light management	8
2.4	Optical loss channels	8
2.5	Electromagnetic waves at interfaces	14
2.5.1	Fresnel equations without interference	14
2.5.2	Fresnel equations with interference and design guidelines for an ARC	16
2.6	Light trapping schemes in ray optics	19
2.6.1	No light trapping	20
2.6.2	The Lambertian limit	22
2.6.3	Path length enhancement Z	24
2.6.4	Surpassing the Lambertian limit	25
2.7	Device parameters in solar cells	27
2.8	Electrochemical etching of macropores in silicon	29
2.8.1	Dissolution reactions	29
2.8.2	Current-voltage characteristics of Si/HF interface	31
2.8.3	Macropore formation model	35
2.8.4	Pore growth kinetics	38
3	Experimental and simulation methods	41
3.1	Spectrophotometer	41
3.2	Measuring the effective carrier lifetime	44
3.2.1	Infrared lifetime mapping (ILM)	46
3.2.2	Photoconductance decay	48
3.3	Etching tool and wafer preparation	49
3.4	Raytracing	51
4	Characterization of macropore etching	55
4.1	Characteristic current density J_{ps}	55
4.2	Correlation between pore pitch and pore morphology	56
4.3	Impact of current density on pore morphology	57
4.4	Impact of voltage on pore morphology	60
4.5	Pore growth rate and HF diffusion	61

4.6	Summary	64
5	Multilayer etching for natively textured sheets of macroporous Si	65
5.1	The multilayer concept	65
5.2	Preventing pore reorganization	66
5.3	The multilayer etch protocol	68
5.4	Limits of multilayer etching	70
5.5	Alternative approach: One-by-one detachment	72
5.6	Summary	74
6	Macroporous blind hole texture	75
6.1	Introduction	75
6.2	Sample preparation and texture morphology	76
6.3	Optical characterization	78
6.3.1	Absorptance spectra	79
6.3.2	Analysis of optical losses	81
6.3.3	Performance under oblique incidence	85
6.4	Electrical characterization	88
6.5	Quality factor	94
6.6	Summary and discussion	95
7	Pigmented diffuse rear reflectors using Si nanopowder	97
7.1	Introduction	97
7.2	Properties and preparation of Si nanopowder PDR	102
7.3	Optical model for two absorbing layers	105
7.4	Optical characterization of samples without surface passivation	108
7.4.1	Impact of pigment concentration	108
7.4.2	Sensitivity analysis of optical model	115
7.4.3	Impact of refractive index of matrix material	116
7.4.4	Impact of external rear mirror	117
7.5	Characterization of samples with POLO junctions	120
7.5.1	Preparation of POLO cell precursor	121
7.5.2	Optical and electrical characterization of POLO samples	122
7.6	Application of PDR to solar cells	127
7.7	Summary and discussion	129
8	Efficiency limit of crystalline Si solar cells with Lambertian light trapping	133
8.1	Calculating the limiting efficiency	133
8.2	Lambertian limit absorptance with free carrier absorption	135
8.3	Impact on efficiency limit	137
8.4	Summary	137
9	Summary	139
A	Clear sky insolation on a collecting surface	143
A.1	Sun's position	143

A.2 Insolation in dependence of air mass and tilt of solar cell	145
B Etching parameters for macropore samples	147
Bibliography	151
List of publications	171
Curriculum vitae	175

Chapter 1

Introduction

Photovoltaics (PV) is a form of renewable energy source, where the sunlight is absorbed in a solar cell and directly converted into electrical power. The German administration, among other governments of industrialized countries, addresses their dependence on limited fossil fuels and the socio-economic challenge of the global climate change by promoting renewable energy sources like PV under the term "Energiewende" [1, 2]. Driven by political incentives, the installed PV capacity in Germany increased from 0.3 GW in 2002 to 42.98 GW in 2017, which makes up for 21 % of the total electric power production capacity and for 7% of the total electric energy production [3]. The governmental claim to increase the share of renewable energy production to 80% of the total energy production by 2050 underlines the significance of PV and other renewables in the future.

In about 94 % of the terrestrial photovoltaic systems, the semiconductor silicon (Si) is used as absorbing material [4]. The wafers make up for about 40 % of the costs of a PV module with crystalline Si solar cells [4]. The reasons are on the one hand the costly production of poly-Si with the Siemens process. On the other hand up to 40 % of the Si ingot is wasted as kerf-loss if it is sawn into wafers [4]. Wafer sawing also sets a lower limit to the wafer thickness of currently 170 to 180 μm [4]. In principle, wafers this thick are not mandatory to achieve highest efficiencies [5], as long as the wafer possesses a certain light trapping ability. With respect to the cell efficiency, light trapping compensates for fact that thinner wafers absorb less sunlight. A benchmark for excellent light trapping is the Lambertian light trapping scheme, which assumes an isotropic light distribution in the absorber. With this scheme and the assumption of no front surface and perfect rear surface reflectance (Lambertian limit), the theoretical efficiency limit for Si has been calculated to be 29.4% for a thickness of 110 μm [5], however, with an approximated formula for the absorptance.

One route to reduce the wafer costs is to slice a single Si wafer with a relatively large thickness of a few hundreds of μm into many layers with a thickness of a few tens of μm by using a technique that avoids the kerf-loss of conventional wafer sawing. Reported techniques rely on the implantation of hydrogen and subsequent heat treatment [6, 7], thermomechanical spalling [8, 9], lateral alkaline etching of (111)-oriented Si substrates [10] or electrochemical etching of macropores [11, 12]. The first three techniques produce one thin layer per process cycle. In addition, these layers are planar which requires them to be surface textured in an additional process step for the sake of light trapping if used as a solar cell absorber. The electrochemical etching of macropores, that have typical diameters of a few μm , however, produces layers that are natively textured and exhibit Lambertian light trapping [13]. Macropore etching furthermore has the potential to produce multiple layers in a single process cycle which has not been reported before. After introducing the theoretical and experimental basics of light management in Si and macropore formation in **Chapters 2, 3 and 4**, we evaluate the feasibility of this multilayer etching concept in **Chapter 5**.

It turns out that the multilayer etching of thin macroporous layers is quite challenging. Thus, the question arises in how far the outstanding light trapping ability of macropores can be used for highly efficient Si solar cells with standard absorber thicknesses. The Si solar cell with the highest reported efficiency of 26.7% [14] has a pyramidal front surface texture that is produced by anisotropic etching of Si [15]. In **Chapter 6** we benchmark a texture that consists of macroporous blind holes with a depth of a few μm against a pyramidal texture regarding both optical and electrical properties.

The maximum conversion efficiency of Si solar cells is limited by thermalization losses of photogenerated carriers and by the non-absorption of photons with an energy below the bandgap of the semiconductor [16]. One option to overcome this is to interconnect absorbers with different bandgap energies in a tandem or multijunction device. The bandgap of silicon qualifies it to be used as an absorber in a bottom cell in combination with wide-band gap top cell [17–19]. A textured front side, which is the common way to implement light trapping in Si solar cells, is a hindrance when the top cell is deposited by epitaxy or spin-coating. This leaves the rear side of the Si bottom cell as the only option to implement light trapping by randomizing the light propagation direction. In **Chapter 7** we compare a so-called pigmented diffuse reflector (PDR) that consists of Si particles with diameters of a few hundreds of μm embedded in a dielectric matrix with a pyramidal texture on the rear side. We combine the PDR with poly-Si on oxide (POLO) junctions which not only allow for highest cell efficiencies [20] but also for a spatial separation of the electronically active surface of the absorber and the PDR by a highly doped poly-Si layer.

In **Chapter 8** we re-evaluate the maximum theoretical efficiency of Si solar cells by using the accurate expression for Lambertian light trapping. This complements the part of the thesis about advanced light trapping structures. **Chapter 9** gives a summary of the work.

Chapter 2

Theoretical background

This chapter sets the theoretical background for the work. It introduces the photogenerated current density J_{sc}^* , implied open circuit voltage V_{oc}^* and the implied fill factor FF^* of a solar cell. We identify optical loss channels, discuss their impact on the photogeneration and introduce the concept of a Lambertian scatterer that is a widely used benchmark for excellent light trapping. Furthermore, a literature review on the etching of macropores is given.

2.1 Solar spectrum

The spectral radiance of the sun is approximately equal to that of a black body with a temperature of $T_s = 5780$ K. T_s is the temperature of the sun's surface. The spectral radiance of a body is the amount of energy it emits as radiation of different wavelengths and is measured in power per area of the body, per solid angle that the radiation is measured over, per wavelength. For calculating the photogenerated current density (see Sec. 2.3), we need the spectral irradiance of the sun $\Phi(\lambda)$. We calculate the spectral irradiance from the spectral radiance by accounting for the solid angle $\Omega_s = 6.8 \times 10^{-5}$ sr under which an observer on the earth sees the sun. Figure 2.1 shows the spectral irradiance of a black body with T_s as well as the AM1.5G spectrum [21] between 280 and 1250 nm where silicon has a non-vanishing absorptance (see Sec. 2.2). The AM1.5G spectrum is, by convention, the standard spectrum for measuring conversion efficiencies of solar cells and considers light absorption in the earth's atmosphere. The air mass (AM) factor specifies the effective thickness of the atmosphere and the "global" (G) expression states that the spectrum includes both direct and diffuse radiation. Figure 2.1 additionally shows the photon flux which has its maximum at 670 nm.

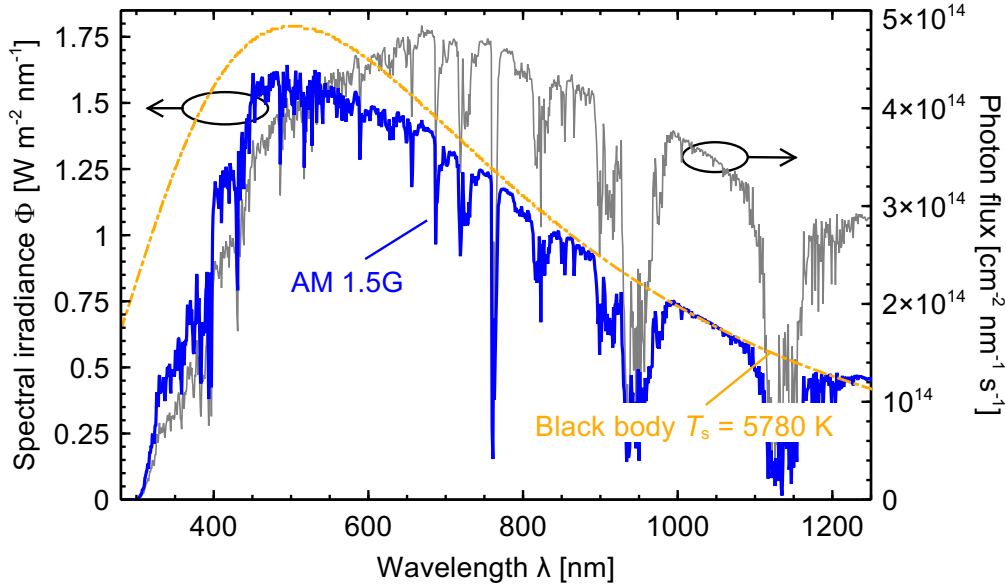


Figure 2.1: The figure shows the spectral irradiance Φ of a black body (orange line) with a temperature $T_s = 5780$ K and the AM1.5G spectrum (blue line) according to Ref. [21]. The thin grey line shows the AM1.5G photon flux.

2.2 Absorption in silicon

The prerequisite for the conversion of the spectral irradiance of the sun into electrical energy is the generation of electron-hole pairs in a semiconductor. This section focuses on the absorption probabilities of silicon. The propagation of electro-magnetic waves in media can be described by Maxwell's equations and the complex dielectric function $\epsilon = \epsilon_0 \epsilon_r$ of the respective medium, where ϵ_0 is the vacuum permittivity. In non-magnetic media, the complex refractive index reads

$$\tilde{n} = \sqrt{\epsilon_r} = n + ik \quad (2.1)$$

The real part of the refractive index $n = c/c_m$ is the ratio of the speed of light in vacuum c and within the material c_m and determines, e.g. refraction processes. The imaginary part k leads to an attenuation factor of the field amplitudes and is thus proportional to the light absorption in the material. The absorption coefficient α for a material depends on k via

$$\alpha = \frac{4\pi k}{\lambda} \quad (2.2)$$

The real and imaginary part of the refractive index depend on the wavelength of the light λ . This effect is referred to as dispersion. Figure 2.2a) and b) show a plot of the real part of the refractive index n and the absorption coefficient α for silicon [22]. The band gap wavelength $\lambda_g^{\text{Si}} = 1108$ nm is marked as well. The absorption coefficient of Si rises rather slowly for photons with $\lambda < \lambda_g^{\text{Si}}$ since Si has an indirect band gap, i.e. the maximum

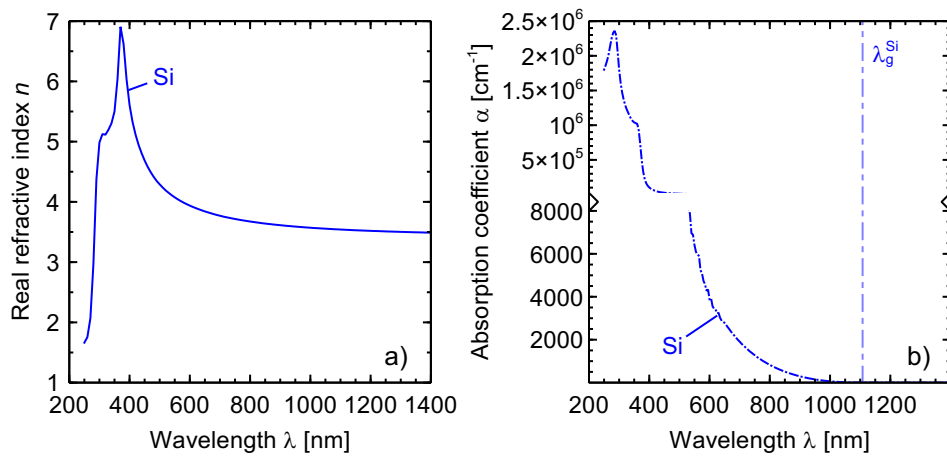


Figure 2.2: The figure shows a) the real part of the refractive index n and b) the absorption coefficient α for Si [22] at a temperature of 295K. The wavelength λ_g marks the band gap energy.

of the valence band and the minimum of the conduction band have different momenta in k -space. The electron-hole pair generation thus additionally requires a phonon that is either emitted or absorbed to conserve the momentum. The involvement of a third particle reduces the absorption probability especially for photons with energies slightly above the band gap. The larger the energy of the photons, the higher the possibility for a direct band transition, which is why the absorption coefficient increases for smaller wavelengths and becomes comparable to direct semiconductors like GaAs.

While the absorption coefficient α is characteristic for the material, the absorption probability A also depends on the geometrical form of the material. In its easiest form, A increases exponentially with the light path length l within the material, which is known as the Lambert-Beer law

$$A(\lambda, l) = 1 - \exp(-\alpha(\lambda) l) . \quad (2.3)$$

Figure 2.3 illustrates the absorptance from Eq. 2.3 for different wavelengths. Light with $\lambda < 450$ nm becomes absorbed within the first μm of the Si absorber. The thickness of typical Si solar cell wafers is $W = 150 - 300 \mu\text{m}$, i.e. most of the light with $\lambda < 900$ nm becomes absorbed before it reaches the rear side of the absorber. Weakly absorbed light with $900 \text{ nm} < \lambda < 1200 \text{ nm}$, however, may traverse the absorber multiple times before it is absorbed or emitted again. Light trapping schemes for solar cells aim for an absorption enhancement of this weakly absorbed light, as will be discussed in Sec. 2.4 and in Chs. 5, 6 and 7.

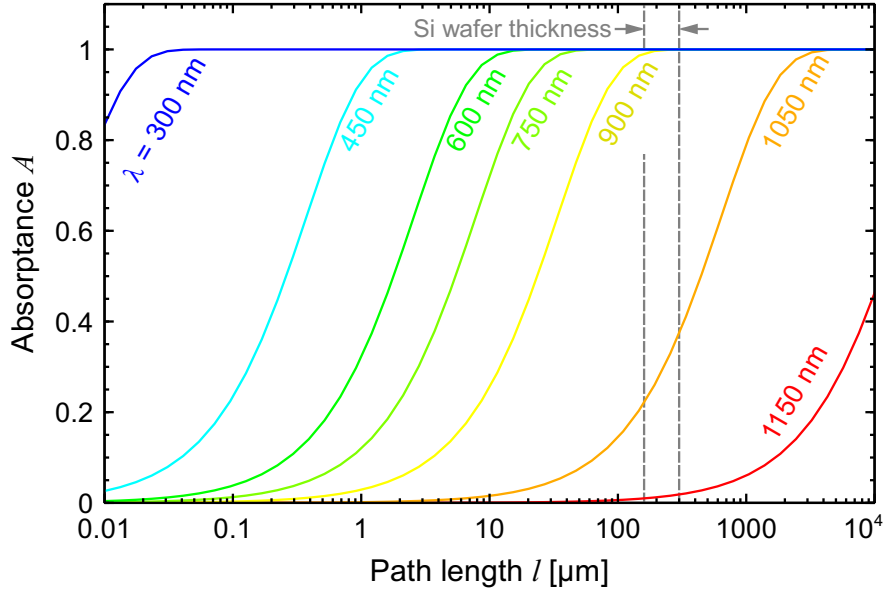


Figure 2.3: The plot shows the absorbance A in silicon according to Eq. 2.3 for different wavelengths, depending on the path length of the light l within the absorber.

2.3 J_{sc}^* – A metric for light management

We define the maximum photogenerated current density

$$J_{\text{sc}}^* = \frac{q}{hc} \int_{300 \text{ nm}}^{1250 \text{ nm}} \lambda A(\lambda) \Phi(\lambda) d\lambda \quad (2.4)$$

where $A(\lambda)$, $\Phi(\lambda)$, q , h , and c denote the band-to-band absorbance in the structure, the spectral irradiance of the AM1.5G spectrum from Fig.2.1, the elementary charge, Planck's constant and the speed of light in vacuum, respectively. The sun has a negligible irradiance for wavelengths below 300 nm and silicon, which is the absorbing material within this work, has a negligible absorbance beyond 1250 nm (see Fig.2.2), which explains the integration boundaries. The maximum photogenerated current density is the metric that we use throughout this work to quantify the light management of Si structures. It sets an upper limit to the short-circuit current density $J_{\text{sc}} < J_{\text{sc}}^*$ if the structure is used as a solar cell. The inequality originates from recombination losses within the solar cell [23].

2.4 Optical loss channels

The share of the incident light that is not absorbed by a band-to-band transition, i.e. becomes reflected, transmitted, or parasitically absorbed by the material, represents

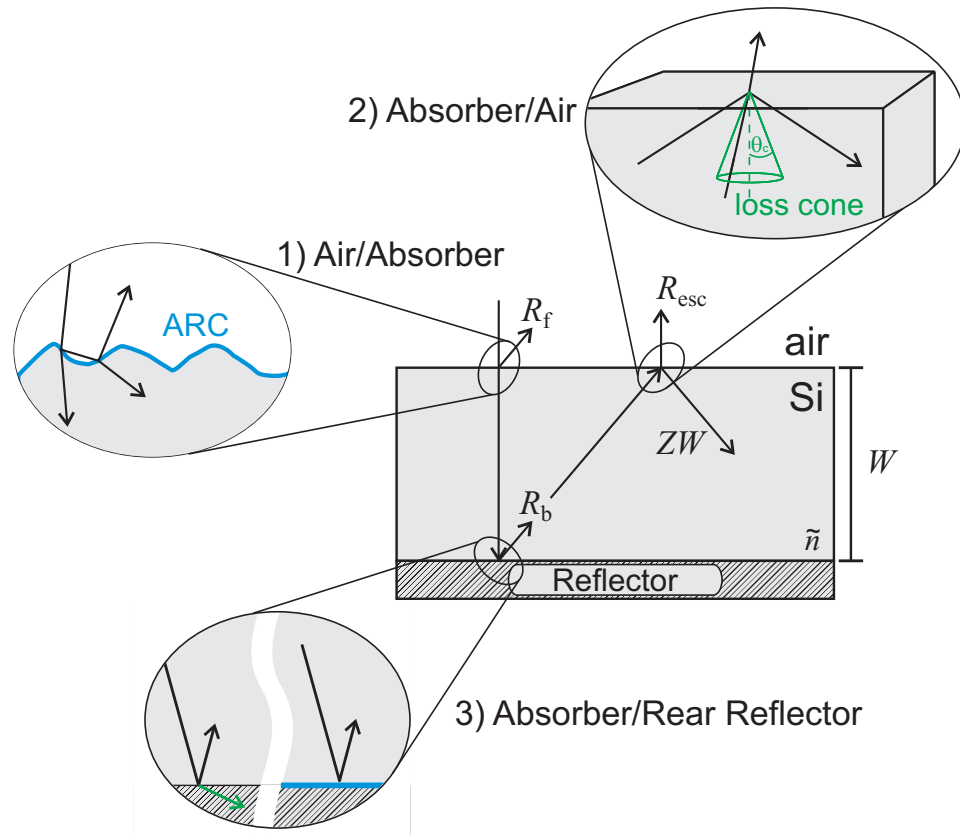


Figure 2.4: The figure shows possible light paths and loss channels in a material. The insets show the transition at the interfaces 1) air/absorber, 2) absorber/air and 3) absorber/rear reflector. The transition 1) can be manipulated by a surface texture and/or an ARC. Transition 2) underlies total internal reflection or transmission. The latter occurs when light hits the interface under an angle $\theta < \theta_c$ as illustrated by the loss cone. Transition 3) can result in reflection back into the absorber or absorption in the rear reflector as indicated by the green arrow. A dielectric interlayer reduces the probability of the latter.

the optical loss. Figure 2.4 shows a sketch of an absorbing material, characterized by its complex refractive index \tilde{n} and macroscopic thickness W , and defines different optical loss channels that may be distinguished by the light transitions at the interfaces air/absorber, absorber/air and absorber/rear reflector. Here, the rear reflector is not necessarily constrained to a rear side metalization of a solar cell but can also stand for, e.g., a detached back sheet that serves as protection layer in a solar module [24]. Arrows indicate potential light paths. In this section, we discuss optical loss channels, how they can be manipulated and how they depend on each other:

External reflectance R_f : At the transition air/absorber, the light is reflected before it enters the absorbing material. R_f depends on the angle of incidence and the difference in the refractive indices of the two materials at the boundary. It can be reduced by depositing anti-reflection coatings (ARC) on the front surface that

grade the refractive index of the absorber and the surrounding medium, air in case of Fig. 2.4 [25, 26]. The refractive index n_{ARC} and the thickness d of the ARC can be designed to minimize R_f at a specific wavelength, e.g. at the peak of the solar photon flux at 670 nm (see Sec.2.5). However, the J_{sc}^* becomes higher if the design wavelength of the ARC is around 600 nm for reasons that become apparent in the next loss channel discussion. Another way to diminish R_f is to use a front surface texture, which allows the reflected rays to hit the surface more than once as shown in Fig. 2.4.

Escape reflectance R_{esc} : This is the cumulative share of photons that exit the absorber at the transition absorber/air. Due to the reciprocity of the optical path, the escape probability increases with a lower external reflectance. Thus, the use of ARCs and/or a surface texture, enhance R_{esc} . Especially the weakly absorbed light makes up for the escape reflectance. This explains why the ARC is best designed for 600 nm instead of 670 nm. Since the transition absorber/air is from the material with a higher refractive index n to the one with lower n , total internal reflection can occur for rays that hit the front (or rear) surface at an angle

$$\theta > \theta_c = \arcsin\left(\frac{1}{n}\right) \quad (2.5)$$

The critical angle θ_c spans the loss cone. For a Si/air interface this angle is 16.4° for weakly absorbed light of $\lambda = 1100$ nm. Only light that hits the surface within this cone can escape the structure.

Back surface reflectance R_b : At the transition absorber/rear reflector the photons are lost when they are transmitted through the rear side and not reflected back into the absorber. R_b can be increased by the deposition of a reflecting layer, like Al or Ag, or a Bragg reflector [27]. A metal layer absorbs fractions of the light parasitically, that means without generating electron-hole pairs [28, 29]. The green arrow at the absorber/reflector interface in Fig. 2.4 indicates this loss channel. Parasitic absorption also occurs in case of frustrated total internal reflection at the rear side since the amplitude of the light wave does not abruptly drop to zero behind the interface but decays exponentially in the reflector material (evanescent wave [30]). A dielectric interlayer between the mirror and the absorber helps to reduce this absorption [31–33].

Dielectric absorptance A_{die} : The application of dielectric layers on the surface of the absorber bears the possibility of parasitic absorption when the dielectrics have a non-vanishing k -value. This already implies how this loss channel can be omitted: by using non-absorbing dielectrics.

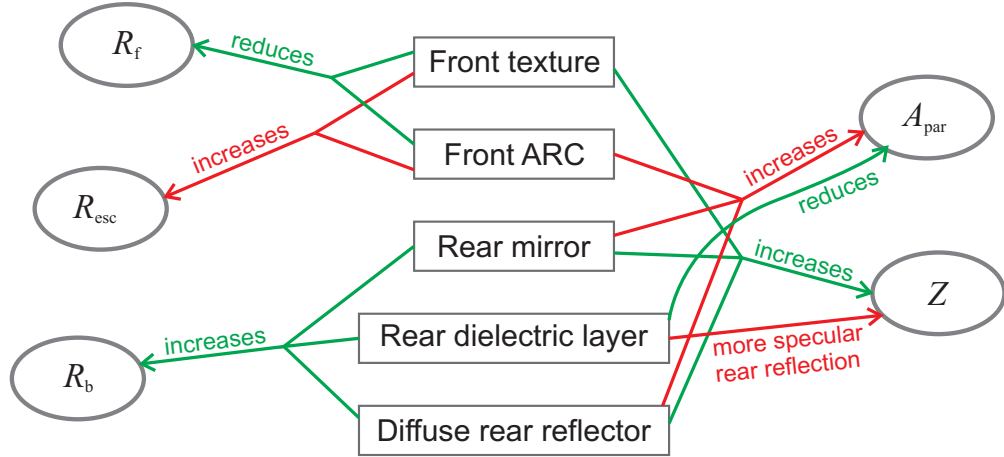


Figure 2.5: The figure illustrates the effect of measures (written in boxes) to manipulate the light absorptance of a structure (written in ovals). The figure distinguishes between positive (green lines) and negative (red lines) effects on the total absorptance.

Free carrier absorptance A_{fca} : Another parasitic absorption mechanism is the so-called free carrier absorption (FCA) [34]. Free carriers in the conduction or valence band of the absorber may absorb light without the generation of an electron-hole pair. The photon energy in this process is then transferred to the lattice by phonon-assisted thermalization. As is predicted by the Drude model, the absorption coefficient for FCA α_{fca} depends linearly on the free carrier concentration and is thus pronounced in, e.g., diffused regions with a higher dopant concentration.

The absorption in the rear reflector, the dielectrics and the free carrier absorption do not generate e-h pairs and add up to the overall parasitic absorptance A_{par} . The magnitude of R_{esc} , R_b and A_{par} determines the *light trapping* capability of an absorber. It states how well the light is confined within the absorber once it has entered it. The path length enhancement factor Z gives the average path length $\bar{l} = ZW$ for a certain wavelength in terms of the absorber thickness W . Light trapping can be quantified by Z for weakly absorbed light with $\lambda \approx 1200$ nm. Since the critical angle of total internal reflection is only 16.4° in Si for $\lambda = 1100$ nm, the light steering into shallow angles by a surface texture or a diffuse rear reflector not only increases Z by an oblique traversal through the absorber but also by a higher probability for total internal reflection at the surfaces. Pyramidal textures, either randomly [35] or regularly arranged [36], are state-of-the-art surface textures for mono-crystalline Si absorbers. They are produced by alkaline etching of mono-crystalline Si that have a orientation-dependent etch rate [37]. Figure 2.6 shows the random pyramid texture on a Si wafer. Silicon solar cells with $Z \approx 26$ at $\lambda = 1180$ nm have been reported [38]. A derivation of the optimum light trapping scheme is part of Sec. 2.6.

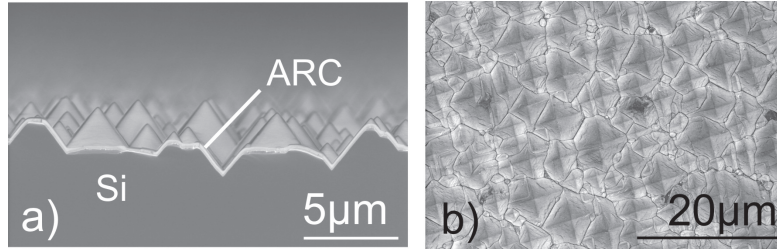


Figure 2.6: The figure shows scanning electron microscope (SEM) images of a) the cross-sectional view and b) the top view of a silicon wafer with a random pyramid texture. The surface is also covered by an anti-reflection coating (ARC) of silicon nitride.

Figure 2.5 summarizes the measures that allow the control of optical loss channels as well as their effect on the specific optical properties. Each measure has positive and negative effects on the total light absorptance as indicated by the green and red color, respectively. There are also secondary effects of the measures that are not displayed. Examples for secondary effects are the front texture that, if combined with an ARC, implies a more oblique traversal through the ARC and therefore a higher parasitic absorptance or, by steering the light, enhancing the total internal reflection at the rear side.

It becomes obvious that by manipulating one optical loss channel, other loss channels are affected as well. This must not obscure the fact that for all measures the benefit in J_{sc}^* generally outweighs these secondary absorptance losses. This is exemplarily shown in Fig. 2.7 which depicts the photogenerated current density J_{sc}^* (see Eq. 2.4) of a silicon wafer with a thickness of $W = 200 \mu\text{m}$ under isotropic illumination after certain measures are applied. We choose isotropic illumination due to the fact that under this condition a so-called Lambertian surface, i.e. a surface that fully randomizes the propagation direction of the reflected and transmitted light for all wavelengths, sets an upper for light trapping and it is yet not clear whether any geometrical light trapping scheme can perform better. The J_{sc}^* -values in Fig. 2.7 are obtained from raytracing simulations with SUNRAYS [39]. The raytracer will be explained in more detail in Ch. 3.

We distinguish between single and successively combined practical measures, indicated by red circles and green squares in Fig. 2.7, respectively. Practical measures means that they are experimentally accessible, e.g. a *random pyramid texture* as *front texture*. The blue diamonds indicate the J_{sc}^* for the optimum value of each single measure, e.g. a *perfect ARC* with $R_f = 0$ as *ARC*. Table 2.1 lists the practical measures, the limits of each measure and the respective relative improvement they have on J_{sc}^* for two absorber thicknesses $W = 10$ and $200 \mu\text{m}$. The J_{sc}^* -values of the blank and planar Si absorbers are 18.74 mA/cm^2 and 25.51 mA/cm^2 , respectively.

The photogeneration of a structure with a fully randomizing (also Lambertian surface, see Sec.2.6) front surface is calculated via Eq. 2.46 with $R_f = 1 - T_f$ being the external

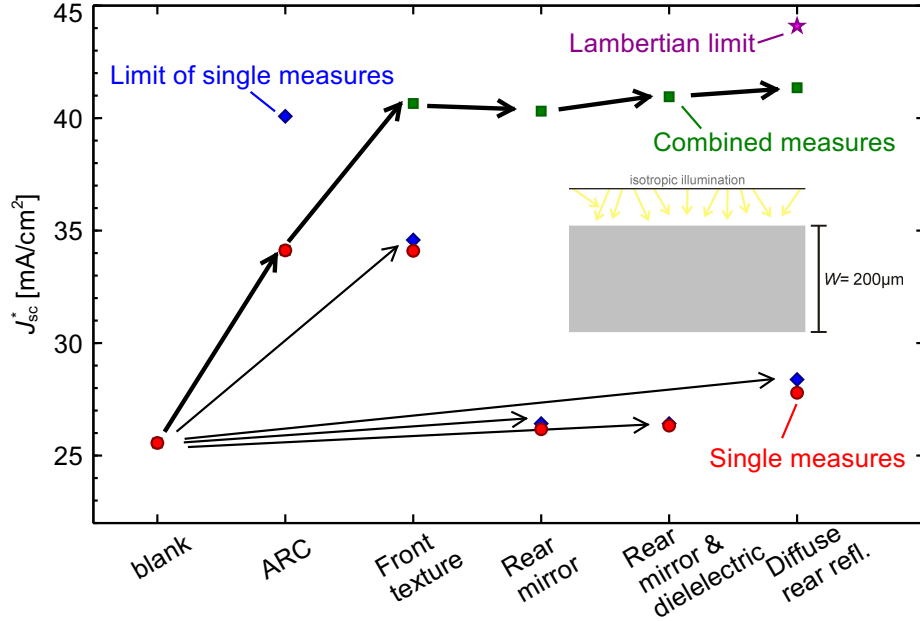


Figure 2.7: The figure shows the impact of single practical measures (red circles, see Tab. 2.1) on the photogenerated current density J_{sc}^* of a silicon wafer with a thickness $W = 200 \mu\text{m}$ under isotropic illumination. The blue diamonds symbolize the maximum improvement on J_{sc}^* for each measure. The green squares and the magenta star mark the J_{sc}^* for the successive combination of practical measures and the Lambertian limit. All values are simulated with the SUNRAYS except for the Lambertian limit that is calculated as described in Sec. 2.6.2.

front reflectance of an uncoated random pyramid surface and $R_b = 1 - T_{\text{planar}}/n^2$. T_{planar} is the transmittance of isotropic illumination through a planar and uncoated air/silicon interface and n is the real part of the refractive index of Si. The practical diffuse rear reflector is "white paint" and is assumed with $R_b = 0.9$ and a Lambertian factor of $\Lambda_b = 0.5$ to reproduce the gain in J_{sc}^* from Ref. [40]. The Lambertian factor of a surface states the fraction of light that is fully randomized in its direction after it is transmitted or reflected from the surface. The Lambertian limit is calculated via Eq. 2.47 and represents the combination of the optimum value for each measure.

The quantification of the optical losses yields that the reduction of the external front reflectance R_f by the application of an ARC and/or a surface texture has the largest impact on the photogeneration. The introduction of light trapping by a textured surface as well as the properties of the rear side become increasingly important for thinner absorber layers: The combination of all optical measures increases J_{sc}^* by 99.2% for the $10 \mu\text{m}$ absorber and 61.7% for the $200 \mu\text{m}$ absorber. The random pyramid texture almost fully randomizes the light direction and approaches the performance of a Lambertian surface to 93.1% and 94.6% for $W = 10 \mu\text{m}$ and $W = 200 \mu\text{m}$, respectively. It is interesting to see that the application of a metallic rear mirror to a Si absorber that has

Table 2.1: The table shows the simulated relative impact on J_{sc}^* of single (red, blue) and combined (green, magenta) measures to suppress optical loss channels and contrasts them for two silicon absorber thicknesses W . The J_{sc}^* -values of the blank planar Si sheets are 18.74 mA/cm² for $W = 10 \mu\text{m}$ and 25.51 mA/cm² for $W = 200 \mu\text{m}$.

Measure	practical / limit	rel. gain in J_{sc}^* [%]	
		$W = 10 \mu\text{m}$	$W = 200 \mu\text{m}$
Blank Si/ Reference		18.74 mA/cm ²	25.51 mA/cm ²
ARC	80nm SiN _{x,n=1.9} / $R_{\text{front}}=0$	+37.0/+59.0	+33.5/+56.8
Front texture	random pyramids / fully randomizing	+59.6/+64.0	+33.4/+35.3
Rear mirror	Al mirror & 200nm SiO _x / $R_{\text{rear}}=1$	+10.7/+12.1	+3.0/+3.4
Diffuse rear reflector	'white paint' / $R_{\text{rear}} = 1, \Lambda_b = 1$	+26.0/+37.9	+7.4/+11.0
Combined	practical / Lambertian limit	+99.2/+113.4	+61.7/+72.5

a random pyramid texture and ARC on the front side decreases J_{sc}^* (see Fig. 2.7). A benefit only occurs when the mirror is combined with a dielectric spacer between metal and Si that prevents parasitic absorption [41]. Finally, the combination of all measures increases J_{sc}^* by a value that is less than the sum of the gain due to the single measures. This again stresses the interdependence of the optical losses.

2.5 Electromagnetic waves at interfaces

The previous section has stressed the importance of controlling the external front reflectance. How much light is reflected/transmitted from/through an interface depends on the refractive index on both sides of the interface, the state of polarization of the light wave and on its angle of incidence. This section gives expressions for reflectance and transmittance at interfaces without and with thin anti-reflection layers and is based on Ref. [30].

2.5.1 Fresnel equations without interference

Figure 2.8 shows an incoming wave with an electric field vector \mathbf{E}_{II} that is perpendicular to the plane of incidence (s -polarization). The subscript specifies whether the field is of an incoming (i), reflected (r) or transmitted (t) wave and the respective boundary (I or II) under consideration. We first consider only boundary I and assume that the

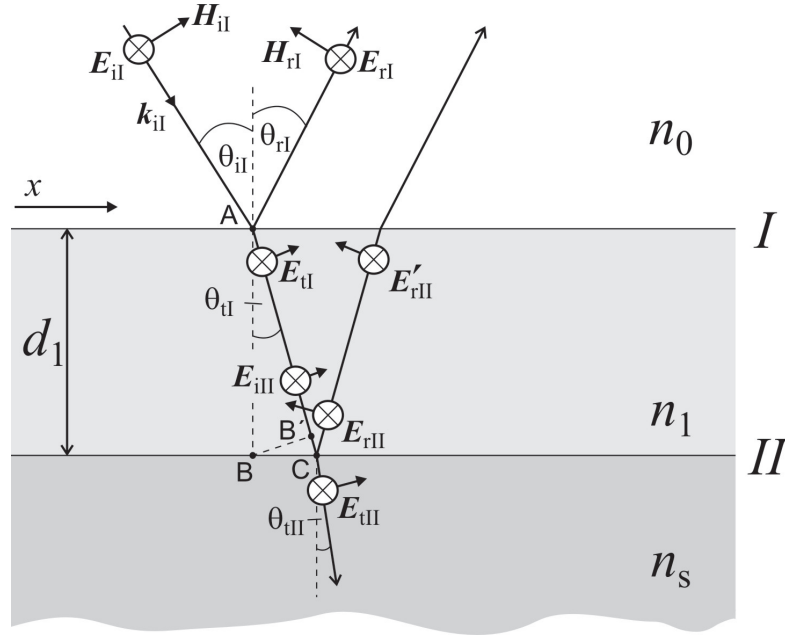


Figure 2.8: The sketch illustrates the electromagnetic fields at the boundaries I and II between the ambient (n_0), the ARC (n_1, d_1) and the substrate (n_s). The incoming wave is s -polarized.

thickness of layer 1 is large compared to the wavelength of the incoming wave ($d_1 \gg \lambda$). The derivation of i) the laws of refraction/reflection and ii) the Fresnel equations follows from the continuity of the tangential components of the (\mathbf{E}) and magnetic (\mathbf{H}) fields on both sides of the interface. We consider plane waves of the form $\mathbf{E} = \mathbf{E}_0 \exp(\mathbf{k} \cdot \mathbf{r} - \omega t)$. As the frequency ω does not change at the interface, it follows that the tangential component of the wave vector must fulfill $\mathbf{k}_{iI}^{\parallel} = \mathbf{k}_{rI}^{\parallel} = \mathbf{k}_{tI}^{\parallel}$. With the definition of the tangential wave vector, $\mathbf{k}_x^{\parallel} = \omega n_x \sin(\theta)/c$, follows the law of reflection (Eq. 2.6) and Snell's law of refraction (Eq. 2.7):

$$\theta_{iI} = \theta_{rI}, \quad (2.6)$$

$$n_0 \sin(\theta_{iI}) = n_1 \sin(\theta_{tI}). \quad (2.7)$$

For the Fresnel equations, we consider the amplitudes of the fields instead of the phase. The continuity of the tangential components implies

$$\mathbf{E}_{iI} + \mathbf{E}_{rI} = \mathbf{E}_{tI}, \quad (2.8)$$

$$(\mathbf{H}_{iI} - \mathbf{H}_{rI}) \cos(\theta_{iI}) = \mathbf{H}_{tI} \cos(\theta_{tI}). \quad (2.9)$$

Here we used the reflection law $\theta_{rI} = \theta_{iI}$. Inserting a plane wave function into Maxwell's equation yields the general relationship

$$\hat{\mathbf{k}} \times \mathbf{E} = \frac{c}{n} \mu \mathbf{H}, \quad (2.10)$$

where $\hat{\mathbf{k}}$ is the unit propagation vector and μ is the magnetic permeability. With this and the assumption of non-magnetic media ($\mu_1 = \mu_s = \mu_0$), Eq. 2.9 can be written as

$$\frac{n_0}{\mu_0}(E_{iI} - E_{rI}) \cos(\theta_{iI}) = \frac{n_1}{\mu_0} E_{tI} \cos(\theta_{tI}) . \quad (2.11)$$

With Eqs. 2.8 and 2.11, we can write the Fresnel equations for *s*-polarized light

$$r_s \equiv \left(\frac{E_{rI}}{E_{iI}} \right)_s = \frac{n_0 \cos(\theta_{iI}) - n_1 \cos(\theta_{tI})}{n_0 \cos(\theta_{iI}) + n_1 \cos(\theta_{tI})} , \quad (2.12)$$

$$t_s \equiv \left(\frac{E_{tI}}{E_{iI}} \right)_s = \frac{2n_0 \cos(\theta_{iI})}{n_0 \cos(\theta_{iI}) + n_1 \cos(\theta_{tI})} . \quad (2.13)$$

The same arguments apply for *p*-polarized light and the Fresnel equations read

$$r_p \equiv \left(\frac{E_{rI}}{E_{iI}} \right)_p = \frac{n_1 \cos(\theta_{iI}) - n_0 \cos(\theta_{tI})}{n_1 \cos(\theta_{iI}) + n_0 \cos(\theta_{tI})} , \quad (2.14)$$

$$t_p \equiv \left(\frac{E_{tI}}{E_{iI}} \right)_p = \frac{2n_0 \cos(\theta_{iI})}{n_1 \cos(\theta_{iI}) + n_0 \cos(\theta_{tI})} . \quad (2.15)$$

The Fresnel equations 2.12, 2.13, 2.14 and 2.15 relate the amplitudes of the electric field of the incoming, reflected and transmitted wave for two different polarizations. The experimentally accessible external reflectance R (and transmittance T) at the interface, however, relates the intensities $I = \langle S \rangle = c\epsilon_0/2 E^2$ (W/m²) (norm of the Poynting vector \mathbf{S}). Considering the reflection law (Eq. 2.6) and Snell's law of refraction (Eq. 2.7), they can be written as

$$R \equiv \frac{I_{rI} \cos(\theta_{iI})}{I_{iI} \cos(\theta_{iI})} = rr^* , \quad (2.16)$$

$$T \equiv \frac{I_{tI} \cos(\theta_{tI})}{I_{iI} \cos(\theta_{iI})} = \frac{n_1 \cos(\theta_{tI})}{n_0 \cos(\theta_{iI})} tt^* . \quad (2.17)$$

As the refractive index is generally complex, so are the Fresnel coefficients r and t which is why we use their complex conjugates r^* and t^* .

2.5.2 Fresnel equations with interference and design guidelines for an ARC

The reflection/transmission from/through an interface has to be treated differently when dielectric layers are involved that have a thickness in the range of the coherence length ($d_1 \approx$ few tenths of λ). These so-called anti-reflection layers allow interference of the

waves that are reflected at each interface. In case of destructive interference, the external reflectance is reduced and more light is coupled into the substrate. The difference to the derivation of the Fresnel equations is that for the boundary condition at interface I in Fig. 2.8 also the tangential component of the reflected wave from interface II, $\{\mathbf{E}'_{rII}, \mathbf{H}'_{rII}\}$, needs to be accounted for.

The wave that traverses the dielectric layer experiences a phase shift k_0h , where h is the optical path between the points A and B' in Fig. 2.8¹.

$$h = n_1 \overline{AB'} = n_1 d \cos(\theta_{tI}) . \quad (2.18)$$

The phase shift for a traversal then leads to

$$E_{iII} = E_{tII} \exp(-ik_0h) , \quad (2.19)$$

$$E_{rII} = E'_{rII} \exp(+ik_0h) . \quad (2.20)$$

The boundary conditions at both interfaces I and II can be written in matrix form as

$$\begin{pmatrix} E_{iI} + E_{rI} \\ E_{iI} - E_{rI} \Upsilon_0 \end{pmatrix} = \begin{pmatrix} \cos(k_0h) & i \sin(k_0h)/\Upsilon_1 \\ i \sin(k_0h) \Upsilon_1 & \cos(k_0h) \end{pmatrix} \begin{pmatrix} E_{tII} \\ E_{tII} \Upsilon_s \end{pmatrix} = \mathbf{M}_I \begin{pmatrix} E_{tII} \\ E_{tII} \Upsilon_s \end{pmatrix} , \quad (2.21)$$

with

$$\Upsilon_0 \equiv \frac{\mu_0}{c} n_0 \cos(\theta_{iI}), \quad \Upsilon_1 \equiv \frac{\mu_0}{c} n_1 \cos(\theta_{tI}), \quad \Upsilon_s \equiv \frac{\mu_0}{c} n_s \cos(\theta_{tII}) . \quad (2.22)$$

For p -polarization the result is the same but the cosine terms in Eq. 2.22 are in the denominator. The characteristic matrix \mathbf{M}_I relates the fields at the two adjacent boundaries of the ARC. This formalism can be extended to any number N of ARC layers, each with a specific n and h , by simply multiplying the matrices $\mathbf{M}_I \mathbf{M}_{II} \dots \mathbf{M}_N = \mathbf{M}$.

With the two equations of Eq. 2.21 and the elements $(m_{ij})_{i,j \in \{1,2\}}$ of the characteristic matrix \mathbf{M} we can write the reflection and transmission coefficient for any film configuration and angle of incidence

$$r = \frac{E_{rI}}{E_{iI}} = \frac{\Upsilon_0 m_{11} + \Upsilon_0 \Upsilon_s m_{12} - m_{21} - \Upsilon_s m_{22}}{\Upsilon_0 m_{11} + \Upsilon_0 \Upsilon_s m_{12} + m_{21} + \Upsilon_s m_{22}} \equiv \frac{\Upsilon_0 B - C}{\Upsilon_0 B + C} , \quad (2.23)$$

$$t = \frac{E_{tII}}{E_{iI}} = \frac{2\Upsilon_0}{\Upsilon_0 m_{11} + \Upsilon_0 \Upsilon_s m_{12} + m_{21} + \Upsilon_s m_{22}} \equiv \frac{2\Upsilon_0}{\Upsilon_0 B + C} , \quad (2.24)$$

¹The phase shift is between A and B' rather than between A and C because the transfer matrix formalism always describes the relationship between fields for constant x -coordinate. Thus, h corresponds to the difference between the phase front through A and B in Fig. 2.8.

where we define the complex quantities $B = m_{11} + \Upsilon_s m_{12}$ and $C = m_{21} + \Upsilon_s m_{22}$. The reflectance R and transmittance T follow then similarly to Eqs. 2.16 and 2.17 and, in general form, read [42]

$$R = \left(\frac{\Upsilon_0 B - C}{\Upsilon_0 B + C} \right) \left(\frac{\Upsilon_0 B - C}{\Upsilon_0 B + C} \right)^* , \quad (2.25)$$

$$T = \frac{4\Upsilon_0 \operatorname{Re}(\Upsilon_s)}{(\Upsilon_0 B + C)(\Upsilon_0 B + C)^*} . \quad (2.26)$$

The absorptance in the ARC follows from the condition $A + R + T = 1$ and reads

$$A = \frac{4\Upsilon_0 \operatorname{Re}(BC^* - \Upsilon_s)}{(\Upsilon_0 B + C)(\Upsilon_0 B + C)^*} . \quad (2.27)$$

Figure 2.9 shows the impact of ARCs on the reflectance R of an air/silicon interface. All curves are calculated for normal incidence $\theta_{iI} = \theta_{tI} = \theta_{tII} = 0^\circ$. The red curve is the reference reflectance without any ARC, calculated by Eqs. 2.12/2.14 and 2.16. The blue curves illustrate the reflectances of a single (SARC) and a double layer (DARC) dielectric coating of the silicon substrate, calculated by Eq. 2.25. The minimum reflectance is reached for $k_0 h = \pi/2$, which is equivalent to the claim that the optical film thickness h is an odd multiple of a quarter wavelength:

$$n_1 d_1 = \lambda_0 / 4 , \quad (2.28)$$

where λ_0 is the design wavelength at which the reflectance is minimized. At λ_0 and normal incidence, the reflectance becomes zero for the SARC if the refractive index of the ARC n_1 holds

$$n_1^2 = n_0 n_s . \quad (2.29)$$

The SARC in Fig. 2.9 has a constant refractive index $n_1 = 1.9$ and a thickness of $d_1 = 80$ nm and is designed to minimize the reflectance at a wavelength of $\lambda_0 = 600$ nm. The green circles correspond to the minimum position of the reflectance R_{\min} when the refractive index is fixed at 1.9 and the thickness d_1 varies between 50 – 110 nm in steps of 5 nm. The ARC thickness affects the design wavelength according to Eq. 2.28. The minimum reflectance remains approximately zero as long as the refractive index of silicon does not vary too much and (nearly) satisfies Eq. 2.29 with $n_1 = 1.9$. It looks different when the ARC thickness remains constant at 80 nm and the refractive index n_1 varies. This is shown by the orange squares in Fig. 2.9 for n_1 -values between 1.6 and 2.2 in steps of 0.05. Variations in the refractive index affect both Eqs. 2.28 and 2.29 and prevents the reflectance from becoming zero.

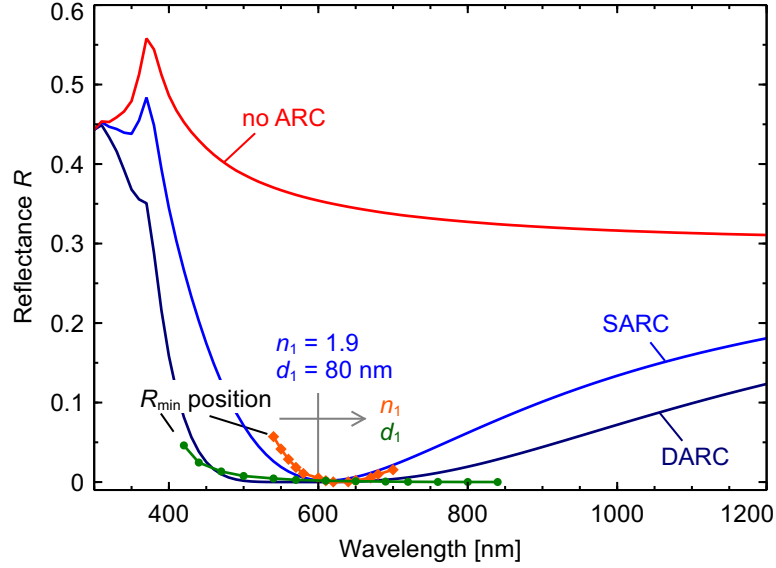


Figure 2.9: The figure shows the reflectance of a silicon substrate in air with no ARC layer (red curve), a single ARC (SARC) layer ($n_1 = 1.9$, $d_1 = 80\text{nm}$) and a double ARC (DARC) layer ($n_1 = 1.46$, $d_1 = 103\text{nm}$; $n_2 = 2.9$, $d_2 = 52\text{nm}$). Both ARC stacks are designed to minimize the reflectance at 600 nm. The green circles and orange diamonds denote the reflectance minimum R_{\min} of the SARC case for when d_1 or n_1 are varied, respectively.

For the DARC, if both AR layers have the same λ_0 , the reflectance becomes zero if

$$\left(\frac{n_2}{n_1}\right)^2 = \frac{n_s}{n_0} . \quad (2.30)$$

with $n_0 < n_1 < n_2 < n_s$. The DARC in Figure 2.9 consists of $n_1 = 1.46$, $d_1 = 103\text{ nm}$ and $n_2 = 2.9$, $d_2 = 52\text{ nm}$. It produces a wider reflectance minimum than the SARC, given that both layers are optimized to the same wavelength. The second ARC layer can also be tuned with respect to the first one to create a reflectance minimum at a different design wavelength. This results in two distinct reflectance minima in the spectrum.

2.6 Light trapping schemes in ray optics

We introduce two light trapping schemes, one with no light trapping and the other with Lambertian light trapping. The latter refers to a structure, where the light that is transmitted through the front surface into the structure is fully randomized in its propagation direction at the first transition. This serves as benchmark for excellent light trapping. Both structures have an effective absorber thickness

$$W_{\text{eff}} = V/A , \quad (2.31)$$

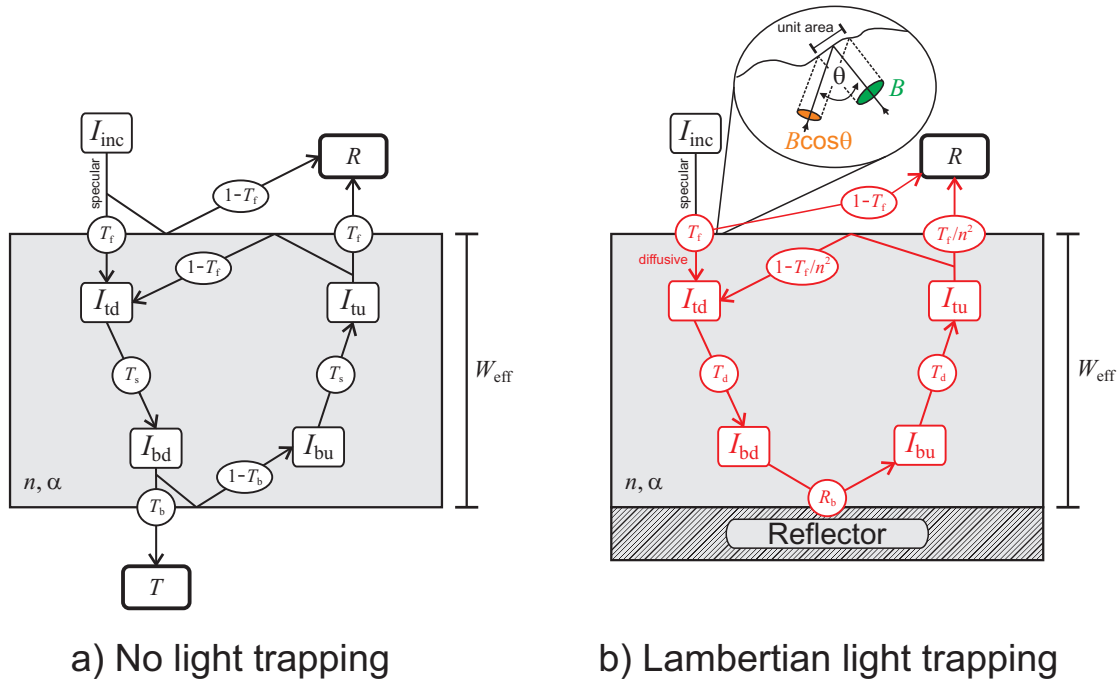


Figure 2.10: The sketch introduces the intensities within the absorber for the case of a) no light trapping and b) Lambertian light trapping with arbitrary front and back transmittance $T_f = 1 - R_f$ and $T_b = 1 - R_b$. The inset in b) illustrates the Lambertian cosine law that describes isotropic internal photon flux density per solid angle (see Sec 2.6.2).

which is the ratio of the volume V of the experimental absorber that is to be qualified to its macroscopic area A . This accounts for the surface roughness introduced by the texture that is not present in these two reference structures. Thus, for a planar wafer the effective thickness corresponds to the actual thickness.

The next subsections introduce analytical expressions for the absorptance in these two reference structures, following the approach of Refs. [23, 43]. The derivation neglects the wave character of light and is thus set in frame of ray optics. This approximation can only be valid when i) the thickness of the wafer is large compared to the wavelength of the incident light λ and ii) the surface texture is either random or has a period that is much larger than λ so that diffraction and interference effects can be neglected.

2.6.1 No light trapping

Figure 2.10 a) sketches the light power fluxes I_{ij} in a planar wafer with refractive index n , absorption coefficient α and effective thickness W_{eff} . The index $i = t, b$ specifies whether the flux is at the top or bottom of the wafer. The top side is directed towards the incoming light. The index $j = u, d$ specifies whether the light propagates upwards or downwards within the wafer, where downwards is the direction of the incoming light.

Specular light of intensity I_{inc} impinges normally onto the wafer. It has the probability T_m ($m = f, b$) to become transmitted and $1 - T_m$ to become reflected at the *front* or *back* interface. These probabilities do not account for parasitic absorption in the ARC or dielectric layers at the back. Since the wafer has no light trapping, the light is not scattered and remains specular throughout the passes within the wafer as indicated by the black color of the arrows. The transmittance of specular light through the wafer is

$$T_s = \exp(-\alpha W_{\text{eff}}) . \quad (2.32)$$

The absorption of the planar wafer A_{pl} is the part of the power flux that is not being transmitted during the propagation within the material and reads

$$A_{\text{pl}} = (1 - T_s)(I_{\text{t,d}} + I_{\text{b,u}}) . \quad (2.33)$$

The equations for the various power fluxes can be set up by following the arrows and collecting the multipliers on these paths. For an incoming power flux of $I_{\text{inc}} = 1$ they read

$$I_{\text{t,d}} = T_f + (1 - T_f)I_{\text{t,u}} , \quad (2.34)$$

$$I_{\text{b,d}} = T_s I_{\text{t,d}} , \quad (2.35)$$

$$I_{\text{b,u}} = (1 - T_b)I_{\text{b,d}} , \quad (2.36)$$

$$I_{\text{t,u}} = T_s I_{\text{b,u}} . \quad (2.37)$$

This linear equation system has a distinct solution for the fluxes in Eq. 2.33 and yields an absorptance of

$$A_{\text{pl}} = (1 - T_s)T_f \left(\frac{1 + (1 - T_b)T_s}{1 - (1 - T_b)(1 - T_f)T_s^2} \right) . \quad (2.38)$$

In a similar manner, expressions for the reflectance R_{pl} and transmittance T_{pl} can be set up:

$$R_{\text{pl}} = (1 - T_f) + T_f I_{\text{t,u}} = (1 - T_f) + \left(\frac{(1 - T_b)T_f^2 T_s^2}{1 - (1 - T_b)(1 - T_f)T_s^2} \right) , \quad (2.39)$$

$$T_{\text{pl}} = T_b I_{\text{b,d}} = \frac{T_f T_s T_b}{1 - (1 - T_b)(1 - T_f)T_s^2} . \quad (2.40)$$

The sum of the three terms $A_{\text{pl}} + R_{\text{pl}} + T_{\text{pl}}$ equals the incoming power flux, which is 1 in this case. In practice, the absorptance of a wafer with polished surfaces, known optical thickness αW_{eff} and known front and back transmittance, T_f and T_b , respectively, can be described by Eq. 2.38. In the limit case of no light trapping ($T_f = T_b = 1$), however, the absorptance reduces to an expression that directly follows from the Lambert-Beer

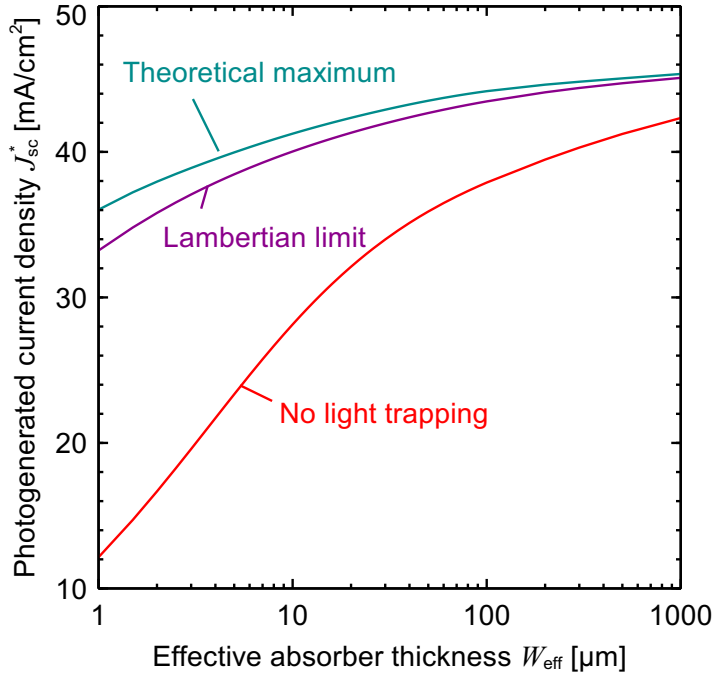


Figure 2.11: The plot shows the photogenerated current densities J_{sc}^* according to Eq. 2.4 in dependence of the effective absorber thickness W_{eff} and the light trapping schemes no light trapping (red, see Eq. 2.41), the Lambertian limit (magenta, see Eq. 2.47) and the theoretical maximum (cyan, see Eq. 2.51).

law of Eq. 2.3

$$A_{\text{noLT}} = 1 - T_s = 1 - \exp(-\alpha W_{\text{eff}}). \quad (2.41)$$

The red line in Fig. 2.11 illustrates the photogenerated current density J_{sc}^* according to Eq. 2.4 for different absorber thicknesses W_{eff} for the structure with no light trapping.

2.6.2 The Lambertian limit

Figure 2.10 b) illustrates the same power fluxes in a structure with Lambertian light trapping. Light that is reflected from or traverses a Lambertian surface is, by definition, fully randomized in its propagation direction. This is indicated by the red color of the arrows in Fig. 2.10 b). The randomization leads to an isotropic photon flux per solid angle within the structure which implies that the internal light intensity B per unit internal solid angle is angle-independent [44]. The total internal light intensity I_{int} that is incident on a unit surface area thus reads [45–47]:

$$I_{\text{int}} = \int_{\Omega} B \cos\theta \, d\Omega, \quad (2.42)$$

where $\cos\theta$ is the reduction of the intensity on the area element due to oblique incidence and $d\Omega = \sin\theta \, d\theta \, d\phi$ corresponds to the solid angle differential with the azimuth ϕ and

polar angle θ , respectively. This is illustrated in the inset of Fig. 2.10 b). The diffuse light flux allows for total internal reflection at the interfaces for light with an angle of incidence $\theta > \theta_c$ (see Eq. 2.5). Accordingly, only light that hits the surface within the "loss cone", which is defined by $\theta < \theta_c$, can exit the structure with the probability T_f (see Fig. 2.4). For a uniform internal intensity per solid angle, the fraction of light f within the loss cone is

$$f = \frac{\int_0^{\theta_c} \int_0^{2\pi} B \cos\theta \sin\theta \, d\theta \, d\phi}{\int_0^{\pi} \int_0^{2\pi} B \cos\theta \sin\theta \, d\theta \, d\phi} = \sin^2\theta_c = \frac{1}{n^2}. \quad (2.43)$$

The last step follows from Eq. 2.5. Thus, in contrast to the planar wafer, the transmission probability of diffuse light through the surface is T_f/n^2 . Note that the transmission probability T_f is in fact a weighted average over the angle of incidence, i.e. $T_f = \overline{T_f(\theta)}$. At the rear side, the structure has a reflector with a reflection probability of R_b^2 .

Similarly to the structure with no light trapping, the transmittance T_d of diffuse light through a wafer equals the ratio of the internal intensities at the top and bottom surface [48]:

$$T_d = \frac{\int_0^{\pi/2} \int_0^{2\pi} B \cos\theta \sin\theta \exp\left(-\frac{\alpha W_{\text{eff}}}{\cos\theta}\right) \, d\theta \, d\phi}{\int_0^{\pi/2} \int_0^{2\pi} B \cos\theta \sin\theta \, d\theta \, d\phi}. \quad (2.44)$$

The cosine in the exponential accounts for the oblique traversal of light through the wafer. The substitution $t = \left(\frac{\alpha W_{\text{eff}}}{\cos\theta}\right)$ and two partial integrations yield [49, 50]

$$T_d = \exp(-\alpha W_{\text{eff}})(1 - \alpha W_{\text{eff}}) + (\alpha W_{\text{eff}})^2 \int_{\alpha W_{\text{eff}}}^{\infty} t^{-1} \exp(-t) dt. \quad (2.45)$$

The exponential integral can be solved numerically or approximated by a polynomial expression with a precision of 10^{-5} [51]. The absorptance of the sample with Lambertian light trapping, external front reflectance $R_f = 1 - T_f$ and back reflectance R_b is derived similarly to Eq. 2.38 and reads

$$A_{\text{Lamb}} = (1 - T_d)T_f \left(\frac{(1 + R_b T_d)n^2}{n^2 - (n^2 - T_f)R_b T_d^2} \right). \quad (2.46)$$

²A more general expression for a detached rear reflector is given in Ref. [13, 23].

The Lambertian limit follows from setting $T_f = 1$ and $R_b = 1$ in Eq. 2.46 and yields

$$A_{\text{Lamb,limit}} = \frac{(1 - T_d^2)n^2}{n^2 - (n^2 - 1)T_d^2}. \quad (2.47)$$

Figure 2.11 depicts the performance of the Lambertian limit in magenta.

2.6.3 Path length enhancement Z

In Fig. 2.4 we have introduced a path length enhancement factor Z that can be associated with a light trapping scheme. In this section, we derive the Z factor for both reference structures in Fig. 2.10. We assume that weakly absorbed light with $\alpha W_{\text{eff}} \ll 1$ has an average path length of $\bar{l} = ZW_{\text{eff}}$ and hence Z can be expressed as [23]

$$Z = \lim_{\alpha W_{\text{eff}} \rightarrow 0} \left(\frac{A}{\alpha W_{\text{eff}}} \right). \quad (2.48)$$

We start with the planar case and insert Eq. 2.38 into Eq. 2.48. Expanding the transmittance to the lowest order in αW_{eff} , i.e. $T_s \approx 1 - \alpha W_{\text{eff}}$, yields

$$Z_{\text{pl}} = \frac{T_f(1 + R_b)}{1 - R_b(1 - T_f)}. \quad (2.49)$$

For the limit case of no light trapping ($T_f = 1$, $R_b = 0$), the path length enhancement is $Z_{\text{pl}} = 1$, i.e. light traverses the wafer once and is emitted again.

In case of Lambertian light trapping, Eq. 2.46 has to be inserted in Eq. 2.48. The expansion of Eq. 2.45 yields $T_d \approx 1 - 2\alpha W_{\text{eff}}$ and hence

$$Z_{\text{Lamb}} = \frac{2T_f(1 + R_b)n^2}{n^2 - (n^2 - T_f)R_b}. \quad (2.50)$$

In case of ($T_f = 1$, $R_b = 1 - 1/n^2$), i.e. the rear side is characterized by total internal reflection, the path length enhancement is $Z_{\text{Lamb}} = 2n^2$. For the Lambertian limit with a perfect rear reflector we obtain $Z_{\text{Lamb,limit}} = 4n^2$ [46, 52]. Thus, the average path length for weakly absorbed light can be extended up to a factor ≈ 50 for a silicon absorber in the Lambertian limit. For a single traversal, i.e. $R_b = 0$, the result becomes $Z_{\text{Lamb}} = 2$. This means that the average path length of fully randomized light is the same as light that traverses the wafer under an angle of $\bar{\theta} = 60^\circ$.

2.6.4 Surpassing the Lambertian limit

Yablonovitch and Cody derived the $4n^2$ limit in two ways by using statistical mechanics and geometrical optics [46]. The derivation by geometrical optics, as in this work, relies on the assumption of an idealized surface texture that has the same transmittance T_f for all angles of incidence. Minano and Luque extended the analysis by using non-imaging optics and showed that the average path length of the Lambertian limit $\bar{l} = 4n^2 W_{\text{eff}}$ equals the maximum achievable average path length \bar{l}_{max} for *any* geometrical light trapping scheme under isotropic illumination [48, 53]. Brendel then showed that this also holds for structures with non-zero surface reflectance [23].

An average path length of $\bar{l} = 4n^2 W_{\text{eff}}$ can be realized with various path length distributions $f(l)$. The theoretical maximum absorptance $A_{\text{theo,limit}}$ is reached when all rays have the same path length $\bar{l}_{\text{max}} = 4n^2 W_{\text{eff}}$, as the following steps show [53]. The absorptance A can be written as

$$\begin{aligned}
 A &= 1 - \int_0^{\infty} f(l) \exp(-\alpha l) dl \\
 &= 1 - \int_0^{\infty} f(l) \exp(-\alpha(l - \bar{l})) \exp(-\alpha \bar{l}) dl \\
 &\leq 1 - \int_0^{\infty} f(l) (1 - \alpha(l - \bar{l})) \exp(-\alpha \bar{l}) dl \\
 &= 1 - \exp(-\alpha \bar{l}) \\
 &\leq 1 - \exp(-\alpha 4n^2 W_{\text{eff}}) = A_{\text{theo,limit}} ,
 \end{aligned} \tag{2.51}$$

where we have used the definition $\bar{l} = \int_0^{\infty} f(l) l dl$ and the power series expansion of the exponential function $\exp(x) \geq 1 - x$. For maximum absorptance, the path length distribution thus must be the Dirac distribution $f(l) = \delta(l - 4n^2 W_{\text{eff}})$ which cannot be realized under isotropic illumination. The Lambertian light trapping scheme, that comprises all other path distributions $f(l)$ that result in an average path length of $\bar{l} = 4n^2 W_{\text{eff}}$, can therefore be regarded as the highest achievable degree of light trapping under isotropic illumination. Figure 2.11 shows the theoretical maximum performance in comparison with no light trapping and the Lambertian limit.

In nature, there is no material that fulfills the Lambertian cosine law exactly, let alone the optimum light trapping scheme. Materials approaching the Lambertian case are sintered polytetrafluorethylene (PTFE), known as Spectralon, dull paper or the emitting surface of a LED [54]. In silicon solar cells, the random pyramid texture provides light scattering that approaches the Lambertian surface, as will be shown in Chs. 6 and 7.

The discrepancy arises from the fact that random pyramids, compared to a Lambertian surface, scatter less light into large angles [55].

The $4n^2$ -limit under isotropic illumination can be surpassed by restricting the angular acceptance of the cell. It was shown that a restriction to θ , i.e. only rays within a cone of angle θ to the surface normal of the absorber can enter it, leads to an average path length of [53, 56]

$$\bar{l} \leq \frac{4n^2 W_{\text{eff}}}{\sin^2(\theta)} = \bar{l}_{\text{max}}(\theta) \quad (2.52)$$

The upper bound of the path length is reached when not only the illumination but also the light that escapes from the absorber is restricted to θ . If the absorber emitted light under a larger angle than θ , this would imply (due to the reversibility of light paths) that not all possible ray paths inside the cell are illuminated. Parabolically shaped reflecting microconcentrators [56, 57] or an angle-selective anti-reflection coating on the surface of the cell [56] have been suggested to restrict illumination. Campbell and Green demonstrated theoretically that a structure with 2-D grooves at the front and rear side which are oriented perpendicular to each other performs better than the Lambertian light trapping scheme under normally incident illumination [52]. More information on light concentration and restricted illumination can be found in Ref. [58].

While the restriction of the acceptance angle of a solar cell is an option for specific systems that have a fixed or at least predictable illumination direction, it is not suited for the integration of large-scale photovoltaic systems into an existing infrastructure, like roofs of buildings. As the sun moves across the sky during the day, the solar cells would have to be mounted on mechanical tracking systems which are expensive and require maintenance. Furthermore, in a climate region like Germany nearly 50% of the incident light is diffuse rather than direct [59]. Diffuse illumination cannot be collected even by a concentrator lens. Therefore, light trapping schemes for large-scale PV systems should be optimized for isotropic rather than normally incident illumination.

Another way to exceed the $4n^2$ limit is to take the wave character of light and therefore effects like interference or diffraction into guided modes into consideration [60]. This can be realized with regular textures that have feature sizes and a periodicity in the range of the wavelength of the incoming light λ . Yu *et al.* showed that a maximum path length enhancement of $Z = 8\pi n^2/\sqrt{3}$ is feasible with 2-dimensional triangular dielectric diffraction gratings that have a periodicity $a = 2\lambda/\sqrt{3}$ [61]. As this enhancement applies only for a specific wavelength and, in addition, is sensitive on the angle of incidence, it is difficult to show an advantage of periodic light trapping schemes over random ones on device level where the whole convertible spectrum is involved [55]. Optical simulations

have also shown that introducing a certain asymmetry to periodic light trapping schemes can be beneficial for reaching a higher absorptance [62, 63].

2.7 Device parameters in solar cells

We have discussed the light management and its impact on the photogenerated current density J_{sc}^* . However, the power generated by a solar cell is defined as the product of the current and the voltage at maximum power point conditions [41]. The implied open-circuit voltage V_{oc}^* of an absorber refers to the separation of the quasi-Fermi levels under a fixed illumination when no current is extracted. For an n -type absorber with a doping density N_{D} it can be written as

$$V_{\text{oc}}^* = V_{\text{th}} \ln \left(\frac{\Delta p (N_{\text{D}} + \Delta n)}{n_{\text{i}}^2} \right), \quad (2.53)$$

$n_{\text{i}} = 8.7 \times 10^9 \text{ cm}^{-3}$ [5] and $V_{\text{th}} = 25.7 \text{ mV}$ are the intrinsic carrier concentration and the thermal voltage at a temperature of $T = 298.15 \text{ K}$, respectively. Δn and Δp are the excess electrons and holes. The term "implied" shall symbolize that this voltage is also defined for solar cell precursors without contacts or surface passivated absorbers without an emitter [64]. It can be regarded as the maximum open-circuit voltage V_{oc} of the latter device, i.e. $V_{\text{oc}} < V_{\text{oc}}^*$ when illuminated by a photon flux equivalent to 1 sun.

Equation 2.53 yields that the excess carrier density under steady-state conditions for a fixed illumination determines the voltage of the cell. The dynamics of the excess carrier concentration are described by the continuity equation

$$\frac{d}{dt} \Delta n(t) = G(t) - U(t) \quad (2.54)$$

$$= G(t) - \frac{\Delta n(t)}{\tau_{\text{eff}}(\Delta n)}, \quad (2.55)$$

where $G(t)$ is the generation rate and $U(t)$ the recombination rate of excess carriers. The spatial distribution of $\Delta n(t)$ and $G(t)$ within the absorber can be assumed to be uniform if the surface recombination rate is small and the carrier generation is spatially homogeneous.³ Surface textures that improve the light management in a solar cell and thus the generation rate G , usually increase the surface area and therefore the recombination rate U . This way a higher generation rate due to light trapping may be overcompensated by a higher recombination rate, resulting in a lower excess carrier density under steady-state condition and a lower voltage.

³For the same reason, the current term $+\frac{1}{q} \text{div} \mathbf{J}$ on the r.h.s. of Eq. 2.54 is neglected.

Equation 2.55 introduces the effective minority carrier lifetime τ_{eff} of the sample that in general depends on the injection level Δn . τ_{eff} and Δn are measured experimentally (see Ch. 3). For steady-state condition, i.e. $G = U$, we can derive an expression for V_{oc}^* if we assume a homogeneous generation rate ($G = J_{\text{sc}}^*/qW_{\text{eff}}$) as well as charge neutrality ($\Delta n = \Delta p$). Inserting Eq. 2.53 into Eq. 2.55 and solving for V_{oc}^* yields

$$V_{\text{oc}}^* = V_{\text{th}} \ln \left(\frac{1}{n_i^2} \left(\frac{J_{\text{sc}}^*}{qW_{\text{eff}}} \tau_{\text{eff}} + \frac{N_{\text{D}}}{2} \right)^2 - \frac{N_{\text{D}}^2}{4n_i^2} \right). \quad (2.56)$$

If not mentioned otherwise, the effective lifetime τ_{eff} is taken at an absorbed photon flux that is equivalent to 1 sun.

The photogenerated current density J_{sc}^* corresponds to the current density from a solar cell if it is short-circuited, i.e. all photogenerated carriers are extracted. The implied open-circuit voltage V_{oc}^* yields the highest possible voltage if no current is extracted. However, the generated power is the product of current and voltage and therefore zero under both operating conditions. The solar cell gives the largest power at the maximum power point ($V_{\text{mpp}}, J_{\text{mpp}}$) which relates to the short-circuit current density and the open-circuit voltage by the fill factor FF [41]. The fill factor is determined by the injection-dependence of the carrier lifetime and by parasitic resistances like series and shunt resistance. The efficiency η of the solar cell relates to the three device parameters by

$$\eta = \frac{P_{\text{out}}}{P_{\text{in}}} = \frac{J_{\text{sc}} \times V_{\text{oc}} \times FF}{P_{\text{in}}}, \quad (2.57)$$

where P_{in} is the incident illumination intensity. In this work, we take an empirical expression for the fill factor FF^* where we neglect parasitic resistances [65]:

$$FF^* = \frac{v_{\text{oc}}^* - \ln(v_{\text{oc}}^* + 0.72)}{v_{\text{oc}}^* + 1}, \quad (2.58)$$

with the normalized voltage $v_{\text{oc}}^* = V_{\text{oc}}^*/mV_{\text{th}}$ and the ideality factor m . The fill factor expression in Eq. 2.58 again gives an upper limit for the fill factor of the real solar cell, i.e. $FF < FF^*$. The ideality factor is a measure of how much the current-voltage behavior of a solar cell, as described in the one-diode equation

$$J(V) = J_{\text{sc}} - J_0 \exp \left(\frac{V}{mV_{\text{th}}} - 1 \right), \quad (2.59)$$

differs from an ideal diode. J_0 symbolizes the dark saturation current density. m varies with the current level and takes a value of 2 if the recombination is limited by both carrier types, as for SRH recombination in high injection or recombination in the depletion region, to 1 if the recombination is limited by the minority carriers, like for SRH recombination in low injection. The ideality may decrease to $m = 2/3$ if the recombination is

limited by Auger processes [41, 66].

We define a quality factor QF as the normalized product of the three device parameters J_{sc}^* , defined by Eq. 2.4, V_{oc}^* , defined by Eq. 2.56, and FF^* , defined by Eq. 2.58:

$$QF = \frac{J_{sc}^* \times V_{oc}^* \times FF^*}{J_{sc,0}^* \times V_{oc,0}^* \times FF_0^*} . \quad (2.60)$$

The subscript 0 symbolizes the quantities for an appropriate reference sample. The quality factor reflects the impact of light trapping and increased surface recombination on the limiting efficiency. It allows to compare different light trapping schemes over a reference and shows whether they can prove to be useful in the solar cell.

2.8 Electrochemical etching of macropores in silicon

This section gives the theoretical background of macropore⁴ formation in n -type silicon by means of electrochemical anodization with an HF containing electrolyte. Anodization means applying an anodic voltage across a Si/electrolyte interface (see Fig. 3.5 on p. 47). We introduce the suggested mechanisms for the chemical dissolution reactions, discuss the current-voltage curve with respect on the band diagrams of the Si/electrolyte interface and summarize the space charge region model that has been suggested to explain pore formation. For more comprehensive reviews on the matter we refer to the literature [37, 68–70].

2.8.1 Dissolution reactions

The basic requirement for the growth of pores is the electrochemical dissolution of silicon at the Si/electrolyte interface. In HF-based electrolytes, two dissolution mechanisms prevail: direct and indirect dissolution [68].

Direct dissolution – The suggested reaction mechanism for direct dissolution of silicon is [71]



Figure 2.12 illustrates the proposed reaction scheme. The reaction is initiated by a hole from the solid approaching the Si/electrolyte interface. This hole allows for a nucleophilic substitution⁵ during which the surface terminating Si-H bond gets replaced by a Si-F bond (step 1 in Fig. 2.12). This is the rate-limiting step of the reaction. Then, a second

⁴Macropores refer to pores with a diameter > 50 nm [67].

⁵A nucleophile, here the fluoride species, donates an electron pair to an electrophile, here the Si with the hole, to form a chemical bond.

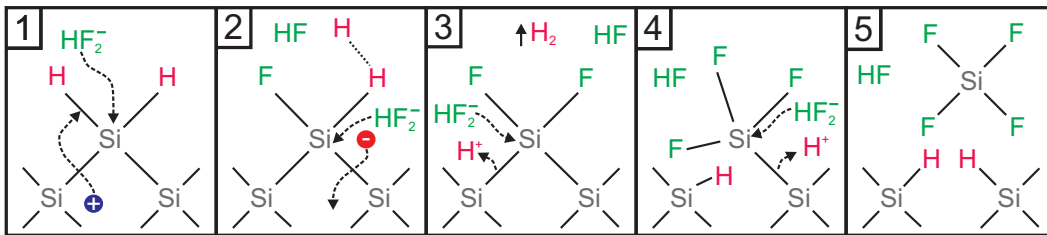


Figure 2.12: Proposed reaction scheme for the direct dissolution of silicon electrodes in HF under anodic conditions. Fluoride species and hydrogen are coloured in green and red, respectively. The figure is adapted from [71].

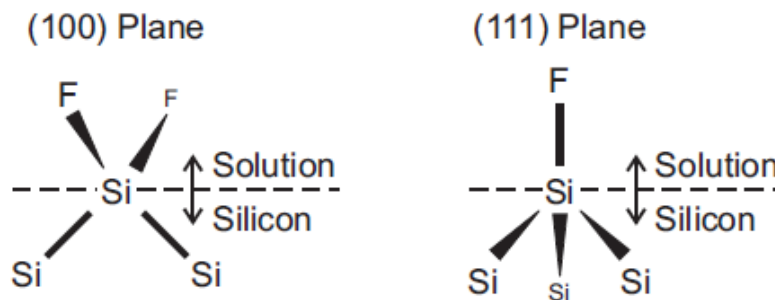
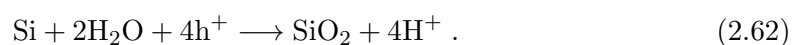


Figure 2.13: Bond orientation for two different crystal planes, which explains the crystal orientation dependence of the direct dissolution mechanism. The figure is adapted from [74].

nucleophilic attack occurs under injection of an electron, resulting in another Si-F bond (step 2). Step 2 is not initiated by a charge carrier and the electron injection is a mere result of the reaction. Hydrogen, as reaction product, escapes in the form of gaseous H_2 . The Si-F bonds polarize the two remaining Si backbonds which are eventually broken by HF or H_2O (steps 3 and 4). The new Si surface atoms establish Si-H bonds again (step 5). The SiF_4 reacts with two HF molecules to SiF_6^{2-} and two protons and stays in solution. Only two charge carriers per dissolved silicon atom flow through the external circuit, yielding a dissolution valence of $n = 2$ [72]. The polarizing effect of the Si backbonds causes an anisotropy of the dissolution reaction [73, 74]: Figure 2.13 illustrates the Si backbonds for two surface orientations and shows that while for {100} surfaces two F atoms polarize two Si backbonds, only one F atom polarizes three Si backbonds for {111} surfaces. This resembles the alkaline dissolution reaction of Si with the difference that for alkaline etching no hole is required for initiation [68]. As a consequence, the etch rate in (100)-direction is larger than in (111) direction.

Indirect dissolution – The indirect dissolution is a two step process and starts by the formation of a silicon oxide at the Si/electrolyte interface under an anodic voltage:



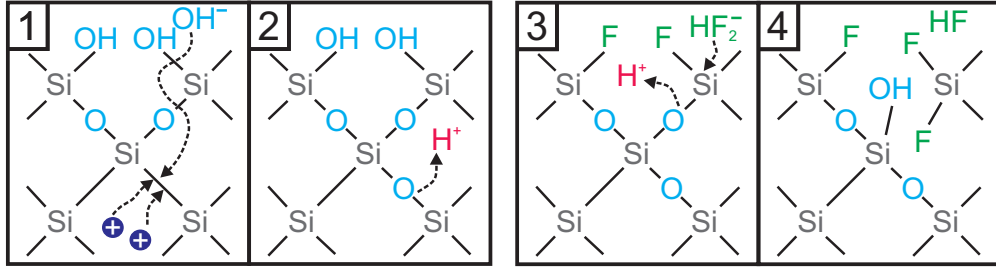
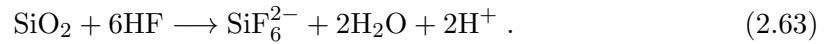


Figure 2.14: Proposed reaction scheme for the indirect dissolution of silicon electrodes in HF under anodic conditions. Fluoride and oxygen species and hydrogen are coloured in green, blue and red, respectively. The figure is adapted from [71].

Figure 2.14 illustrates the proposed reaction scheme. The anodic potential enables OH^- ions to diffuse through the oxide film and to establish a Si-O-Si bond under the consumption of two holes (steps 1 and 2 in Fig. 2.14). Thus, for one Si atom, four holes are required yielding a dissolution valence of $n = 4$ [68]. In the second step, the anodic oxide dissolves by a nucleophilic attack of Si by a fluoride species and an electrophilic attack of the oxygen backbonded to Si by H^+ (steps 3 and 4) [37, 68] as can be described by the overall reaction [72]:



In contrast to the direct dissolution, no hydrogen evolves and no crystal orientation dependence is observed. Depending on whether the oxide formation or the dissolution of the oxide is the rate-limiting step, either pores grow or the surface gets electropolished, as will be explained in the following.

2.8.2 Current-voltage characteristics of Si/HF interface

As in this work we anodize n -type Si, we have to provide the holes for the dissolution initiation externally by illuminating the sample from the rear side. When the Si electrode then dissolves, charge carriers flow across the interface and through the external circuit. This current flow depends on the illumination level as well as on the applied voltage. Figure 2.15 shows the current-voltage curve of the n -type Si/electrolyte system in the dark, i.e. without external illumination, (sample 1) and for three different illumination intensities I_1 (sample 2), I_2 (sample 3) and I_3 (sample 4). The experimental conditions can be found in Table B.1 in the Appendix B under samples 1 through 4. The voltage is measured with respect to a reference electrode (platinum wire close to the Si/electrolyte interface, see Fig. 3.5).

For a better understanding of the current-voltage behaviour, we also look at the energy band diagrams of the Si/electrolyte interface for different voltage conditions in Fig. 2.16. The energy level representation in the electrolyte is taken from Gerischer [75, 76]. Each redox couple in the electrolyte, e.g. $\text{H}_2/\text{H}_3\text{O}^+$, has a specific redox potential E_{redox}^0 . Furthermore, the oxidized species, e.g. H_3O^+ , and the reduced species, e.g. H_2 , have characteristic energy levels E_{ox}^0 and E_{red}^0 , respectively. The oxidized species can consume an electron from the semiconductor and be transferred to the reduced species. The reverse process is the consumption of a hole from the silicon by the reduced species which becomes oxidized. The redox potential E_{redox}^0 is the analogue to the Fermi level E_F in the semiconductor. As the electrolyte contains various redox couples, the redox potential is strictly a mixed potential [77]. We discuss the current-voltage curves for different voltage regions and compare it with the interface band structure.

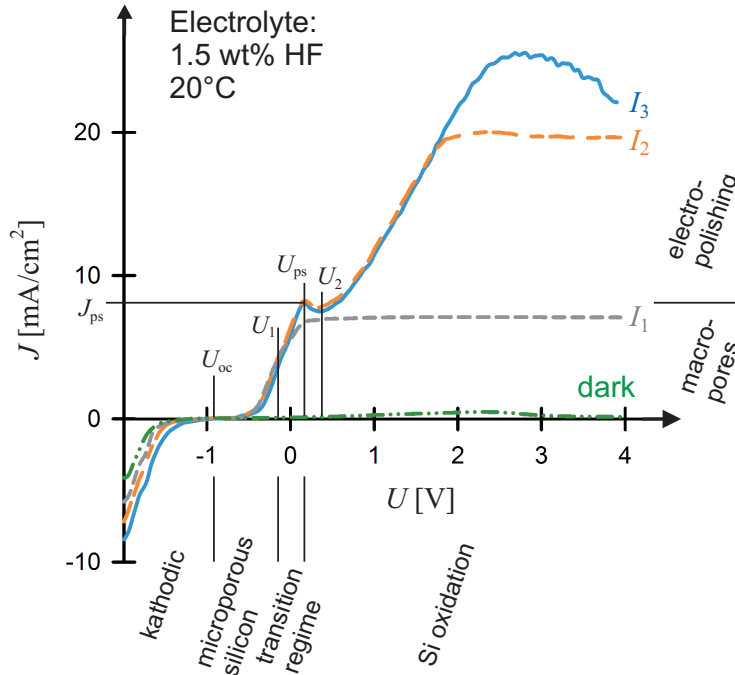


Figure 2.15: The figure shows the J - U curve of the Si/HF system under dark conditions and three different illumination intensities $I_1 < I_2 < I_3$. The named voltages mark changes in the interface chemistry which lead to characteristic morphologies of the Si electrode. The parameter space for macropores is for $U > U_{\text{ps}}$ and $J < J_{\text{ps}}$.

Cathodic regime $U \leq U_{\text{oc}}$: If the voltage across the interface U is smaller than the open-circuit voltage U_{oc} , the n -type Si electrode is under forward bias and the cathodic current is caused by majority carriers. Figure 2.16 a) shows the corresponding band structure of the interface. Electrons are transferred across the interface, reduce the hydrogen ions and gaseous H_2 is produced. The silicon

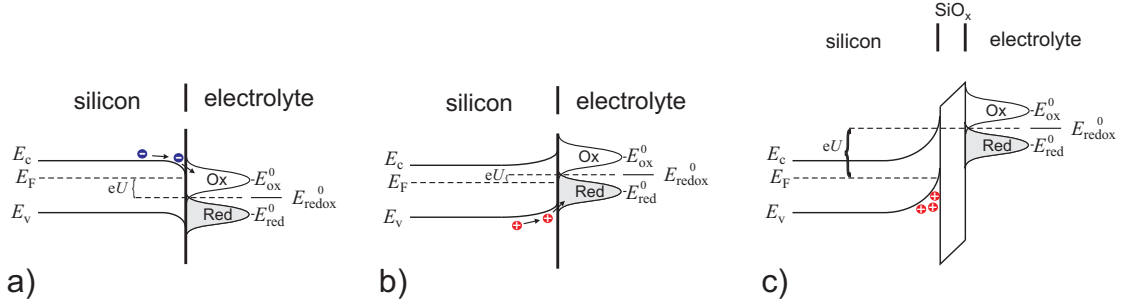


Figure 2.16: The figure shows the band diagram of the Si/electrolyte interface under a) forward bias $U < U_{oc}$, b) small reverse bias $U_{oc} < U < U_1$ and c) large reverse bias $U > U_{ps}$. In the latter case, a silicon oxide grows at the solid/electrolyte interface.

atoms are chemically inert. The cathodic current rises with illumination level due to the additional photogenerated electrons. The junction behaves like a forward-biased Schottky diode [78]. The open-circuit voltage for our samples is $U_{oc} = -(0.9 \pm 0.1)$ V and, in general, depends on the illumination level, substrate doping level, HF concentration and dissolved oxygen concentration in the electrolyte [68].

Small anodic potentials $U_{oc} < U \leq U_1$: The Si electrode is under reverse bias and a depletion region forms at the Si/electrolyte interface, as shown in Fig. 2.16 b). (Photogenerated) Holes approach the interface from the Si half-space and trigger a divalent dissolution reaction that results in microporous silicon. The hole concentration under dark conditions is too small to support a significant current flow. Only defect states at the interface that are occupied by holes may support a small current that decays over time as the defect centers become etched. The junction behaves like a Schottky diode under reverse bias. The current flow under illumination on the other hand follows an exponential Tafel characteristic which indicates that the reaction is diffusion-limited by the charge carriers. Under illumination, the junction behaves like a Schottky diode under forward bias in this voltage regime [79].

High anodic potentials $U \geq U_1$: The voltage U_1 marks an inflexion point in the current-voltage curve above which the current does no longer rise exponentially with U . The reason is that the hole concentration at the surface is (locally) large enough to oxidize the Si electrode, as shown in Fig. 2.16 c). The Si electrode condition at the interface changes from depletion to inversion. The oxide hampers the current flow across the interface until it becomes dissolved by HF according to the tetravalent dissolution reaction in Eq. 2.63. For the illumination intensity I_1 , the current density saturates above a voltage that is sufficient to drive all the photogenerated carriers to the interface. The value of the saturation current is controlled by the charge carrier density and thus the illumination intensity. This

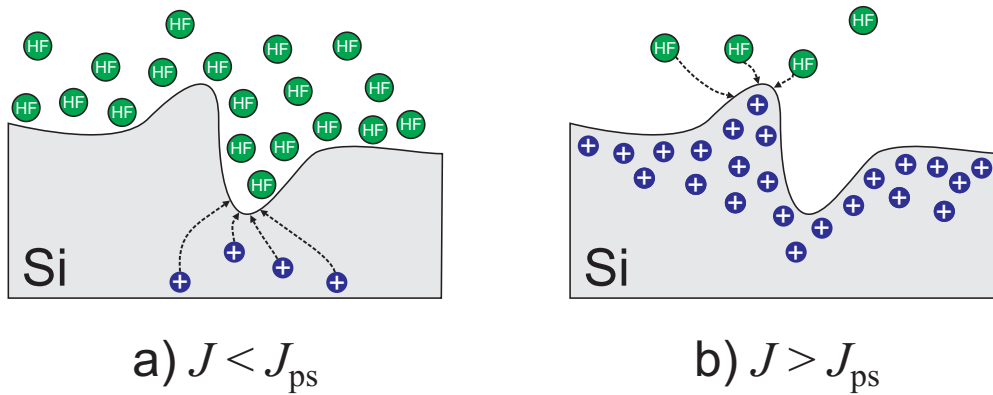


Figure 2.17: The sketch shows the Si/electrolyte interface for surface for depletion of a) charge carriers resulting in pore etching, and b) HF molecules resulting in electropolishing. The two regimes are separated by J_{ps} .

is the standard macropore etching regime of the so-called *illumination mode* (see description of etching tool on pp. 47-49).

For higher illumination intensities I_2 and I_3 , the current takes a local maximum at (U_{ps}, J_{ps}) . The subscript stands for porous silicon [68]. This point marks the turnover from a charge carrier transport limited reaction to an HF mass transport limited reaction, i.e. the timescale for the transport of HF molecules and the clearance of the reaction products (and therefore the oxide dissolution) exceeds the oxidation timescale. Figure 2.17 illustrates the impact of the change in reaction kinetics on the morphology of the electrode. For current densities below J_{ps} , the electrode is only locally oxidized and pores are etched deep into the Si electrode while for current densities above J_{ps} the mass transport in the electrolyte limits the reaction and the electrode becomes electropolished. Above voltages $U > U_2$, the current starts to flow through the anodic oxide and increases again up to another maximum that marks a change in the oxide growth kinetics [68]. However, these illumination intensities are irrelevant for growing macropores.

The current density J_{ps} that marks the onset of electropolishing depends on the composition and temperature of the electrolyte and can be regarded as a measure for its "dissolution capability". It can be written as an Arrhenius law [73]:

$$J_{ps} = A c^\alpha \exp\left(-\frac{E_a}{kT}\right), \quad (2.64)$$

where A is a constant with dimensions $[\text{A cm}^{-2}(\text{wt } \%)^{-\alpha}]$, c is the HF concentration of the electrolyte in wt%, α is a dimensionless constant, E_a is the activation energy in eV, k is Boltzmann's constant and T is the absolute temperature of the electrolyte. We experimentally determine values for A , α and E_a in Ch. 4.

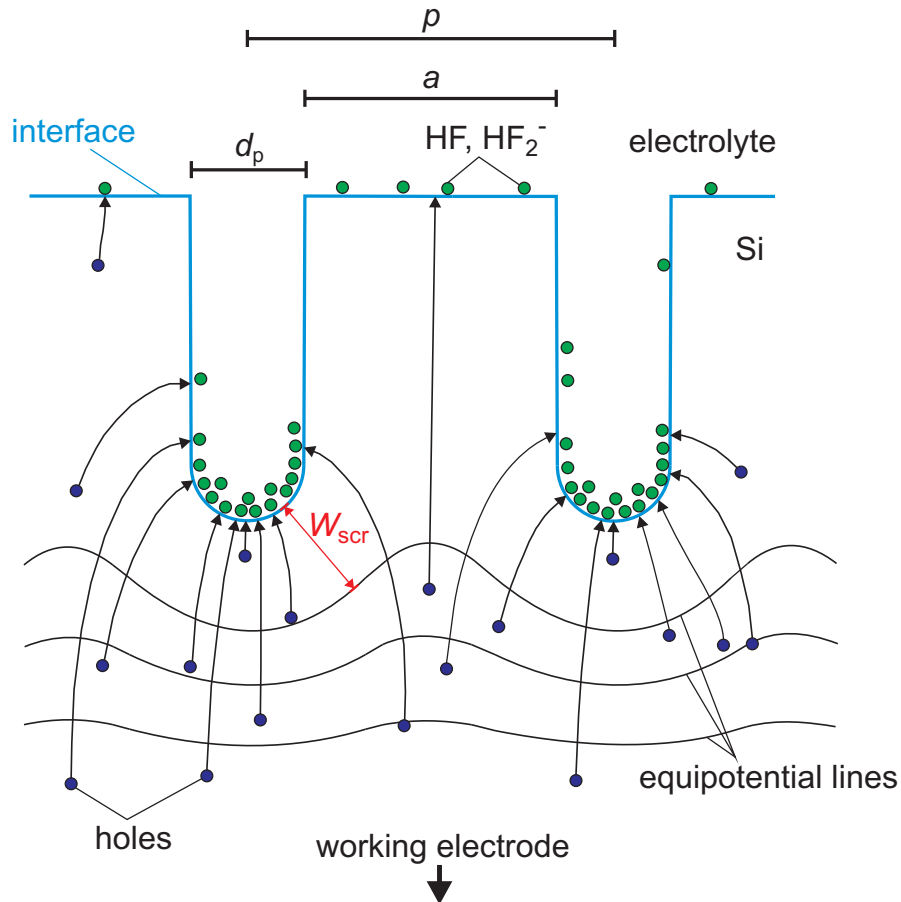


Figure 2.18: The sketch illustrates the space charge region model. The equipotential lines direct the holes (blue) towards the pore tip where they react with the fluoride species (green) and support the etching current and, thus, the pore growth. The pore walls are passivated from dissolution, as long as the width of the wall between the pores a does not exceed twice the width of the space charge region W_{scr} . The distance between the pores or pitch is labeled p and the diameter of the pores d_p .

2.8.3 Macropore formation model

In the early 1990s, Lehmann and Foell phenomenologically studied the macropore formation in n -type silicon under backside illumination for different substrate doping levels [73, 80]. Two important findings were that i) for a constant etching current density J , the pore diameter d_p increased with the substrate resistivity while the overall porosity Φ remained the same and that ii) the pore diameter d_p increased with current density J while the pore growth rate r was unchanged. The porosity Φ is defined as the ratio of the cross-sectional area of the pore A_p to the area of the unit cell (Wigner-Seitz cell) of the pore A_{tot}

$$\Phi = \frac{A_p}{A_{tot}}. \quad (2.65)$$

This led to a model of the pore formation which is often referred to as space charge region model. Figure 2.18 illustrates the concept and shows the Si/electrolyte interface under

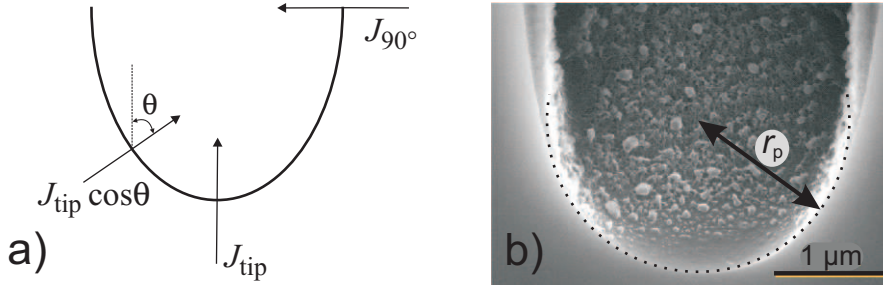


Figure 2.19: a) Current densities across the Si/electrolyte interface. b) SEM micrograph of a pore tip grown at a current density of $J/J_{ps} \approx 0.35$ and a voltage of $U/U_{ps} \approx 3$. The dotted line is a sphere with a diameter adopted to the curvature of the pore.

anodic bias and back side illumination. The black lines show the equipotential lines that are bended around the pores. Holes that approach the Si/electrolyte interface from the Si bulk follow the electric field that is perpendicular to these lines and are focused towards the pore tip region where they initiate a dissolution reaction resulting in pore growth. Only very few holes diffuse into the region between the pores and participate in a dissolution reaction at the pore wall. The width of the pore wall a thus depends on the width of the space charge region W_{scr} which is given by

$$W_{scr} = \sqrt{\frac{2\epsilon\epsilon_0(U - U_{bi})}{eN_D}}, \quad (2.66)$$

where $\epsilon_0 = 8.854 \times 10^{-12}$ As/Vm is the vacuum permittivity, $\epsilon = 11.9$ is the relative permittivity of silicon, $U_{bi} = -0.54$ V is the built-in voltage [81], i.e. the difference of the Fermi levels of each medium before the contact, U is the applied external voltage and N_D is the doping concentration. Thus, the maximum pore wall width a for which straight pores can be grown is twice the width of the space charge region

$$a \leq 2W_{scr}. \quad (2.67)$$

This explains the dependence of the pore width d_p on the substrate doping as described under i): As the distance a between the pores increases with substrate resistivity and the total amount of dissolved material, expressed by a constant J , is unchanged, the pore diameter has to increase. Furthermore, the space charge region model predicts that the pore walls become etched if $a > 2W_{scr}$. However, Hejjo Al Riffai *et al.* experimentally found that this holds strictly only for lowly doped ($> 20 \Omega\text{cm}$) silicon and that straight pores with pore wall widths up to $a = 10W_{scr}$ can be realized with higher substrate doping levels [82]. A possible explanation for this is that holes have a lower diffusion length in highly doped substrates which reduces the probability for them to participate in a dissolution reaction before they recombine in the pore wall region [83].

Figure 2.19 a) illustrates the current flow through the pore tip region and is used in the following to explain the experimental findings described under ii). In case of a hemispherical curvature of the pore tip, the local current density $J_p(\theta)$ can be written as [84]

$$J_p(\theta) = J_{\text{tip}} \cos \theta + J_{90^\circ} . \quad (2.68)$$

The current density J_{90° is caused by the dissolution due to holes which penetrate the interpore region and holes that are not photogenerated. The maximum local current density J_{tip} is at the pore tip. Lehmann found that at the pore tip the dissolution is limited by the mass transport in the electrolyte [73]. Thus, for anodic voltages $U > U_{\text{ps}}$ and a sufficiently high illumination intensity, there is a *steady-state condition* between mass transport in the electrolyte and charge transfer in the Si which implies that J_{tip} equals J_{ps} . If we neglect the leakage current density J_{90° , the total global etching current density J flows through the tip and we can write:

$$J = \frac{I_p}{A_{\text{tot}}} = \frac{2\pi \int_0^{\pi/2} J_p(\theta) r_p^2 \sin \theta d\theta}{A_{\text{tot}}} = J_{\text{ps}} \Phi , \quad (2.69)$$

where I_p is the current through a single pore and Φ the porosity according to Eq. 2.65 with $A_p = \pi r_p^2$ as the cross-sectional area of a single pore and r_p being the radius of the pore tip. Equation 2.69 is the result of the steady-state condition between mass transport and carrier transfer at the pore tip and is often referred to as *Lehmann formula* [73]. It states that the current density J controls the diameter of the pores which is the first part of the finding described under ii). The SEM micrograph in Fig. 2.19 b) shows a pore tip of sample 17 as described in Appendix B and illustrates the current flow across the interface of Eq. 2.68 via its appearance: While the pore walls are covered with a microporous film, indicating divalent dissolution and a local current $J < J_{\text{ps}}$, the pore tip itself is electropolished as we would expect for a tetravalent dissolution and a local current density of J_{ps} .

The growth rate of the pores in units length per time is given by

$$r = \frac{J_{\text{tip}}}{nqN_{\text{Si}}} , \quad (2.70)$$

where q symbolizes the elementary charge and $N_{\text{Si}} = 5 \times 10^{22} \text{ cm}^{-3}$ the atomic density of silicon. n is the valence of the dissolution reaction and states how many charge carriers flow through the external circuit per dissolved Si atom. As will be shown in Ch. 4, the valence depends on the current density J and the anodic voltage U [73, 85, 86] and takes values between 2 and 4. We determine the dissolution valence gravimetrically by applying a constant etching current density J for a certain time t_{etch} under an anodic

voltage U . The valence then follows from

$$\frac{m_1 - m_2}{m_{\text{Si}}} = \frac{A}{e} \frac{J}{n(J, U)} t_{\text{etch}} , \quad (2.71)$$

where m_1 and m_2 refer to the mass of the sample before and after etching, respectively. $m_{\text{Si}} = 4.6638 \times 10^{-23}$ g and $A = 1 \text{ cm}^2$ symbolize the atomic mass of silicon and the etched area which is defined by the size of the rubber ring of the etching cell as described in Ch. 3. Equation 2.70 shows that by the steady-state condition at the pore tip all pores grow at the same rate if $U > U_{\text{ps}}$. This describes the second part of the finding described under ii). The growth rate depends solely on the electrolyte concentration c_{tip} at the pore tip via J_{ps} .

2.8.4 Pore growth kinetics

Equations 2.64 and 2.70 relate the pore growth rate r with the HF concentration at the pore tip c_{tip} . The mass transport in the electrolyte is diffusion-based [73] which implies that c_{tip} decreases with increasing pore depth l_{p} . The concentration at the pore tip is defined as $c_{\text{tip}} = c(l_{\text{p}})$. We follow the approach in Ref. [87] that derives a self-consistent expression for c_{tip} in dependence of l_{p} and the HF concentration in the electrolyte bath c_0 .

Because the diffusion of HF is much faster than the pore growth rate, the change in HF concentration over time can be neglected and the stationary diffusion equation can be applied to describe $c(l)$

$$D \frac{\partial^2 c}{\partial l^2} = 0 , \quad (2.72)$$

where D is the diffusion coefficient of HF in the electrolyte. The two boundary conditions are

$$c(l = 0) = c_0 , \quad (2.73)$$

$$-D \frac{\partial c}{\partial l} = F . \quad (2.74)$$

The second boundary condition is Fick's first law with F being the flux of HF molecules, i.e. the rate at which HF is consumed at the pore tip. The solution to Eq. 2.72 is thus [68]

$$c(l) = c_0 \left(1 - \frac{F}{Dc_0} l\right) , \quad 0 \leq l \leq l_{\text{p}} . \quad (2.75)$$

Under steady-state conditions at the pore tip, the flux is [73]

$$F = \frac{m}{ne} J_{\text{ps}} = K c_{\text{tip}}^\alpha , \quad (2.76)$$

where the constant $K = A/e \exp(-E_a/kT)$ is defined by Eq. 2.64. We assume that the number of HF molecules consumed per dissolved Si atoms m is equal to the dissolution valence n [87]. Substituting Eq. 2.75 into Eq. 2.76 and then into Eq. 2.70 gives the depth dependent growth rate [87]:

$$r = r_0 \left(1 - \frac{l_p r}{l_{p0} r_0} \right)^\alpha, \quad (2.77)$$

with the abbreviations for the initial growth rate r_0 and the characteristic depth of the system l_{p0} :

$$r_0 = \frac{K c_0^\alpha}{n N_{\text{Si}}}, \quad (2.78)$$

$$l_{p0} = \frac{D}{K c_0^{\alpha-1}}. \quad (2.79)$$

Equation 2.77 can be solved analytically by applying a Taylor expansion the right hand side (assuming $l_p r \ll l_{p0} r_0$) [87]. The etch rate thus becomes

$$r(l_p) \approx r_0 \left(\frac{1}{1 + \alpha \frac{l_p}{l_{p0}}} \right). \quad (2.80)$$

Combining this result successively with Eq. 2.70 and Eq. 2.76 yields the HF concentration at the pore tip for a given pore depth:

$$c_{\text{tip}}(l_p) \approx c_0 \left(\frac{1 + (\alpha - 1) \frac{l_p}{l_{p0}}}{1 + \alpha \frac{l_p}{l_{p0}}} \right). \quad (2.81)$$

The separation of variables in Eq. 2.80 allows to set up an relationship between the etch time t_{etch} and the pore depth l_p :

$$t_{\text{etch}} = \frac{\alpha}{2 l_{p0} r_0} l_p^2 + \frac{1}{r_0} l_p. \quad (2.82)$$

Chapter 3

Experimental and simulation methods

In this chapter, some of the experimental methods applied during this thesis are described in more detail, starting with characterization tools for the optical and electrical properties of the samples and followed by the description of the anodization tool for electrochemical etching of macropores into silicon and the raytracing method.

3.1 Spectrophotometer

We use a dual beam photospectrometer (Cary 5000 from Varian) to measure reflectance, absorptance and transmittance spectra of Si samples. The light source consists of a deuterium lamp for the spectral range of 185-350 nm and a halogen lamp for the spectral range of 350-3300 nm. First, the light becomes spectrally resolved by a double monochromator. Then, it falls onto a chopper wheel that has three positions: in the first position the light is blocked (position b), in the second position it gets directed through a depolarizer towards the sample port (s) and in the third position towards the reference port (r) of an integrating sphere. The sphere, as illustrated in Fig. 3.1, has a diameter of 150 mm and consists of polytetrafluoroethylene (PTFE) that has a high reflectance and a nearly Lambertian behavior (see also Sec. 2.6.4). Its design allows to collect the specular as well as the diffusive component of the reflected and/or transmitted light of a sample. A baffle, that consists of PTFE as well, shields the detector from a potential specular reflex. Thus, all the light within the sphere is made completely diffusive by multiple interactions with the wall before it falls on the detector. The detector consists of a photomultiplier for the spectral range 160-940 nm and a lead sulfide (PbS) detector for the spectral range 940-3000 nm. Depending on the position of the chopper wheel,

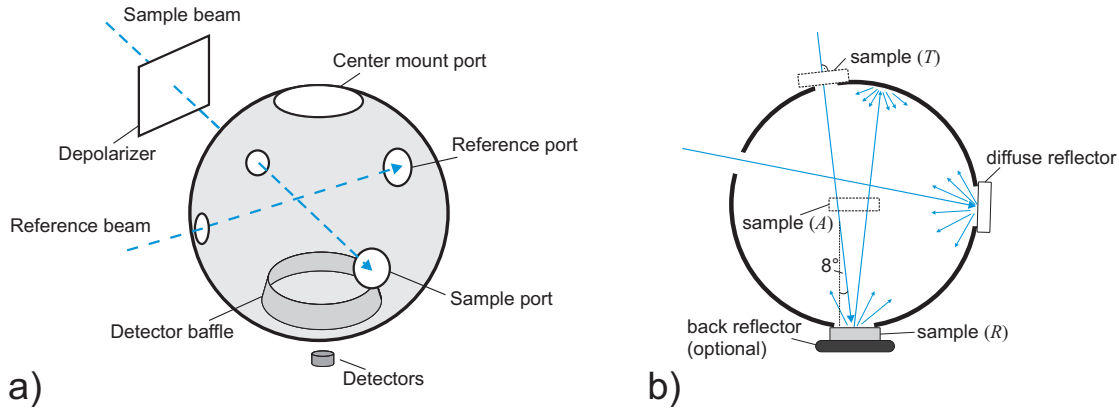


Figure 3.1: The figure shows a) a 3D view and b) a top view of incoming beam plane of the integrating sphere. b) shows the sample position for measuring the three quantities: reflectance R , absorptance A and transmittance T .

the detector gives three signal intensities: S_b , S_s , or S_r . The software converts these three quantities into a quantity M by

$$M = \frac{S_s - S_b}{S_r - S_b}. \quad (3.1)$$

M is deprived of the dark signal from the detector and of background light that does not originate from the light source (contained in S_b). Also variations in the intensity of the light source are eliminated since they are contained in both signals S_s and S_r . The chopper wheel frequency is 30 Hz.

The quantity M itself contains no absolute information on the optical properties of the sample, since the signals S_s and S_r are not necessarily equal in amplitude even with the same material at both ports. For this we have to calibrate the setup with a standard that has a known reflectance R_{std} , absorptance A_{std} or transmittance T_{std} . For all measurements in this work, we place a PTFE reflector with the same reflectance as the inner sphere surface at the reference port.

The system calibration is carried out with an optical standard at the sample position. The calibration procedure is then followed by the measurement of the actual sample with unknown optical properties at the sample position. Depending on whether reflectance, absorptance or transmittance is measured, the standard and the sample position differ:

Reflectance R : The sample position is at the sample port which is marked with an R in Fig. 3.1 b). We use a PTFE standard with a tabulated reflectance R_{std} that is traceable to an official standard of the "Physikalisch-Technische Bundesanstalt" (PTB). In accordance with Eq. 3.1, we term the measured signal with the standard at the sample port M_{std} . What follows is a baseline measurement where we remove the standard from the sample port and replace it by a light trap, e.g. the dark

laboratory. We term this signal M_0 . M_0 is non-zero if a part of the sample beam impinges on the rim of the port opening and is reflected back into the sphere. This can be the case if an aperture with a diameter close to the beam spot size is placed in front of the sample. Afterwards, the signal with the actual sample at the sample port M_s is taken. The sample reflectance R_s follows from

$$R_s(\lambda) = \frac{M_s(\lambda) - M_0(\lambda)}{M_{\text{std}}(\lambda) - M_0(\lambda)} \times R_{\text{std}}(\lambda). \quad (3.2)$$

Absorptance A : The sample position is at the center of the integrating sphere, marked by the A -symbol in Fig. 3.1 b). For this we use a mounting bracket that is inserted through the center mount port in Fig. 3.1 a). The mount has a baffle of its own to shield the detector from any specular reflectance of the sample. The sample port is covered by a PTFE reflector just as the reference port. We use a polished Si sample with a known absorptance A_{std} to acquire the signal M_{std} . After the calibration, we mount the actual sample into the sphere and obtain M_s . The absorptance of the sample A_s then follows from

$$A_s(\lambda) = \frac{M_s(\lambda)}{M_{\text{std}}(\lambda)} \times A_{\text{std}}(\lambda). \quad (3.3)$$

Transmittance T : The sample position is at the entrance of the integrating sphere, marked by the T -symbol in Fig. 3.1 b). We place a PTFE reflector at the sample port as in the absorptance measurement. The standard for transmittance measurements is the empty sample holder. The acquired signal M_{std} then refers to a transmittance of $T_{\text{std}} = 100\%$ [88]. After that the actual sample is placed at the sample position to obtain M_s , which leads to the sample transmittance T_s

$$T_s(\lambda) = \frac{M_s(\lambda)}{M_{\text{std}}(\lambda)}. \quad (3.4)$$

The relative uncertainty has been determined to be 1% for reflectance measurements and 0.4% for transmittance measurements with $T > 0.25$ if the samples are planar and have no light trapping scheme [89]. Samples with a scattering surface however have an increased uncertainty for the weakly absorbed light. The reason for this is illustrated in Fig. 3.2 a). Two possible paths of weakly absorbed light in the reflectance configuration are shown. The textured surface scatters light into oblique angles which can hinder the ray to find its way back into the sphere and eventually become detected. Figure 3.2 b) shows the absorptance of a 285 μm -thick sample with a random pyramid texture on the front side that has been determined by three different measurements. For the first two lines, the reflectance has been measured with two different apertures, 6 mm and 35 mm in diameter. Afterwards the transmittance is measured with a constant aperture of

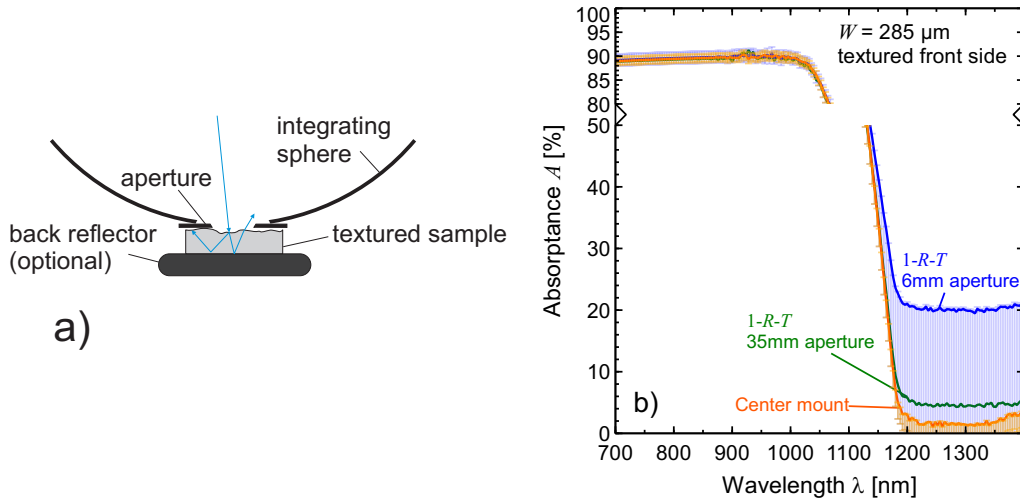


Figure 3.2: The figure shows a) possible paths of weakly absorbed light for a textured sample during a reflectance measurement. A fraction of the incident light does not re-enter the integrating sphere. This leads to an underestimation of the reflectance and to an overestimation of the absorbance if it is determined via $A = 1 - R - T$ as shown in b) for two sample apertures. The most adequate absorbance spectrum for textured samples is obtained by mounting the sample in the sphere's center. The asymmetric error bars account for the overestimation.

15 mm. The sample beam spot has a size of $(2 \times 3) \text{ mm}^2$. The absorbance then follows from $A = 1 - R - T$. The third line is obtained from measuring the absorbance directly by mounting the sample in the sphere's center. The non-collection underestimates the reflectance and thus leads to an overestimation of the absorbance. The magnitude of this overestimation decreases with increasing aperture size and is proportional to the beam spot size, the sample thickness and the scattering efficiency of the sample. The absorbance from the measurement with the sample in center position, which is unaffected by the uncertainty due to non-collected photons, drops to a value of $\approx 2\%$ instead of 0% for $\lambda > \lambda_g$. We take this deviation as the absolute uncertainty of the absorbance measurement configuration for $\lambda > 1135 \text{ nm}$. The reason for the deviation is that also in the center mount configuration some light exits the integrating sphere as it is not completely closed. For $\lambda < 1135 \text{ nm}$, the relative uncertainty is the same as for reflectance measurements of non-scattering samples, i.e. 1% . Figure 3.2 b) shows the uncertainties for the center mount measurement and for the 6 mm aperture in the reflectance measurement. The overestimation leads to asymmetric error bars.

3.2 Measuring the effective carrier lifetime

The effective carrier lifetime τ_{eff} as introduced by Eq. 2.55 is determined by different recombination processes. In the most general form, these processes can be separated

into recombination that takes place in the bulk with a rate U_{bulk} (in $\text{cm}^{-3}\text{s}^{-1}$) or at the surface at a rate U_{surf} (in $\text{cm}^{-2}\text{s}^{-1}$). If the excess carrier density Δn is spatially homogeneous, U_{bulk} is

$$U_{\text{bulk}} = \frac{\Delta n}{\tau_{\text{bulk}}} = \Delta n \left(\frac{1}{\tau_{\text{aug}}} + \frac{1}{\tau_{\text{rad}}} + \frac{1}{\tau_{\text{srh}}} \right). \quad (3.5)$$

The bulk lifetime τ_{bulk} comprises the intrinsic Auger and radiative lifetime [90], τ_{aug} and τ_{rad} , as well as the extrinsic lifetime τ_{srh} . Richter *et al.* have given the most recent parameterization for the intrinsic lifetime in silicon in dependence of bulk doping concentration N_{dop} and Δn [91]. The extrinsic or Shockley-Read-Hall lifetime describes recombination via defect states within the band gap [92, 93]. The surface recombination rate relates to the excess carrier densities at the surface Δn_{surf} by the so-called surface recombination velocity S . However, surface charges often induce a band bending towards the semiconductor surface which makes it useful to define an effective surface recombination velocity S_{eff} with the excess carrier concentration taken at the edge of the space charge region Δn_{scr} [94, 95]:

$$U_{\text{surf}} = S_{\text{eff}}(\Delta n) \Delta n_{\text{scr}}. \quad (3.6)$$

S_{eff} is, in general, injection-level dependent. The surface recombination rate U_{surf} in Eq. 3.6 contains all recombination losses that occur between the surface and the edge of the space charge region. If the surface recombination rate is small (see below), the effective carrier lifetime can be written as

$$\frac{1}{\tau_{\text{eff}}} = \frac{1}{\tau_{\text{bulk}}} + \frac{1}{W_{\text{eff}}} (S_{\text{f}} + S_{\text{r}}), \quad (3.7)$$

where S_{f} and S_{r} symbolize the effective surface recombination velocity at the front and rear side, respectively. Equation 3.7 is an approximation [95, 96] that is correct to within 4% if $S_{\text{f,r}} < D_{\text{e,h}}/4W_{\text{eff}}$ [97]. $D_{\text{e,h}} = V_{\text{th}}\mu_{\text{e,h}}$ symbolizes the minority carrier diffusion coefficient for electrons and holes, respectively. The carrier mobility $\mu_{\text{e,h}}$ depends on the doping concentration [98] and $V_{\text{th}} = kT/q = 25.7 \text{ mV}$ is the thermal voltage at $T = 298.15 \text{ K}$ with the k and q being Boltzmann's constant and the elementary charge, respectively. W_{eff} is the effective thickness of the absorber. In this work, we use samples with a large bulk lifetime for which we use the intrinsic limit by Richter *et al.* [91]. Hence, we can determine S_{eff} by Eq. 3.7, if τ_{eff} is known.

To determine τ_{eff} from Eq. 2.55 of a sample at different injection levels Δn , one has to measure a quantity that is related to the excess carrier density Δn and a quantity that is related to the generation rate G . In this work we use two different techniques: infrared lifetime mapping and photoconductance decay.

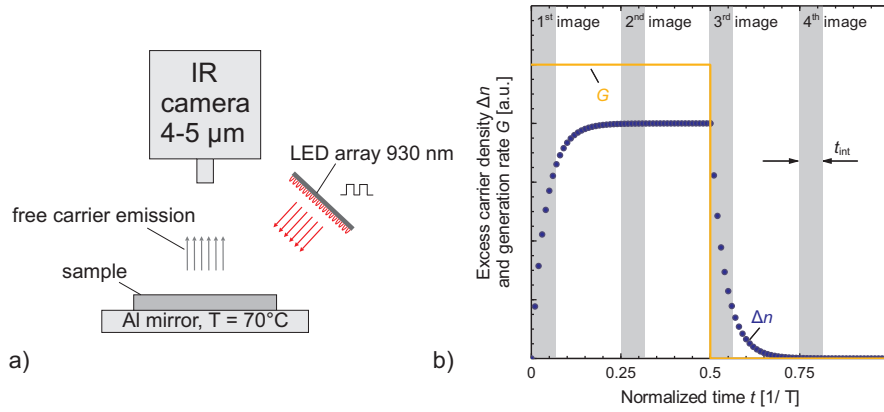


Figure 3.3: The figure shows a) the ILM setup and b) the generation rate G , excess carrier density Δn and image acquisitions (shaded area) during a measurement period T . All 4 images allow a calibration-free determination of the effective lifetime (dynamic-ILM). The figures are adapted from [101].

3.2.1 Infrared lifetime mapping (ILM)

The camera-based ILM technique gives spatially resolved images of the effective minority carrier lifetime of the sample [99]. Figure 3.3 a) shows a sketch of the measuring setup. An LED array with a wavelength of 930 nm excites charge carriers in the sample. The excitation wavelength and the size and position of the LED arrays guarantee a spatially homogeneous generation rate. The measurement principle relies on the free carrier emission which is the inverse process to the free carrier absorption [34] (see Sec. 2.4). The free carrier emission, whose probability is proportional to the free carrier density within sample, is detected by a midIR-camera with a detection wavelength of 4-5 μm . The sample is placed on an Al mirror that has a temperature of 70 $^{\circ}\text{C}$. The elevated temperature of the sample against the background assures that a change in the sample's emissivity due to free carriers results in a change of the camera signal and thus reduces the signal-to-noise ratio (SNR) ([100], Eq. 3.8). The camera signal S can thus be regarded as the quantity that is related to the excess carrier density. We first use a dynamic measurement method, which in contrast to steady-state techniques also includes the time dependence of the camera signal under modulated excitation [100–102]. The dynamic approach has the advantage that it requires no knowledge about the generation rate and no calibration of the camera signal versus Δn . Figure 3.3 b) illustrates the measuring procedure. It shows the step-like generation rate $G(t)$ and the excess carrier density $\Delta n(t)$ during an excitation period T . For a further SNR improvement, a lock-in technique is applied which requires 4 images. The first image is acquired directly after switching on the excitation source, the second after reaching steady-state conditions, the third one directly after switching off the excitation and the fourth after the excess carrier density has reached its equilibrium value. All images have the same integration time t_{int}

and a camera signal S_i ($i=1, 2, 3, 4$ specifies the image number) that is proportional to

$$S_i \propto \int_{t_i}^{t_i+t_{\text{int}}} \Delta n(t) dt, \quad (3.8)$$

with the integration boundaries $t_i = (i - 1)T/4$ as shown in Fig.3.3b). With the assumption of a mono-exponential rise and decay, i.e. a carrier lifetime τ_{eff} that is independent of Δn , Eq. 2.54 is solved by

$$\Delta n(t) = G\tau_{\text{eff}} \begin{cases} \left(1 - \exp\left(-\frac{t}{\tau_{\text{eff}}}\right)\right), & 0 < t < T/2 \\ \exp\left(-\frac{t - T/2}{\tau_{\text{eff}}}\right), & T/2 < t < T. \end{cases} \quad (3.9)$$

By inserting Eq. 3.9 into Eq. 3.8, we can calculate the camera signal for each image. The lock-in data processing accounts for the constant background signal and provides two new measures, the amplitude and the phase factor Ψ . The phase factor contains quantitative information of the excitation function and the response of the sample. It relates to the camera signals by

$$\Psi = \arctan\left(\frac{S_2 - S_4}{S_1 - S_3}\right) \quad (3.10)$$

$$= \arctan\left(\frac{t_{\text{int}} - 2\tau_{\text{eff}} \left[\exp\left(-\frac{T}{4\tau_{\text{eff}}}\right) - \exp\left(\frac{T + 4t_{\text{int}}}{4\tau_{\text{eff}}}\right) \right]}{t_{\text{int}} - 2\tau_{\text{eff}} \left[1 - \exp\left(-\frac{t_{\text{int}}}{\tau_{\text{eff}}}\right) \right]}\right). \quad (3.11)$$

This equation contains the effective lifetime τ_{eff} as the only unknown. The integration time in our experiments is $t_{\text{int}} = 400 \mu\text{s}$ and the period length is $T = 25 \text{ ms}$.

The assumption of an injection-independent carrier lifetime in the dynamic approach leads to an overestimation of the lifetime by 20% over the steady-state technique, which only uses images 2 and 4. We therefore take the effective lifetime from the dynamic approach to calibrate the steady-state lifetime image as described in Ref. [101].

The photon flux Φ of the LED array controls the generation rate in the sample. Φ has to be calibrated via a photodiode or a calibrated solar cell. The excess carrier density is then determined via Eq. 2.54 with the generation rate

$$G = \frac{\Phi(1 - R_{930\text{nm}})}{W_{\text{eff}}}, \quad (3.12)$$

where $R_{930\text{nm}}$ is the reflectance of the sample at the excitation wavelength.

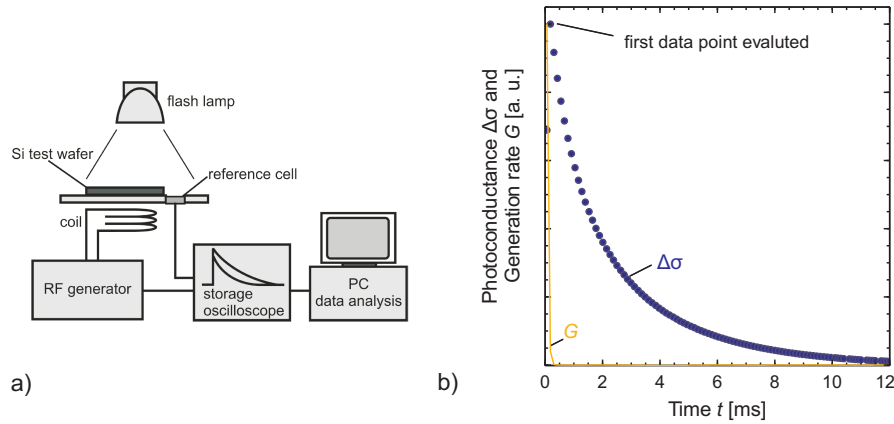


Figure 3.4: The figure shows the PCD setup a) and the generation rate and photoconductance of the sample b). a) is adapted from [103].

3.2.2 Photoconductance decay

Another way to determine τ_{eff} is to measure the photoconductance decay (PCD). For this we use commercially available setup (WCT-120 from Sinton Instruments) as depicted in Fig. 3.4 a). The sample and a reference cell are illuminated by a Xenon flash lamp that can be operated with two different decay times. We use the shorter decay time of 0.3 ms if not stated otherwise. In this so-called transient mode, the generation rate $G(t)$, which is measured by the reference cell as described in [103], is effectively zero throughout the evaluation period which has a duration of 10-20 ms. An IR-pass filter in front of the flash guarantees a homogeneous generation rate throughout the sample [104]. The measured quantity that relates to Δn in this setup is the photoconductance σ [64]. It is indirectly measured by an inductive feedback in a coil below the sample. The coil is part of a radio frequency bridge circuit and induces eddy currents within the sample. These currents in turn induce an additional voltage in the coil that is measured and translated into an change in photoconductance $\Delta\sigma$. Figure 3.4 b) shows the time dependence of the generation rate and the photoconductance. The latter depends linearly on the excess carrier density

$$\Delta\sigma = qW(\mu_n + \mu_p)\Delta n, \quad (3.13)$$

where μ_n and μ_p are the electron and hole mobilities, respectively¹. A semi-empirical model accounts for the dependence of the charge carrier mobility on Δn [105]. τ_{eff} then follows directly from Eq. 2.54.

The PCD measurement differs from ILM by its spatial resolution which is limited by the coil diameter/area of 18 mm/250 mm². All measurements are averaged over this area. Another difference is that τ_{eff} can be evaluated for every pair of data points from

¹Equation 3.13 is strictly an approximation where we assume a Δn that is independent of the position along the thickness of the wafer.

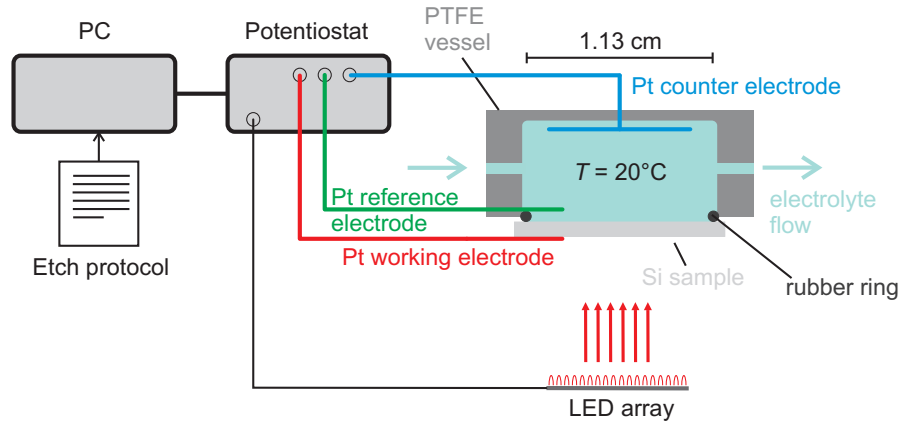


Figure 3.5: The figure shows a sketch of the etching tool. A potentiostat controls the current, voltage and illumination intensity across the Si/electrolyte interface. The electrolyte flows through the PTFE vessel chamber. A rubber ring defines the etched area to 1 cm^2 .

Fig. 3.4 b). This accounts for deviations from a mono-exponential decay and allows to study the injection dependence of τ_{eff} from a single light flash.

3.3 Etching tool and wafer preparation

The anodic etching of macropores into silicon is an important experimental technique for preparing samples within this work. Figure 3.5 shows a sketch of the experimental setup (Elypor-3 from ET&TE Etching and Technology GmbH). The Si sample is in contact with an aqueous electrolyte that contains 3 wt% hydrofluoric acid (HF) and 7.5 vol% acetic acid. The HF is for the dissolution of oxidized Si while the acetic acid improves surface wetting of the electrolyte and minimizes leakage currents through the pore walls. A thermostat keeps the electrolyte at a temperature of $T = 20^\circ\text{C}$. A peristaltic pump drives a constant electrolyte flow across the sample and thus maintains a stable HF concentration within the electrolyte container that consists of HF-resistant PTFE. The contact area is defined by a rubber ring to 1 cm^2 . The dissolution reaction of Si does not initiate spontaneously as, e.g., in alkaline solutions but needs to be activated. Therefore an anodic voltage is applied across the Si/electrolyte interface between a Pt working electrode at the rear side of the semiconductor and a Pt counter electrode within the electrolyte. The effective voltage U is measured between a Pt reference electrode in front of the Si/electrolyte interface and the working electrode to exclude potential fluctuations within the electrolyte². In this work, we use *n*-type silicon and the anodic voltage drives holes towards the Si/electrolyte interface. Holes trigger the dissolution reaction and

²The potential drop within the semiconductor can be accounted for by a sense electrode that contacts the front side of the silicon. However, this voltage drop is neglected in this setup and the sense electrode is short-circuited with the working electrode.

a current flows through the external circuit. However, as the hole concentration in *n*-type silicon is rather low, we create additional charge carriers by illuminating the semiconductor from the rear side with an LED array with a wavelength of 890 nm. There are three etching parameters: current density J^3 , voltage U and illumination intensity I .

We operate the potentiostat that controls the etching parameters in three different modes. These differ by control variables that are set by the user and by the reacting variable that is self-adjusting according to the current-voltage characteristics of the etching cell. Here, we term the modes after the reacting variable: In the *illumination mode*, the current and the voltage are specified by the etch protocol and the potentiostat controls the illumination intensity via a feedback loop to maintain the desired current under the preset anodic voltage. This is the standard mode to etch straight pores. In the *voltage mode* (in literature also *galvanostatic mode*), the current density and the illumination intensity are set and the voltage adapts accordingly. This mode allows for the strongest diameter modulations, as will be shown in Ch. 5. We use the *current mode* (in literature also *potentiostatic mode*) for a defect etch and for acquiring J - U curves of the system prior to the actual etch protocol. The defect etch, which is the application of an anodic voltage without illumination, aims to minimize the dark current at the beginning of an etch process. The defect etch is stopped when the dark current is below 0.1 mA/cm^2 . For the J - U curve, the illumination is set to 30 mW/cm^2 and the voltage is linearly increased from -1 to 4 V over 30 sec. It serves to measure U_{ps} and to verify that a sufficiently high current density close to J_{ps} can be achieved⁴. Table 3.1 summarizes the three etching modes.

Table 3.1: The table lists the three etching modes and their typical application.

etch mode	control variables	reacting variable	used for
illumination	J, U	I	straight pores moderate diam. modulation
voltage	J, I	U	strong diam. modulation
current	I, U	J	$J - V$ curve defect etch

Prior to etching, the Si samples are prepared as follows. We use two different *n*-type (100)-oriented Si wafers. The first is shiny-etched Czochralski (Cz) Si with a thickness of $(305 \pm 5) \mu\text{m}$ and a resistivity of $(1.5 \pm 0.3) \Omega\text{cm}$. This material is used in Chs. 2, 4 and 5. The second material is double-side polished float-zone (FZ) Si with a thickness of $(285 \pm 5) \mu\text{m}$ and a resistivity of $(3 \pm 0.2) \Omega\text{cm}$. This material is used in Ch. 6. After an

³For simplicity, we work with the current density rather than the absolute current, since the current flow through the Si/electrolyte is homogeneous for this relatively small etching area.

⁴The most probable reason for a too low maximum current density is that the diffusion on the rear side of the Si electrode is too weak [106].

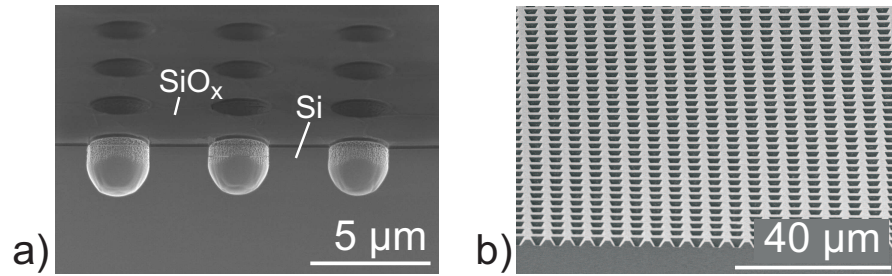


Figure 3.6: The figure shows SEM micrographs of a tilted cross-sectional view of the front surface after the RIE process a) and after pyramid etching b).

RCA standard cleaning step [107], an 80 nm-thick thermal silicon oxide layer grows in an oxidation oven on both sides. We remove the oxide layer on one side with hydrofluoric acid (HF). The samples then receive a 10 Ω /sq-phosphorous diffusion on the rear side to form an ohmic contact with the working electrode. The front side gets structured with inverted pyramids that serve as nucleation seeds for electrochemical pore etching⁵. Fabricating the pyramids involves three steps: 1) A standard lithography with a hard mask, 2) reactive ion etching (RIE) in an SF₆ gas ambient to transfer the structure into the oxide layer and 3) etching in a KOH/IPA-based solution to form inverted pyramids. The RIE does not only locally remove the oxide layer but also parts of the Si as shown in the scanning electron microscope (SEM) image in Fig. 3.6 a) which shows the sample surface after the RIE step.

The inverted pyramids are arranged on a square lattice with a lattice constant of p between 4 and 11 μm . At the end, the samples are dipped in HF to remove the remaining oxide and phosphosilicate glass. Figure 3.6 b) shows a SEM image of the front surface after the prestructuring process and prior to pore etching.

3.4 Raytracing

The Eqs. 2.38 and 2.46 give analytical expressions for the absorptance of structures with no and Lambertian light trapping under normally incident light, respectively. The optical performance of practical solar cells, however, depends on many more factors like the size of the texture, absorbing ARCs, polarization and spectrum of the incident light, etc.. The impact of these factors can be studied by Monte-Carlo ray tracing [108]. We use Fig. 3.7 to explain the basic idea of this statistical concept. A light ray that consists of N photons is generated within the top plane of the top layer, here point A, and falls upon an AR-coated and textured Si structure with a thickness W , the mid layer,

⁵The prestructuring is not a prerequisite for pore etching as pores also nucleate self-organized [82]. Prestructuring, however, offers a better control over the morphology, as will be shown in Chs. 5 and 6.

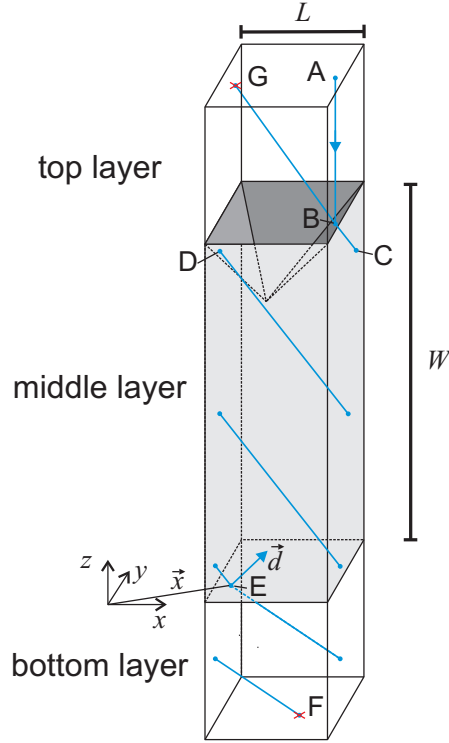


Figure 3.7: The figure shows the unit cell of a raytracing simulation. A light ray with N photons is generated in the top layer at point A. The trajectories of the photons are traced until they become absorbed in one of the layers or exit the domain through the top (point G) or bottom layer (point F). The Si layer is coloured in grey.

coloured in grey. Every photon is characterized by its position (x, y, z) , its propagation direction (d_x, d_y, d_z) , its state of polarization and its wavelength λ .

The simulation domain is characterized by optical properties that are translated into probabilities P . For example, the probability for a photon k to become absorbed in the top layer $P_{\text{abs,top}} = 1 - \exp(-\alpha_{\text{top}}(\lambda)l)$ depends on the absorption coefficient α_{top} of the top layer material and the path length l of the light ray within the top layer. Therefore, the distance to the next interface $\overline{AB} = l$ is calculated. Next, a random number m_k with $0 \leq m_k \leq 1$ and $k \in \{1, N\}$ is determined for each photon and compared with the probability. The photon k is absorbed in the top layer, if the condition

$$m_k \leq P \quad , k \in \{1, N\} \quad , \quad (3.14)$$

with $P = P_{\text{abs,top}}$ becomes true and translated to the next intersection point B if it is false. Thus, the condition 3.14 is evaluated N times. $N_{\text{abs,top}}$ photons are absorbed in the top layer.

At point B, the photons are either reflected, absorbed by the ARC or refracted into the middle layer. Before the condition for reflection is evaluated, the photons with a

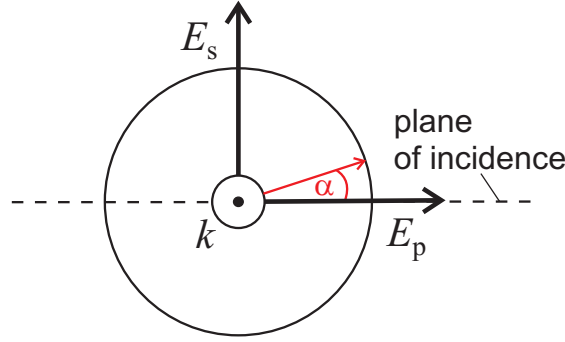


Figure 3.8: The figure shows the polarization angle α , the wave vector \mathbf{k} directing out of the paper, the plane of incidence and the two polarization eigenstates of the electric field \mathbf{E}_s and \mathbf{E}_p .

polarization angle α have to be projected in one of the two eigenstates, s or p . For this, the plane of incidence is evaluated by the photon direction of the incoming and reflected wave. Figure 3.8 shows the definition of the polarization angle α with respect to the plane of incidence. The probability of the k -th photon to be p -polarized is $P_{\text{pol},p} = \cos^2(\alpha)$ ⁶. With this probability, the condition 3.14 is evaluated for $(N - N_{\text{abs,top}})$ photons. If it is true, the photon is p -polarized, otherwise it is s -polarized.

Now that the k -th photon has a defined polarization state, the reflectance for the condition 3.14, P_{ref} , is calculated by Eq. 2.16 and the Fresnel equations 2.12, 2.14 without ARC and 2.25 with ARC. N_{ref} photons become reflected under consideration of the reflection law (Eq. 2.6) if condition 3.14 is true. How many photons $N_{\text{abs,ARC}}$ are absorbed in the ARC is evaluated with the probability $P_{\text{abs,ARC}} = A/(1-R)$ with A from Eq. 2.27. The denominator results from the fact that the reflection has been accounted for in the previous decision. The decision with $P_{\text{abs,ARC}}$ is evaluated for $(N - N_{\text{abs,top}} - N_{\text{ref}})$ photons. The remaining $(N - N_{\text{abs,top}} - N_{\text{ref}} - N_{\text{abs,ARC}})$ photons are transmitted under consideration of Snell's law (Eq. 2.7) into the substrate. A part of the reflected photons trajectories ends at the top plane (point G) or intersects at another point with the mid layer where the decision process starts anew.

The unit cell in Fig. 3.7 corresponds to the simulated geometry. Once a ray hits a boundary that is parallel to the z -direction, e.g. at point C, it is translated to the opposing plane of the unit cell, here point D. The translation from point C to D does not contribute to the path length and hence no absorption occurs. The simulation runs until all photons are either absorbed or have left the simulation domain by reflection towards the top surface (point G) or transmission towards the bottom surface (point F). Random surface textures are realized by randomizing the position of the rays in certain x - y planes of the structure, e.g. at the middle/bottom layer interface. The raytracing simulation approaches the physical model for a sufficiently large number of rays and photons, usually

⁶Hence, the probability to be s -polarized is $P_{\text{pol},s} = \sin^2(\alpha)$.

10000-20000 photons per wavelength. Except for the AR-coated interfaces, the raytracer applies geometrical optics and does not consider diffraction effects that can occur when the features sizes of the unit cell, W and L , approach the wavelength of the incident light. The Fresnel number $F = a^2/d\lambda$ is a coarse criterion that describes in how far geometrical optics are applicable. F is defined for an electromagnetic wave with wavelength λ that traverses an aperture with size a and impinges on a screen at distance d . If $F \gg 1$, diffraction effects can be neglected. The structure sizes within this work are $a \approx \text{few } \mu\text{m}$, which means that diffraction cannot be completely excluded. However, we will show in Ch. 7 that by introducing a Lambertian factor for the rear side, experimental spectra can be modelled by raytracing. Within this work we use the well-established raytracing software SUNRAYS [39]. For more specific geometries, we use the software Daidalos [24].

Chapter 4

Characterization of macropore etching

After introducing the theoretical background of macropore etching in Ch. 2, we experimentally test the formation model and characterize the etching setup used in this work. The experiments in this chapter, despite already reported in literature, help to clarify the etch protocol in Ch. 5.

4.1 Characteristic current density J_{ps}

Both the porosity Φ (via Eq. 2.69) and the growth rate r (via Eq. 2.70) of the macropores depend on the characteristic current density J_{ps} . Equation 2.64 describes the dependence of J_{ps} on the HF concentration c and the temperature T of the electrolyte. The literature gives contradicting values for the parameters A , α and E_a [73, 86, 109–112] which is why we determine them for our setup and electrolyte composition by measuring the current-voltage characteristic for different values of c and T . We identify the characteristic peak in the forward and reverse voltage scan under illumination (see Fig. 2.15) to check the reproducibility of the peak position. The maximum illumination intensity of the LED array limits the detectable current density to $J_{max} = 33 \text{ mA/cm}^2$. Details of the experimental conditions can be found in the Appendix B under samples 5 through 9.

The resulting parameters are obtained from a fit of the extracted data with Eq. 2.64 and are listed in Tab. 4.1. The deviation from the values of Ref. [73] may result from a different wetting agent in the electrolyte and/or differences in the temperature or current measurement/regulation.

Table 4.1: Parameters for determining the current density J_{ps} in Eq. 2.64. The results from Lehmann are shown as well [73].

	Ref. [73]	this work
A [$\text{A cm}^{-2}(\text{wt } \%)^{-\alpha}$]	3300	1350 ± 500
α	1.5	1.414 ± 0.020
E_a [eV]	0.345	0.314 ± 0.020

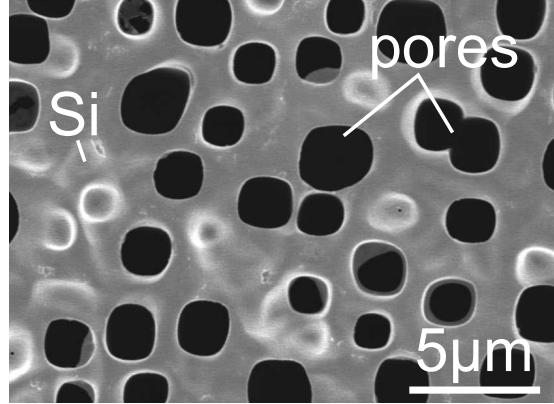


Figure 4.1: SEM micrographs of top-view on porosified sample without predefined etch seeds. The substrate resistivity is $\rho = (1.5 \pm 0.2) \Omega\text{cm}$ and the average pore pitch is $p_{\text{unstr}} = (4.5 \pm 1.2) \mu\text{m}$.

4.2 Correlation between pore pitch and pore morphology

The pore pitch p can be set by lithographically defined inverted pyramids as described in Ch. 3. The space charge region model predicts that for a specific substrate doping density N_D , the pore wall width a must be at least twice the width of the space charge region W_{scr} in order to get distinguishable pores. The model can thus be used to make a choice for an appropriate pore pitch, if the doping density of the material is known. In this section, we study the impact of the predefined pore pitch p on the morphology of the macropores for Si with a substrate resistivity of $\rho = (1.5 \pm 0.2) \Omega\text{cm}$. For an applied voltage of $U = 0.5 \text{ V}$, Eq. 2.66 yields a value of $W_{\text{scr}} = 0.7 \mu\text{m}$ and hence a pore wall width of at least $1.4 \mu\text{m}$ is to be expected. Figure 4.1 shows a top-view of a porosified sample without inverted pyramids. Under this condition, the pores grow self-organized after a nucleation phase of a few μm [82]. The experimental details can be found under sample number 10 in Appendix B. We measure an equilibrium pore pitch of $p_{\text{unstr}} = (4.5 \pm 1.2) \mu\text{m}$ and an average pore diameter of $d_{\text{unstr}} = (2.2 \pm 0.6) \mu\text{m}$. We find thus an average pore wall width of approximately $2.3 \mu\text{m}$.

Figure 4.2 shows SEM micrographs of cross-sectional views of samples that have been porosified with different pitches p but the same etching current density $J \approx 0.35 J_{ps}$. The experimental details can be found under sample numbers 11 through 14 in Appendix B. We measure pore wall widths of 2.3, 2.7, 3.7 and $3.8 \mu\text{m}$ for predefined pore pitches

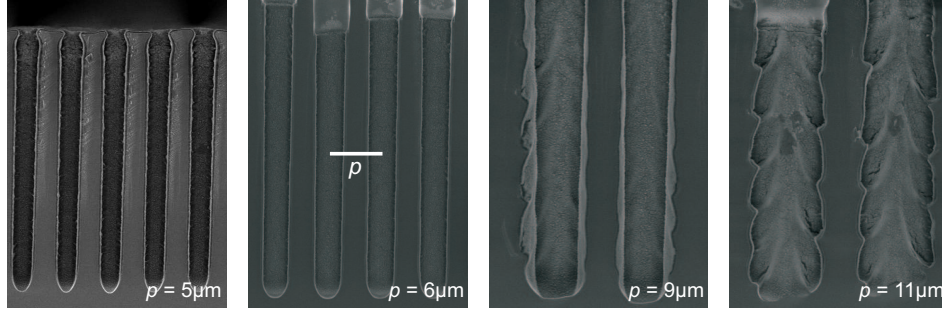


Figure 4.2: SEM micrographs of macropores within an array of different pitch p , etched under equal conditions. The larger the pitch and thus the wall width between the pores, the stronger the tendency for the growth of side pores. The substrate resistivity is $\rho = (1.5 \pm 0.2)\Omega\text{cm}$.

of $p = 5, 6, 9$ and $11 \mu\text{m}$. Straight pores are achieved for $p = 5$ and $6 \mu\text{m}$ while for $p = 9$ and $11 \mu\text{m}$ the pore walls are roughened and a tendency to grow side pores, i.e. pore branching, can be observed. This dependency can be explained by the space charge region model which predicts that holes enter the pore walls if the pitch and hence the wall width becomes too large with respect to W_{scr} . We conclude that the more the pitch exceeds the equilibrium pitch of the unstructured sample, which itself depends on the applied voltage U and the doping density N_{D} via W_{scr} , the larger the current flow through pore walls J_{90° (see Eq. 2.68) and the rougher the morphology of the pore surface.

4.3 Impact of current density on pore morphology

In this section, we study the impact of the etching current density J on the pore morphology. The Lehmann formula in Eq. 2.69 relates the current density with the porosity Φ . We check the validity of this formula by etching samples with a constant current density between $J = 4$ to 16 mA/cm^2 for 40 minutes. Details of the experimental conditions are listed under samples 15 through 20 in Appendix B. We determine the porosity Φ i) gravimetrically by weighing the sample before (m_1) and after (m_2) porosification and ii) geometrically by measuring the average pore diameter in the SEM and assuming either square-shaped or circular-shaped pores. The gravimetric porosity is calculated by

$$\Phi_{\text{grav}} = \frac{m_{\text{p}}}{m_{\text{tot}}} = \frac{m_1 - m_2}{l_{\text{p}} \rho_{\text{Si}} A_{\text{tot}}}, \quad (4.1)$$

where $m_{\text{p}} = m_1 - m_2$ is the mass of the dissolved material in the porosified volume $V_{\text{p}} = A_{\text{tot}} l_{\text{p}}$ and m_{tot} is the mass of Si in this volume in the unporosified state. l_{p} , $A_{\text{tot}} = 1 \text{ cm}^2$ and $\rho_{\text{Si}} = 2.33 \text{ g/cm}^3$ symbolize the pore depth, the porosified area and the density of Si, respectively. Since the pores are arranged in an orthogonal lattice with

a pitch p , the geometric porosity of square-shaped pores is

$$\Phi_{\text{geo}}^{\square} = \left(\frac{d}{p}\right)^2, \quad (4.2)$$

and for circular-shaped pores

$$\Phi_{\text{geo}}^{\circ} = \frac{\pi}{4} \left(\frac{d}{p}\right)^2. \quad (4.3)$$

d symbolizes the average pore diameter.

Figure 4.3 shows the impact of J on the pore morphology for a pre-defined pitch of $p = 6$ to $7 \mu\text{m}$. As J approaches J_{ps} , pores overlap and become indistinguishably wide and eventually the whole Si surface is electropolished. If the current density becomes small compared to J_{ps} , some pores die out which points to different growth rates r between individual pores. This circumstance limits the porosity, and therefore J , to values of $0.2 < \Phi < 0.5$ for which individual pores are distinguishable and grow at the same speed. We therefore exclude the samples 15 and 20 from the geometric evaluation of the porosity. Figure 4.4 a) shows the result from the different approaches. The porosity depends linearly on the current density as is predicted by the Lehmann formula in Eq. 2.69. The porosity from the gravimetric method is between the two geometric approaches. The fact that the pores have neither completely square-shaped nor a circular-shaped cross-section as shown in the SEM micrograph in Fig. 4.4 b) explains this. The error bars of the geometric approaches result from the statistical uncertainty of the pore diameter (10 measurements points). The error bars from the gravimetric approach result from the uncertainty in the pore depth and the sample weight. The slope of the line from gravimetric approach is (0.0364 ± 0.006) which yields a characteristic current density of $J_{\text{ps}} = (27.47 \pm 0.46) \text{ mA/cm}^2$. The nominal HF concentration of the electrolyte is 3.5 wt % which corresponds to $J_{\text{ps}} = 31.1 \text{ mA/cm}^2$ according to the parameters from Tab. 4.1. The reason for this discrepancy is that the HF concentration of the electrolyte has declined to 3.2 wt % due to numerous etched samples while the parameters in Tab. 4.1 were obtained from fresh electrolytes.

Figure 4.3 illustrates that not only individual pores grow at different rates for small current densities but that the overall growth rate decreases for larger current densities. For example, the average pore depth of sample 16 with $J = 6 \text{ mA/cm}^2$ is $l_p = 33.1 \mu\text{m}$ while sample 20 with $J = 16 \text{ mA/cm}^2$ has an of $l_p = 27.2 \mu\text{m}$. The reason for this is that the dissolution chemistry, described by the valence n , changes with J . We include more samples, listed under numbers 21 through 26 in Appendix B, from which we determine the weight before and after porosification. We then calculate the valence according to Eq. 2.71. Figure 4.5 shows that the valence takes values between 2, corresponding to a fully divalent dissolution, and 4, corresponding to electropolishing for current densities

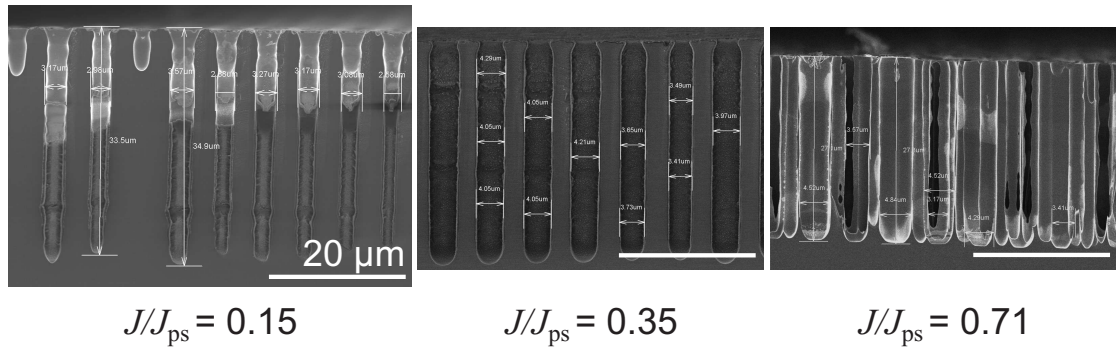


Figure 4.3: SEM micrographs of macropore arrays, grown at three different etching current densities $J = 4, 10$ and 16 mA/cm^2 . While for low current densities, some pore die out, high current densities lead to an overlapping of pores and they become indistinguishable. The white line corresponds to $20 \mu\text{m}$.

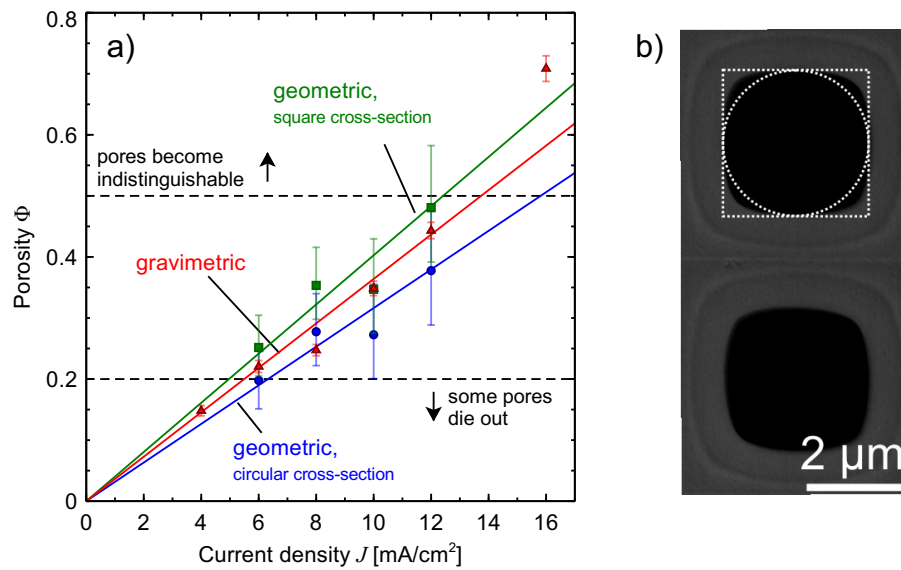


Figure 4.4: The figure shows a) a plot of the porosity versus the etching current density J . The porosity has been determined gravimetrically and geometrically by assuming square-shaped or circular shaped pores. b) shows an SEM micrograph of the top view of two neighboring pores. The pore shape is neither completely square nor circular.

approaching J_{ps} . Dissolution valences between 2.3 to 3 result in macropores with a porosity between 0.2 and 0.5. The dissolution valence is the result of a local coexistence of electropolishing at the pore tips where $J_{tip} = J_{ps}$ and a rather divalent dissolution towards the pore walls for larger θ (see Fig. 2.19). If the current density becomes too low, the pore tips are not in a steady-state condition ($J_{tip} < J_{ps}$) and pores grow at individual rates r . If the current density becomes larger, the dissolution valence increases and according to Eq. 2.70 the growth rate decreases.

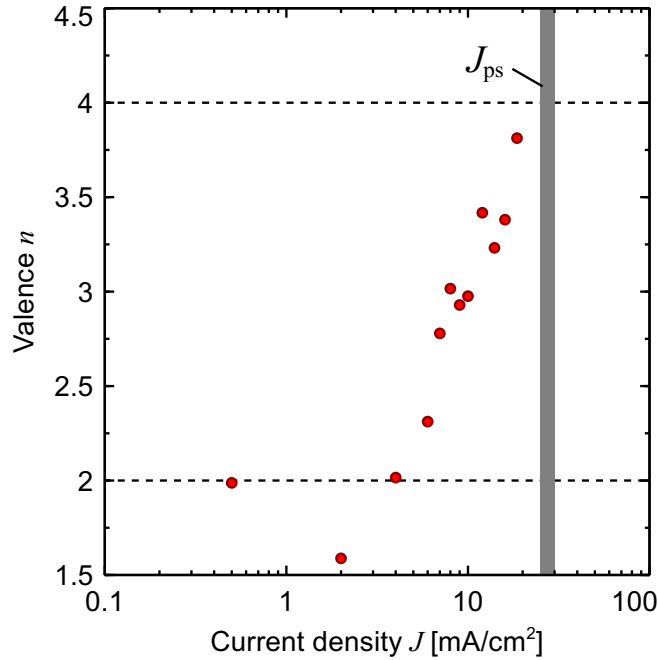


Figure 4.5: The figure shows a plot of the dissolution valence n versus the etching current density J . The grey bar marks the characteristic current density J_{ps} . The dashed lines are guides to the eye and mark the valence 2 and 4, respectively.

4.4 Impact of voltage on pore morphology

The samples discussed in the previous sections are etched with anodic voltages of $U = 0.5 - 2$ V (see Appendix B). Figure 2.15 shows that this is above the voltage U_{ps} which is about (0.1 ± 0.1) V. In this section, we study the impact of the voltage on the pore morphology by etching samples with values for $U - U_{ps}$ between -0.3 to 1 V. The etching current density is fixed to $J = 8$ mA/cm². Details of the experimental conditions can be found under sample numbers 27 through 31 in Appendix B. Sample 27 is etched in the voltage mode with a fixed illumination intensity. This results in an average voltage of $U - U_{ps} = -0.3$ V.

Figure 4.6 shows SEM micrographs of the cross-sectional view of samples 28, 29 and 31. For anodic voltages below the characteristic voltage U_{ps} , we observe that the pores become wider and the pore length is smaller compared to samples with $U > U_{ps}$. Sample 27 shows a porosity/pore length of $\Phi = 0.48/l_p = 23$ μ m compared to $\Phi = 0.39/l_p = 26.5$ μ m for sample 31. We furthermore observe that the pore tips are tapered or pyramidal-like in shape for $U < U_{ps}$ and circular for $U > U_{ps}$. The magnified micrograph of the pore tip as shown in the inset of Fig. 4.6 yields that for $U < U_{ps}$ the pore tip is not electropolished but covered with a microporous film.

We determine the valence of the different samples gravimetrically by using Eq. 2.71. Figure 4.7 shows the resulting valence in blue. We use the obtained valence $n(U)$ to calculate the pore tip current density J_{tip} by Eq. 2.70. The results are plotted in green in Fig. 4.7. Both the valence n and the current through the pore tip J_{tip} decrease if the voltage drops below U_{ps} . Under the condition of constant current density J , they remain constant for $U > U_{\text{ps}}$ ¹. These findings can be interpreted within the frame of the space charge region model: For voltages $U \geq U_{\text{ps}}$, the concentration of holes at the pore tip is large enough to support the indirect dissolution with valence $n = 4$ and the current density at the tip is $J_{\text{tip}} = J_{\text{ps}}$. For voltages $U \leq U_{\text{ps}}$, the SCR becomes more narrow and the hole concentration at the pore tip is insufficient to support the oxidation of Si, indicated by the microporous film at the pore tip. The holes then diffuse along the interface until they participate in a divalent dissolution reaction, resulting in wider pores and a lower effective valence. The tapered morphology of the pore tip can be explained by the anisotropy of the divalent dissolution reaction as described in Sec. 2.8.

The characteristic voltage U_{ps} is thus the minimum voltage that enables oxidation of Si at the pore tips. If the voltage U is below U_{ps} , the growth rate is no longer limited by mass transport but by the charge transfer to the interface. The results are similar to the case of a too low current density J : Small perturbations in pore size become self-reinforcing, meaning that a larger pore attracts more holes and grows faster and wider than its neighbouring pores which eventually die out. The pores then grow self-organized, as would be the case in the leftmost image in Fig. 4.6 for a longer etch time. Note that voltages below U_{ps} allow for the growth of macropores only in the transition regime of the $J - U$ curve in Fig. 2.15. If the voltage becomes lower than $\approx U_1$, the valence approaches a value of 2 and the current density drops, leading to micropore formation [73].

4.5 Pore growth rate and HF diffusion

In this section, we study the pore growth kinetics as theoretically described in Sec. 2.8.4. Therefore, we determine the local growth rate $r(l_p)$ experimentally by increasing the etch current density J periodically every 5 min for 15 sec to create an etch mark. The experimental details can be found under sample number 32 in Appendix B. Figure 4.8a) shows an SEM micrograph of the cross-sectional view of a segment of a pore. The etch marks are clearly visible. Figure 4.8b) shows the result of the correlation of the etch marks with the etching time t_{etch} . For the sake of readability, we only plotted every

¹The voltage must not be set to arbitrarily large values. Depending on the substrate doping and the pore curvature, junction breakdown leading to dendritic pore growth occurs for voltages above 10 V [68, 80]

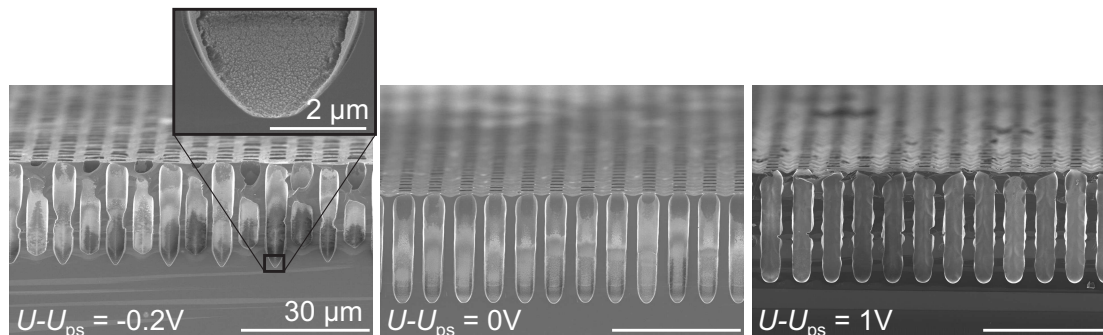


Figure 4.6: The figure shows SEM micrographs of macropore arrays that are grown under the conditions $J/J_{ps} = 0.35$ and $c = 3\text{ wt}\%$, at $T = 20^\circ\text{C}$ for 45 min. The voltage is varied with respect to U_{ps} . The inset shows a zoomed image of the pore tip.

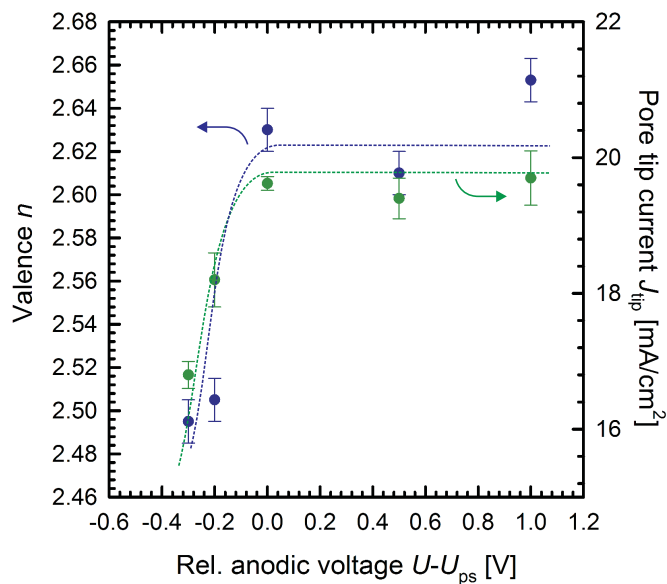


Figure 4.7: The figure displays the influence of the applied voltage on the valence n and the current density through the pore tip J_{tip} . At the threshold voltage U_{ps} , both values saturate. All samples are etched with the same global current J . The datapoint for the lowest voltage is the minimum that allows for the demanded etching current. Dashed lines are guides to the eye.

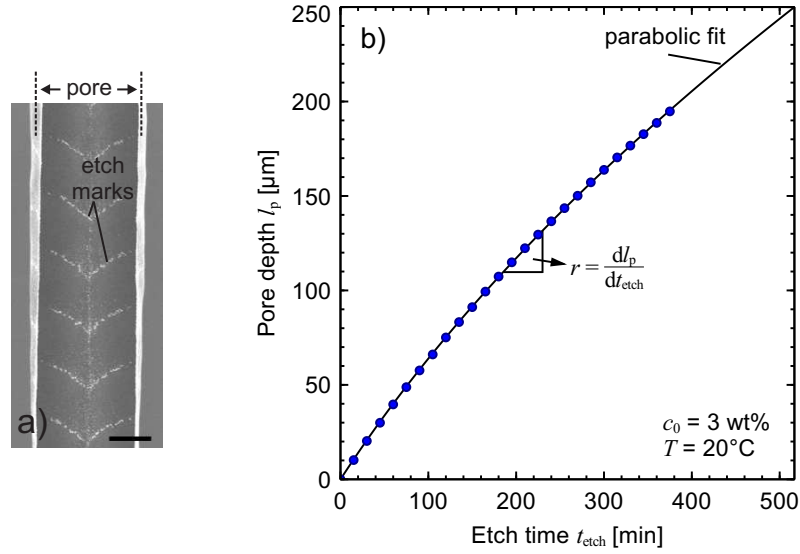


Figure 4.8: a) SEM micrograph of pore with distinct etch marks. An etch mark is set every 5 min. The black bar corresponds to a length of 2 μm . b) Plot of the achieved pore depth versus the etching time. The parabolic behaviour shows that the pore growth becomes retarded with increasing pore depth.

third data point. We fit the data with the parabolic relation between pore depth and etching time from Eq. 2.82. From the best fit parameters, we calculate the initial growth rate r_0 and the characteristic depth of the system l_{p0} . If we take the parameters from the characteristic current density in Tab. 4.1, we furthermore determine the valence of the process n and the diffusion constant of HF D from Eqs. 2.78 and 2.79.

Table 4.2 summarizes the results. We determine a diffusion coefficient of $D = 6 \times 10^{-6} \text{cm}^2 \text{s}^{-1}$ which is in good agreement with the values reported in literature (between 2×10^{-6} and $2 \times 10^{-5} \text{cm}^2 \text{s}^{-1}$ [113]). In this work, we etch pores with $l_p \ll l_{p0}$, which implies that Eq. 2.81 is a valid approximation. The knowledge of the HF concentration at the pore tip allows to adjust the current density J to the decrease in J_{ps} to maintain a, e.g., constant porosity Φ according to Eq. 2.69.

Table 4.2: Values for physical parameters for a HF concentration of 3 wt% and a temperature of 293 K.

Physical parameter	Value
Dissolution valence n	2.63 ± 0.01
Diffusion constant D	$(6 \pm 0.2) \times 10^{-6} \text{cm}^2 \text{s}^{-1}$
Initial growth rate r_0	$0.72 \pm 0.02 \mu\text{m s}^{-1}$
Characteristic depth l_{p0}	$349 \pm 3 \mu\text{m}$

4.6 Summary

In this chapter, we have tested the formation model from Ch.2 experimentally and characterized macropore etching in *n*-type silicon. We define the parameter space for macropore formation in the current-voltage characteristic of the Si/electrolyte junction: For a steady-state condition between mass transport and charge carrier transfer, and hence an oxidation of Si at the pore tip, the anodic voltage has to fulfill $U > U_{ps}$. The steady-state guarantees that all pores grow at the same rate. The etching current density J is directly proportional to the porosity, i.e. the cross-sectional area of the pore. Distinguishable macropores with a straight shape grow for total current densities J that fulfill $0.25 < J/J_{ps} < 0.5$. The current density J_{ps} , which is characteristic for the electrolyte, marks the onset of electropolishing. The parameters to calculate J_{ps} for a given HF concentration and temperature of the electrolyte are evaluated for the etching setup used in this work. The pitch between the pores, usually defined by etch seeds in the form of inverted pyramids, has to be adapted to the doping density of the Si material according to the space charge region model. We apply a diffusion model for the electrolyte that allows determining the HF concentration at the pore tip for any pore depth. With the help of this model and due to the correlation between HF concentration and J_{ps} , it is possible to account for the depletion of HF and achieve a certain porosity by adapting the etching current accordingly.

Chapter 5

Multilayer etching for natively textured sheets of macroporous Si

In this chapter, we exploit the tunability of the macropore diameter as discussed in the previous chapter to detach thin macroporous sheets of Si from the substrate. These sheets can be used as absorber layer in thin film Si solar cells as was demonstrated before [114, 115]. The macroporous structure of the sheets allows for excellent light trapping that can compensate for the reduced effective thickness of the absorber [13]. This work concentrates on the creation of multiple thin sheets within one etching process. Parts of this chapter have been published in Ref. [116].

5.1 The multilayer concept

The motivation to produce thin absorber layers with a slicing technique that avoids or reduces the kerf-loss of Si material has already been discussed in Ch.1. In contrast to the other techniques, macropore etching offers the possibility to generate more than one film in a single process cycle making it economically more attractive¹. Figure 5.1 shows a sketch of the concept. The etch protocol distinguishes between absorber layers A that have a relatively low porosity and embody the bulk material for a solar cell, and separation layers S with a high porosity that induce a weak link to separate the absorber layers. Hence, every absorber layer A_i is accompanied by a separation layer S_i .

Figure 5.2 illustrates the current density profile that we apply for etching multiple absorber layers in a row. The current density for the absorber layer J_A and separation

¹In the Smart Cut technique, for example, the substrate wafer has to undergo the cycle (oxidation → implantation → wafer bonding → heat treatment → lift-off) for the detachment of each subsequent thin layer.

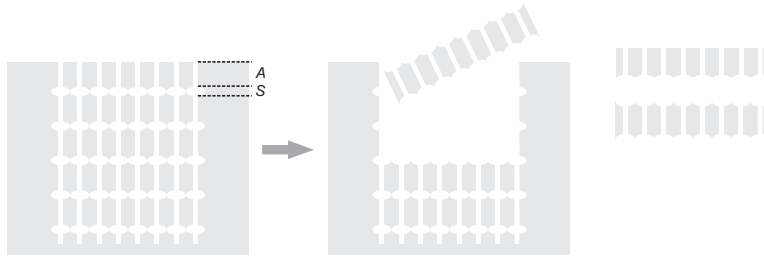


Figure 5.1: Scenario for splitting a Si wafer into many thinner absorber layers A by the formation of separation layers S with a higher porosity. The porosity is modulated repeatedly to create several layers A - S in one etching process. After pore etching, the layers are separated mechanically.

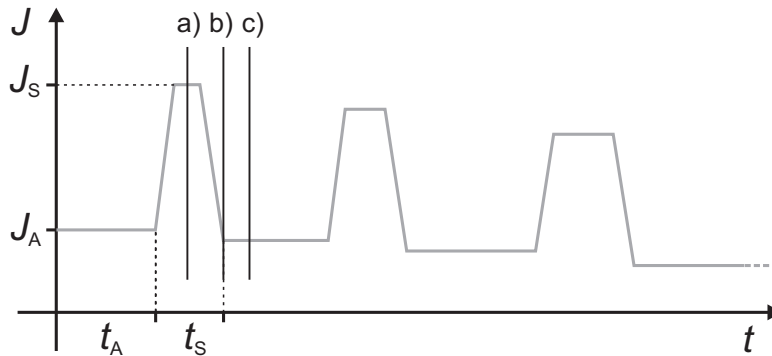


Figure 5.2: The figure schematically shows the typical current density profile for etching multiple macroporous layers. The indices a), b) and c) refer to Fig. 5.4.

layer J_S decrease with the pore depth to account for the decreasing HF concentration at the pore tip (see Eq. 2.81). For the same reason, the etch duration t_A and t_S are prolonged from layer to layer. The thickness of the absorber layers is $< 30 \mu\text{m}$. Figure 4.8 b) suggests that the assumption of a constant growth rate r and thus a constant HF concentration (with $c_0 = 3 \text{ wt}\%$) for this length scale is valid and we therefore keep the current density within the layers on a constant level.

Within this chapter, we exclusively work with pre-patterned samples that have inverted pyramids to initiate the pore growth at a defined position. The advantage is that the pores widen homogeneously and allow a better detachment. It furthermore makes samples comparable and facilitates to study the impact of etching parameters, e.g. J_S , on the outcome of the experiment.

5.2 Preventing pore reorganization

The main challenge of the multilayer concept is to find a way to prevent pore reorganization after etching the separation layer S . As the layer S_1 , for example, has a porosity close to 1 (at least so large that detachment is possible), the Si surface is electropolished

for a certain time. This implies the possibility of "erasing" the pore lattice that has been lithographically defined for the absorber layer A_1 . The pores then "forget" their position in the lattice and grow self-organized². This effect manifests itself in *pore branching* as illustrated in Fig. 5.3. Another form of reorganization is *pore dying* as illustrated in Fig. 5.7. The reasons for pore dying will be discussed in section 5.4.

Branching of a single large pore into many smaller pores occurs after a porosity modulation from high to low porosity (here from S to absorber layer A). Figure 5.3 shows the cross-sectional view of sample 33 specified in Appendix B. The voltage U is above U_{ps} during the whole etching time. We observe that the more the predefined pore pitch exceeds the equilibrium pore pitch p_{unstr} from Fig. 4.1, the more pronounced and the more probable is pore branching. This is in accordance with the macropore formation model from Ch. 2 and the existence of an equilibrium pore pitch p_{unstr} and pore diameter d_{unstr} from Ch. 4. Surprisingly, we experimentally verify for predefined pore pitches between $p = 6 \mu\text{m}$ and $8 \mu\text{m}$ that branching occurs irrespective of the voltage level above U_{ps} . This means that for any voltage $U > U_{ps}$, pores repeatedly split into smaller pores after the strong diameter modulation of S . Based on the formation model, one expects that a larger voltage enhances the "lense effect" of the space charge region on the holes, directing them predominantly towards the pore tip and thus preventing branching. It was indeed shown in literature that a higher anodic voltage is helpful for intermediate porosity modulations of $\Phi < 1$ [119, 120]. However, separation layers with a porosities close to 1 call for different measures.

The novelty in this work is to prevent pore branching after strong porosity modulations by taking the dissolution chemistry and its effect on the pore morphology into account. We achieve this by applying a minimized anodic voltage during t_S . In practice, we switch from the *illumination mode*, where the illumination intensity is the reacting variable, to the *voltage mode* when etching S . In the voltage mode, we apply a sufficiently large illumination intensity that ensures that the demanded current density is achieved with the lowest possible voltage U . Figure 5.4 shows the cross-section of samples 34 through 36 in Appendix B and illustrates the pore shape at stages a), b) and c) of the current profile from Fig. 5.2. The samples have the same pore pitch as the one shown in Fig. 5.3. The branching is prevented because a voltage $U < U_{ps}$ induces a more divalent dissolution reaction and leads to tapered pore tips. This shape facilitates the transfer of the prepatterned pore distribution across the separation layer into the subsequent absorber layer. The inset in Fig. 5.4 b) shows that, similar to Fig. 4.6, a microporous film covers the pore tip after decreasing the pore diameter. The pore tip is electropolished again after re-establishing the steady-state condition after the first pore diameter modulation [see inset of Fig. 5.4 c)].

²Straight pores without separation layers can be etched to depths of hundreds of μm [109, 117, 118].

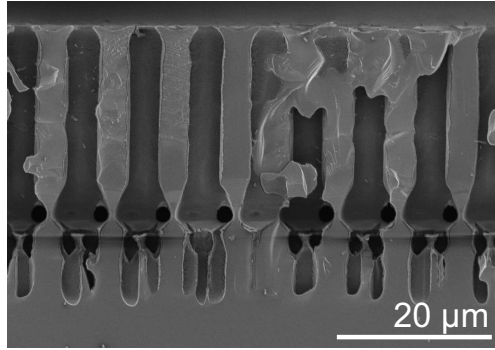


Figure 5.3: The figure shows pore branching as an example for reorganization after a pore diameter modulation.

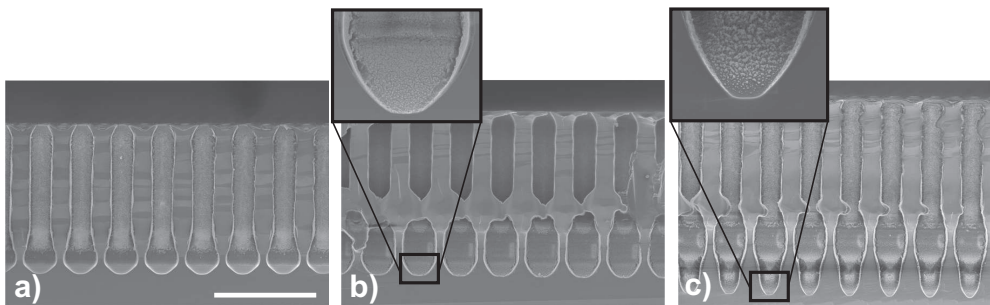


Figure 5.4: The figure shows micrographs of cross sections of a sample with lattice constant $p = 8 \mu\text{m}$ at the three different stages of the separation layer that are marked in Fig. 5.2. The samples are etched with minimized anodic voltage, which prevents reorganization of the pores after the separation layer. The insets show the distribution of the mesoporous film at the pore tip.

5.3 The multilayer etch protocol

We devise an etch protocol that accounts for the voltage minimization during the separation layers and for the depletion of HF at the pore tip. Figure 5.5 illustrates the time profile of the etch parameters for the first two layers of the multilayer process. The complete etch protocol comprises four absorber layers and can be found under sample 37 in Appendix B. For the *illumination mode*, we apply a voltage $U = 0.5 \text{ V}$ which is above $U_{\text{ps}} = 0.1 \pm 0.1 \text{ V}$. We use the diffusion model and calculate current densities of $J_{\text{A}}[\text{mA}/\text{cm}^2] = 7, 6.5, 6, 5.6$ and etch times of $t_{\text{A}}[\text{min}] = 29.5, 32, 35, 37.5$ to obtain absorber layers with a thickness of $W = 20 \mu\text{m}$ and a porosity of $\Phi = 0.3$. For the *voltage mode*, however, the same current density leads to wider pores. We empirically find current densities of $J_{\text{S}}[\text{mA}/\text{cm}^2] = 16.3, 15, 13.9, 13$ and $t_{\text{S}}[\text{min}] = 7.5, 8, 8.7, 9.4$ to be sufficient for detachment. This yields that the minimized voltage during the voltage mode leads to a 15-20% higher porosity compared to the illumination mode in which the pore tip is in a steady-state condition. The HF consumption rate increases when etching the separation layer. We thus pause the etch process for 20 s after each separation layer

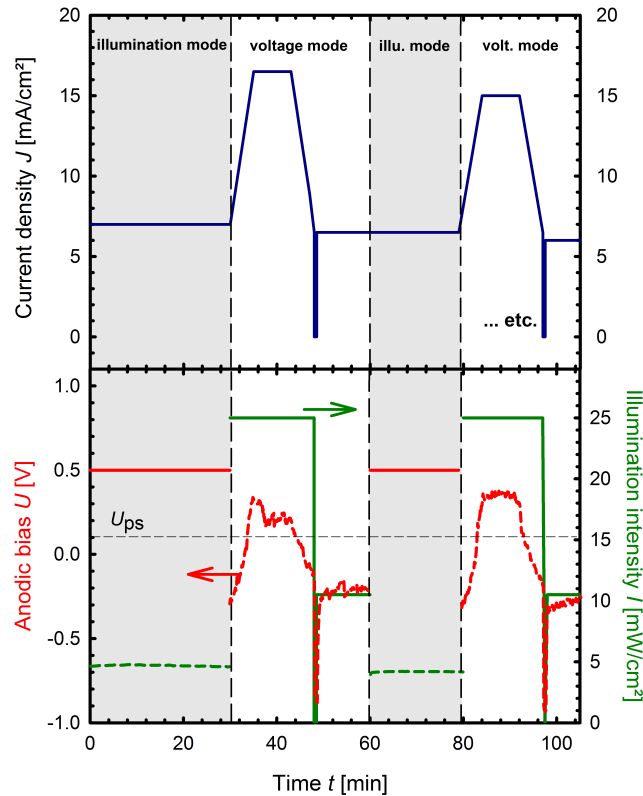


Figure 5.5: The figure shows the parameter profile for etching multiple macroporous layers at once. The actuating variable, depicted as dashed line, changes with the etch mode. The values are for an HF concentration of the electrolyte of 3 wt% and a temperature of 20 °C.

for the electrolyte to replenish at the pore tip. We switch to the illumination mode not directly after the current plateau and keep the voltage mode for an additional 10 min until the pore diameter takes its reduced value again.

Figure 5.6 shows an SEM micrograph of the etched stack and four mechanically detached macroporous sheets with a thickness of $W = (18 \pm 1) \mu\text{m}$. The layers are detached from the substrate by rinsing it with the pressure of a water jet. It also proves helpful to dip the stack into a diluted potassium hydroxide solution at room temperature for a few seconds. Here, an adhesive tape helps to subdivide the layers. The size of the sheets is $(0.5 \times 0.5) \text{cm}^2$ which corresponds to the region with lithographically defined etch seeds with $p = 6 \mu\text{m}$. We determine the porosity of the subdivided layers from the pore diameter d under the assumption of a square-shaped pore, i.e. $\Phi = d^2/p^2$. The first layer and the three subsequent layers yield porosities of $\Phi = (69 \pm 5.5) \%$ and $\Phi = (32 \pm 4) \%$, respectively. This is the first time, that the multilayer process has been demonstrated.

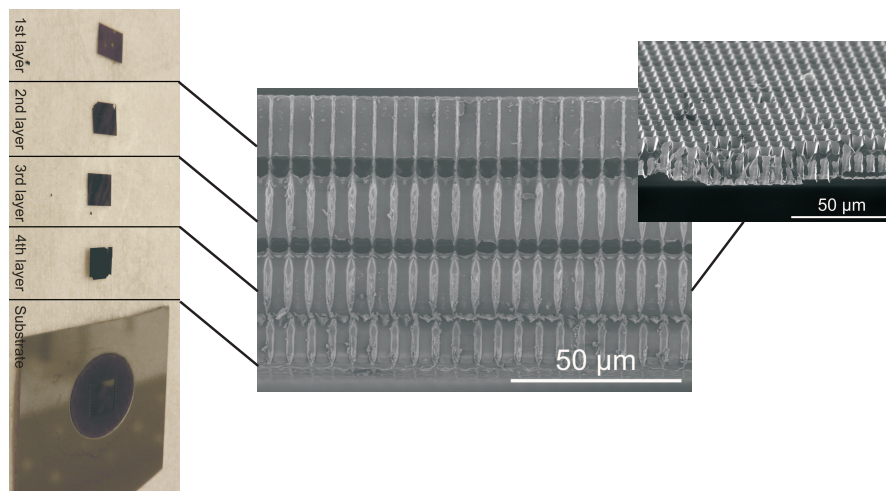


Figure 5.6: The figure shows four detached layers of $W = (18 \pm 1) \mu\text{m}$ and a size of $(0.5 \times 0.5) \text{cm}^2$. The substrate is etched on a circular area of about 1 cm in diameter. The SEM micrographs depict a cross section of a similarly etched sample with slightly decreased J_S and a free-standing macroporous layer.

5.4 Limits of multilayer etching

The maximum number of layers separated from a sample substrate in this work is 4. Efforts to increase the yield were not successful. We first discuss the reason for this limitation.

While the thickness of the detached sheets and the porosity of layers 2, 3 and 4 are in the expected range, the porosity of the first detached layer is much higher than expected. We furthermore find that the etch front in the 5th layer is characterized by pores that stop growing and die out. This is shown in Fig. 5.7 that depicts a cross-sectional view of the fifth absorber layer of a sample etched with a similar protocol as sample 37. In addition, the pore wall etching of the absorber layers, in particular the first layer, is proportional to i) the porosity and ii) the number of the separation layers. The inset of Fig. 5.7 shows a tilted view into the pores after S . The microporous layer that remains on the pore walls suggests that the original pore temporarily splits up into four smaller pores during the current enhancement, making it vulnerable to branching. This illustrates the instability of the ordered pore growth immediately after the separation layer even if the branching is prevented.

The combination of high illumination intensity and low anodic voltage results in an enhanced hole concentration in the pore wall region. As has been described in Ch. 4, an anodic voltage $U < U_{ps}$ already results in wider pores when compared to $U > U_{ps}$. In the multilayer etch protocol, the periods of low voltage are additionally combined with an elevated illumination intensity, i.e. with an excessive hole supply. These holes

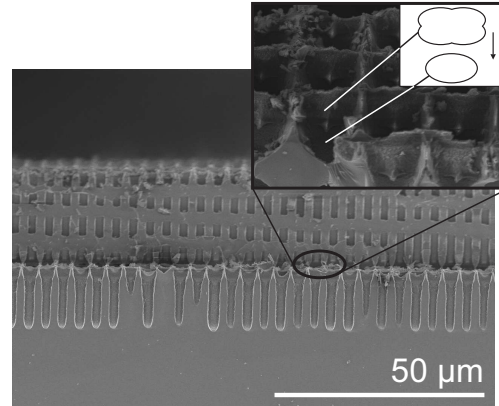


Figure 5.7: The figure shows dying of pores as another example for reorganization after a pore diameter modulation. Three layers have been detached from the sample and we see the fourth absorber layer (not detached) and the beginning of the fifth absorber layer. The inset shows a tilted view into the pores after the diameter enlargement. Also for the voltage minimization, the pore growth becomes instable during the separation layer in a way that one large pore forms four smaller pores. This can be seen by the remaining microporous film in the SEM micrograph and the sketch of the tilted cross-section of the pore within the separation layer and after the rejuvenation. The reduced anodic voltage causes the four smaller pores to eventually re-merge into one larger pore again when the etching current decreases.

substantiate the pore wall etching. Quantitatively, the first absorber layer experiences the most low voltage/high illumination intensity periods which is why it has an overall higher porosity.

The problem of dying pores in the deeper absorber layers arises from the fact that the holes that contribute to the unwanted pore wall etching also contribute to the global etch current density J . As Eq. 2.68 states, if J_{90° rises, the current through the pore tips must decrease if J stays constant. Thus, J is no longer an appropriate parameter to control the pore growth rate and the porosity. From a certain pore surface area, and hence pore depth, onwards, the demanded current density does not suffice to maintain the growth of all pores and some of them die out. In addition to the growing divergence between the pore tip current and J over the etching time, the pore tips themselves are not in a steady-state condition for $U < U_{ps}$. This further enhances the instability of the growth rate among the pores. Note that pore dying occurs also for $U > U_{ps}$ for large pore depths. This is due to the fact that J_{90° is smaller but still non-zero for $U > U_{ps}$ and thus a similar problem as for minimized anodic voltage occurs. Furthermore, the deeper the pores are the more holes are photogenerated in the pore wall region due to the large absorption length of $30 \mu\text{m}$ of the light of the LED array. It is thus difficult to overcome eventual dying of pores without a negative impact on the absorber layers: One could increase the current density J_A for the deeper absorber layers which would delay the pore dying. This on the other hand increases J_{90° as well resulting in enhanced pore

wall etching in the more shallow layers. Both pore dying and pore wall etching become more severe for an increasing number of separation layers.

Pore reorganization can also occur due to extrinsic effects that cannot be controlled by the etch protocol. This includes local inhomogeneities in the charge carrier transfer, e.g. by local doping inhomogeneities, inhomogeneous carrier generation due to illumination or the ohmic back contact, or the mass transport within the electrolyte, e.g. by insufficient replenishment or agitation. The HF diffusion can also be impaired by the formation of hydrogen bubbles at the Si surface.

Pore branching and pore dying are both irreversible and self-enhancing. This means that once the pores start to reorganize, they capture a different amount of holes and carry a different current that ultimately affects the neighboring pores as well. Once reorganized, the ordered pore array cannot be re-established, as the etch parameters apply globally for the whole etching area. A "repair" of the reorganized pore would require to control the etch parameters for the pores individually. The reorganization severely impedes the detachment of the absorber layer and poses a limit on the multilayer etching. We find that if 5% of the pores reorganize and leave Si bridges with a few 100 nm in diameter between the absorber layers, detachment can become impossible without breaking the absorber layer.

The presented multilayer process relies on the illumination intensity as the third etching parameter to allow both high current densities and minimized voltage. It is therefore limited to *n*-type Si. Macropore formation in *p*-type Si is carried out under galvanostatic conditions with the current limited by the voltage [83].

5.5 Alternative approach: One-by-one detachment

The discussion of the limitations of the multilayer process shows that a high yield of detached sheets with reproducible porosity calls for an in-situ monitoring of the etch conditions (growth rate, valence, etc.) at the pore tip and continuous adaption of the etch protocol. There are also alternative routes to use electrochemical etching as wafer slicing technique. One example is to detach the absorber layers one by one which takes four steps: i) etch a single $A - S$ profile, ii) dismount the sample from the etch cell for detachment of the absorber layer, iii) recondition the surface of the substrate by a mixture of KOH and polyethylene glycol (PEG) (stirred solution of 25 wt% KOH and 6.25 g/l PEG at 50° C, etch time of 30 min during which the rear side ohmic contact has to be protected by a SiN_x layer), and iv) remount the sample. Afterwards the process starts anew as described under sample 38 in Appendix B. The PEG in the solution for

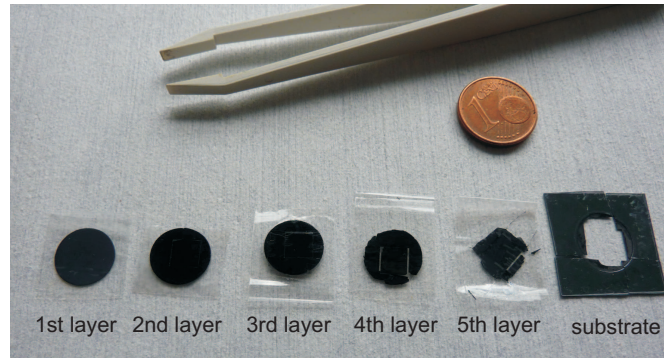


Figure 5.8: The figure shows 5 detached layers with a thickness of 40 μm and the substrate which broke at the last detachment. The Si sheets are detached one by one and the surface of the substrate was reconditioned in a KOH/PEG solution after each detached layer.

reconditioning the etch seeds acts as a surfactant and, in this concentration, reduces the etch rate of KOH to 40 nm/min. The reconditioning transforms the pore tips into small inverted pyramids again. This one-by-one process has been evaluated within this work as well and is more relaxed with respect to the monitoring of the etch parameters. We were able to detach 5 layers of 40 μm thickness and have thus used about 75% of the original substrate thickness. Figure 5.8 shows the results.

Another approach is to extend the pore diameter moderately by porosification and then separate the absorber layers ex-situ, either by *thermal oxidation - oxide etch* cycles [121], modified alkaline etching [122] or high temperature annealing [120, 123]. All these alternatives, however, question the economical benefit of wafer slicing by macropore formation.

One may also argue that the pore etching is strictly not a kerfless technique when it comes to minimize sacrificial material. In fact, about 30% of the absorber layer is dissolved. The macropores, however, embody a "native" texture that allows for ultra-low reflectance and nearly Lambertian light trapping [13]. As Fig. 2.11 shows, good light trapping can compensate for a thinner effective thickness with respect to the photogeneration. Ernst *et al.* demonstrated a conversion efficiency of 13.1% on a 35 μm -thick macroporous solar cell with an epitaxially grown emitter [114]. The short-circuit current density amounted to a relatively large value of 37.1 mA/cm². For a classification of this efficiency and current density, see Ref. [124].

5.6 Summary

In this chapter, we discussed the applicability of electrochemical etching of macropores as a kerf-less wafering technique. For the first time, we were able to detach 4 individual macroporous Si sheets with a thickness of 18 μm from a substrate that are etched within a closed process, i.e. without dismounting the substrate from the etching cell. This has been realized by finding appropriate etching conditions for the prevention of reorganization of the pores after the highly porous separation layer. We discover two forms of reorganization, branching of a single pore into many smaller pores and dying of individual pores; both severely impede the detachment of absorber layers.

We overcome the reorganization by pore branching by etching the separation layers in the voltage mode with a fixed and elevated illumination intensity. This allows to minimize the applied voltage and thus change the interface chemistry towards a more divalent dissolution, as described in Ch.4. As a further novelty in this work, we use this voltage dependence of the valence, which is disregarded by the space charge region model, to form a rather tapered pore tip during the transition from high to low porosity. The higher the desired porosity of the separation layer, the more necessary it is to reduce the voltage.

The voltage minimization inherits the yield limitation of the multilayer process: as the current does no longer predominantly flow through the pore tip, the global etching current density becomes unpinned from the porosity at the pore front and leads to eventual pore reorganization by pore dying. The severeness of this effect increases with the Si/electrolyte interface area or, here, the amount of separation layers that have been etched. The reorganization can thus be delayed but not completely averted by the voltage minimization. The prevention of pore reorganization calls for an in-situ monitoring with continuous adaption of the etch parameters.

Chapter 6

Macroporous blind hole texture

In the previous chapter, we have shown that while the macroporous absorber sheets allow for a large photogeneration, it is difficult to establish a reproducible etching process that would allow to detach multiple sheets from a substrate. In this chapter, we benchmark a texture made of macroporous blind holes, i.e. pores that have a depth much smaller than the wafer thickness, against the state-of-the-art random pyramid texture. We characterize the optical as well as electrical properties.

6.1 Introduction

As we have shown in Ch. 2, the design of the front surface of an absorber should allow for low external reflectance. State of the art pyramidal textures, either randomly [35] or regularly [36] arranged, in combination with a dielectric ARC reduce the AM1.5G photon flux-weighted front surface reflectance between 300 and 1000 nm to values of 2.1 to 2.7 %, depending on the properties of the dielectric layer [125, 126]. Random pyramids have the additional benefit of a nearly complete randomization of the light propagation direction (see Tab. 2.1). However, dielectric layers such as SiN_x absorb a fraction of the incoming UV light and thus lower the blue response of the solar cell. A novel kind of surface texture, thus, has to fulfill the requirements of

- i) a lower front surface reflectance than AR-coated pyramids,
- ii) a sufficiently good light trapping,
- iii) a surface passivation quality that does not overcompensate the gain in photogeneration.

The formation of a pyramidal texture on (100)-oriented Si wafers relies on the anisotropic etch rate of alkaline solutions (see Fig. 2.6 on p. 11). Common electrolytes are based on potassium hydroxide (KOH) or tetramethyl ammonium hydroxide (TMAH). The (111)-planes act as etch stop which fixes the texture angle to 54.74° ¹. Alternative surface textures known as black silicon reduce the reflectance effectively without the use of an ARC by featuring steeper facets with a larger texture angle [128, 129]. An interesting property of nm-sized black silicon is that it partially works as an ARC itself as the effective refractive index gradually increases from the refractive index of air to that of the substrate [25, 26, 128]. Recent results with black silicon structures that were produced by cryogenic reactive ion etching (RIE) showed photon flux-weighted reflectance values as low as 0.7% [130, 131] and reached a surface recombination velocity of 7 cm/s after surface passivation with atomic layer deposited AlO_x [132]. The correlation length of nano-scaled black Si is small compared to the incoming wavelength which leads to a weak randomization of light propagation direction and thus an impaired light trapping ability of the texture [129, 133]. For this reason, it has been suggested to use a double-scale texture consisting of nano-scaled black Si on top of micron-scaled pyramids [134] or with black Si on the front side and pyramids on the rear side [135].

Macroporous blind holes, i.e. pores that do not perforate the wafer, embody a less fragile alternative to nano-scaled black Si without impairing the light trapping. Reflectances between 1 to 5% for wavelengths between 300 and 1000 nm with pore depths of 17 to 20 μm have been reported [136, 137]. Previous work, however, lacked the evaluation of the electronic passivation capabilities and the comparison with a state-of-the-art random pyramid texture.

6.2 Sample preparation and texture morphology

Figure 6.1 a) illustrates a sketch of the blind hole texture with a predefined pore pitch $p = 4 \mu\text{m}$, a pore depth l_{pore} , a minimum pore diameter at the bottom d_{min} , a height of the pore tip h and a flat wall width between two adjacent pores w_{wall} . The requirement for a blind hole texture to appear "black" is a minimum width w_{wall} and a sufficiently large depth l_{pore} . We achieve this with an etching current density profile as illustrated for different pore depths l_{pore} in Fig. 6.1 b). All profiles are etched in the *illumination mode* and start with a high current density of $J_{\text{max}} = 25 \text{ mA/cm}^2$ for which the surface is electropolished under the given electrolyte composition. The current density is then gradually lowered according to the diffusion model from Ch. 2.8.4 in order to guarantee a linear decrease in the pore diameter. The lower limit for the current density at which

¹Detailed investigations of real structures yield a texture angle distribution around 50.5° [127].

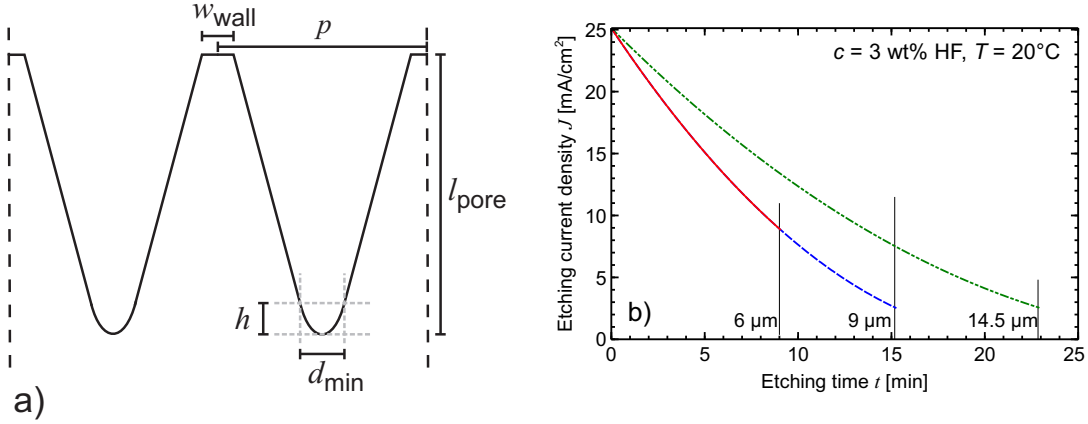


Figure 6.1: The figure shows a) a sketch of the blind hole texture and b) the preset etching current density for textures of different depths l_{pore} .

the steady-state condition at the pore tip breaks down is $J_{\text{min}} = 2.5 \text{ mA}/\text{cm}^2$. The pore depth is controlled via the etching time. For the given pitch of $4 \mu\text{m}$, the lowest pore depth for which J_{min} is reached is $l_{\text{pore}} = 9 \mu\text{m}$. Shallower pores with $l_{\text{pore}} < 9 \mu\text{m}$ are achieved with the same current density profile as pores with $l_{\text{pore}} = 9 \mu\text{m}$ but terminated earlier. Deeper pores with $l_{\text{pore}} > 9 \mu\text{m}$ have an extended etching time as shown in Fig. 6.1 b). The anodic voltage decreases linearly over the etch time from 1.5 V to 1 V to allow for the large etching current densities in the beginning of the profile. The voltage is permanently above $U_{\text{ps}} = (0.1 \pm 0.1) \text{ V}$ which means that the pore tip is electropolished and has a spherical shape as in Fig. 2.19 b).

Figure 6.2 shows a photograph of the low reflecting blind hole samples a) together with SEM cross-sectional micrographs of the texture with two different pore depths b) and c). The etched area appears black while the border area shows a distinct diffraction pattern from the regularly arranged inverted pyramids. Note that the use of predefined etch seeds is not in contradiction with the electropolishing condition at the beginning of the etch profile as the high current is maintained only for a short time. The inset shows an SEM top-view micrograph, yielding a pore wall width of $w_{\text{wall}} = (80 \pm 5) \text{ nm}$.

We remove the recombination-active n^+ -type diffusion at the rear side of the samples. This increases the sensitivity for determining the surface passivation quality of the front side and, in addition, avoids free carrier absorption at the rear side that would otherwise complicate the analysis of the optical measurements. For the removal, we first protect the sensitive texture by coating the front side of the sample with an 80 nm -thick layer of PECVD SiN_x (Plasmalab 80+ from Oxford Instruments). Since the PECVD process is not surface conformal, i.e. the protection layer does not cover the whole pore surface, the etching of the rear side with KOH (50 vol\% KOH , $T = 80^\circ \text{C}$) has to be carried out very carefully. The higher density of the KOH solution compared to Si helps to avoid

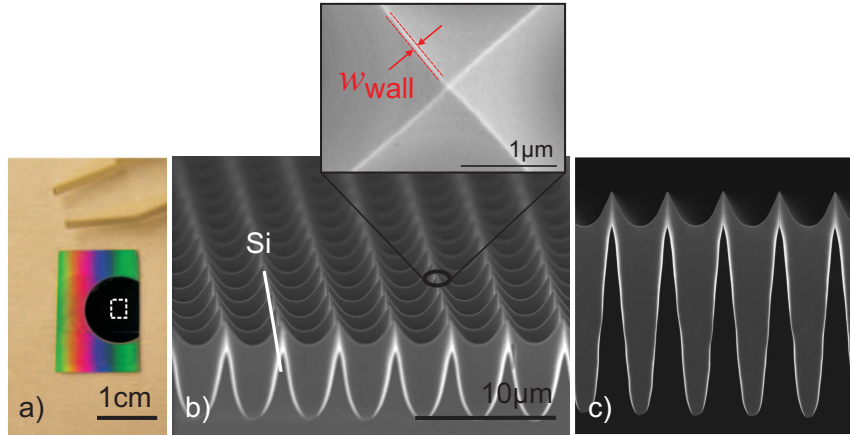


Figure 6.2: The photograph of the samples in a) yields the black porosified area and the border area with regularly arranged inverted pyramids. The white frame marks the size of the illuminated spot in the spectrophotometer. SEM cross-sectional micrographs of the blind hole texture with pore distance $4\ \mu\text{m}$ and pore depths of $6\ \mu\text{m}$ b) and $14.5\ \mu\text{m}$ c). The sample is slightly tilted in b). Both images b) and c) have the same scale.

direct contact of the etch bath with the texture by letting the samples swim on top of the solution for 3 min. Afterwards, the protection layer on the front is removed in HF and the samples are RCA-cleaned. We deposit $20\ \text{nm}$ AlO_x on both sides of the samples by atomic layer deposition (FlexAL from Oxford Instruments) for surface passivation. In contrast to the PECVD process, the standard ALD process is surface conformal for pore depths up to $30\ \mu\text{m}$. For deeper pores, the AlO_x does not cover the whole pore wall down to the bottom without a prior adaption of the deposition process, e.g. a prolonged gas flow in the ALD cycle. The random pyramid textured samples have either a $20\ \text{nm}$ -thick AlO_x surface passivation and/or a PECVD SiN_x layer on the front as ARC depending on whether they serve as reference for the optical or electrical measurement. Table 6.1 lists the investigated samples in this chapter.

6.3 Optical characterization

In this section, we thoroughly characterize the optical performance of the blind hole texture. We study the impact of pore depth, angle of incidence and compare it with an AR-coated random pyramid texture. We analyze the optical losses with respect to front side reflectance and inferior light trapping.

Table 6.1: The table shows the investigated samples of this chapter and specifies the texture geometry and the coating layers. The blind holes have a pitch $p = 4 \mu\text{m}$ and a wall width of $w_{\text{wall}} = (80 \pm 5) \text{ nm}$. Samples marked with an asterisk are also taken for lifetime measurements. The material for all listed samples is n -type FZ Si with a resistivity of $(3 \pm 2) \Omega\text{cm}$.

Name	Texture	W_{eff} [μm]	l_{pore} [μm]	d_{min} [μm]	Front coating	Rear coating
B1*	Blind hole	277.2	4.7	2.6	20 nm AlO_x	20 nm AlO_x
B2	Blind hole	276.8	5.3	2.4	20 nm AlO_x	20 nm AlO_x
B3*	Blind hole	276.4	6.0	2.2	20 nm AlO_x	20 nm AlO_x
B4	Blind hole	275.8	6.5	2.0	20 nm AlO_x	20 nm AlO_x
B5	Blind hole	275.4	7.3	1.8	20 nm AlO_x	20 nm AlO_x
B6*	Blind hole	276.1	8.0	1.6	20 nm AlO_x	20 nm AlO_x
B7*	Blind hole	275.9	9.0	1.4	20 nm AlO_x	20 nm AlO_x
B8*	Blind hole	273.4	14.5	1.4	20 nm AlO_x	20 nm AlO_x
B9	Blind hole	272.1	17.5	1.4	20 nm AlO_x	20 nm AlO_x
B10*	Blind hole	269.5	23.0	1.4	20 nm AlO_x	20 nm AlO_x
B11	Blind hole	265.0	33.0	1.4	20 nm AlO_x	20 nm AlO_x
R1*	Rand. pyr.	250.0	-	-	10 nm $\text{SiN}_{x,2.4}$ + 96 nm $\text{SiN}_{x,1.9}$	25 nm $\text{SiN}_{x,2.4}$
R2*	Rand. pyr.	250.0	-	-	20 nm AlO_x + 96 nm $\text{SiN}_{x,1.9}$	20 nm AlO_x
R3*	Rand. pyr.	250.0	-	-	20 nm AlO_x	20 nm AlO_x
P1*	Planar	253.0	-	-	20 nm AlO_x	20 nm AlO_x
I1	Inv. pyr.	280.0	-	-	96 nm $\text{SiN}_{x,1.9}$	-
I2	Blind hole	275.9	9	1.4	-	-

6.3.1 Absorptance spectra

Figure 6.3 a) illustrates the absorptance spectra of the blind hole samples with varying pore depths. All samples have a 20 nm AlO_x layer on both surfaces. We make sure that the illumination spot of the spectrophotometer with a size of $(2 \times 3) \text{ mm}^2$ is within the porosified region, as indicated in Fig. 6.2 a). The absorptance increases with increasing pore depth l_{pore} . Up to a wavelength of 900 nm, the absorptance is governed by front side reflectance and equals $A = 1 - R_{\text{front}}$. The shape of the absorptance curves in this region looks similar to the reflectance of Si/air in Fig. 2.9 on p. 18. The differences result from multiple light reflections within the pore, that reduce the overall external front reflectance. The number of reflections and thus the absorptance increase with l_{pore} .

We observe an unexpected absorptance of about 12% for wavelengths above 1200 nm for all blind hole samples. We speculate that this effect stems from impurity-mediated absorption in the nonporosified border area of the sample. Impurities, e.g. sulfur [138, 139], are likely to be incorporated during the RIE step [140]. While the sulfur is removed in the region with the blind holes during etching, it is not removed in the nonetched region. Although the border area is not illuminated directly, multiple internal reflections

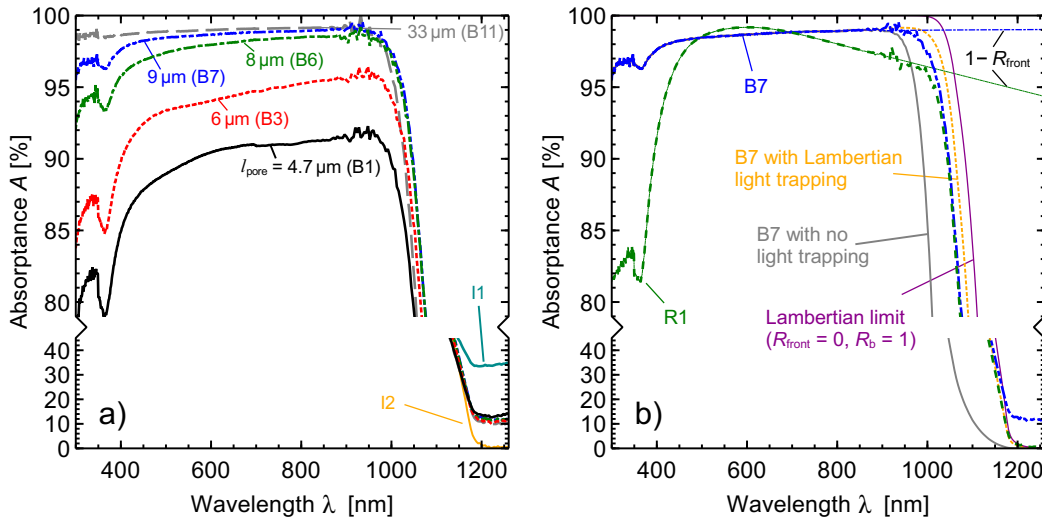


Figure 6.3: The figure shows an excerpt of the measured absorptance spectra of the samples in Tab. 6.1 with a) the blind hole samples and b) the comparison with the random pyramid sample. b) additionally shows calculated references with different light trapping schemes as well as the extrapolated front side reflectance for samples B7 and R1.

in the sample still allow for weakly absorbed light to reach this area and cause sulfur-related absorption. Figure 6.3 a) also shows the absorptance for $\lambda > 1100 \text{ nm}$ of two control samples I1, prior to porosification, and I2, a sample where the non-porosified region has been cut off by a laser. The sample I1 shows an even higher absorptance of sub-bandgap photons while that of sample I2 vanishes. This supports our interpretation. We refrain, however, from cutting all samples as I2 due to size-related issues during measurement and handling. Figure 6.3 b) shows the absorptance spectra of the random pyramid textured sample R1. As it has not been reactive ion etched, the absorptance approaches zero for wavelengths above 1200 nm.

While the blind hole texture reaches a relatively high absorptance A for the whole wavelength region up to 900 nm, the AR-coated random pyramids exhibit a high absorptance especially for the design wavelength, here 600 nm. We extrapolate the external front reflectance R_{front} for the whole spectrum up to 1200 nm linearly for the random pyramid samples [131]. For the blind hole samples, we use a power function of the form [13]

$$R_{\text{front}} = a \left(\frac{(n-1)^2 + k^2}{(n+1)^2 + k^2} \right)^b. \quad (6.1)$$

n and k symbolize the real and imaginary part of the refractive index of Si and a , b are fit parameters. The extrapolation of R_{front} with a power function that includes the refractive index of Si is more appropriate for textures that work by multiple reflections at the Si/air interface than the linear option for AR-coated textures. The 20 nm-thick

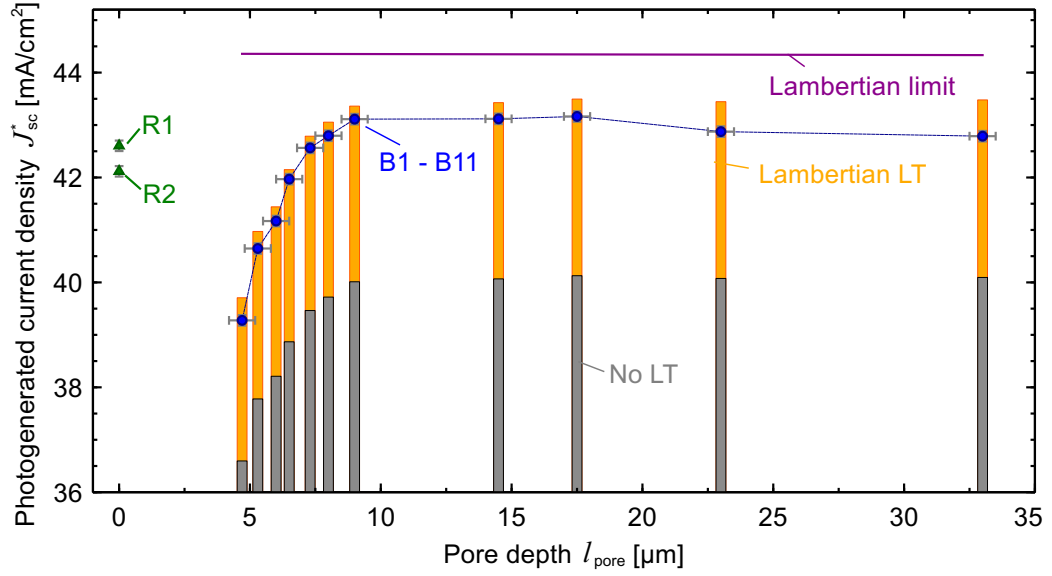


Figure 6.4: The figure shows the photogenerated current densities (blue dots) compared to the simulated references that have i) no light trapping but the same external front reflectance R_{front} as the blind hole textured samples (grey bars), ii) a Lambertian front side and R_{front} (orange bars) and iii) the Lambertian limit for each sample thickness.

AlO_x layer has only a small AR effect of less than $0.15 \text{ mA}/\text{cm}^2$ on the photogenerated current density for the smallest pore depth². Figure 6.3 b) shows the calculated R_{front} for two samples.

6.3.2 Analysis of optical losses

Figure 6.3 b) shows the calculated absorptance for samples that have the R_{front} of sample B7 but either no light trapping scheme, A_{noLT} , or a completely randomizing front surface, A_{Lamb} , as well as for the Lambertian limit ($A_{\text{Lamb,limit}}$, see Eq. 2.47). We calculate A_{noLT} and A_{Lamb} by inserting R_{front} of sample B7 into Eqs. 2.38 and 2.46, respectively. For the Lambertian sample, we assume $R_{\text{b}} = 1 - T_{\text{b}}/n^2$. We simulate T_{b} , which is the transmittance through a planar Si surface coated with 20 nm AlO_x , with the raytracer SUNRAYS. We assume a pyramidal shaped pore and calculate the effective thickness by $W_{\text{eff}} = W - l_{\text{pore}}/3$, where $W = 280 \mu\text{m}$ is the wafer thickness prior to porosification. The calculated A_{Lamb} serves to correct for the absorption by impurities. For this, we assume that the absorptance of the blind hole sample A_{BH} cannot exceed A_{Lamb} . If for the measured absorptance we find $A_{\text{BH}} > A_{\text{Lamb}}$, which occurs for wavelengths larger than 1160 nm, we take $A_{\text{BH}} = A_{\text{Lamb}}$ for these datapoints. The corresponding photogenerated current densities are J_{noLT}^* , J_{Lamb}^* and $J_{\text{Lamb,limit}}^*$, respectively.

²This value is based on raytracing simulations with Daidalos.

Photogenerated current densities

Figure 6.4 shows a plot of the photogenerated current densities J_{sc}^* for the samples B1 through B11. The values are listed in Tab. 6.2. The photoabsorption rises with pore depth to a maximum of 43.16 mA/cm^2 for $l_{\text{pore}} = 17.5 \text{ }\mu\text{m}$. For deeper pores, J_{sc}^* slightly decreases again. The uncertainty in the absorptance measurement and from the correction for the impurity absorptance results in an overall uncertainty of 0.1 mA/cm^2 in J_{sc}^* , which is about as much as the symbol size in Fig. 6.4. The bar plot helps to distinguish the optical losses. The top of the grey and orange bars symbolize J_{noLT}^* and J_{Lamb}^* , respectively. The position of the measured J_{sc}^* in relation to J_{noLT}^* and J_{Lamb}^* is a measure for light randomization of the blind hole texture: the closer the measured J_{sc}^* is to J_{Lamb}^* , the more randomizing is the texture. The drop of J_{sc}^* with respect to the top of the orange bars for the two largest values for l_{pore} points to the fact that the light trapping becomes worse for deeper pores. A possible reason for this is the different angular acceptance of deeper pores that we will discuss in the next subsection. As both J_{noLT}^* and J_{Lamb}^* saturate above a certain pore depth, we can conclude that the external front reflectance under normally incident light saturates as the absorptance spectra already indicate.

Table 6.2: The table shows the photogenerated current density J_{sc}^* as well as the loss current density due to front reflectance J_{front} and imperfect light trapping and rear reflectance J_{res} for the samples. In addition, the AM1.5G-weighted front reflectance R_w and the absorbed current density in the ARC J_{ARC} are listed.

Name	J_{sc}^* [mA/cm ²]	J_{front} [mA/cm ²]	R_w [%]	J_{res} [mA/cm ²]	J_{ARC} [mA/cm ²]
B1	39.28	4.45	10.59	1.05	-
B2	40.65	3.12	7.61	0.86	-
B3	41.17	2.61	6.47	0.85	-
B4	41.97	1.86	4.75	0.77	-
B5	42.56	1.18	3.14	0.82	-
B6	42.80	0.91	2.38	0.81	-
B7	43.11	0.59	1.48	0.76	-
B8	43.12	0.51	1.26	0.82	-
B9	43.16	0.44	1.07	0.83	-
B10	42.87	0.49	1.13	0.98	-
B11	42.79	0.44	1.02	1.16	-
R1	42.60	1.26	3.56	0.43	0.15
R2	42.12	1.64	5.95	0.52	-
P1	27.48	14.90	33.61	1.93	-
I1	41.57	2.20	4.57	0.58	-

We emulate the trends of the different optical losses with the raytracer Daidalos. Figure 6.5 shows a CAD representation the simulated geometry which is a simplified version of the sketch in Fig. 6.1 a). We approximate the shape of the pore by a frustum of a pyramid that has a smaller pyramid on top. The smaller pyramid that should represent

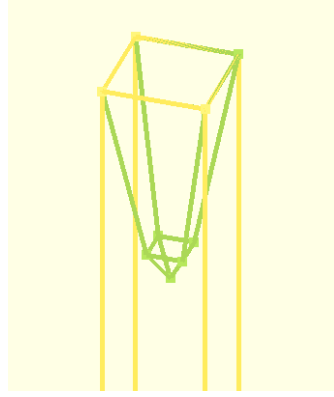


Figure 6.5: The figure shows a CAD representation of the geometry that is simulated with the raytracer Daidalos.

the pore tip has a fixed height of $h = 1.3 \mu\text{m}$ for all pore depths and a depth-dependent base length of d_{min} . The height is based on the evaluation of several SEM micrographs. The frustum has a base length of $p - w_{\text{wall}}$, a height of $l_{\text{pore}} - 1.3 \mu\text{m}$ and a top width of d_{min} . We determine d_{min} from SEM measurements. The values are listed in Tab. 6.1. The inner pore surface has a 20nm-thick AlO_x coating just as the actual samples.

Front surface reflectance

Figure 6.6 a) shows the measured (symbols) and simulated (dashed lines) loss currents due to external front reflectance J_{front} , which are calculated by substituting A by the respective R_{front} in Eq. 2.4. The values for J_{front} are listed in Tab. 6.2. The comparison with the simulated J_{front} yields a good agreement when we assume the experimentally verified wall width of $w_{\text{wall}} = 80 \text{ nm}$. If we multiply the J_{front} -value of a planar Si surface coated with 20 nm AlO_x , which is 14.9 mA/cm^2 , with the surface ratio of the flat 80 nm-wide walls, which is 4%, we end up with a reflected current density of 0.6 mA/cm^2 . This approximates the saturation value quite well and yields that from a certain pore depth onwards, light is predominantly reflected from the flat parts between the pores³. The assumption of a zero wall width, as illustrated by the black dashed line in Fig. 6.6 a), yields that J_{front} becomes essentially independent of the pore depths for $l_{\text{pore}} > 25 \mu\text{m}$. Table 6.2 also lists the AM1.5G-weighted front reflectance R_w . We achieve a reflectance of less than 1.5% for pore depths of $l_{\text{pore}} > 9 \mu\text{m}$, i.e. from sample B7 onwards, which is competitive to nm-sized black silicon structures for photovoltaics [128, 141–145].

Light trapping and rear reflectance

Figure 6.6 b) shows the residual current density $J_{\text{res}} = J_{\text{Lamb,limit}} - J_{\text{sc}}^* - J_{\text{front}}$. It describes the loss due to imperfect randomization and rear reflectance, i.e. imperfect light

³The underestimation of J_{front} for larger pore depths is probably related to Daidalos, as Sunrays reproduces the value of 0.6 mA/cm^2 to within 0.01 mA/cm^2 . Sunrays, however, cannot account for the shape of the pore tip, increasing the inaccuracy in J_{res} .

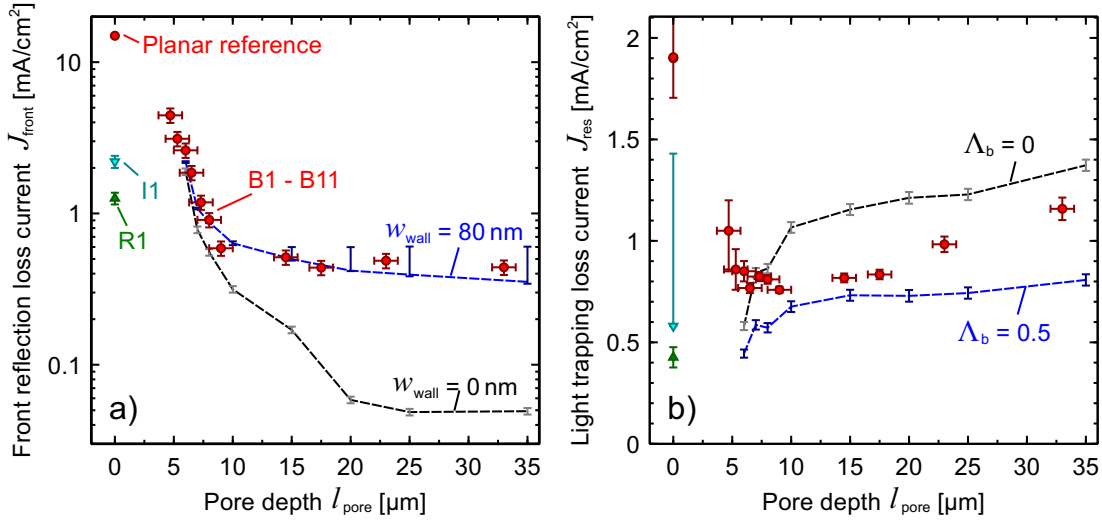


Figure 6.6: The figure shows the optical loss current density due to a) external front reflectance, J_{front} , and b) due to imperfect light randomization and rear reflectance, J_{res} for different surface textures. The dashed lines are from raytracing simulations.

trapping. The values for the samples are listed in Tab. 6.2. As expected, J_{res} is highest for the planar sample. Among the blind hole samples, we observe a higher J_{res} for the two deepest pores, as Fig. 6.4 already indicates. This trend is also reflected in the raytracing simulation (dashed lines), which are shown for two different Lambertian characters of the rear side Λ_b . This character specifies the probability for the reflected light from the rear side to become fully Lambertian.

The simulation, however, predicts a better light trapping for more shallow pores, which we do not observe experimentally. This is probably due to the oversimplified geometry, as the result is more sensitive on the shape of the pore tip for shorter pores. Note also that the unporosified surface of the blind hole samples has inverted pyramids. Thus, J_{res} does not correspond to the pure blind hole texture but to a mixture between blind holes and inverted pyramids. The J_{res} of inverted pyramids is symbolized by the cyan triangle in Fig. 6.6 b). We easily overestimate the light trapping performance of sample I1 by the evaluation method to determine J_{res} due to the large parasitic absorption. Therefore, we perform a raytracing simulation of sample I1 and determine a J_{res} of 1.45 mA/cm² ($\Lambda_b = 0$), which we take into account by the error in Fig. 6.6 b).

Although the rear side of the samples is planar, absolute values of J_{res} are best modeled with $0 < \Lambda_b < 0.5$. It is known from random pyramid textures that the assumption of a rear side roughness leads to a better agreement between raytracing simulations and the measured absorptance spectra [146]. This might be due to neglected wave optical effects that become important for feature sizes in the range of the typical wavelength, e.g. the tips of the pyramids or between the blind holes. The raytracing framework does,

for example, not consider diffraction into guided modes [61] or the anomalous parallel interface refraction [147].

The random pyramid sample has the best light trapping performance and loses only 0.43 mA/cm^2 due to imperfect light randomization and rear reflectance. This could be attributed to the random arrangement of the pyramids as the sample I1 with regular inverted pyramids has a comparable J_{res} as the blind hole textures. It is known from literature that breaking the symmetry of the texture results in a better light trapping performance as it helps to populate the phase space [62, 63].

Blind holes versus random pyramids

Figure 6.7 compares the optical performance of the blind hole sample B7 with the random pyramid sample R1 and a simulated random pyramid sample with an optimized DARC that consists of 40 nm $\text{SiN}_{x,1.9}$ and 100 nm MgF_2 (on top of 20 nm AlO_x for surface passivation). The effective thickness of the simulated structure equals the one of sample B7. The figure depicts the deviation from the Lambertian limit (corresponding to 100%) due to external front reflectance, non-Lambertian light trapping and rear surface transmittance. The parasitic absorption in the ARC of sample R1 amounts to $0.3\%_{\text{abs}}$ (0.15 mA/cm^2) of the total optical loss of $4.1\%_{\text{abs}}$, which has been determined by raytracing with Sunrays. The loss channels, as described in Ch. 2, are inversely proportional to each other. The blind hole sample shows the highest share of absorbed photons and well-balanced losses. The random pyramid samples have rather unbalanced losses, either with an inferior front surface reflectance (sample R1) or light trapping performance in case of a DARC on random pyramids. The lower R_{front} due to the second AR layer improves the share of absorbed photons from 95.9% to 96.9%. The higher front surface transmittance, however, also applies for photons that are incident from the silicon half-space, which deteriorates the light trapping. Thus, the advantage in optical performance of the blind hole texture over the random pyramids also holds for a DARC and amounts to an $0.3\%_{\text{abs}}$ (0.15 mA/cm^2) higher photogenerated current density.

6.3.3 Performance under oblique incidence

The morphology of the blind hole texture with its steep facets suggests a better angular acceptance compared to random pyramids [130]. In addition, an ARC is usually optimized for normal incidence. We measure the absorptance spectra of the samples under angles of incidence α between 15° and 55° . From each absorptance spectra we calculate

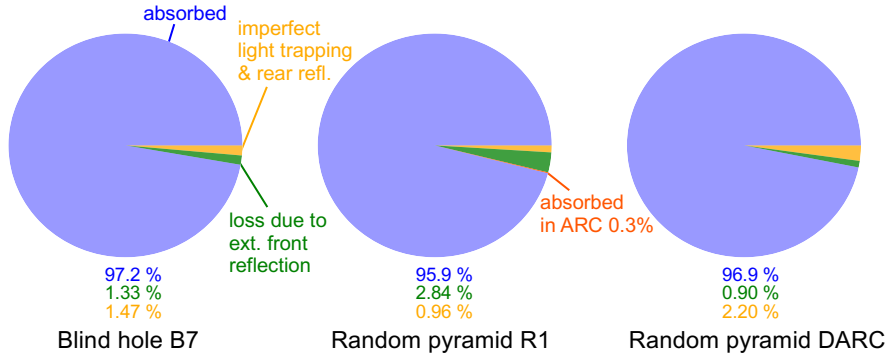


Figure 6.7: The figure compares the optical performance the light trapping structures with respect to their Lambertian limit. It lists the share of photons that become absorbed, externally reflected or lost due to non-Lambertian light trapping and imperfect rear reflectance. The ARC of sample R1 absorbs a fraction of light as well. The values for the DARC structure are based on a raytracing simulation.

a $J_{sc}^*(\alpha)$ by Eq. 2.4. Figure 6.8 a) shows the normalized results⁴ for three blind hole textures B3, B7 and B11 and the random pyramid sample R1. The aspect ratio of the blind hole texture affects the angular acceptance in a characteristic manner. Sample B3 with an aspect ratio of 6:4 shows a higher absorptance for $\alpha = 20 - 45^\circ$ than under normal incidence due to an increased number of light bounces between the walls and hence a lower external front reflectance. Sample B7 with an aspect ratio of 9:4 as well as sample B11 with an aspect ratio of 33:4 work best under normal incidence. The large texture angle of B11, however, allows for a large absorptance even for $\alpha > 50^\circ$, for which the more shallow pores show an impaired performance. The sketch in Fig. 6.8 b) explains this behavior. If the texture angle of the blind holes is ϕ , we can describe the incident angle at the pore wall of the n -th bounce by

$$\gamma_n = \phi - \alpha - (n - 1)(180^\circ - 2\phi) \quad , n \geq 1 . \quad (6.2)$$

If γ_n becomes negative, the light ray travels upwards within the pore and eventually exits it⁵. Samples B7 and B11 have texture angles of $\phi = 81^\circ$ and 88° , respectively, which results in $n = 2$ bounces for B7 and $n = 8$ bounces for B11 until γ_n becomes negative for an incident angle of $\alpha = 55^\circ$. The different angular acceptance explains the increased light trapping loss for larger l_{pore} , as shown in Figs. 6.4 and 6.6 b): The time-reversal invariance guarantees that the fraction $T_{\text{in}}(\alpha)$ of light transmitted through the textured surface equals the fraction $T_{\text{out}}(\tilde{\alpha})$ of light escaping the absorber through the surface [46]. α and $\tilde{\alpha}$ are the angle of incidence and the corresponding refraction angle that follows from Snell's law. Now, as the surface reflectance of samples B10 and B11 remains low and thus T_{in} high for larger angles of incidence, this also holds for T_{out} .

⁴For simplicity, we refer to the measurement under $\alpha = 8^\circ$ as the normal incidence case $J_{sc}^*(\alpha = 0^\circ)$.

⁵We neglect the bounces at the pore tip in this simplified treatment.

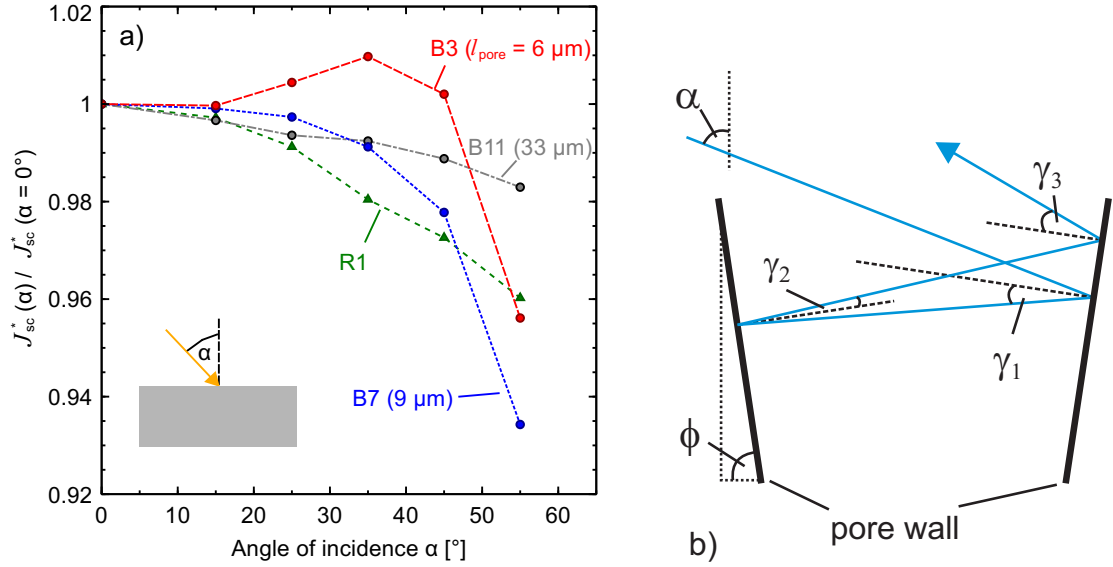


Figure 6.8: The figure shows a) the normalized photogenerated current densities under different angles of incidence and b) a sketch of a possible light path under oblique incidence.

Due to light randomization within the absorber, light from the Si half-space hits the textured surface with a distribution of angles $\tilde{\alpha}$ and can thus exit the absorber more easily as for textures with a higher angular selectivity. The random pyramid sample R1 shows a constant decrease in absorptance with α and performs worse than the blind hole textures.

We estimate the gain of the blind hole texture over random pyramids for a whole year, as the altitude of the sun β and thus the angle of incidence varies with season. For this, we focus on the direct-beam radiation and neglect diffuse and reflected radiation from the albedo of the environment. We take the clear sky beam radiation I_{BC} at a solar cell that is tilted by $\Sigma = 30^\circ$ and faces south, i.e. a cell's azimuth angle of $\phi_c = 0^\circ$, that is explained in Appendix A [148]. We then integrate the product of $J_{sc}^*(\alpha)$ and I_{BC} over the hour angle H to account for the angle dependent absorptance and for the lowered insolation for larger α . We assume an encapsulation material with a refractive index of $n_{\text{en}} = 1.5$ which is appropriate for the commonly used EVA [149]. We apply the refraction law from Eq. 2.7 and change the angle of incidence in Eq. A.6 to $\alpha_{\text{en}} = \arcsin(\sin(\alpha)/n_{\text{en}})$.

Figure 6.9 shows the result for the blind hole samples, normalized by the respective value of the random pyramid sample. In Fig. 6.9 a), we fix the latitude to $L = 50^\circ$. The encapsulant material limits the angle of incidence on the absorber to maximum values of 37 to 40°, depending on the latitude L . This leads to the interesting result that in fact the intermediate pore depths of 9 and 14.5 μm perform better than the deeper pore depths of 23 and 33 μm (samples B10 and B11) for a realistic illumination throughout

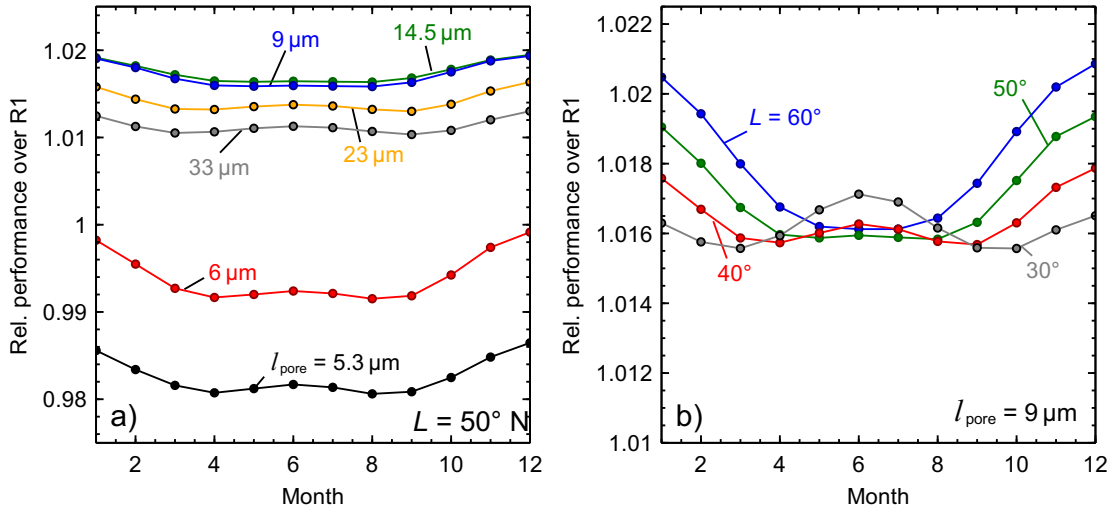


Figure 6.9: The figure shows the relative optical performance of the blind hole texture over random pyramids over the year under direct illumination for a) different pore depths l_{pore} and fixed latitude L and b) different latitudes and a fixed pore depth. We assume that the absorber faces directly south and has a tilt $\Sigma = 30^\circ$. The cell is covered by an encapsulant material with a refractive index of $n_{\text{en}} = 1.5$.

the whole year. This would not hold if the encapsulant was air with $n_{\text{en}} = 1$. Shallow pores with depths of 5.3 and 6 μm (samples B2 and B3) approach the performance of the random pyramid sample only for larger angles of incidence in the winter season. In Fig. 6.9 b), we fix the pore depth to 9 μm and vary the latitude L ⁶. The performance of the blind hole texture exceeds that of the random pyramids for all investigated latitudes. The advantage becomes especially apparent for larger angles of incidence as is the case for large L in the winter season.

The evaluation of the angular acceptance shows that the absorptance enhancement of the blind hole texture over random pyramids increases even more under realistic illumination conditions and explains why the samples with the deepest pore depths investigated have a worse light trapping ability compared to more shallow pores under normal incidence.

6.4 Electrical characterization

Up to this point, we have discussed the blind hole texture solely with respect to its optical absorption. Since we aim to qualify the blind hole texture for solar cell application, the optics cannot be discussed without considering the surface recombination rate that increases with l_{pore} . In this section, we study the impact of surface area enhancement on the electrical performance that manifests in the effective minority carrier lifetime τ_{eff} .

⁶The choice of an intermediate pore depth for the comparison is in anticipation of the electrical properties of the samples that are discussed in the next section.

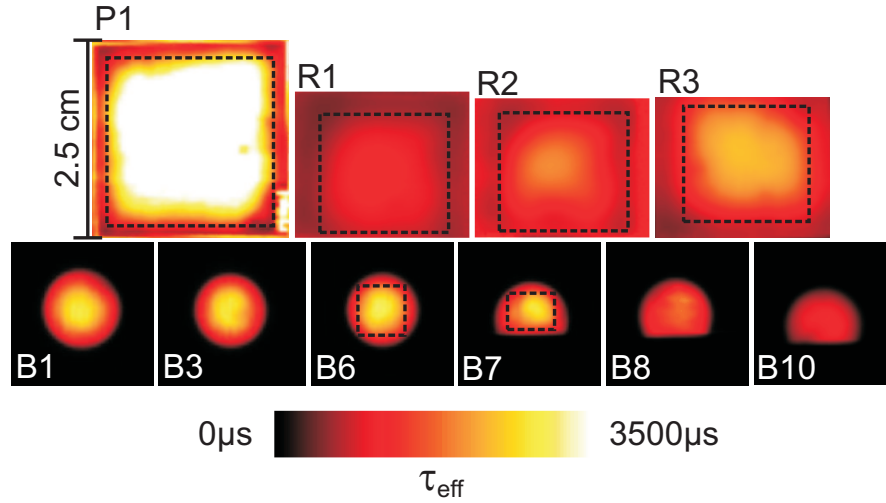


Figure 6.10: The figure shows the ILM effective minority carrier lifetime images of the samples at a photon flux equivalent to 0.14 suns. The base material is 3 Ω cm n -type Si. The samples are to scale to the 2.5 cm-rule.

We measure τ_{eff} of the samples marked with an asterisk in Tab. 6.1. Figure 6.10 shows the dynamically calibrated steady-state ILM image under an absorbed photon flux equivalent of 0.14 suns. The untextured side of the samples faces the LED arrays to exclude differences in front side reflectance. We average τ_{eff} over the area enclosed by the black dashed line. The samples B7, B8 and B10 are cleaved prior to surface passivation for SEM analysis. The planar sample P1 has the highest lifetime with (3.8 ± 0.4) ms. AlO_x that is deposited in a plasma-ALD reactor passivates Si surfaces better than PECVD- SiN_x irrespective of the doping type of Si [150]. The deposition of a SiN_x layer on top of AlO_x proves to be important for firing processes but slightly degrades the surface passivation quality if no high temperature process is involved [151]. These trends are manifested in the lifetimes of samples R1, R2 and R3 which are (1.05 ± 0.15) ms, (1.3 ± 0.20) ms and (1.75 ± 0.40) ms, respectively. The blind hole samples show area-averaged lifetimes between (2.2 ± 0.25) ms and (1.05 ± 0.10) ms, depending on the pore depth. The lifetime for these samples is highest in the center and decreases towards the edge of the porosified area. The reason is the low minority carrier lifetime in the non-porosified region that probably originates from the surface damage introduced when structuring the oxide by RIE. Excess carriers that are generated outside the center have a shorter distance to diffuse into the recombination active border area. The inversion layer that forms at the $\text{AlO}_x/n\text{-Si}$ interface facilitates the lateral carrier transport to the border area [152]. This leads to a significant underestimation of the carrier lifetime [153] which is why the τ_{eff} -values of the blind hole samples with this size must be regarded as a lower limit.

We compare the front surface recombination velocity (SRV) S_f of the different samples. The front side refers to the side with the pores/texture. From Eq. 3.7 we can write

$$S_f(\Delta p) = \frac{W_{\text{eff}}}{\tau_{\text{eff}}(\Delta p)} - \frac{W_{\text{eff}}}{\tau_{\text{bulk}}(\Delta p)} - S_r(\Delta p). \quad (6.3)$$

This formula for S_f implies that it is the effective SRV with respect to the macroscopic area and is not to be confused with the microscopic SRV S_{micro} . For the planar sample, the microscopic SRV is equal to its macroscopic effective SRV. In general, the SRV depends on the excess carrier density Δp [150]. It is thus important to compare the SRV of the different samples at the same injection level rather than at different photon fluxes of the ILM setup as the same photon flux can lead to different excess carrier densities in the investigated sample types. We measure τ_{eff} of the samples at different photon fluxes between 0.14 and 1.1 suns. The excess carrier density then follows from

$$\Delta p = G \tau_{\text{eff}} = \frac{a \times \Phi_{1\text{sun}} \times OF \times \tau_{\text{eff}}}{W_{\text{eff}}}, \quad (6.4)$$

where a is the photon flux in suns, $\Phi_{1\text{sun}} = 2.78 \times 10^{17} \text{ s}^{-1} \text{ cm}^{-2}$ is the 1 sun photon flux density that equals the photon flux density of the AM1.5G spectrum between 300 and 1200 nm and $OF = 1 - R_{f@930\text{nm}}$ symbolizes the optical factor that accounts for the absorbance at the excitation wavelength. In the present case, the optical factor is determined by the front reflectance $R_{f@930\text{nm}}$ and has a value of 0.7. The planar sample has equal surfaces on both sides and is used to determine $S_r(\Delta p)$. We assume the intrinsic limit $\tau_{\text{bulk}} = \tau_{\text{intr}}$ for the bulk lifetime from Ref. [91]. Figure 6.11 shows a plot of S_f over the surface area enhancement factor f that is calculated by

$$f = \frac{1}{p^2} \left((p + d_{\text{min}}) \sqrt{(p - d_{\text{min}})^2 + 4l_{\text{pore}} + d_{\text{min}}^2} + d_{\text{min}}^2 \right). \quad (6.5)$$

In Eq. 6.5, we approximate the shape of the pore as a frustrum of a pyramid with d_{min} being the minimum pore diameter at the top of the frustrum, as illustrated in Fig. 6.5. The smaller pyramid on top of the frustrum is neglected here. Table 6.3 lists the results at an excess carrier density of $\Delta p = 2 \times 10^{15} \text{ cm}^{-3}$.

Figure 6.11 a) shows that the blind hole texture exhibits similar surface recombination velocities S_f as the random pyramid sample despite the larger surface area and the enhanced recombination in the unporosified border area. The blue line serves as an orientation to qualify the measured S_f . It shows the linear increase of the effective macroscopic S_f with the surface area enhancement f , starting from the SRV of the planar sample P1, $S_{f,\text{planar}}$. The blue line, thus, states the S_f -value for a texture with a specific f , if it had the microscopic SRV of the planar sample. All blind hole samples exhibit values for S_f that are below the orientation line while all random pyramid samples lie

Table 6.3: The table lists the results of the electrical characterization of the samples. The effective carrier lifetimes are measured at an excess carrier density of $\Delta p = 2 \times 10^{15} \text{ cm}^{-3}$.

Name	l_{pore} [μm]	d_{min} [μm]	f	τ_{eff} [ms]	S_f [cm/s]
B1	4.7	2.6	4.34	2.35 ± 0.17	8
B3	6	2.2	5.00	2.22 ± 0.14	8.5
B6	8	1.6	5.82	2.52 ± 0.16	6.9
B7	9	1.4	6.26	1.55 ± 0.09	14.0
B8	14.5	1.4	9.95	1.58 ± 0.08	13.1
B10	23	1.4	15.67	0.71 ± 0.04	27.7
R1	-	-	1.73	0.78 ± 0.09	27.3
R2	-	-	1.73	1.31 ± 0.26	14.5
R3	-	-	1.73	1.86 ± 0.36	9.8
P1	-	-	1	4.10 ± 0.42	2.5

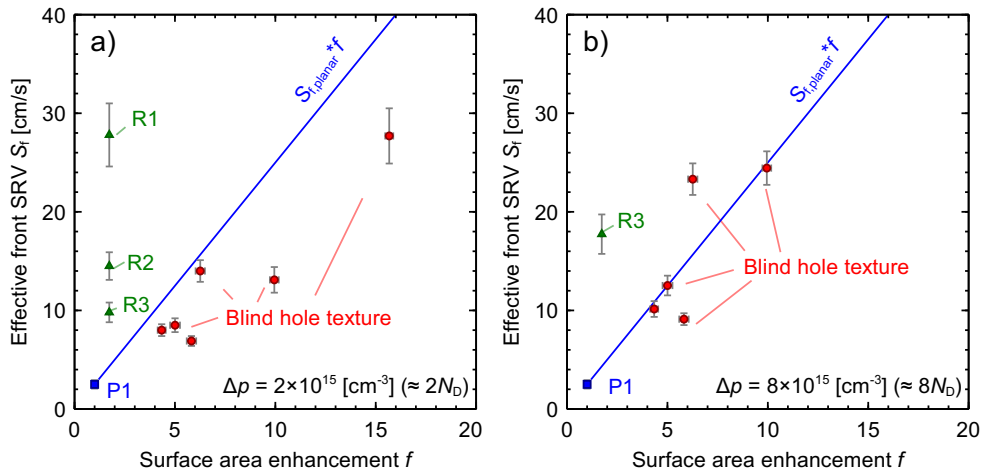


Figure 6.11: The figure shows plots the front surface recombination velocity S_f versus the surface area enhancement f of the investigated samples. The blue line is a linear extrapolation of the surface recombination velocity of the planar sample. The figures a) and b) differ in the injection level Δp .

above it. This suggests that the blind hole texture allows for lower surface recombination velocities with respect to its microscopic surface area than the planar sample.

A similar effect was observed for nm-sized black silicon surfaces [132, 154] and nanowire solar cells [155]. Xiong *et al.* showed analytically that a linear relationship between the effective SRV and the total surface area only holds if the charge carrier distribution in the textured region, here the pore walls, is uniform [156]. According to Ref. [156], this is the case for, e.g., a regular texture with a pitch of 250 nm and a texture height of up to 400 nm. For larger aspect ratios, less charge carriers reach the surface area at the top of the texture and the effective SRV increases sublinearly with the surface area [156]. This effect is further influenced by the field effect passivation due to the fixed negative charge density at the AlO_x/Si interface of, in this case, $Q_f = -2 \times 10^{12} \text{ cm}^{-2}$

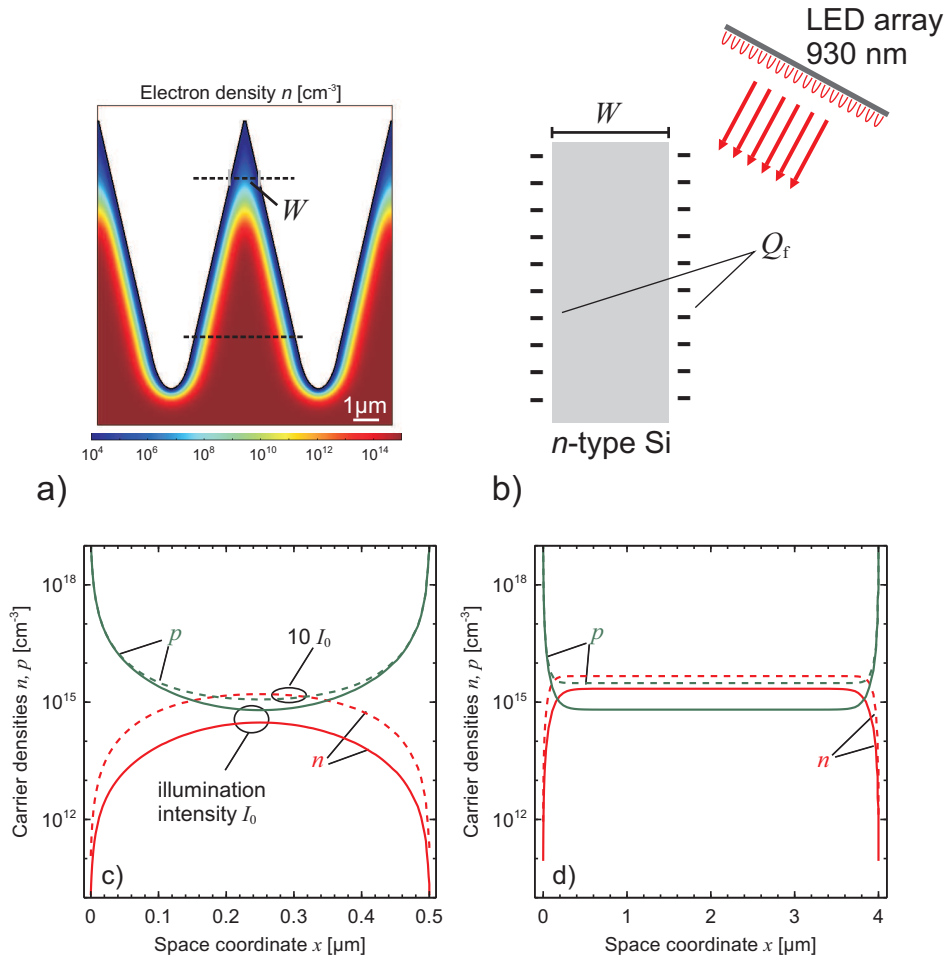


Figure 6.12: The figure shows a) a finite element simulation (FEM) of the electron density distribution of the AlO_x -passivated blind hole texture in the dark. b) shows a sketch of the simulated 1-D sample with thickness W with PC1D. c) and d) show the carrier concentration in the top of the pore wall region $W = 0.5 \mu\text{m}$ and the bottom of the pore wall region $W = 4 \mu\text{m}$, respectively. The carrier densities are shown for small (solid lines) and high injection level (dashed lines), generated with an illumination intensity of I_0 and $10 I_0$.

[157, 158]. Although the field effect passivation is present at planar surfaces as well, the typical morphology of the blind holes (and other black silicon textures) may further reduce the majority carrier concentration in the pore wall region and thus reduce the surface recombination.

Figure 6.12 a) illustrates this effect of an enhanced surface charge density for the blind hole texture: It depicts the electron density of the blind hole texture ($l_{\text{pore}} = 9 \mu\text{m}$, $3 \Omega \text{ cm}$ n -type Si) that we obtain by a finite element simulation (COMSOL Multiphysics). In the 2-D simulation, we assume a fixed charge density at the interface of $Q_f = -2 \times 10^{12} \text{ cm}^{-2}$ and neglect the photogeneration. The depletion regions overlaps at the tips where, due to the absence of one of the recombination partners, the total recombination

rate is reduced. For a more precise description, we perform a 1-D simulation with the program PC1D⁷ [159] at the dashed lines in Fig. 6.12 a). Figure 6.12 b) shows a sketch of the simulated 1-D structure which is an *n*-type Si wafer with $Q_f = -2 \times 10^{12} \text{ cm}^{-2}$ on both sides being illuminated with monochromatic light with a wavelength of 930 nm. The surface recombination is modelled with a Shockley-Read-Hall (SRH) equation with a single defect level located in the middle of the Si band gap [160]. For the SRV parameters, we assume $S_{p0} = 1300 \text{ cm/s}$ and $S_{n0} = 5200 \text{ cm/s}$ from Ref. [161]. For the bulk lifetime we assume $\tau_{\text{bulk}} = 20 \text{ ms}$. The solid lines in Fig. 6.12 c) and d) show the carrier concentrations for $W = 0.5 \mu\text{m}$ and $4 \mu\text{m}$, respectively. The illumination intensity I_0 is fixed for both W -values so that it results in an excess carrier density of $\Delta p = 2 \times 10^{15} \text{ cm}^{-3}$ in the bulk with $W = 280 \mu\text{m}$. The electrostatic repulsion of electrons inverts the carrier concentration in the top of the pore wall region where the hole concentration exceeds the electron concentration, $n < p$. The overall surface recombination, which is proportional to the product of the carrier concentrations $n_s \times p_s$ at the surface [160], is reduced by a factor of 8 at the pore tip in comparison to the bottom of the pore wall region. This explains why the effective SRV does not simply rise linearly with the surface area for the blind hole texture. As the sample is in open-circuit, the product of the charge carriers is constant throughout W .

The dashed lines in Fig. 6.12 c) and d) show the carrier distribution at an illumination intensity $10 I_0$ that gives an excess carrier density of $\Delta p = 8 \times 10^{15} \text{ cm}^{-3}$ in the bulk with $W = 280 \mu\text{m}$. The carrier concentrations are reverted again to $n > p$ for the center of the pore walls for $W = 0.5 \mu\text{m}$. The results indicate that at a higher injection level, the width of the space charge region is reduced and the charge carrier distribution in the pore wall region becomes more uniform. We experimentally evaluate S_f at a higher injection level of $\Delta p = 8 \times 10^{15} \text{ cm}^{-3}$, which is illustrated in Fig. 6.11 b). Indeed we find that the S_f -values of the blind hole samples lie on the extrapolation line of the planar sample. A few samples from Fig. 6.11 a) are missing in Fig. 6.11 b) since for them the applied maximum illumination intensity of 1.1 suns does not suffice to inject the required amount of excess carriers.

In conclusion, we have found that the high aspect ratio of the pore texture leads to a non-uniform distribution of charge carriers in the pore wall region. This reduces the surface recombination at the top of the pore walls and the resulting effective SRV is smaller as one would expect from the total surface area enhancement. The repulsion of electrons by the fixed charge density at the AlO_x/Si interface attributes to the non-uniformity of the carrier distribution and further reduces the surface recombination in the top of the pore wall. A higher photon flux, however, increases the electron concentration in the

⁷This program solves the 1-D coupled transport equations of electrons and holes in semiconductor devices, with emphasis on photovoltaic devices.

pore walls, makes the carrier distribution more uniform and S_f approaches the value one would expect from the surface area enhancement.

Due to the smaller aspect ratio, random pyramids have a rather uniform carrier distribution in the texture and should thus show an SRV that lies on the blue line in Fig. 6.11⁸. One reason why the random pyramid samples have a comparatively high S_f even above the blue line is their crystallographic orientation. It is known that the (111) surface has a higher density of surface atoms and hence a higher density of potential surface defects than the (100) surface [162]. This is another argument in favour of the blind hole texture.

6.5 Quality factor

In this section, we determine the pore depth that embodies an optimum trade-off between optical and electrical performance. For this, we calculate a quality factor for each sample as defined by Eq. 2.60. As a reference, we take the hypothetical sample R^* that has the photogenerated current density J_{sc}^* of the random pyramid sample R1 and the effective carrier lifetime τ_{eff} of the random pyramid sample R3. For calculating the fill factor FF^* by Eq. 2.58, we assume an ideality factor of $m = 1$. Figure 6.13 shows the quality factor QF for the different samples. We find that the samples B6, B7 and B8 with pore depths of $l_{pore} = 8, 9$ and $14.5 \mu\text{m}$, respectively, outperform the random pyramid textured samples. This holds even if we assume the optimum measured absorptance and surface passivation for the pyramidal texture (R^*). The best blind hole sample B6 and pyramidal sample R2 have quality factors of $QF = 1.027^{+0.017}_{-0.02}$ and $QF = 0.974^{+0.019}_{-0.023}$, respectively. The asymmetric errors stem from the log-function in Eq. 2.56. Thus, the blind hole texture has the potential to improve the efficiency of a all back-contacted solar cell relatively by 2.0 to 5.3 %_{rel}. The lower limit of 2 %_{rel} includes the case of a double ARC on random pyramids, where we again have assumed the optimum τ_{eff} of sample R3. The large error bars in Fig. 6.13 mainly result from the uncertainty in the lifetime measurement and the error propagation. For more shallow pores, the QF becomes limited by external front side reflectance while deeper pores have a detrimental surface recombination that cannot be compensated by the superior optical performance.

⁸The thickness of the AlO_x layer plays a crucial role for the passivation of textured pyramidal textures ([161], p. 14.)

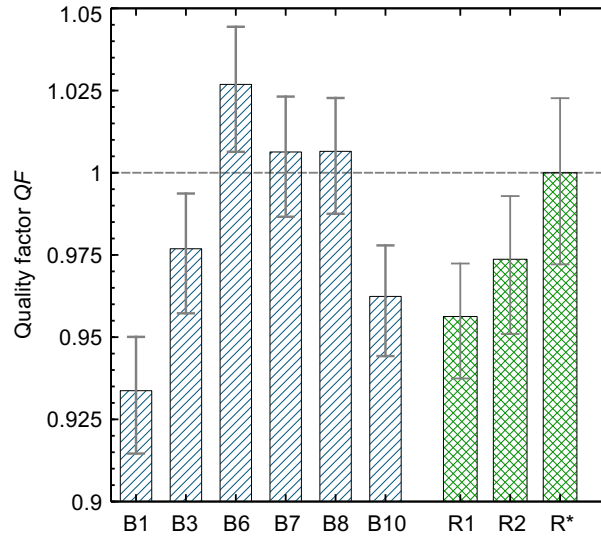


Figure 6.13: The figure shows the quality factors QF of the blind hole (BX) and random pyramid samples (RX). The hypothetical sample R^* combines the optimum random pyramid characteristics and has a defined $QF = 1$.

6.6 Summary and discussion

In this chapter, we characterized the blind hole texture, made by the electrochemical etching of macropores, and benchmarked it against random pyramids as a potential candidate for highly efficient solar cells. We have analyzed the optical losses and distinguish between i) front surface reflectance and ii) imperfect light randomization and rear reflectance. While the loss i) becomes smaller and eventually saturates, the loss ii) increases with increasing pore depth. We find the pore depth of $17.5 \mu\text{m}$ to give the highest photogenerated current density which corresponds to 97.2% of the Lambertian limit compared to 95.9% of the random pyramids. A comprehensive raytracing study shows that the saturation value of the front reflectance can be traced back to reflection at the flat parts at the top of the pore walls and thus correlates with the wall width. The random pyramids exhibit a better light randomization than the pores which reflects in a lower optical loss for photons that reach the rear surface of the absorber and become reflected. The raytracing simulations also yield a higher escape reflectance for deeper pores. A characterization of the absorptance of the blind hole texture for larger angles of incidence furthermore shows that the angular acceptance of the texture critically depends on the pore depth. We find that a blind hole texture with intermediate pore depths of 9 to $14.5 \mu\text{m}$ gives the highest photogenerated current density under realistic illumination conditions over the year and when the texture is covered with an encapsulation material.

The consideration of the surface recombination yields that despite its larger surface area

the blind hole texture allows for very high effective minority carrier lifetimes τ_{eff} . We measure values for τ_{eff} above 2 ms. These exceptionally high lifetimes can be attributed to a non-uniform carrier distribution within the pore walls which is due to the high aspect ratio of the texture and the fixed negative charge density at the $\text{AlO}_x/\text{c-Si}$ interface reducing the electron concentration and thus the surface recombination in that region.

We expect the blind hole texture with an optimum pore depth of $l_{\text{pore}} \approx 8 \mu\text{m}$ to allow for a relative gain in efficiency of 2.0 to 5.3%_{rel} when applied in an all back-contacted solar cell instead of a pyramidal front side texture. This holds even if the random pyramids are coated by a double layer ARC. This is the first time that the blind hole texture has been thoroughly characterized with respect to its electrical and optical performance and benchmarked against the state-of-the-art random pyramid texture.

The preparation of the blind hole texture is rather complex which is why, at the present state, we envisage the blind hole texture for the demonstration of highly efficient lab-type solar cells only. The solar cells should be all back-contacted [130, 163] as it has been demonstrated in literature that metal fingers are difficult to deposit on black silicon textures [131]. For a demonstration on device level, however, the texture first has to be transferred to a larger area. Omitting the prestructuring of the pore lattice would offer a great deal of simplification of the process and, in addition, might improve the light randomization of the texture. The different stages of pore nucleation on an unstructured substrate [82], however, pose a challenge on etching a "black" blind hole texture without an impaired front reflectance.

Chapter 7

Pigmented diffuse rear reflectors using Si nanopowder

In this chapter, we study the impact of a pigmented diffuse reflector (PDR) on the absorptance of a Si wafer and compare it with a random pyramid texture. We introduce Si nanopowder as scattering pigment on the rear side and compare the absorptance enhancement in dependence of pigment concentration and refractive index of the embedding matrix material. We furthermore introduce an analytical optical model that allows to separate the parasitic absorptance in the PDR from the relevant absorptance in the Si wafer.

7.1 Introduction

Texturing the front side of a solar cell has the advantage that, in addition to the randomization of light propagation direction, the front surface reflectance is lowered. In some cases, however, the front surface of a solar cell has to be planar. An example for this are Si-based tandem or multijunction devices. Figure 7.1 a) shows a sketch of a tandem cell with a top cell that has a band gap $E_{g,top}$ on top of a Si bottom cell with band gap $E_{g,Si} < E_{g,top}$. Both sub-cells have carrier selective junctions for charge carrier separation and a coupling layer which is either insulating to operate the cells independently from each other (4-terminal device) or consists of a tunnel junction (2-terminal device). The top cell is monolithically grown or bonded onto a crystalline Si bottom cell [17–19] and has a larger band gap than Si, thus absorbing photons with a lower thermalization loss. Growing the top cell on textured surfaces with deposition techniques like epitaxy or spin-coating is an unsolved challenge which is why the Si bottom cell has to have a

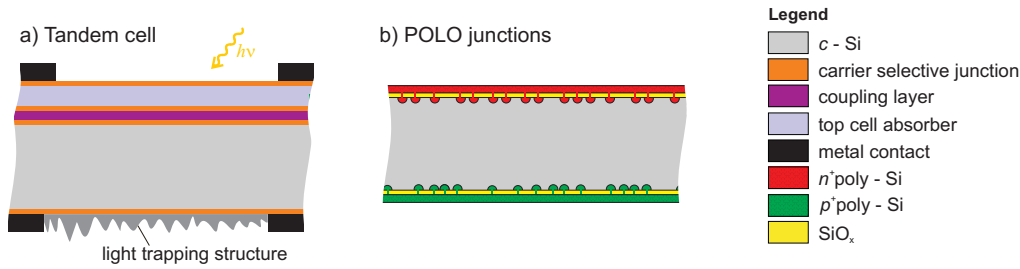


Figure 7.1: The figure illustrates a) the principle structure of a 2-terminal tandem solar cell with two absorbers, Si being the bottom absorber. In such devices, the light trapping structure has to be implemented on the rear side of the Si cell. b) illustrates the concept of a poly-Si on oxide (POLO) junction.

planar front side. Consequently, the light trapping structure must then be implemented on the rear side of the silicon bottom cell, as illustrated in Fig. 7.1 a).

In Fig. 7.1 a), the carrier selective junctions of the cells are not described in detail. Figure 7.1 b) shows polysilicon (poly-Si) on oxide (POLO) junctions as an example for the Si cell [164, 165]. Poly-Si layers doped with phosphorous/boron on top of a 1-2 nm-thin silicon oxide layer form an electron/hole selective junction. An annealing step at around 1000 C° for about 30 min leads to a local breakup of the oxide and a diffusion of dopants from the poly-Si into the Si bulk [166, 167], which is also illustrated in Fig. 7.1 b). POLO junctions show extremely low recombination current densities J_0 and junction resistivities ρ_c [168] of 1 fA/cm² and 0.6 mΩcm² for n^+ and 4 fA/cm² and 0.2 mΩcm² for p^+ on planar (100) surfaces. Recently, we have reported on a record solar cell conversion efficiency of $\eta = 26.1\%$ with a POLO-back-junction back-contacted cell architecture [169, 170]. This stresses the significance of POLO junctions in future Si photovoltaics. However, it turned out to be challenging to transfer the junction quality to random pyramid textured surfaces for which the J_0 -values are about one order of magnitude higher than on planar Si [164, 171]. This holds for both polarities.

Both challenges are addressed by a light trapping scheme on the rear side that is optically rough but electronically planar. We now discuss solutions for such schemes from the literature. We use the gain in photogenerated or short-circuit current density for a certain absorber thickness as the metric to compare the quantitative impact of the different approaches.

a) Nanostructuring the rear side layer

A sub-micron grating as shown in Fig. 7.2 a) directs the light into different diffraction modes and works as an optical grating [172–175]. The diffraction is maximized for a specific wavelength that is controlled by the grating period. The grating dimensions,

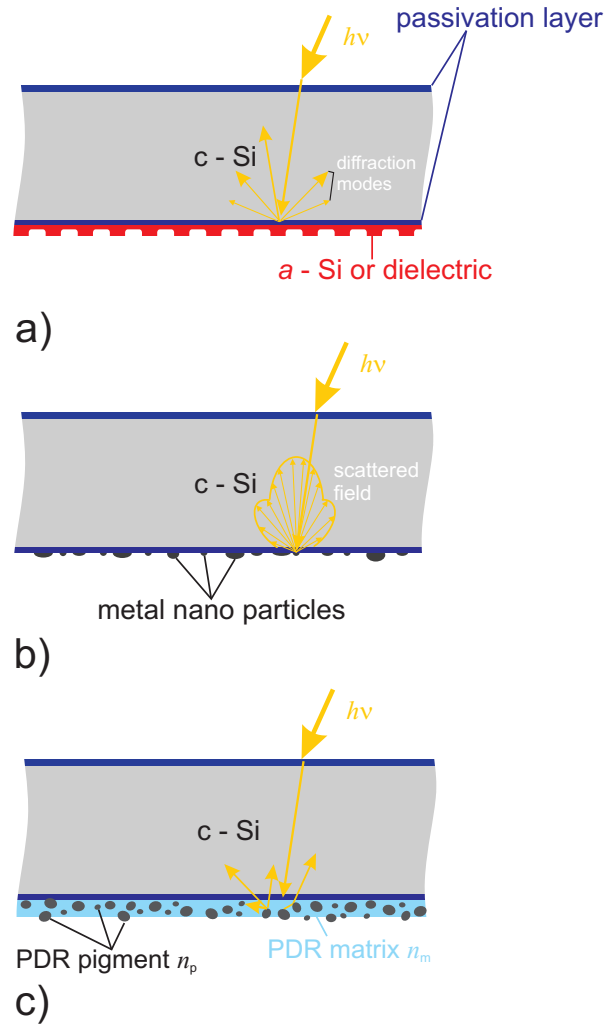


Figure 7.2: The figure illustrates three light trapping schemes for the rear side where the electrical surface remains planar: a) nanostructured grating within a rear side layer, b) plasmonic metal particles and c) a pigmented diffuse reflector (PDR).

i.e. depth and width of the indentations, have an impact on how the light gets distributed over the different diffraction modes. Mellor *et al.* simulated a gain in J_{sc}^* of $\approx 3.3 \text{ mA/cm}^2$ for a $200 \mu\text{m}$ -thick silicon absorber with an optimized binary grating over a reference structure with a perfect rear mirror [173]. Peters *et al.* predicted a gain of $\approx 1.8 \text{ mA/cm}^2$ for a $40 \mu\text{m}$ -thick silicon absorber with a one-dimensional grating over the reference without grating by wave-optical simulations [174]. Eisenlohr *et al.* measured gains in J_{sc} of 1.2, 1.6 and 1.8 mA/cm^2 for 250, 150 and $100 \mu\text{m}$ -thick silicon solar cells with binary rear grating over reference cells without grating, respectively [175].

b) Plasmonic light trapping by metal nanoparticles

Plasmonic light trapping as shown in Fig. 7.2 b) involves the excitation of localized surface plasmons in discrete metal nanoparticles [29, 60, 176–179]. The metal particles work as effective "antennas" for the incident light and scatter it with a certain angular

spread that is required for light trapping. If the particle is placed between two different materials, e.g. air and passivation layer/Si, the light is scattered preferentially into the material with larger permittivity ϵ_r [29]. The size, shape, material of the particles, their distance to the absorber and whether they are embedded in a dielectric affect the scattering efficiency [180]. Alternatively, surface plasmon-polaritons that propagate along the metal/semiconductor interface can induce light trapping for a continuous metal film¹. Beck *et al.* reported a gain of $2.25\text{mA}/\text{cm}^2$ in J_{sc} for a $22\text{ }\mu\text{m}$ -thick silicon solar cell with Ag plasmonic particles on the rear side over a reference without particles [181]². The gain is $0.9\text{mA}/\text{cm}^2$ when an Ag mirror is placed behind the sample with Ag nanoparticles as well as the reference without particles.

c) Pigmented diffuse rear reflector (PDR)

A pigmented diffuse reflector consists of two components with different refractive indices n_i : the pigment or particle (i=p), i.e. small particles with a characteristic wavelength-selective absorptance, and the matrix material (i=m) in which the pigment is dispersed [see Fig. 7.2 c)]. Light within a PDR is either scattered back into the direction of incoming light, which is desired for the light trapping application, scattered in forward direction or absorbed by the pigment/particle. The scattering efficiency Q_{sca} is largest, if the pigment size is comparable to the wavelength of the light. The corresponding theory has been described by Mie, which why it is referred to as Mie³ scattering [182]. The reflectance of a PDR is high if the scattering efficiency

$$Q_{sca} = \frac{C_{sca}}{G}, \quad (7.1)$$

is high which is defined as the ratio of the optical scattering cross-section C_{sca} of a pigment and its geometrical cross-section G [183]. In case of a spherical pigment with radius r_p , G equals $G = \pi r_p^2$. We do not go into detail of scattering theory but instead use the open-source software MiePlot [184] that calculates Q_{sca} for a single sphere. The results are shown in Fig. 7.3. There are three major impact factors on the scattering efficiency Q_{sca} .

Pigment diameter: Figure 7.3 shows the scattering efficiency Q_{sca} in dependence of the pigment diameter d_p . The wavelength of the incoming light in both figures is $\lambda = 1000\text{ nm}$. Q_{sca} is highest, if the pigment diameter is in the range of the

¹The metal film needs to have a ridge or indentation as light-incoupling structure [29].

²In Ref. [181] only relative gains are given. We therefore digitize the shown EQE and transfer it to absolute J_{sc} -values.

³In contrast to Rayleigh scattering, which refers to scattering processes for which the pigment is small compared to the wavelength, as occurs in, e.g., the earth's atmosphere. If the pigment is large compared to the wavelength, scattering is described by the Fresnel equations and Snell's law of refraction.

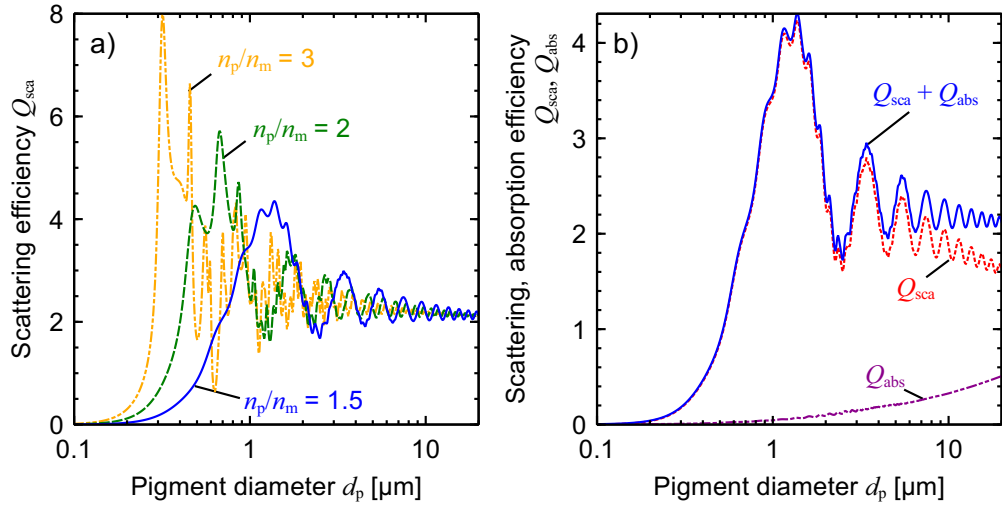


Figure 7.3: The figure shows a plot of the Mie scattering efficiency Q_{sca} of a spherical particle versus the pigment diameter d_p for a) non-absorbing pigments with different ratios of refractive index n_p/n_m of the pigment and the matrix and b) for $n_p/n_m = 1.5$ where the pigment has an imaginary value of the refractive indices of $k = 0.003$. The wavelength of the incoming light is $\lambda = 1000 \text{ nm}$. The results are obtained by the software MiePlot [184].

wavelength. An approximation for the optimum pigment diameter is [185, 186]

$$d_{\text{opt}} \approx \frac{2\lambda}{\pi(n_p - n_m)} \quad (7.2)$$

Ratio of refractive indices: Figure 7.3 a) shows the scattering efficiency for different ratios of the refractive indices n_p/n_m of the pigment and the matrix material. The maximum Q_{sca} increases for increasing ratios. This can be ascribed to an enhanced internal reflectance at the pigment/matrix interface. Figure 7.3 b) illustrates the impact of an absorbing pigment with an imaginary value of the refractive index of $k = 0.003$. The absorption efficiency increases with increasing pigment diameter and leads to a decrease in Q_{sca} .

Volumetric fraction: The dependence of Q_{sca} on the volumetric fraction $\sigma = V_p/V_{\text{PDR}}$ of all pigments with volume V_p in the PDR with a total volume of V_{PDR} has an optimum at $\sigma = 50\%$ [186, 187]. For volumetric fractions $\sigma < 10\%$, Q_{sca} increases linearly with σ . For $10\% < \sigma < 50\%$, the increase in Q_{sca} is sub-linear due to a higher probability of multiple scattering events. For $\sigma > 50\%$, the roles of pigment and matrix become reversed and Q_{sca} decreases again to 0 if the PDR consists only of pigment material ($\sigma = 1$).

Regarding the position of the PDR at the rear side of the Si wafer, one has to keep in mind that a matrix material with a refractive index that is low with respect to the

refractive index of Si will decrease the probability for entering and leaving the matrix material from and into the silicon wafer, respectively. Cotter also pointed out that the light distribution becomes focused into a solid angle of $\theta \leq \arcsin(n_{\text{PDR}}/n_{\text{Si}})$ at the transition PDR \rightarrow Si according to Snell's law [188]. He derived a "focus factor" of $(n_{\text{Si}}/n_{\text{PDR}})^2$ that alters the Lambertian distribution $B \cos \theta d\Omega$ from Eq. 2.42 in the PDR to $B (n_{\text{Si}}/n_{\text{PDR}})^2 \cos \theta d\Omega$ after entering the Si absorber. The symbol n_{PDR} is either n_{p} or n_{m} depending on whether the interface transition is pigment \rightarrow Si or matrix \rightarrow Si.

We distinguish between PDR structures that have a higher refractive index of the pigment than for the matrix or vice versa. We term the first type-I PDRs and the latter type-II PDRs. For the more common type-I PDRs, TiO₂ nanoparticles were used as pigment ($n_{\text{p}} \approx 2.7$) either in pure form [40, 189, 190] or, as "white paint", in combination with a binding medium [40, 186, 187, 191]. The reported gain in extracted current density of a 200 μm -thick and planar Si cell with a white paint PDR over a cell with specular rear reflector amounted to 0.8 mA/cm² [40]. In case of type-II PDRs, silica microspheres with $n_{\text{p}} \approx 1.5$ were used as low-n pigments and the matrix, either amorphous titanium oxide $n_{\text{m}} \approx 2.38$ [192] or *n*-type poly-Si $n_{\text{m}} \approx 3.5$ [193] as the component with the higher refractive index. In the latter case, the gain over a 200 μm -thick planar cell without light randomization scheme amounted to 1.4 mA/cm² [193].

In this work, we study the PDR as light trapping structure for electronically flat surfaces in more detail. We focus on type-I PDRs. They are particularly easy-to-apply compared to the other approaches, including type-II PDRs, as it does not require nanostructuring, chemical vapour deposition equipment and/or vacuum technologies. We introduce Si nanopowder as scattering pigment, as it has a yet higher refractive index than the more common TiO₂ nanoparticles which, in theory, allows for a higher scattering efficiency.

7.2 Properties and preparation of Si nanopowder PDR

We use commercially available silicon nanopowder [194] with a median particle size (D50) of 500 nm as pigment. The SEM micrograph in Fig. 7.4 shows a top view of the particles. The shape of the particles is random. The optical appearance of the powder is yellow brown which probably originates from the native oxide on the particles surface [195]. The purity of the powder is stated to be 99.9 at%.

Figure 7.4 shows the deposition process of the PDR. First, the Si nanopowder is dispersed in isopropanol (IPA). The dispersion is then sonicated for 5 min prior to spin-coating. The spin-coating procedure takes place in two steps: the first step uses a rotation speed of 600 rpm for 10 s during which about 1 ml of the dispersion is dropped onto the wafer

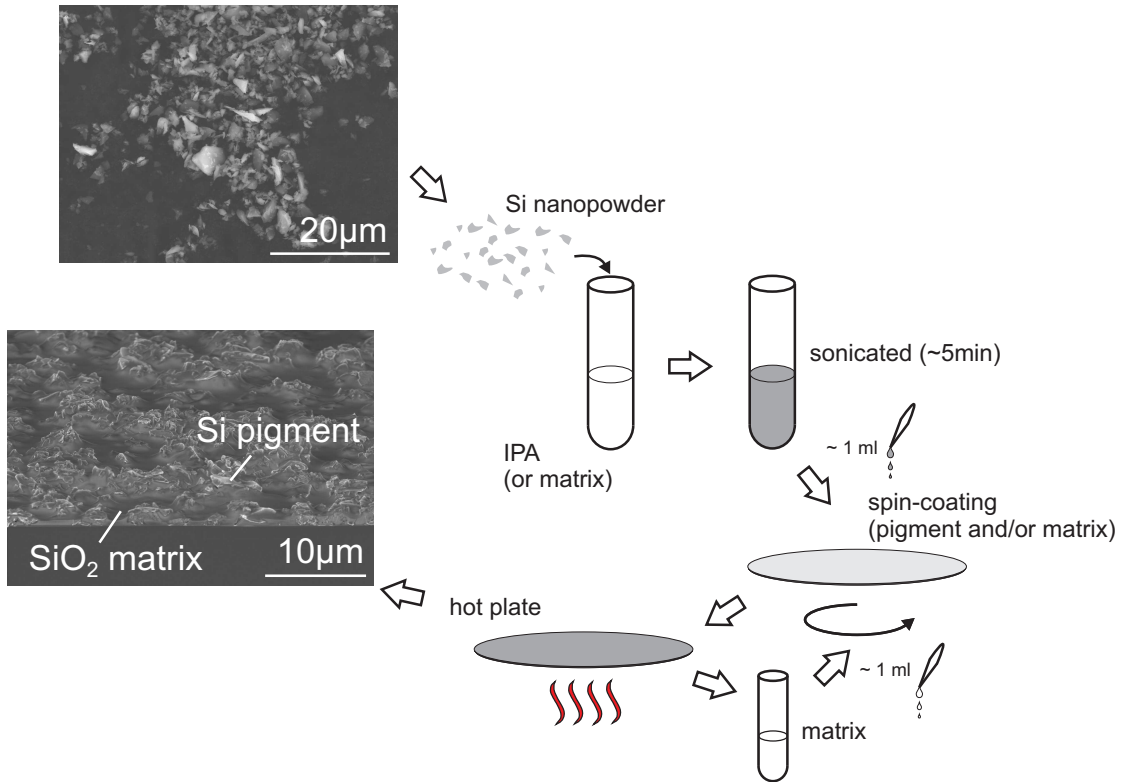


Figure 7.4: The figure illustrates the deposition of the PDR via spin-coating and annealing. If the Si nanopowder is dispersed in IPA first, the matrix material is deposited on top of the nanopowder in a second spin-coating step. The SEM micrograph shows a tilted cross-sectional view of a Si sample with PDR.

material. The second step uses a speed of 1000 rpm for 5 s without further dropping. The IPA evaporates when placing the sample on a hotplate at $\approx 100^\circ\text{C}$. Within this work, we use two types of matrix materials: a liquid siloxane-based SiO_2 precursor [196, 197] and PECVD SiN_x . In the first case, about 1 ml of the SiO_2 precursor is deposited in a second spin-coating procedure with identical parameters as for the Si nanopowder. The post-deposition annealing of the matrix takes place at 220°C for 2 min. We use SiN_x as matrix material to study the impact of a varying refractive index n_m on the absorptance enhancement. In our study we also vary the pigment concentration c_p within the PDR. Therefore, we mix varying amounts of Si nanopowder with a fixed IPA volume of 5 ml. The SEM micrograph in Fig. 7.4 shows a tilted cross-sectional view of the PDR at the rear side of a Si sample where the matrix material is SiO_2 . The thickness of the PDR is $W_{\text{PDR}} = (1.5 \pm 1) \mu\text{m}$ and is locally determined by the pigment size.

Absorptance of PDR

We measure the absorptance of the PDR by spin-coating it on a glass substrate with the same parameters we use for the Si samples. Figure 7.5 shows the effective absorptance of the PDR with a pigment concentration of $c_p \approx 0.24 \text{ g/ml}$. The absorptance is measured

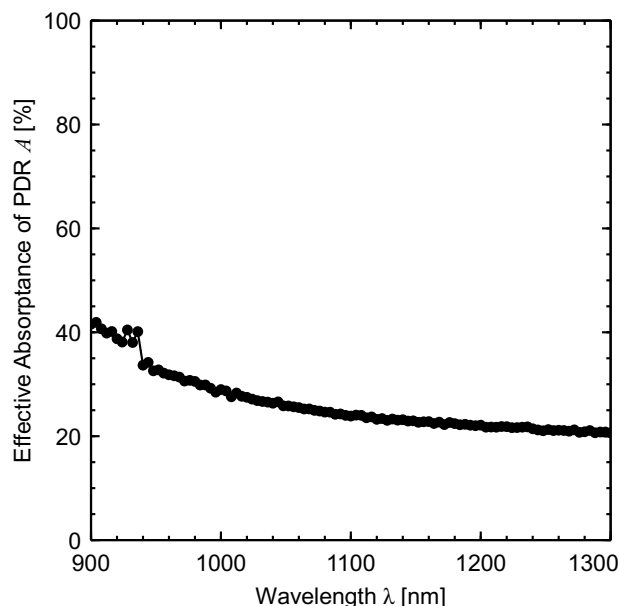


Figure 7.5: The figure shows the effective absorptance of a PDR with a pigment concentration of $c_p \approx 0.24$ g/ml.

with a spectrophotometer. In the relevant wavelength region between 900 – 1300 nm, the PDR absorbs 20 – 40 % of the incoming photons. The origin of this relatively constant sub-bandgap absorptance can have two reasons, either impurity-related absorption processes or additional absorption by free carriers. We have already observed sulfur-related absorption for the reactive ion etched regions of the samples from Ch. 6. The supplier of the Si nanopowder claims a maximum sulfur content of 10 ppm. For a sub-bandgap absorptance of this magnitude the sulfur concentration has to be ≈ 1 at% [138, 139], i.e. a factor of 1000 larger than claimed. To exclude sulfur as source of parasitic absorption, we perform an energy-dispersive X-ray spectroscopy (EDX) of the Si particles with the SEM. This analytical technique allows the identification of elements in the sample down to a detection limit of 1000 ppm. The EDX works by exciting electrons in an inner shell with a high-energy beam of particles, electrons in the case of SEM, and detecting the X-ray radiation that is emitted when an electron from an outer shell relaxes to the unoccupied state in the inner shell. The energy of the emitted photon E_x is characteristic for the nucleus as described by Moseley's law [198]. Figure 7.6 shows the result of the EDX analysis of a single Si particle. None of the investigated samples shows traces of sulfur. However, next to the large K_α -peak of Si we observe a smaller peak that is attributable to phosphorous. The size of the peak can be translated into a P-content of 0.25 at% which corresponds to a P-concentration of about 10^{20} cm $^{-3}$. The high P-concentration could explain the results from Fig. 7.5 by free carrier absorption within the particles [199].

The two peaks at lower energies E_x correspond to the K_α -transition for carbon and

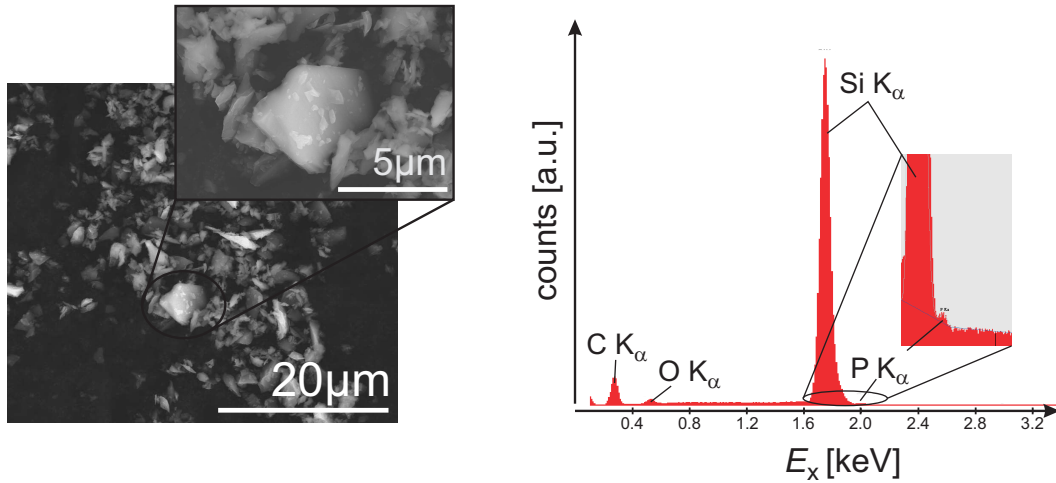


Figure 7.6: The left figure shows an SEM micrograph of the Si particles that are used as pigment in the PDR. The particles are mounted on an adhesive carbon pad. The right figure shows a plot of the EDX spectrum of a Si particle which indicates the presence of P atoms.

oxygen, respectively. The carbon originates from the adhesive pad the Si nanopowder sticks to and the surroundings like the walls of the vacuum chamber. The oxygen originates from the native oxide that forms on the Si surface [195] as well as from the surroundings.

7.3 Optical model for two absorbing layers

The share of photons that are absorbed in the PDR do not contribute to the short-circuit current as the PDR is electronically decoupled from the solar cell. The spectrophotometer measures the total absorptance of the Si/PDR stack $A = A_{\text{Si}} + A_{\text{PDR}}$ and does not distinguish between useful and parasitic absorptance, A_{Si} and A_{PDR} , respectively. We therefore introduce an optical model that allows for a separation of the two parts.

The optical model is illustrated in Fig. 7.7 and is similar to that presented in Ref. [200]. We distinguish fully specular (black lines) and fully diffusive light (red lines) that coexist in the structure. The structure is composed of two stacked silicon layers: a planar Si wafer and a second thin layer with a rough rear side that shall mimic the impact of PDR. The two layers have a thickness W_i , a refractive index n_i and an absorption coefficient α_i ($i = \text{Si}, \text{PDR}$). Simplifying the real situation, we assume that

- i) scattering takes place only at the rear side of the PDR,
- ii) both Si and the PDR have the same refractive index $n_i = n$, i.e. there is no reflection at the interface,

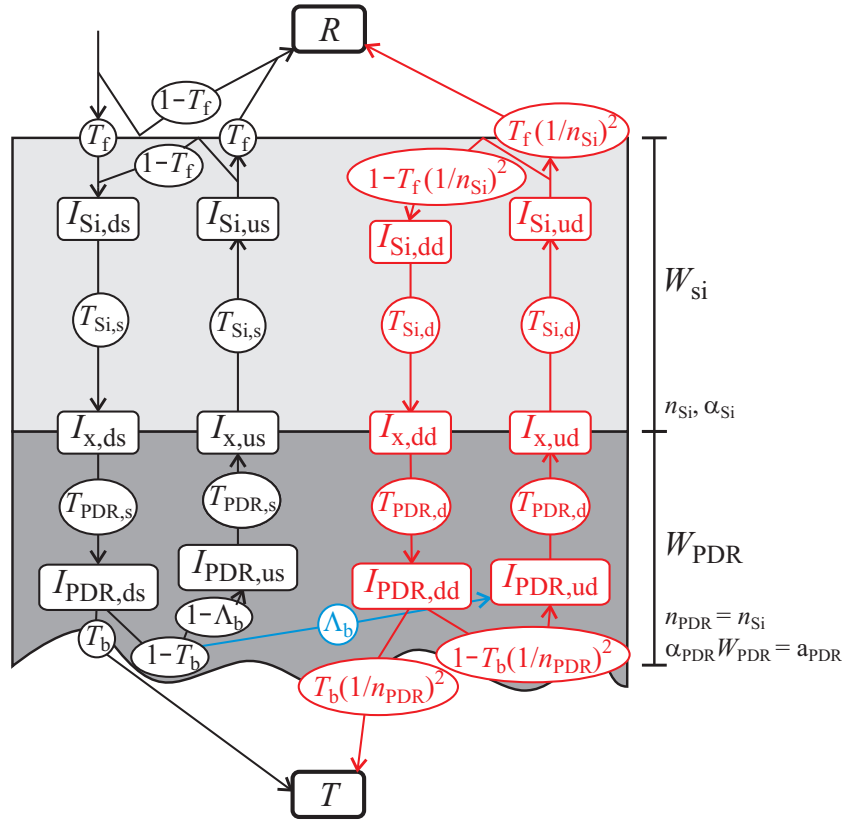


Figure 7.7: The figure shows a schematic of the 12 optical power fluxes $I_{i,j,k}$ in the two absorbing layers silicon and PDR. The black and red colors denote the specular and fully randomized optical power flux. The blue arrow symbolizes the power transfer from the specular channel to the diffusive channel with the probability Λ_b .

- iii) the absorption coefficient in the PDR α_{PDR} is constant in the range 900 – 1300 nm, i.e. $\alpha_{\text{PDR}} W_{\text{PDR}} = a_{\text{PDR}}$.

The validity and the motivation for these assumptions will be discussed later in this section after having fully described the model.

The 12 power fluxes I_{ijk} are distinguished by 1) their location in the stack, specified by index i with $i = \text{Si}$ for the top of the Si layer, $i = \text{PDR}$ for the bottom of the PDR or $i = x$ at their interface, 2) whether the flux propagates upwards or downwards in the stack, specified by index $j = u, d$ and 3) specular and diffusive light, specified by index $k = s, d$. The flux transfer probability from specular to fully randomized light upon reflection at the rear side of the PDR is given by the Lambertian character Λ_b . The expressions for the transmittances of specular and diffuse light, T_s and T_d , are given in Eqs. 2.41 and 2.45 on p. 20. The model follows the same logic in deriving the expressions for absorptance, reflectance and transmittance as the description of the structures with no light trapping and Lambertian light trapping in Fig. 2.10 on p. 19. The twelve power

fluxes are solved for in a Python script using the Sympy library [201]. The absorptance in the upper Si layer, A_{Si} , and the PDR, A_{PDR} , read

$$\begin{aligned} A_{\text{Si}} &= (1 - T_{\text{Si,s}})(I_{\text{Si,ds}} + I_{\text{x,us}}) + (1 - T_{\text{Si,d}})(I_{\text{Si,dd}} + I_{\text{x,ud}}) \\ &= \frac{T_{\text{f}}}{C(B(T_{\text{f}} - 1) + 1)} \times \left[T_{\text{PDR,d}} T_{\text{Si,s}} T_{\text{PDR,s}} \Lambda_{\text{b}} n^2 (T_{\text{b}} - 1) \times \dots \right. \\ &\quad \left. (T_{\text{Si,d}} - 1)(T_{\text{Si,d}}(T_{\text{f}} - n^2) - n^2) - (T_{\text{Si,s}} - 1) \left(\frac{B}{T_{\text{Si,s}}} + 1 \right) C \right], \end{aligned} \quad (7.3)$$

$$\begin{aligned} A_{\text{PDR}} &= (1 - T_{\text{PDR,s}})(I_{\text{x,ds}} + I_{\text{PDR,us}}) + (1 - T_{\text{PDR,d}})(I_{\text{x,dd}} + I_{\text{PDR,ud}}) \\ &= \frac{T_{\text{f}} T_{\text{Si,s}}}{C(B(T_{\text{f}} - 1) + 1)} \times \left[T_{\text{PDR,s}} \Lambda_{\text{b}} n^2 (T_{\text{b}} - 1) (T_{\text{PDR,d}} - 1) \times \dots \right. \\ &\quad \left. (T_{\text{Si,d}}^2 T_{\text{PDR,d}} (T_{\text{f}} - n^2) - n^2) - (T_{\text{PDR,s}} - 1) \left(\frac{B}{T_{\text{Si,s}}^2 T_{\text{PDR,s}}} + 1 \right) C \right], \end{aligned} \quad (7.4)$$

where B and C are the abbreviations

$$B = T_{\text{Si,s}}^2 T_{\text{PDR,s}}^2 (T_{\text{b}} \Lambda_{\text{b}} - T_{\text{b}} - \Lambda_{\text{b}} + 1), \quad (7.5)$$

$$C = T_{\text{Si,d}}^2 T_{\text{PDR,d}}^2 (T_{\text{b}} - n^2)(T_{\text{f}} - n^2) - n^4. \quad (7.6)$$

Similarly, we can write for the transmittance T and the reflectance R

$$\begin{aligned} T &= T_{\text{b}} \left(I_{\text{PDR,ds}} + \frac{1}{n_{\text{PDR}}^2} I_{\text{PDR,dd}} \right) \\ &= \frac{T_{\text{f}} T_{\text{b}} T_{\text{Si,s}} T_{\text{PDR,s}}}{B(T_{\text{f}} - 1) + 1} \times \left[1 - \frac{1}{C} T_{\text{Si,d}}^2 T_{\text{PDR,d}}^2 \Lambda_{\text{b}} (T_{\text{b}} - 1) (T_{\text{f}} - n^2) \right], \end{aligned} \quad (7.7)$$

$$\begin{aligned} R &= 1 - T_{\text{f}} + T_{\text{f}} \left(I_{\text{Si,us}} + \frac{1}{n_{\text{Si}}^2} I_{\text{Si,ud}} \right) \\ &= 1 - T_{\text{f}} + T_{\text{f}}^2 \left[\frac{B}{B(T_{\text{f}} - 1) + 1} + \frac{T_{\text{Si,d}} T_{\text{PDR,d}} T_{\text{Si,s}} T_{\text{PDR,s}} \Lambda_{\text{b}} n^2 (T_{\text{b}} - 1)}{C(B(T_{\text{f}} - 1) + 1)} \right]. \end{aligned} \quad (7.8)$$

The sum of the four terms $A_{\text{Si}} + A_{\text{PDR}} + R + T$ equals the incoming power flux which is 1 in this case. The three assumptions reduce the number of free parameters to three: Λ_{b} ,

a_{PDR} and T_{b} . The Lambertian character Λ_{b} mainly addresses the degree of scattering, a_{PDR} the parasitic absorptance and T_{b} the probability for the light to become reflected back into the Si absorber. The three parameters are not fully independent of each other.

Justification of model assumptions

The simplifications of the model are justified as follows. Assumption i) is valid due to the fact that the PDR is much thinner than the silicon $W_{\text{PDR}} \ll W_{\text{Si}}$ and that it is thus not important for the description of the absorptance spectra where exactly in the PDR scattering occurs. By introducing an "effective" scattering parameter Λ_{b} , we avoid the rigorous simulation of light interaction with individual particles, which would be challenging as their shape is random. At first glance, assumption ii) appears non-physical as the scattering relies on the fact that the PDR has a different refractive index from the absorber layer. Furthermore, the refraction at the Si/PDR interface prohibits a full randomization of light within the Si layer as has been described in the Sec. 7.1. Note, however, that a non-zero reflectance at the Si/PDR interface can be accounted for by a reduced value of T_{b} in combination with an enhanced value for a_{PDR} and/or Λ_{b} . Figure 7.5 gives the experimental verification of assumption iii). The absorptance within the PDR of light that actually interacts with the PDR, which for an absorber thickness of 150 μm is for wavelengths $\lambda > 950 \text{ nm}$ (see Fig. 2.3), varies by less than 5%.

7.4 Optical characterization of samples without surface passivation

We split the optical characterization into a group of samples without surface passivation [see Fig. 7.8 a)-c)] and a group with surface passivating POLO junctions [see Fig. 7.8 d)-f)]. We use the unpassivated samples to validate the optical model and to study the impact of the pigment concentration, the refractive index of the matrix material and an external rear mirror on the absorptance enhancement in the Si wafer.

7.4.1 Impact of pigment concentration

Sample preparation

We use 6" shiny-etched float-zone (FZ) Si wafers with a thickness of $W_{\text{Si}} = (300 \pm 5) \mu\text{m}$ and a resistivity of $\rho = (200 \pm 15) \Omega\text{cm}$ as base material. The wafer is laser-cut into $(2.5 \times 2.5) \text{ cm}^2$ -sized samples and RCA-cleaned. We mix 5 ml isopropanol (IPA) with varying amounts of Si nanopowder. The resulting pigment concentrations c_{p} are listed in Tab. 7.1. We use a liquid SiO_2 precursor as matrix material (see Fig. 7.8b)) which

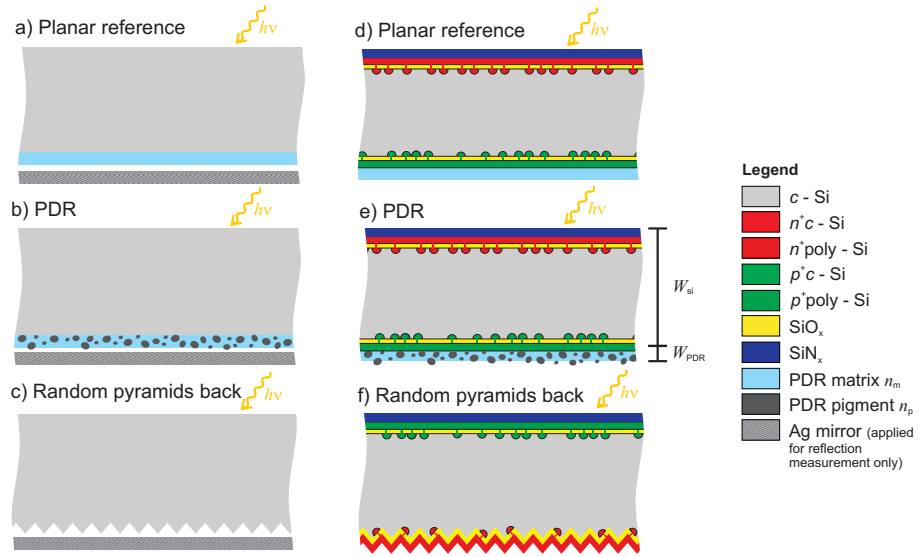


Figure 7.8: The figure shows a schematic of the sample structures investigated in this chapter. We distinguish between samples with no light trapping scheme a) and d), samples with PDR b) and e) and samples with random pyramids at the rear side c) and f). The samples a)-c) are unpassivated while the samples d)-f) are passivated by poly-Si on oxide (POLO) junctions.

has a refractive index of $n_m=1.39$ at 633 nm as determined by ellipsometry. For sample P5*, we use a siloxane based SiO_2 precursor from a different supplier [197]. This one has a higher refractive index of $n_m=1.45$ at 633 nm. As a reference, we choose sample P0 with no light trapping scheme, i.e. no pigments [see Fig. 7.8 a)], and a sample RP with random pyramids on the rear side [see Fig. 7.8 c)].

Table 7.1: The table lists the investigated samples with its light trapping scheme, absorber thickness W_{Si} and pigment concentration in the PDR c_p . The sample P5* has been prepared with a different siloxane precursor.

Name	LT scheme	W_{Si} [μm]	c_p [g/ml]
P0	Fig. 7.8 a)	300	0
P1	Fig. 7.8 b)	300	0.03
P2	Fig. 7.8 b)	300	0.07
P3	Fig. 7.8 b)	300	0.14
P4	Fig. 7.8 b)	300	0.25
P5*	Fig. 7.8 b)	300	0.30
P6	Fig. 7.8 b)	300	0.34
RP	Fig. 7.8 c)	280	-

Figure 7.9 shows SEM micrographs of a 15° -tilted cross-sectional view of the rear side of the samples with PDRs of different pigment concentrations c_p . The pigment concentration c_p influences the packing density of the particles rather than the thickness of the PDR. Thus, while the sample with $c_p = 0.03$ g/ml exhibits uncovered parts of the surface, the Si pigments fully cover the surface for $c_p = 0.34$ g/ml. Figure 7.9 shows the samples with POLO junctions, described in Sec. 7.5, where the base material has a

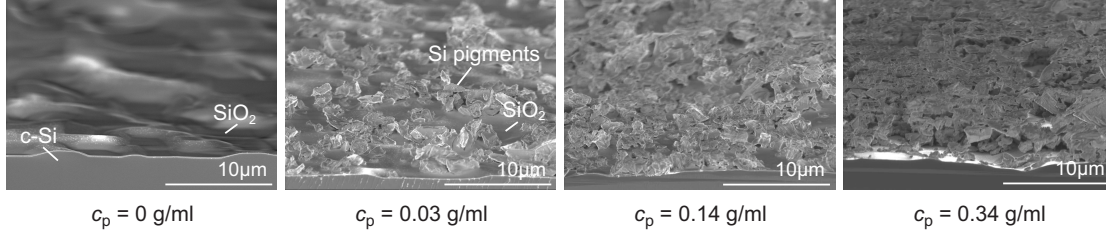


Figure 7.9: The figure shows SEM micrographs of the tilted cross-sections of the PDR rear side with Si pigments embedded in a spin-on SiO_2 with varying pigment concentrations c_p . The thickness of the PDR is $(1.5 \pm 1) \mu\text{m}$.

surface roughness that originates from wafer sawing. The samples P0 through P6 in this section have a shiny-etched surface that is illustrated in the SEM micrograph in Fig. 7.4 on p. 101.

Absorbance spectra

Figure 7.10 a) displays the measured absorbance spectra of samples P0 through P6 and RP. In addition, the Lambertian light trapping reference with the experimental front reflectance and rear transmittance is shown. We focus on the wavelength region between 900 and 1300 nm where light absorption in Si becomes unlikely and where therefore the pigments enhance the absorbance. The spectra give five key results: i) The PDR increases the absorbance when compared to sample P0 with no pigments. ii) This increase in absorbance increases with c_p . iii) As we would have expected from the results in Fig. 7.5 on p. 102, the samples with PDR absorb photons with wavelengths above 1200 nm. iv) This sub-bandgap absorbance also increases with c_p . v) The absorbance of samples with PDR is inferior to random pyramids.

Table 7.2: Overview of the best fit parameters and the photogenerated current densities from the measured, J_{meas}^* , and calculated, J_{Si}^* , absorbance spectra. The measure S is defined in Eq. 7.10 and the difference $J_{\text{meas}}^* - J_{\text{fit}}^*$ describes the fit quality.

Name	Λ_b	a_{PDR}	T_b	J_{meas}^* [mA/cm ²]	S	J_{Si}^* [mA/cm ²]	$J_{\text{meas}}^* - J_{\text{fit}}^*$ [mA/cm ²]
P0	0	0	0.775	13.75	1	13.75	0.05
P1	0.121	0	0.672	13.96	1	13.96	0.04
P2	0.214	0.0005	0.598	14.21	0.999	14.20	0.05
P3	0.337	0.0041	0.467	14.59	0.985	14.37	0.005
P4	0.397	0.0075	0.317	15.25	0.964	14.71	0.002
P5*	0.402	0.0042	0.292	15.25	0.977	14.90	0.001
P6	0.415	0.0104	0.238	15.66	0.947	14.82	0.005
RP	1	0	0.277	16.03	1	16.03	0.03

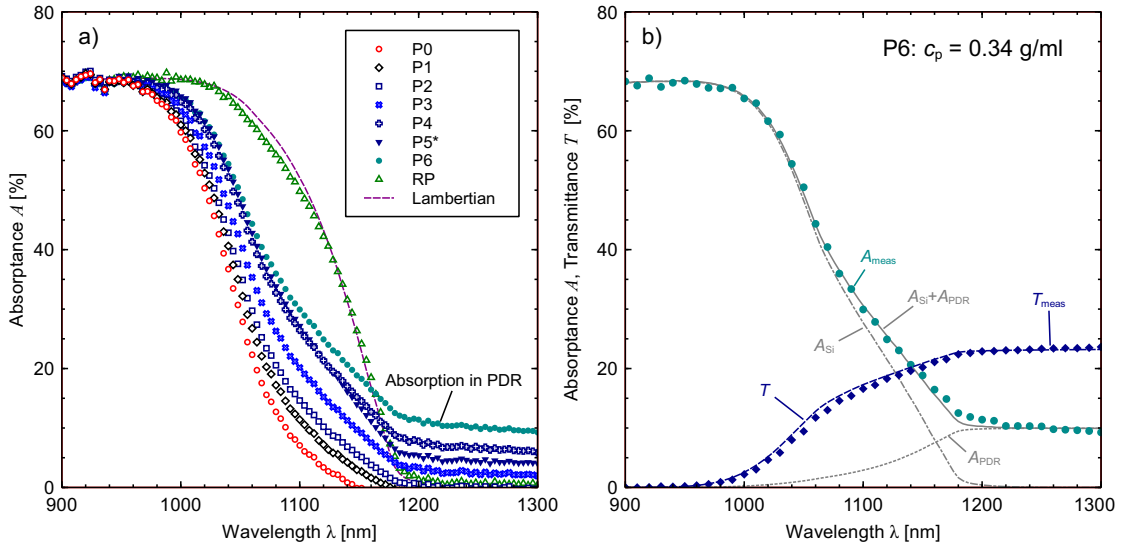


Figure 7.10: The figure shows a) the measured absorptance spectra for the samples from Tab. 7.1 and a Lambertian light trapping reference. b) illustrates the application of the analytical model and shows the simultaneous fit of the absorptance ($A_{\text{Si}} + A_{\text{PDR}}$) and transmittance (T) spectra of sample P6. The symbols show the measured absorptance A_{meas} and transmittance T_{meas} .

Application of optical model

We use the above described optical model to separate the two absorptance components A_{Si} and A_{PDR} . We therefore simultaneously fit the measured absorptance and transmittance spectra, A_{meas} and T_{meas} , for each sample by the sum of Eqs. 7.3 and 7.4 and Eq. 7.7, respectively. Figure 7.10 b) shows the fit result for sample P6 and illustrates the accuracy with which the spectra can be modeled. Figure 7.11 shows the fit of the rest of the PDR samples. Table 7.2 lists the best fit parameters for the different samples. We observe an increase in the Lambertian character Λ_b and the absorptance parameter a_{PDR} and a decrease in the rear transmittance T_b with increasing pigment concentration c_p in the PDR. The random pyramid sample even takes a Lambertian character of 1. We refrain from interpreting the values of the fit parameters as they are not independent from each other. We rather translate the measured, A_{meas} , and modeled, A_{Si} and A_{PDR} , absorptance spectra into photogenerated current densities J_{meas}^* , $J_{\text{Si,mod}}^*$ and $J_{\text{PDR,mod}}^*$ by inserting them into Eq. 2.4. The integration boundaries are switched to 700 to 1400 nm. The photogenerated current density in the Si wafer J_{Si}^* is calculated by the product of

$$J_{\text{Si}}^* = J_{\text{meas}}^* \times S, \quad (7.9)$$

where S is the ratio

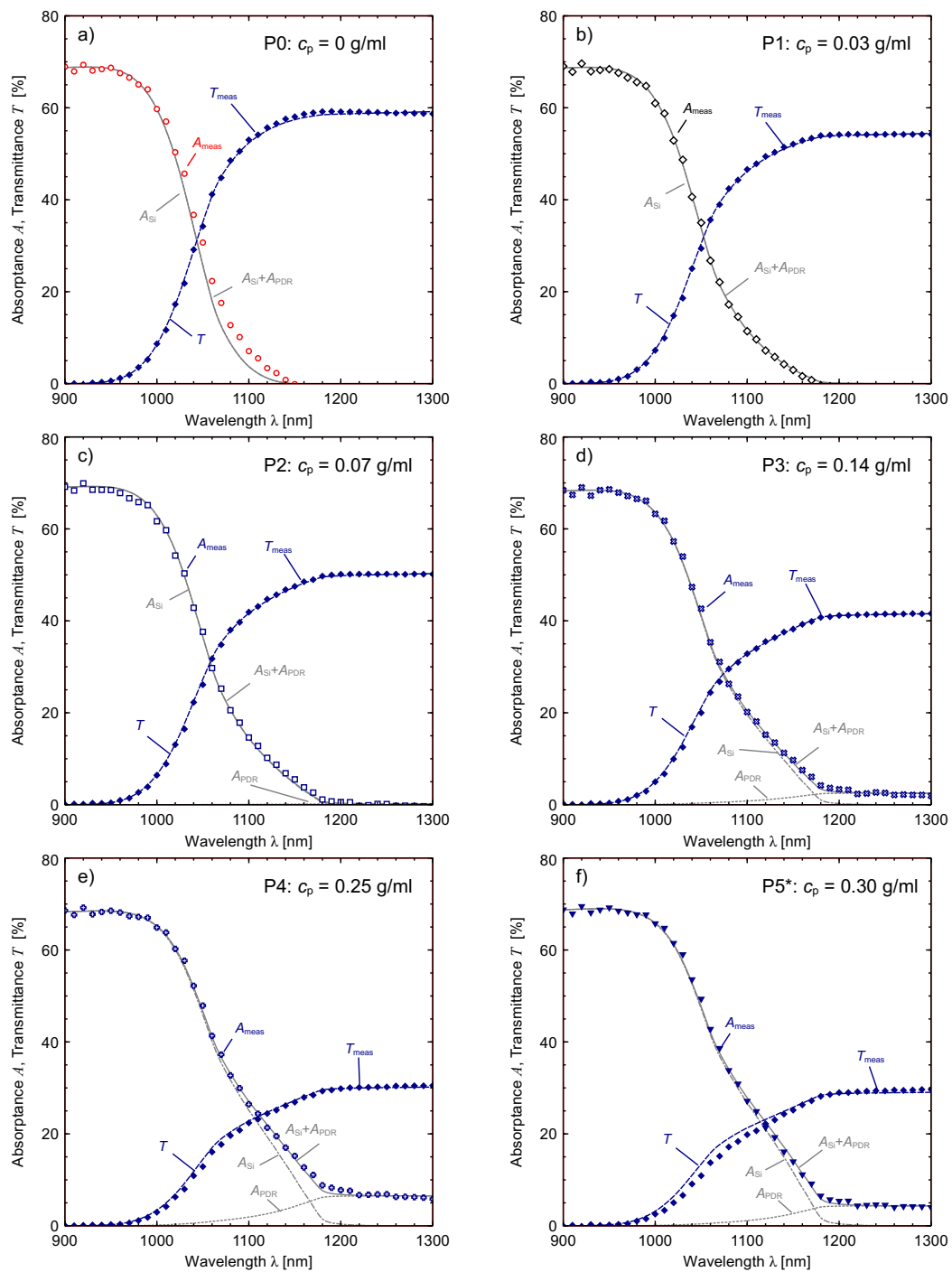


Figure 7.11: The figure shows the application of the analytical model for the remaining PDR samples.

$$S = \frac{J_{\text{Si,mod}}^*}{J_{\text{Si,mod}}^* + J_{\text{PDR,mod}}^*}. \quad (7.10)$$

The results are listed in Tab. 7.2 as well as the absolute difference $J_{\text{meas}}^* - J_{\text{fit}}^*$, where $J_{\text{fit}}^* = J_{\text{Si,mod}}^* + J_{\text{PDR,mod}}^*$. The latter is a measure for the quality of the fit and is highest for the samples with negligible parasitic absorptance a_{PDR} . The deviation takes a maximum value of 0.05 mA/cm^2 for the planar sample and is below 0.005 mA/cm^2 for the PDR samples with a higher parasitic absorptance. The reason for the larger uncertainty for samples with a small a_{PDR} -value is the larger measurement uncertainty of the spectrophotometer for small absorptance signals. This uncertainty becomes apparent when trying to fit the measured spectra with the model. The relatively small deviations support the assumptions we made for the optical model. Another error source arises from the underestimation of the transmittance of weakly absorbed light in scattering samples as described in Ch. 3 for reflectance spectra. The transmittance measurement suffers from the same effect as the samples are positioned outside the integrating sphere. To estimate the error, we perform a raytracing simulation of the random pyramid sample as it shows the highest degree of scattering. We find that about 3% of the absolute transmittance signal for $\lambda > 1200 \text{ nm}$ is lost as it does not enter the sphere. This effect leads to larger negative error bars in Figs. 7.12 and 7.20.

Integrated optical gain

Figure 7.12 shows the absolute gains in J_{meas}^* (empty squares) and J_{Si}^* (full circles) over sample P0. The difference between the symbols corresponds to the parasitic absorptance in the PDR which increases with c_p . The parasitic absorptance of sample P5* is relatively small which is probably related to the newer SiO_2 precursor: The matrix precursor of sample P5* has been taken from a new, previously unopened container, while the one for the other samples had been expired according to the supplier. The age of the matrix certainly affects its flow characteristics and thus the performance as a PDR matrix. This is more important than the small difference in the refractive index of both matrix precursors.

The more relevant gain in J_{Si}^* increases linearly with the pigment concentration. We observe a steeper slope for $c_p < 0.1 \text{ g/ml}$ and a slighter slope for $0.1 < c_p < 0.3 \text{ g/ml}$. We achieve a maximum gain of 1.15 mA/cm^2 for sample P5* with $c_p = 0.3 \text{ g/ml}$. The sample with the highest c_p of 0.34 g/ml shows that the gain does not rise anymore for $c_p > 0.3 \text{ g/ml}$. Our interpretation is that the Si pigments fully cover the surface of the wafer at this concentration, as the SEM micrographs in Fig. 7.9 indicate. Therefore, J_{Si}^* increases with c_p until full area coverage is reached and then saturates or drops again due to a higher parasitic absorptance. We need to investigate a larger number of samples

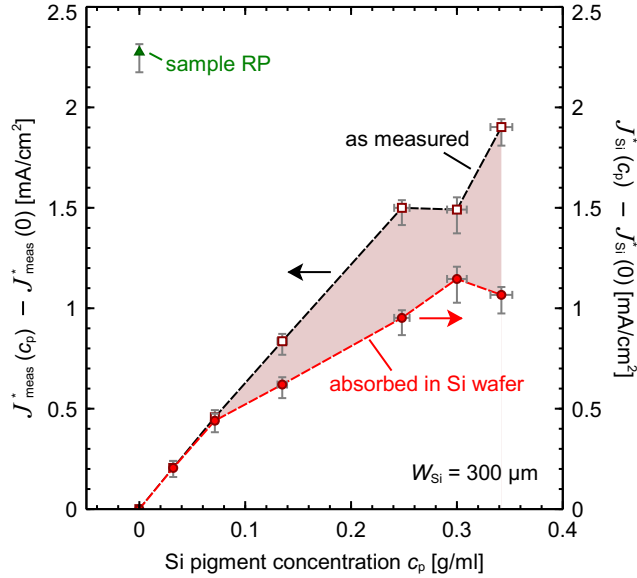


Figure 7.12: The figure shows the absolute gain in photogenerated current density from the measured absorbance spectra of the Si/PDR stack, $J_{\text{meas}}^*(c_p)$, and the useful absorbance in the Si, $J_{\text{Si}}^*(c_p)$, over the sample with no pigments $J_{\text{meas/Si}}^*(0)$ on the rear side for the samples from Tab. 7.1. The empty symbols mark the gain in J_{meas}^* while the full symbols are corrected for the parasitic absorbance (shaded in red) and refer to the gain in J_{Si}^* .

to make sure the optical gain drops for larger c_p . However, besides a higher parasitic absorbance, pigments influence each other in their scattering behaviour if the distance between them becomes too small, which could explain the observed c_p -dependence. This can be seen in Fig. 7.3 on p. 99: A value of $Q_{\text{sca}} = 5$ means that the optical scattering cross section exceeds the geometrical cross section by a factor of 5 and, hence, the distance between the center of the pigments $a_{\text{p-p}}$ should be $a_{\text{p-p}} = \sqrt{5} d_p$, when d_p is the diameter of the pigment, in order to avoid optical interaction of the pigments. It is difficult to determine the volumetric fraction σ that corresponds to the best c_p -value as the pigments are random in size and shape. However, judging from the measured dependence, it should be close to the optimum of $\sigma = 50\%$.

The random pyramid sample RP outperforms sample P5* by 1.13 mA/cm^2 and the planar sample P0 by 2.28 mA/cm^2 and provides the best light trapping scheme evaluated here. The random pyramids have the advantage that the material with the highest refractive index is textured which means that i) light must not traverse an interface, like from Si to PDR and back, to be scattered, i.e. no reflection and refraction occurs and ii) the fraction of total internally reflected light from Eq. 2.43 on p. 22 is largest.

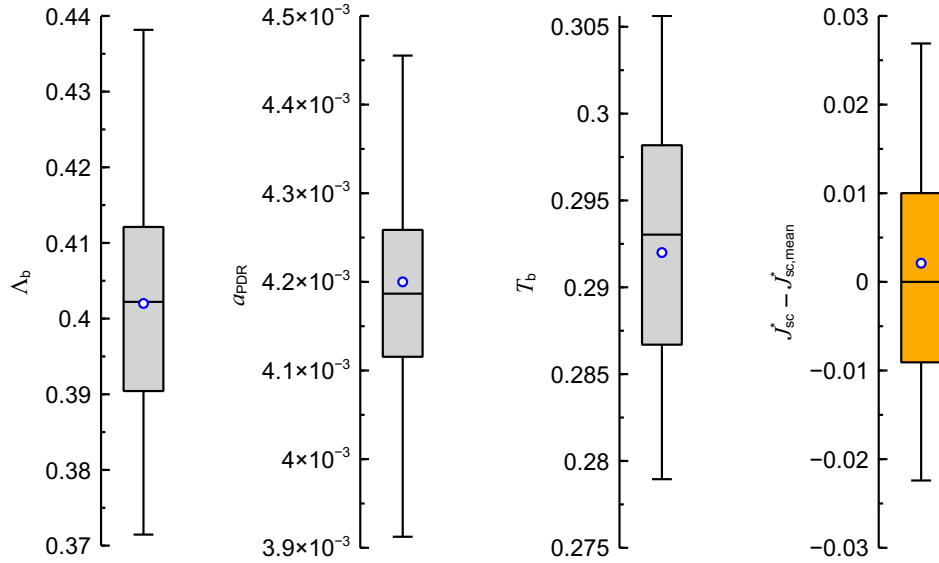


Figure 7.13: The figure shows how uncertainties in the absorptance and transmittance affect the fit parameters of the optical model and the photogenerated current density in the Si absorber. The symbols mark the best fit parameters of sample P5*.

7.4.2 Sensitivity analysis of optical model

We evaluate the sensitivity of the output parameter J_{Si}^* and the fit parameters Λ_b , α_{PDR} and T_b of the optical model on uncertainties of the measured quantities absorptance A_{meas} and transmittance T_{meas} . As we have described in Ch. 3, the uncertainty of the both measurands is enhanced when the sample has a light trapping scheme and is thus difficult to determine. Here, we assume maximum uncertainties of 5%_{rel} for wavelengths $\lambda > 1135$ nm and 1%_{rel} for wavelengths $950 < \lambda < 1135$ nm. Light with wavelengths $\lambda < 950$ nm does not interact with the PDR. We independently and randomly vary the absorptance and transmittance of sample P5* within the assumed uncertainty range and fit the spectra with the model as shown in Fig. 7.11 on p. 110. Figure 7.13 shows the impact on the fit parameters and the resulting J_{Si}^* for a total number of 100 fits. The symbols mark the best fit parameters for sample P5* from Tab. 7.2 on p. 108. The boxplot shows the median, the upper and lower quartile and the minimum and maximum values. The assumed uncertainties in the measured spectra result in an uncertainty of < 0.03 mA/cm² in the photogenerated current density J_{Si}^* .

7.4.3 Impact of refractive index of matrix material

Sample preparation

The refractive index of the matrix material affects the optical performance of the PDR in two antagonizing ways. On the one hand, the scattering efficiency Q_{sca} of the PDR increases, the more the refractive index of the pigment n_p and of the matrix n_m differ from each other, which suggests to pick a material with small n_m . On the other hand, the randomized light becomes more focused towards the surface normal upon the transition from PDR to Si, the lower the refractive index of the matrix is, suggesting to pick a larger n_m . In this section, we study the impact of n_m on the gain in J_{Si}^* through the PDR. For this, we substitute the spin-on SiO_2 matrix by PECVD SiN_x .

The PECVD process allows to vary the refractive index of the resulting SiN_x by the silane mass flow during the deposition. We set the silane flow to values between 2.5 sccm and 12.5 sccm, the deposition temperature to 400° C and the deposition time to 13.5 min. Ellipsometry at a wavelength of 633 nm on planar reference samples yield a resulting layer thickness of (250 ± 20) nm for each variation and refractive indices of $n_m = 1.78, 2.02, 2.24, 2.54$ and 2.77 . We prepare five PDR samples for each refractive index to reduce the statistical uncertainty. These variations are carried out with two pigment concentrations of 0.14 and 0.3 g/ml. As a reference we deposit each SiN_x -layer on a sample without pigments, i.e. $c_p = 0$ g/ml, as well.

Results and discussion

Figure 7.14 shows the results of the optical characterization that is carried out in the same way as described in the previous section. The gain in $J_{\text{Si}}^*(c_p)$ in Fig. 7.14 a) refers to the respective reference $J_{\text{Si}}^*(0)$ with the same refractive index but with zero pigment concentration. The blue triangles indicate the arithmetic mean of the absolute optical gain. The samples below the mean are with the lower pigment concentration. The dependence of the gain on n_m in this configuration is weak with a tendency towards a higher gain with higher n_m . The total difference between the J_{Si}^* -values with $n_m = 1.78$ and 2.77 is 0.20 mA/cm^2 . The findings indicate that for the PDR of the presented form, the probability for light to re-enter the silicon absorber (which increases with n_m) is more important than the internal reflectance and scattering efficiency within the PDR. We add the ΔJ_{Si}^* -value of the SiO_2 -matrix from Fig. 7.12 to Fig. 7.14 to emphasize this statement. The SiO_2 -matrix enhances J_{Si}^* by 1.15 mA/cm^2 compared to a maximum of 1.03 mA/cm^2 for the SiN_x -matrix. The SiO_2 -matrix performs better than SiN_x despite its low n_m . The reason is that the liquid precursor better infiltrates the voids between the pigments compared to the PECVD SiN_x . This is shown in the SEM micrographs of the SiN_x -covered pigments in Fig. 7.15 a) and b) and sketched in c). The PECVD deposition

is not surface conformal, in contrast to atomic layer deposition, and leaves uncovered gaps between the pigments and at the pigment/Si interface. These gaps hamper the re-entrance of light into the silicon wafer. The result thus suggests to evaluate liquid precursors with a higher refractive index, e.g. spin-on titanate [197], in combination with Si nanopowder. Figure 7.14 b) and c) show a plot of two of the fit parameters, T_b and Λ_b , of the respective samples. While the Lambertian character shows no clear trend over n_m . In fact, the mean of samples P3 and P5* with the SiO₂-matrix is lower compared to the samples with SiN_x-matrix. The main differences are in transmission through the rear side which for the PECVD samples decreases with n_m . The samples with SiO₂-matrix have the lowest T_b for the reasons described above. The trend within the SiN_x-samples arise from a higher re-entrance probability into the Si with increasing n_m .

7.4.4 Impact of external rear mirror

Experimental results

We study the optical performance of the PDR in combination with a detached Ag rear mirror that reduces the impact of different rear transmittances T_b of the samples. Furthermore, an external reflector or backsheet better emulates the configuration in the module. We measure the reflectance spectra of the best PDR sample P5* and the references P0 and RP with the Ag mirror as illustrated in Fig. 7.8 a)-c) on p. 107. We fit the spectra with Eq. 7.8 by fixing T_b at a value of 0.01 according to the reflectance of Ag in air. The two remaining free parameters are thus Λ_b and a_{PDR} . The fixation of T_b is a simplification, as the light can bounce several times between the PDR and the Ag mirror before it enters the Si again which would result in a higher T_b . We find, however, no difference in fit quality if we reduce T_b , as a larger T_b -value can be compensated by a smaller a_{PDR} -value. So, instead of introducing a 3-layer system with Si absorber, PDR and rear mirror, we stick with the simplification. Figure 7.16 shows the reflectance spectra (symbols) and the corresponding fit (lines) for the three investigated samples.

Table 7.3 lists the best fit parameters as well as the corresponding photogenerated current density J_{Si}^* that we obtain by using these the fit parameters and Eq. 7.3 to calculate the absorptance A_{Si} . This absorptance is then inserted into Eq. 2.4 to calculate J_{Si}^* . The J_{Si}^* refers to the wavelength region between 700 and 1400 nm.

The sample with no light trapping scheme benefits the most from the detached rear mirror and, accordingly, the optical gain through the PDR and the random pyramids reduce to 0.80 mA/cm² and 1.44 mA/cm², respectively. The optical gain increases again when the samples have a lower external front reflectance as more light enters the absorber.

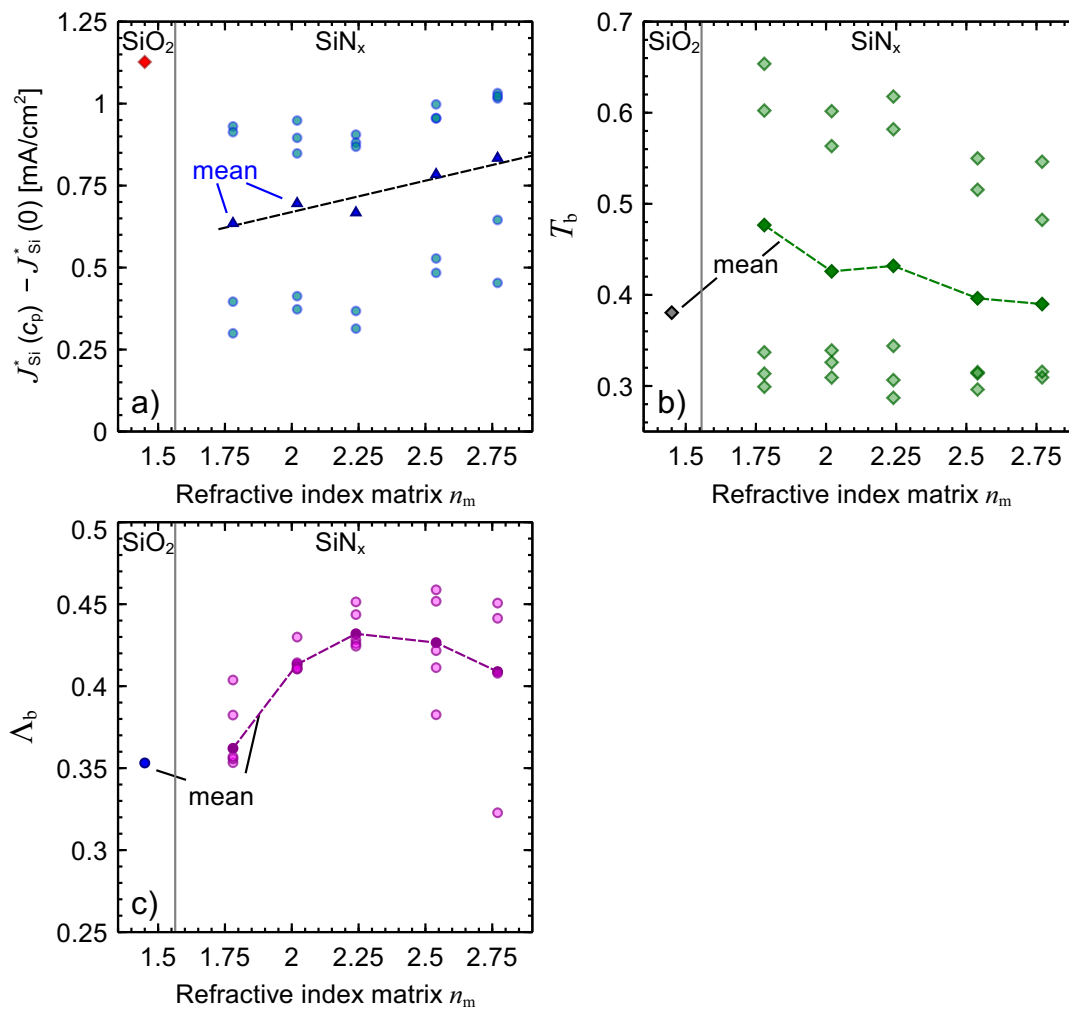


Figure 7.14: The figure shows a) the gain in photogenerated current density $J_{Si}^*(c_p) - J_{Si}^*(0)$ over the sample with no pigments and only the matrix material with refractive index n_m on the rear side. We distinguish between PECVD SiN_x and spin-on SiO_2 as matrix material. b) and c) show the fit parameters T_b and Λ_b , respectively. Besides the results for the five individual samples for each variation, the arithmetic mean is plotted.

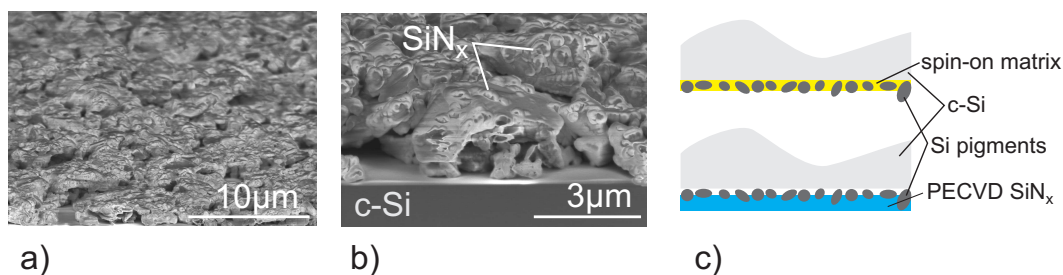


Figure 7.15: The figure shows a) and b) SEM micrographs of the tilted cross sections of the PDR with SiN_x -matrix which is less surface conformal than the liquid SiO_2 precursor illustrated in Fig. 7.4. c) shows a sketch of the difference between the gap-filling spin-on matrix and the PECVD matrix that leaves voids between the pigments.

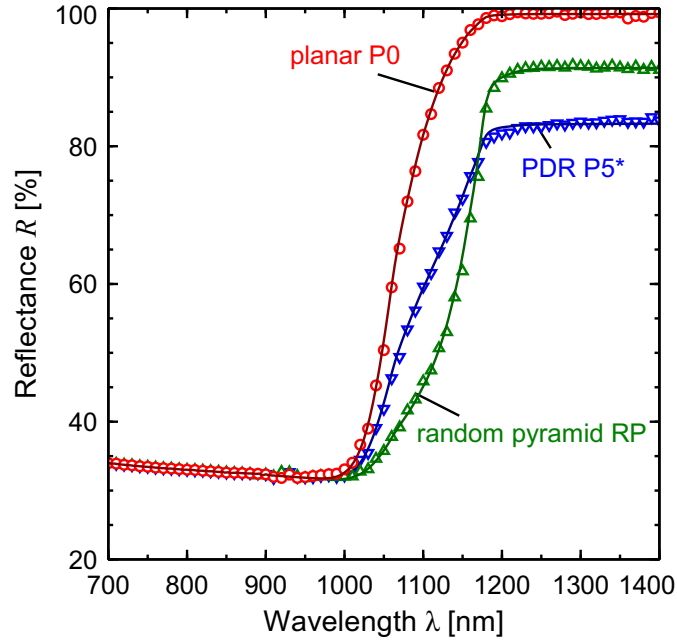


Figure 7.16: The figure shows the measured reflectance spectra (symbols) and the fit via Eq. 7.8 (lines).

Table 7.3: Overview of the best fit parameters and the photogenerated current densities with detached rear reflector. For the J_{Si}^* of the last column we assumed an 80nm-thick $\text{SiN}_{x,n=1.9}$ front side ARC.

Name	Λ_b	a_{PDR}	T_b	J_{Si}^* [mA/cm ²]	J_{Si}^* with ARC [mA/cm ²]
P0	0.008	0	0.01	14.60	19.50
P5*	0.461	0.007	0.01	15.40	20.47
RP	0.819	0.002	0.01	16.04	21.31

The last column in Tab. 7.3 lists the J_{Si}^* for when we assume a 80nm-thick $\text{SiN}_{x,n=1.9}$ ARC on the front side, yielding gains of 0.97 mA/cm² and 1.81 mA/cm² of sample P5* and RP over P0, respectively.

Classification of Si nanopowder PDR

The optical model allows to extrapolate the gain in J_{Si}^* to different absorber thicknesses W_{Si} . This implies the assumption that the PDR works on the same level for any absorber thickness which can be achieved if the size of the Si pigments or pyramids is adapted following Mie theory. In addition, the parasitic absorptance parameter a_{PDR} of the PDR is assumed to be independent of wavelength not only until 900 nm but between 400-1400 nm. We will estimate the error due to this assumption after the description of the results. Figure 7.17 shows the expected gain of the Si nanopowder PDR ($\Lambda_b = 0.461$, $a_{\text{PDR}} = 0.007$) over a sample with no light trapping ($\Lambda_b = 0.008$, $a_{\text{PDR}} = 0$) when applied to an absorber with a planar $\text{SiN}_{x,n=1.9}$ -coated front side and a detached Ag rear reflector. The literature values distinguish between type-I PDRs with a higher

refractive index of the pigment and type-II PDR with a higher refractive index of the matrix. The type-I PDRs, except for Inns *et al.* who use silica nanospheres [202], have TiO₂ particles as pigments either in pure form or as white paint with a binding medium. The error bars of the literature values are, if not stated in the source paper, estimated to account for experimental differences in, e.g., the detached rear side mirror or the front side ARC. As we have shown, a detached rear side mirror diminishes the relative absorptance enhancement due to PDR while a lower front side reflectance increases it. The Si nanopowder PDR outperforms reported type-I PDRs which stresses the performance of Si as pigment.

In practice, the Si nanopowder PDR will absorb more light parasitically with decreasing W_{Si} . This is because of two reasons: First, the weakly absorbed light interacts more often with the PDR at the rear side. Second, the photons with a smaller wavelength have a higher absorption probability in the PDR, as Fig. 7.5 indicates. We estimate the impact of both effects by assuming a 10 times higher parasitic absorptance parameter $a_{\text{PDR}} = 0.07$. However, if we only changed the absorption coefficient in the PDR, the estimate would exaggerate the parasitic absorptance for absorber thicknesses above 100 μm . Therefore, the difference in the photogenerated current densities $\Delta J_{\text{Si}}^* = J_{\text{Si}}^*(a_{\text{PDR}} = 0.007, W_{\text{Si}}) - J_{\text{Si}}^*(a_{\text{PDR}} = 0.07, W_{\text{Si}})$ is additionally weighted by the transmittance factor $\exp(-\alpha_{800\text{nm}} W_{\text{Si}})$, where we choose the absorption coefficient at 800 nm. This assures that the impact of the larger a_{PDR} essentially applies for $W_{\text{Si}} \lesssim 80 \mu\text{m}$. The red dashed line in Fig. 7.17 shows the impact of the assumed parasitic absorptance and is calculated by $J_{\text{Si}}^*(a_{\text{PDR}} = 0.007, W_{\text{Si}}) - \exp(-\alpha_{800\text{nm}} W_{\text{Si}}) \Delta J_{\text{Si}}^*$. It shows that the optical gain is still high compared to the TiO₂ based type-I PDRs under the assumptions.

The type-II PDR of Eisenlohr *et al.* outperforms the type-I PDRs including the one presented here. The reason for this is the large probability of light to re-enter the silicon absorber, as the poly-Si matrix has the same refractive index as the absorber (see previous section).

7.5 Characterization of samples with POLO junctions

While samples without surface passivation are well-suited to study the optical performance of the PDR, they do not reflect the actual structure of a solar cell. We therefore study the performance of the Si nanopowder PDR on solar cell precursors that have carrier selective poly-Si on oxide (POLO) junctions. In this section, we compare the optical as well as the electrical performance of the light trapping schemes that are illustrated

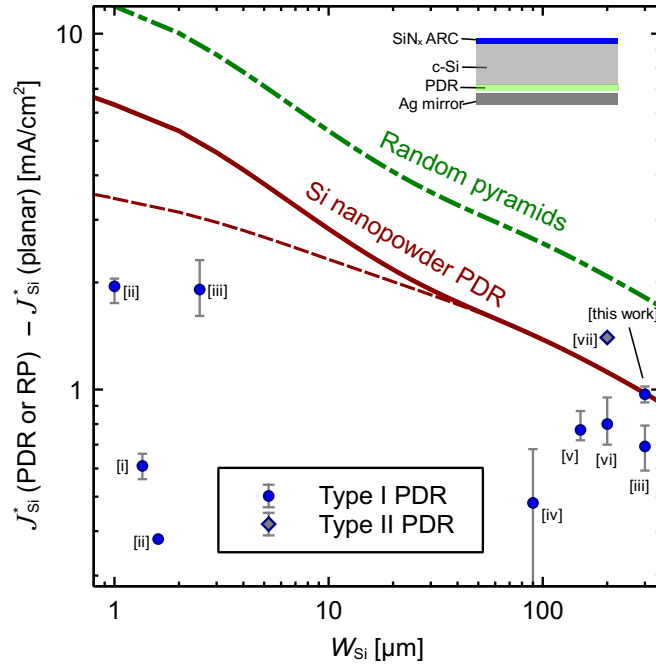


Figure 7.17: The figure shows the gain in photogenerated current density $J_{Si}^*(\text{PDR or RP}) - J_{Si}^*(\text{planar})$ due to a light trapping structure on the rear side for different absorber thicknesses W_{Si} . The inset shows the sample structure with front side ARC and a detached rear mirror. The dashed red line accounts for a higher parasitic absorptance in the PDR. The symbols show literature values of type-I ([i]: [202], [ii]: [187], [iii]: [189], [iv]: [186], [v]: [203], [vi]: [40]) and type-II ([vii]: [193]) PDRs.

in Fig. 7.8 d)-f) on p. 107. The combined analysis gives insight into whether the PDR could yield an efficiency-wise improvement over random pyramids.

7.5.1 Preparation of POLO cell precursor

The base material we use for the POLO junctions is (140 ± 4) μm -thick and (15.6×15.6) cm^2 -sized n -type Cz-Si with a resistivity of $8 \Omega\text{cm}$. The wafers have a surface roughness from wire sawing as can be seen in the SEM micrographs in Fig. 7.9 on p. 109. The POLO junctions are prepared as described in Ref. [204]: After an RCA cleaning, the samples receive a 1.7 nm-thick thermal oxide, followed by a 30 nm-thick LPCVD intrinsic amorphous silicon (a-Si) layer on both sides of the wafer. The a-Si layers are then doped via ion implantation. The boron implantation dose is $2 \times 10^{14} \text{cm}^{-2}$ for a planar surface. The phosphorous implantation dose is $2.5 \times 10^{15} \text{cm}^{-2}$ for a planar surface and $4.25 \times 10^{15} \text{cm}^{-2}$ for a surface textured with random pyramids. Afterwards, the samples are annealed at 950°C for 30 min. During this annealing step, the a-Si transforms to poly-Si and the thin interface oxide locally breaks up and allows dopant diffusion from the poly-Si into the c-Si as indicated in Fig. 7.8 d)-f) [167, 205]. The front side of the

samples gets coated by a 80 nm-thick $\text{SiN}_{x,n=1.9}$ AR-layer. All samples are laser-cut into $(2.5 \times 2.5) \text{ cm}^2$ pieces.

Table 7.4 lists the samples with POLO junctions that we investigate. The matrix for the samples with PDR is the siloxane-based SiO_2 precursor. We evaluate a reduced number of pigment concentrations c_p . This is to verify that the Si pigments have no impact on the passivation quality. The PDR is deposited on the hole selective contact which implies that the electron selective contact is on the front side (see Fig. 7.8 d) and e)). Having a perovskite-Si tandem solar cell in mind, we motivate this choice by the strong absorption of the hole transporting material in the perovskite solar cells [206] that should not directly face the sun. However, changing the polarity has a negligible impact on the photogenerated current density for poly-Si layers that are thinner than 30 nm [207]. The random pyramid reference has a thickness of $W_{\text{Si}} = (160 \pm 5) \mu\text{m}$ which is above the thickness of the PDR samples. We examine the relevant structure with the electron selective contact on the textured side (see Fig. 7.8 f)) as this allows for optimum performance of the Si cell [164, 171].

Table 7.4: The table lists the investigated samples with its light trapping scheme, absorber thickness W_{Si} and pigment concentration in the PDR c_p .

Name	LT scheme	W_{Si} [μm]	c_p [g/ml]
POLO 0	Fig. 7.8 d)	140	0
POLO 1	Fig. 7.8 e)	140	0.07
POLO 2	Fig. 7.8 e)	140	0.15
POLO 3	Fig. 7.8 e)	140	0.25
POLO 4	Fig. 7.8 e)	140	0.34
POLO RP	Fig. 7.8 f)	160	-

7.5.2 Optical and electrical characterization of POLO samples

Optical characterization

We measure the absorptance and transmittance of the samples of Tab. 7.4 and analyze the spectra with the optical model as described for the samples in Fig. 7.10. For the fit procedure, we constrain the values for Λ_b and T_b to lie between 0 and 1. Figure 7.18 shows the measured and fitted absorptance and transmittance spectra. The best fit results for the three parameters Λ_b , a_{PDR} and T_b are listed in Tab. 7.5. The fit uncertainty, as stated in the last column of Tab. 7.5, is below 0.12 mA/cm^2 which is quite satisfactory given that the assumptions of the optical model do not strictly hold for the POLO samples. For example, as the samples have a saw-related roughness and highly doped poly-Si layers that exhibit free carrier absorption on both surfaces, the light scattering and the parasitic absorption do not exclusively occur at the rear side as stipulated in

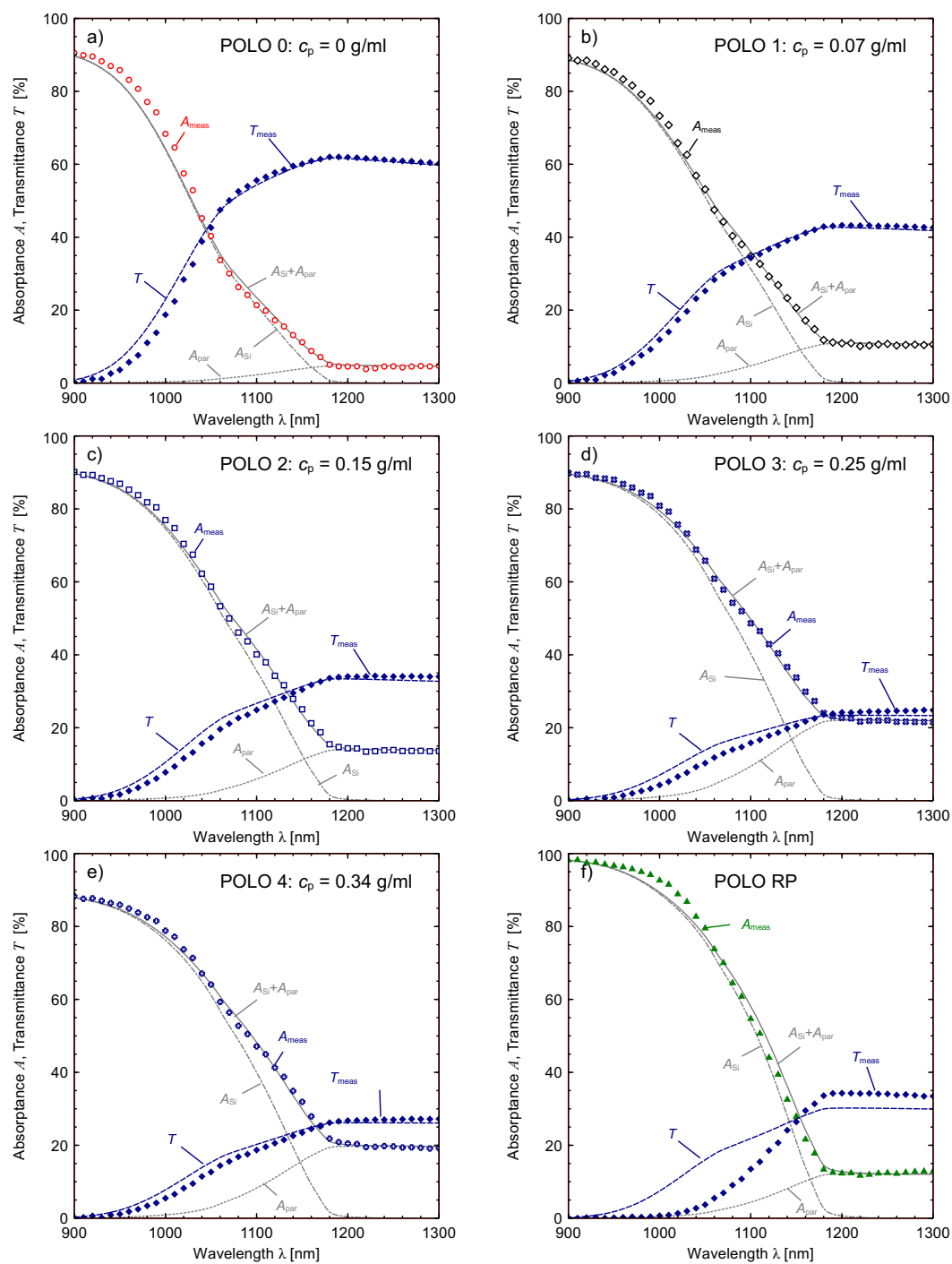


Figure 7.18: The figure shows the measured and fitted absorbance and transmittance spectra of the POLO samples.

the model. This explains the large values for Λ_b and the comparatively small fraction of useful absorptance S , even for sample POLO 0 with no pigments. The absorptance enhancement mainly manifests itself in the transmission probability T_b that decreases with the pigment concentration c_p . This must not obscure that the PDR induces light scattering as we have shown before for the unpassivated samples. We again focus on the photogenerated current density J_{Si}^* as the metric for optical performance. We determine a gain in J_{Si}^* of 1.30 mA/cm^2 over the sample POLO 0 with no pigments. This value is higher than the gain of 0.96 mA/cm^2 (see Tab. 7.2) that we have obtained for the same c_p for the $300 \text{ }\mu\text{m}$ -material due to the difference in the absorber thickness W_{Si} and the presence of a front side ARC. The random pyramid sample shows a high gain of 3.53 mA/cm^2 . Due to its larger absorber thickness, we scale the J_{Si}^* of sample POLO RP by a factor $20.86/22.44=0.93$, which is the ratio of the photogenerated current densities of a Lambertian light trapping scheme with the same external front surface reflectance as POLO RP for absorber thicknesses of 140 and $160 \text{ }\mu\text{m}$. The actual value for J_{Si}^* is thus 20.46 mA/cm^2 . This shows that random pyramids outperform the best PDR structure by 0.69 mA/cm^2 .

Table 7.5: Overview of the best fit parameters and the photogenerated current densities from the measured, J_{meas}^* , and calculated, J_{Si}^* , absorptance spectra. The measure S is defined in Eq. 7.10 and the difference $J_{\text{meas}}^* - J_{\text{fit}}^*$ describes the quality of the fit.

Name	τ_{eff} [μs]	Λ_b	a_{PDR}	T_b	J_{meas}^* [mA/cm^2]	S	J_{Si}^* [mA/cm^2]	$J_{\text{meas}}^* - J_{\text{fit}}^*$ [mA/cm^2]
POLO 0	640 ± 50	1	4.98×10^{-3}	0.632	18.91	0.976	18.47	0.12
POLO 1	508 ± 21	0.972	7.01×10^{-3}	0.398	19.97	0.951	18.98	0.04
POLO 2	475 ± 27	0.922	7.79×10^{-3}	0.293	20.77	0.939	19.51	0.02
POLO 3	520 ± 29	0.944	1.11×10^{-2}	0.197	21.76	0.908	19.77	0.02
POLO 4	518 ± 27	1	9.85×10^{-3}	0.227	21.26	0.916	19.48	0.03
POLO RP	269 ± 14	1	4.55×10^{-3}	0.207	23.06	0.954	22.00 (20.46)	0.07

Electrical characterization

We measure the effective minority carrier lifetime τ_{eff} of the samples with the dynamic ILM technique. Figure 7.19 a) shows the lifetime images at an illumination intensity equivalent to 1 sun. The samples POLO 0, POLO 2 and POLO 4 were cleaved prior to this measurement for SEM characterization (see Fig. 7.9 on p. 108). Table 7.5 lists the values for τ_{eff} with the uncertainty that results from averaging over the sample area. The comparison with the POLO 0 sample shows that the Si nanopowder PDR slightly deteriorates the lifetime. However, as this decrease in τ_{eff} is independent of the pigment concentration c_p , the reason for this difference might relate to the deposition of IPA or the sample handling caused by the additional spin-coating step. All PDR samples have a higher lifetime than the sample with random pyramids. The lifetime level of the investigated POLO samples, planar or textured, is low compared to optimized samples

that have been published in Refs. [164, 171]. Nevertheless, the difference in τ_{eff} between textured and planar POLO junctions that we obtain is also present for samples with optimized junction quality so the following conclusions are valid.

We calculate the quality factor QF for the samples with Eq. 2.60 by translating the measured τ_{eff} into the implied open-circuit voltage V_{oc}^* with Eq. 2.56 and extending the integration boundaries for the calculation of J_{Si}^* to 300-1400 nm to include the whole convertible solar spectrum. For calculating the fill factor FF^* , we determine the differential ideality factor m of the POLO samples from the suns-implied V_{oc}^* curve illustrated in Fig. 7.19 b). The suns-implied V_{oc}^* curve is acquired by the photoconductance decay method [64] and contains the ideality in its slope according to the one-diode equation [208]

$$\log\left(\frac{J_{\text{sc}}^*}{J_0} \times \text{suns}\right) = \frac{V_{\text{oc}}^*}{mV_{\text{th}}}. \quad (7.11)$$

The photogenerated current density J_{sc}^* at 1 sun and the dark saturation current density J_0 do not have to be known to calculate m . We determine a differential ideality factor of $m \approx 0.64$ at an illumination of 1 sun. The value for the ideality indicates that the samples are in high injection and limited by Auger recombination [5, 209].

Figure 7.20 shows the resulting quality factors QF (see Eq. 2.60) that are normalized to the sample POLO 0. For the QF of the sample POLO RP, the J_{Si}^* is scaled to a thickness of 140 μm as described earlier. We find that all samples differ by less than $\pm 3\%$. Two samples with PDR have a higher QF than the random pyramid sample: POLO 3 and POLO 4 show a relative gain in the quality factor over the planar sample of $\Delta QF = (2.6 \pm 0.6)\%$ and $\Delta QF = (2.7 \pm 0.7)\%$, respectively while POLO RP has a $\Delta QF = (1.2 \pm 0.8)\%$. The differences, however, are as large as the measurement inaccuracy which is mainly introduced by the uncertainty in τ_{eff} . The uncertainty in J_{Si}^* plays a minor role. Nevertheless, the result shows that the benefit of the better surface passivation by the planar POLO junction compensates the disadvantage in the optical performance for the samples investigated here. The importance of the pigment concentration c_p is stressed by the difference between the samples POLO 1 through 4. The sample POLO 4 ($c_p \approx 0.34$ g/ml) yields a $\Delta QF = (2 \pm 0.6)\%$ higher quality factor than the sample POLO 1 ($c_p \approx 0.07$ g/ml).

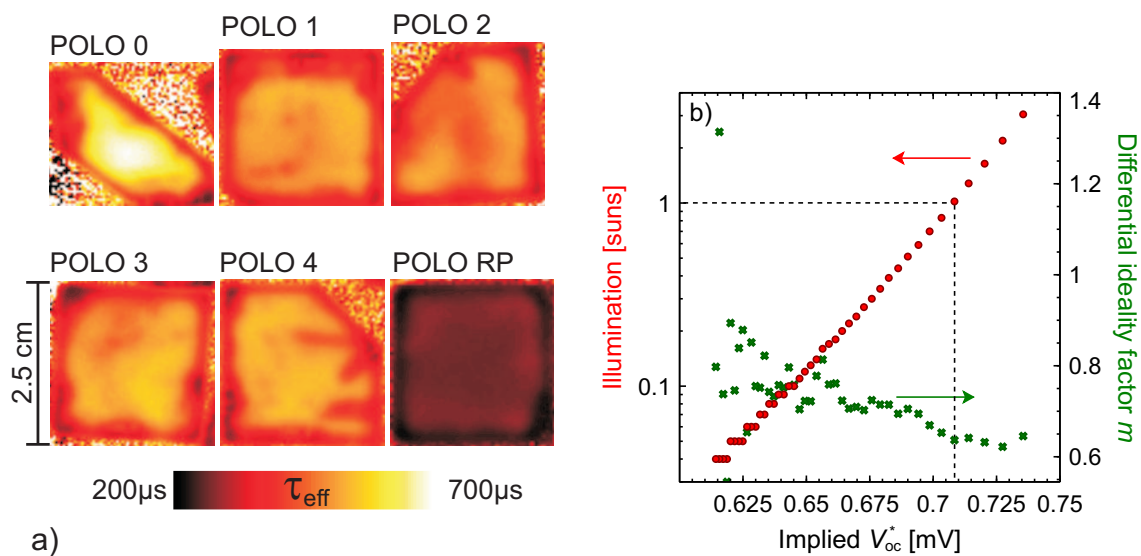


Figure 7.19: The figure shows a) the ILM lifetimes mappings of the samples and b) a suns-implied V_{oc}^* measurement (red circles) together with the differential ideality factor m (green crosses) of a planar POLO cell precursor. The length scale in a) applies for all samples.

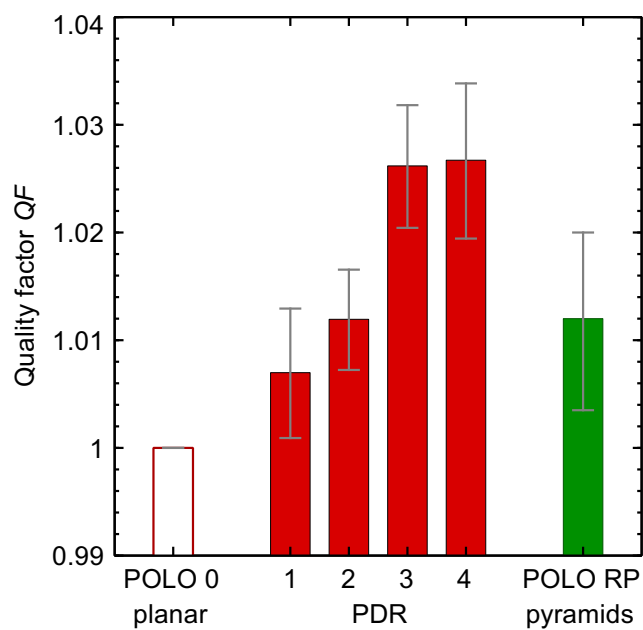


Figure 7.20: The figure shows the quality factors QF as defined by Eq. 2.60 for the POLO passivated samples with the light trapping schemes of Fig. 7.8 d)-f).

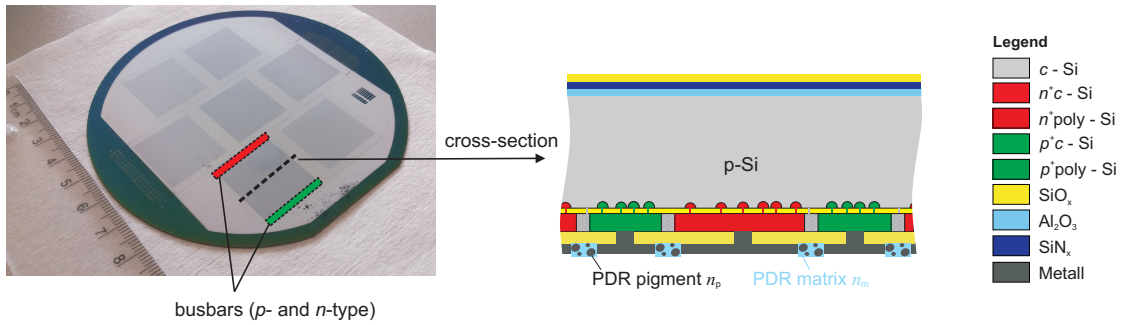


Figure 7.21: The figure shows a photograph prior to PDR deposition of the 4-inch Si wafer with 7 (2×2) cm^2 IBC cells and a sketch of the cross section of the cell. The cells have a planar front side and, after its deposition, a silicon nanopowder PDR between the metal fingers.

7.6 Application of PDR to solar cells

Cell structure

We aim to verify the performance of the silicon nanopowder PDR on solar cells. We therefore fabricate interdigitated back-junction back-contact (IBC) solar cells with carrier selective POLO junctions and a planar front side as illustrated in Fig. 7.21. The Si wafer has a thickness of $280 \mu\text{m}$ and a double layer AR-coating on the front side. The main characteristic of an IBC cell is that it has the carrier selective junction, here the already described POLO junctions, and the metal contact for both polarities at the rear side. Both poly-Si polarities are separated by an undoped intrinsic poly-Si spacer that prevents otherwise occurring carrier recombination when the p^+ and n^+ -poly-Si regions are in contact [204, 210]. 7 cells with a size of $(2 \times 2) \text{cm}^2$ are processed on a 4-inch substrate wafer. As we are mainly interested in the impact of the PDR on the cell performance, we refrain from discussing the cell preparation in detail. These can be found in Refs. [169, 170].

We deposit the PDR with the same spin-coating parameters as described in Sec. 7.2 on p. 99. Figure 7.22 shows an optical microscope image of a part of the rear side of the cell prior and after PDR deposition. In the micrograph, it is possible to distinguish between the different poly-Si polarities. The n^+ -poly-Si region appears yellow while the intrinsic and p^+ -poly-Si regions appear dark and pale blue, respectively. This is due to thickness variations in the thermal silicon oxide between the metal layer and the poly-Si. The oxide growth rate depends on the doping density of the poly-Si. The oxide layer serves as a dielectric spacer and improves the rear side reflectance of the cell. For contact formation, this oxide is locally opened successively by lithography masking and wet chemical etching by a buffered hydrofluoric acid solution. The contact openings are visible through the metal layer in Fig. 7.22 a). From the 7 cells, 5 work as solar cells.

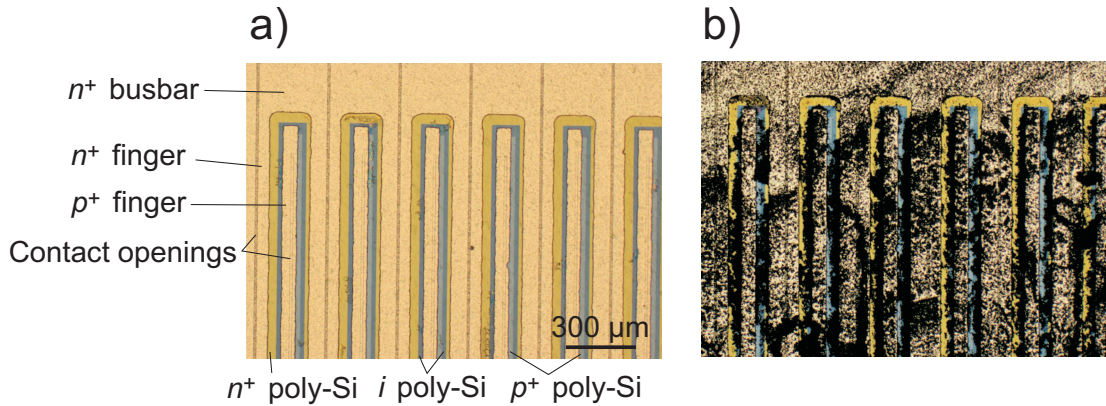


Figure 7.22: The figure shows a microscope image of a part of the cell from the rear side prior a) and after b) PDR deposition. The unmetallized area fraction is 40 %.

These are enumerated from 1 through 5. We calculate the unmetallized area fraction from the microscope image to be 40 % for cells 1 through 4 and 56 % for cell 5. Figure 7.22 b) shows the wafer after deposition of the PDR. It can be seen that the PDR does not fully cover the gap region between the metal fingers, which have a height of 10 μm .

Cell measurement

We measure the solar cells prior and after the deposition of the PDR with an IV-tester (*LOANA* from pv-tools [211]). For this, the cells are placed on a black chuck with pins that contact the busbars. An LED array illuminates the cell with different light intensities, each of which the voltage and current of the cell are measured. A metal plate with an aperture of $(2 \times 2) \text{ cm}^2$ is placed on top of the wafer and assures that only a single cell of the wafer is illuminated. We compare the short-circuit current density J_{sc} , the open-circuit voltage V_{oc} , the fill factor FF and the conversion efficiency η . For the first three parameters, we determine the absolute difference due to the PDR, i.e. $\Delta J_{\text{sc}} = J_{\text{sc,PDR}} - J_{\text{sc,no PDR}}$ and so on. For the efficiency, we determine the ratio $\eta_{\text{PDR}}/\eta_{\text{no PDR}}$ in order to compare the efficiency gain to the quality factor in Fig. 7.20.

Figure 7.23 shows the results of the five cells. All show a higher short-circuit current density after the deposition of the PDR. The gain is between 0.26 to 0.6 mA/cm^2 . The red symbols mark the gain we would expect from the results from Fig. 7.12 on p. 112. It refers to the product of the maximum gain of 1.15 mA/cm^2 and the unmetallized area fraction. The average gain is below the expected gain due to the fact that the unmetallized area is not covered by Si nanoparticles completely as shown in Fig. 7.22. The open-circuit voltage and the fill factor are affected slightly for cells 3 through 5 with changes below 0.5 mV and below 1 %_{abs}. However, while the open-circuit voltage shows no clear trend, the fill factor increases through the PDR deposition for all three cells. This increase is already apparent in the so-called pseudo fill factor pFF , which is

obtained from the currentless J_{sc} - V_{oc} curve. The deposition of the PDR thus improves the injection-dependence of the POLO-IBC cell.

A larger improvement is observed for cell 1. This is due to a slight misalignment of the cell position with respect to the metal mask in the measurement before PDR deposition which means that a small fraction of the cell area is not illuminated. This results in an underestimation of the cell performance. The increase of 0.6 mA/cm^2 in J_{sc} can thus not be attributed to the PDR alone. Cell 2 on the other hand shows a degradation in voltage and fill factor. The reason is a lower shunt resistance of this cell after the PDR deposition which we attribute to a damage from wafer handling. This cell, however, still shows a gain in short-circuit current density due to the PDR.

The cell efficiency improves by $1.1 \%_{\text{rel}}$ and $1.7 \%_{\text{rel}}$ for cells 3 and 4 with a PDR area fraction of 40% and by $2.9 \%_{\text{rel}}$ for cell 5 with a PDR area fraction of 56%. This reflects the expectations from the test samples in Fig. 7.20, given that for the quality factor the improvement in the FF has not been accounted for. The best cell in absolute measures is cell 3 where the efficiency increases from 22.0% to 22.2%. The largest absolute gain is for cell 5 from 21.35% to 22.0% due to the PDR.

7.7 Summary and discussion

In this chapter, we evaluate a light trapping scheme that is compatible with an electrically flat surface. The light trapping structure is an easy-to-apply diffuse rear reflector that consists of Si nanopowder as scattering pigment embedded in a SiO_2 matrix material. The deposition of the PDR simply relies on a spin-coating process where no nanostructuring or vacuum equipment is needed.

The induced absorptance enhancement by this PDR has a useful fraction that is absorbed in the Si wafer and a useless fraction that is absorbed in the PDR. We explain the parasitic absorption by free carrier absorption in the Si pigments because some of the particles show a high phosphorous content. Our analytical optical model helps to separate both fractions and allows the determination of the optical gain from absorptance spectra. The model is a useful tool to characterize light trapping schemes prior to making solar cells.

We study the impact of the composition of the PDR regarding the volumetric fraction of the Si pigments and the ratio of the refractive indices of pigment, n_p , and matrix material, n_m , on the optical gain in the Si wafer. The optical gain increases first linearly then sublinearly with the volumetric fraction, as is expected from Mie theory. However, the optical gain also increases for a smaller ratio n_p/n_m despite a smaller scattering efficiency within the PDR. This is because the re-entrance probability of light into the

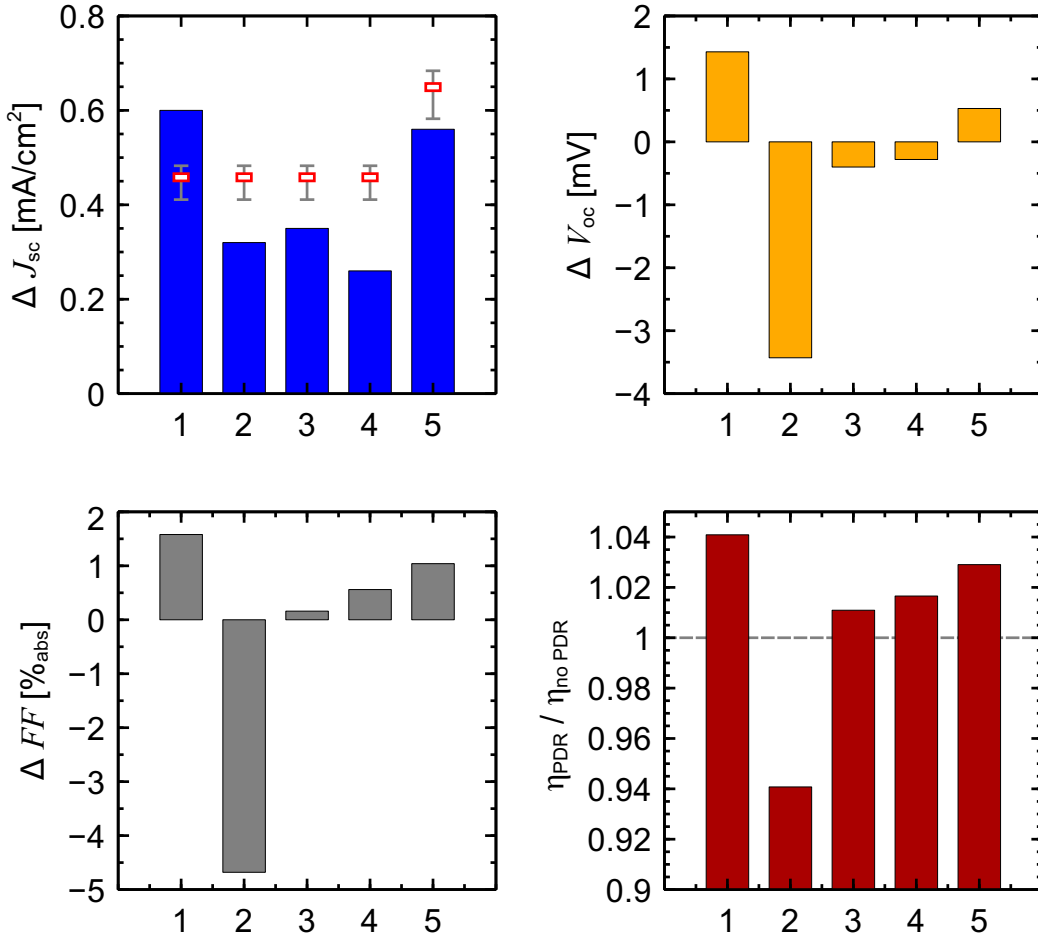


Figure 7.23: The figure shows the difference in short-circuit current density ΔJ_{sc} , open-circuit voltage ΔV_{oc} and fill factor ΔFF induced by the PDR. The efficiency is given as a relative improvement $\eta_{PDR}/\eta_{no\ PDR}$. The red symbols in the ΔJ_{sc} -plot mark the expected gain. The unmetallized area fraction is 40 % for cells 1 through 4 and 56 % for cell 5.

Si wafer, once it has been scattered in the PDR, is more important for its performance as a rear reflector. This explains our findings that the Si nanopowder PDR performs worse than type-II PDRs, where the matrix material has a higher refractive index than the pigment and worse than random pyramids where the light becomes scattered in the Si directly without having to re-enter the absorber. In the best composition, the Si nanopowder PDR outperforms previously reported type-I PDRs that are based on TiO₂ pigments.

We characterize the electrical performance in the presence of a PDR on wafers with passivating POLO (poly-Si on oxide) junctions and compare it with random pyramids. The POLO junctions are suited for the combination with a PDR as the electrically active surface is separated from the recombination active PDR by the thin interface oxide. The random pyramids exhibit a larger surface recombination compared to the PDR samples.

This difference suffices to compensate for the inferior optical performance of the PDR. Compared to the sample with no light trapping scheme, we find that the PDR can enhance the efficiency by $(2.7 \pm 0.7)\%_{\text{rel}}$ while the relatively low lifetime of the random pyramid sample allows for a boost of only $(1.2 \pm 0.8)\%_{\text{rel}}$. Hence, the benefit of the PDR over random pyramids critically depends on the difference in the total recombination rate of POLO junctions on planar (100)-surfaces over (111)-facets and on how much this difference can be reduced in the future. Either way, the Si nanopowder PDR proves to be a promising alternative to a random pyramid rear side texture if the front surface of the silicon solar cell has to remain flat.

We apply the PDR to the rear side IBC solar cells with a planar front side. The PDR is active in the unmetallized region of the rear side. An improvement in the short-circuit current density as well as in the fill factor result in a $2.9\%_{\text{rel}}$ higher cell efficiency compared to no PDR for an unmetallized area fraction of 56 %. The physical reason why the PDR improves the fill factor is yet unclear.

Further improvements of the PDR could be achieved if the re-entrance probability into the Si wafer is enhanced, e.g. by using a liquid matrix precursor that has a higher refractive index than SiO_2 . The flexibility in composing the PDR also allows to make it, e.g., laterally conductive by using a conductive matrix and/or doped Si pigments, however, at the cost of a higher parasitic absorptance. Another option is to apply the PDR before metalization on top of the SiO_2 -layer in Fig. 7.21. This would increase the active area of the PDR.

Chapter 8

Efficiency limit of crystalline Si solar cells with Lambertian light trapping

In this chapter, we change our focus from the development and characterization of light trapping schemes to the impact of the theoretical concept of Lambertian light trapping on the limiting efficiency of crystalline Si solar cells. Previous papers calculated the limiting efficiency of solar cells with an approximate expression for the Lambertian absorptance. Here, we apply the accurate expression for Lambertian light trapping. Parts of this chapter have been published in Ref. [212].

8.1 Calculating the limiting efficiency

In 1960, Shockley and Queisser published a calculation of the limiting efficiency of solar cells by applying the detailed balance principle [16]. Neglecting empirical data for, e.g., the solar spectrum or the absorption coefficient, they assumed the sun and the solar cell to be black bodies at 6000 K and 300 K, respectively. They further assumed the absorptance of the cell as a step function where every photon with an energy above the band gap is absorbed. Over the years, the detailed balance limit has been refined by including the in those days valid empirical data for the solar spectrum, the absorptance and the intrinsic recombination [5, 213, 214]. The latest refinement was published by Richter *et al.* in 2013 [5]. All the refinements, however, use the weak absorption approximation of the Lambertian limit to calculate the absorptance and thereby underestimate it, as Tiedje *et al.* already pointed out [213]. Before we discuss the absorptance in more detail, the approach to calculate the limiting efficiency is briefly discussed.

The efficiency of an ideal crystalline silicon solar cell is limited by intrinsic material properties only. The charge carrier recombination rate is independent of the location within the cell volume and consists only of the intrinsic processes, radiative and Auger recombination. This implies that the solar cell has ideal contacts, no resistance losses and neither defect nor surface recombination. The charge carrier generation is maximized by assuming that the absorber fulfills the Lambertian limit, i.e. light within the cell volume is fully randomized, it exhibits no front surface reflection and has a perfectly reflecting rear mirror. The current-voltage curve of this ideal cell then reads

$$J(V) = J_L(V) - J_{\text{Aug}}(V) - J_{\text{rad}}(V), \quad (8.1)$$

where $J_L(V)$ is the light-generated current density, $J_{\text{Aug}}(V)$ the Auger recombination current density and $J_{\text{rad}}(V)$ the radiative recombination current density. $J_L(V)$ depends on the voltage due to the free carrier absorption (FCA).

The Auger recombination is the dominant intrinsic loss mechanism for solar cells at the maximum power point [5, 213]. We calculate $J_{\text{Aug}}(V) = qWR_{\text{Aug}}$ as in Ref. [5], with q and W symbolizing the elementary charge and the absorber thickness. The parameterization of the Auger recombination rate $R_{\text{Aug}} = \Delta n / \tau_{\text{Aug}}(n_0, p_0, \Delta n)$ is given in dependence of the excess carrier density $\Delta n (= \Delta p)$ and the Auger carrier lifetime τ_{Aug} . In an ideal solar cell, the output voltage V equals the separation of the quasi-Fermi levels and relates to the carrier densities by

$$(n_0 + \Delta n)(p_0 + \Delta n) = n_{i,\text{eff}}^2 \exp\left(\frac{qV}{kT}\right). \quad (8.2)$$

n_0 and p_0 are the equilibrium electron and hole concentrations, respectively. The effective intrinsic carrier concentration $n_{i,\text{eff}}$ is temperature dependent and incorporates band gap narrowing as described in Ref. [5].

We take the generalized Planck law [215] that gives the photon emission rate of an absorber with a band-to-band absorptance A_{bb} and a Fermi-level splitting of V as basis for calculating the net radiative recombination current density,

$$J_{\text{rad}} = qB_{\text{rel}}\pi \int_{250 \text{ nm}}^{1450 \text{ nm}} A_{\text{bb}}(\lambda, V) \frac{2c}{\lambda^4} \left(\frac{1}{\exp\left(\frac{hc}{\lambda kT} - \frac{qV}{kT}\right) - 1} - \frac{1}{\exp\left(\frac{hc}{\lambda kT}\right) - 1} \right) d\lambda. \quad (8.3)$$

The relative coefficient of radiative recombination B_{rel} accounts for the injection-dependence of the radiative recombination: at higher injection levels the Coulomb attraction between the recombination partners decreases due to screening and radiative recombination rate decreases [216]. We have to include B_{rel} as the band-to-band absorption

coefficient α_{bb} in the absorptance A_{bb} is taken at low injection [217]. The subtrahend in the bracket describes the emission of radiation in thermal equilibrium ($V = 0$). The symbols h , c , k and T denote Planck's constant, the vacuum velocity of light, the Boltzmann constant and the temperature of the Si lattice. The generalized Planck law accounts for the effect of photon recycling where photons from radiative recombination become reabsorbed and thus no extra correction factor as in [5, 214] is required.

8.2 Lambertian limit absorptance with free carrier absorption

The light-generated current density J_{L} is calculated as in Eq. 2.4 with integration boundaries between 250 to 1450 nm. The extended integration boundaries are necessary to make the results comparable to the ones from Ref. [5]. For the band-to-band absorptance A_{bb} , previous publications used the weak absorption limit that without consideration of FCA reads [58]:

$$A_{\text{bb,noFCA,wl}}(\lambda) = \frac{1}{1 + \frac{1}{4n^2(\lambda)\alpha_{\text{bb}}(\lambda)W_{\text{eff}}}}. \quad (8.4)$$

It can be calculated from Lambertian limit (Eq. 2.47) by approximating the diffuse transmittance $T_{\text{d}} \approx 1 - 2\alpha_{\text{bb}}W_{\text{eff}}$ for $\alpha_{\text{bb}}W_{\text{eff}} \ll 1$.

The free carrier absorption process (FCA) contributes to the overall absorptance but does not create electron hole pairs. Previous calculations of the limiting efficiency of Si solar cells took this weak absorption approximation and extended it by the absorption coefficient due to FCA, α_{fca} . The share of the band-to-band absorptance in the presence of FCA then reads [5, 213, 214]

$$A_{\text{bb,wl}}(\lambda, V) = \frac{\alpha_{\text{bb}}(\lambda)}{\alpha_{\text{tot}}(\lambda, V)} \times \frac{1}{1 + \frac{1}{4n^2(\lambda)\alpha_{\text{tot}}(\lambda, V)W_{\text{eff}}}}, \quad (8.5)$$

with $\alpha_{\text{tot}}(\lambda, V) = \alpha_{\text{bb}}(\lambda) + \alpha_{\text{fca}}(\lambda, V)$. As the FCA process depends on the injection level and thus the voltage V , the band-to-band absorptance depends on the voltage as well. We take the parameterization for α_{fca} from Ref. [199], just as in Ref. [5].

The accurate absorptance of the Lambertian limit in the presence of FCA, however, is given by Eq. 2.47. We extend it by the FCA and it then reads

$$A_{\text{bb}}(\lambda, V) = \frac{\alpha_{\text{bb}}(\lambda)}{\alpha_{\text{tot}}(\lambda, V)} \times \frac{(1 - T_{\text{d}}^2(\alpha_{\text{tot}}))n^2(\lambda)}{n^2(\lambda) - (n^2(\lambda) - 1)T_{\text{d}}^2(\alpha_{\text{tot}})}. \quad (8.6)$$

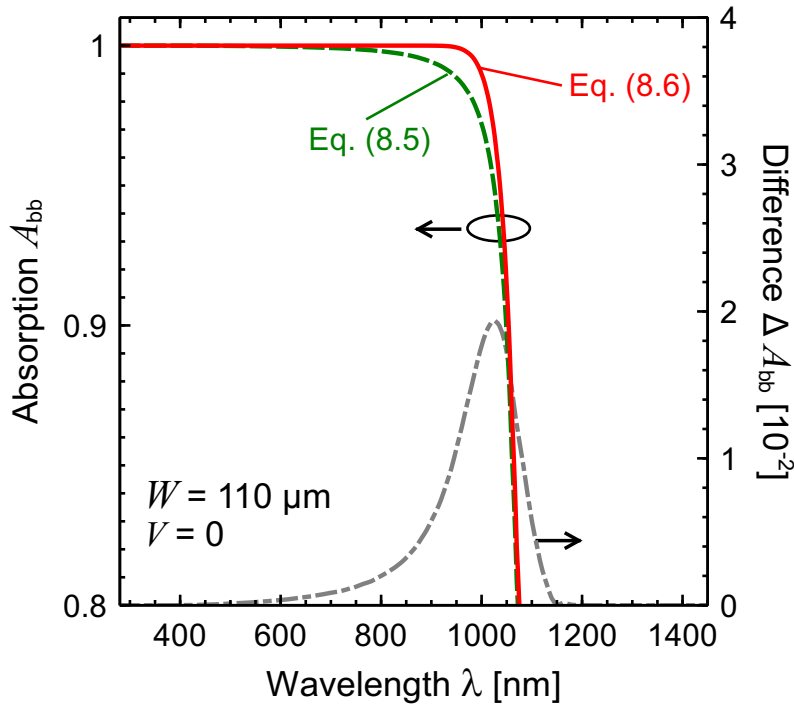


Figure 8.1: The figure shows the band-to-band absorptance spectra as calculated with Eqs. 8.5 (broken line) and 8.6 (solid line) for a crystalline Si wafer with a thickness of $W = 110 \mu\text{m}$ and at short-circuit condition $V = 0$. The integrated difference (dash-dotted line) corresponds to a short-circuit current gain on 0.17 mA/cm^2 .

Figure 8.1 shows the difference between the band-to-band absorptance from the weak absorption limit of Eq. 8.5 and the accurate expression for the Lambertian limit with FCA of Eq. 8.6. The absorptances are calculated for a thickness of $W = 110 \mu\text{m}$ of a virtually undoped ($N_D = 10^{11} \text{ cm}^{-3}$) crystalline Si wafer under short-circuit conditions $V = 0$. Thickness and doping density are chosen to give the maximum efficiency when using the weak absorption limit as in Ref. [5]. The weak absorption approximation underestimates the Lambertian limit especially for wavelengths between 900 and 1100 nm.

Besides the absorption coefficient of the FCA α_{fca} , we take the same sources for the band-to-band absorption coefficient α_{bb} and for the AM1.5G spectrum Φ as Ref. [5] to calculate J_L with Eq. 2.4. We apply trapezoidal integration and a piecewise cubic interpolation of the optical constants at the tabulated wavelength values of the solar spectrum. This leads to values of $J_L = 43.30 \text{ mA/cm}^2$, when using the approximated formula Eq. 8.5 and $J_L = 43.47 \text{ mA/cm}^2$, when using the accurate formula Eq. 8.6 for the band-to-band absorptance.

8.3 Impact on efficiency limit

We calculate the efficiency limit η by evaluating the current-voltage curve from Eq. 8.1 and solving it for maximum power point conditions, i.e. when $d(JV)/dV$ equals zero. We run the model described in Sec. 8.1 with the two formulas for the band-to-band absorptance. When using Eq. 8.5, we find agreement with Ref. [5] in all parameters of the illuminated J-V curve to within 2 counts of the 4th digit. The results are listed in the second row of Tab. 8.1. When using Eq. 8.6, the light-generated current density increases, as described in the previous section, while the open-circuit voltage and the fill factor change by less than 0.1 mV and 10^{-3} in absolute measures, respectively. The results are shown in the third row of Tab. 8.1.

Table 8.1: Limiting efficiency of Si solar cells η with an absorber thickness W as calculated with the band-to-band absorptance from Eq. 8.5 and Eq. 8.6. The open-circuit voltage V_{oc} , the short-circuit current density $J_{sc} = J_L(0V)$ and the fill factor FF are listed as well. The last digit of all figures from this work is rounded. The base doping of the absorber is $N_D = 10^{11} \text{ cm}^{-3}$.

Eq.	W [μm]	η [%]	V_{oc} [mV]	$J_{sc} = J_L(0V)$ [mA/cm^2]	FF [%]	Reference
8.5	110	29.43	761.3	43.31	89.26	[5]
8.5	110	29.43	761.4	43.30	89.28	this work
8.6	110	29.55	761.4	43.47	89.28	this work
8.6	98.1	29.56	763.3	43.36	89.31	this work

Figure 8.2 shows the limiting efficiency for varying absorber thickness when using the different absorptance formulas. The accurate expression for A_{bb} reduces the optimum cell thickness from 110 μm to 98.1 μm . The new limiting efficiency for Lambertian light trapping is 29.56 %. The increase of the limiting efficiency by 0.13 %_{abs} is small but not negligible. This becomes more obvious when considering that the scope of experimental improvements based on the currently best Si solar cell with an efficiency of 26.7 % [15] increases by 5 % relative to at least 2.8 %_{abs} efficiency points until meeting theoretical limit.

8.4 Summary

In this chapter, we recalculated the theoretical maximum of the energy conversion efficiency of a crystalline Si solar cell by using the exact equation for the optical absorptance by a Lambertian light trapping scheme with free carrier absorption, Eq. 8.6. Previously published calculations used an approximated formula that underestimated the absorptance. We furthermore apply the generalized Planck law for simulating the radiative recombination which simplifies the treatment of photon recycling. When using the same

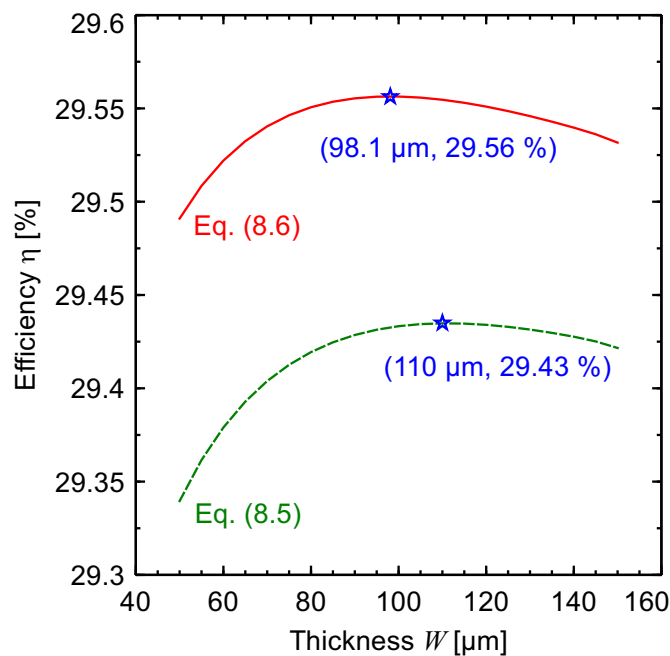


Figure 8.2: The figure shows the limiting efficiency η of an intrinsic crystalline Si solar cell for varying absorber thickness W . The accurate expression for Lambertian light trapping increases the efficiency limit to 29.56% and reduces the optimum cell thickness to 98.1 μm .

material parameters and the same solar spectrum as in Ref. [5], we find that the maximum efficiency for an undoped Si wafer increases from 29.43% to the new value of 29.56%. Furthermore, the optimum wafer thickness reduces from 110 μm to 98.1 μm .

Chapter 9

Summary

The thesis deals with light trapping schemes for silicon solar cells. As light trapping becomes increasingly important for decreasing absorber thickness, we first evaluate the feasibility of a multilayer process, that produces multiple thin macroporous Si layers with excellent light trapping ability. The macropores fully penetrate the wafer. In a second part, we focus on light trapping schemes that represent an improvement over the state-of-the-art random pyramid texture. We use the etching of macropores to form a blind hole texture for the front side of a Si wafer. The macropores extend only a few μm into the wafer. Another scheme addresses the rear side of a Si wafer in form of a pigmented diffuse reflector (PDR). The advantage of this PDR is that it separates the light trapping structure from the recombination active surface. The third part focusses on the theoretical efficiency limit of Si solar cells under Lambertian light trapping.

Part 1: Chapters 4 and 5

The first topic of this thesis deals with the etching of macropores in silicon and in how far it can be used as a kerf-less wafering technique. Therefore, we study the impact of the etching parameters (current, voltage and illumination intensity) on the macropore formation, or, more precisely, on the morphology and dissolution rate. The practical success in this work is the detachment of 4 single 18 μm -thick porosified absorber layers with a size of $(0.5 \times 0.5) \text{ cm}^2$ that are produced in a closed etching process, i.e. without dismounting the sample from setup. We realize this by a minimization of the anodic voltage during the enlargement of the pore diameter. This way, we alter the dissolution chemistry towards a more direct dissolution reaction that results in a tapered pore tip and prevents the branching of a single pore into many smaller pores. The consideration of the interface chemistry exceeds the scope of the well-established space charge region model and makes the multilayer etching concept feasible for the first time.

The drawback of the voltage minimization is that during the time the voltage is below

the characteristic voltage U_{ps} , the pore tip is no longer electropolished, which is characteristic for the steady-state condition between charge transfer in the semiconductor (hole current) and mass transport in the electrolyte (HF flow rate). This results in individual growth rates of the pores until eventually some pores die out completely. This form of irreversible pore reorganization becomes worse with every pore diameter enlargement or separation layer and limits the layer detachment to the here found number of 4.

In order to increase the number of detachable layers and the reproducibility one could modify the process, e.g. by etching and detaching the layers one by one. We demonstrate the detachment of 5 layers which in total make up for 75 % of the substrate wafer. Modifications like this make the overall process yet more elaborate which ultimately questions the usefulness of the multilayer etching compared to other kerf-less techniques.

Part 2: Chapters 6 and 7

This leads over to the second topic of the thesis where we use the tunability of the macropore diameter to create a micron-scaled macroporous blind hole texture. We benchmark blind holes with different pore lengths against AR-coated random pyramids as a texture for the front side of Si solar cells by comparing the optical and electrical properties. The front surface reflectance can be reduced to a AM1.5G-weighted value of 1 %. This residual reflectance is due to the 80 nm-wide flat parts between the individual pores, where the interpore distance is 4 μm . While the front surface reflection decreases monotonously with larger pore depth l_{pore} , the light trapping ability deteriorates. For a pore distance of 4 μm , a pore depth of 17.5 μm has the largest photogeneration which is 97.2 % of the Lambertian limit. The AR-coated random pyramid texture reaches 95.9 % of the Lambertian limit.

The blind hole texture, despite its relatively large surface area enhancement factor, allows for relatively low surface recombination velocities of $< 10 \text{ cm/s}$ when passivated with atomic layer deposited AlO_x . We attribute this low value to a non-uniform distribution of charge carriers in the pore wall region that extenuates the linear correlation between the geometrical surface area and the surface recombination velocity. Taking both the electrical and optical performance of the texture into account, we end up with an optimum pore depth of $l_{\text{pore}} \approx 8 \mu\text{m}$. The texture allows for a 2.0 – 5.3 %_{rel} higher quality factor, a measure that is proportional to the eventual conversion efficiency, than random pyramids coated with an anti-reflection layer.

The blind hole texture is thus a promising candidate to be used as a front side texture in highly efficient lab-type solar cells. For a more widespread use, the process has to be transferred to a larger area first and then reduced in its complexity.

We evaluate a second light trapping scheme that is implemented on the rear side of a silicon absorber. This case is particularly interesting, if the front side of the wafer has to

remain flat, e.g. when used as a bottom cell in a tandem or multijunction device. Polysilicon on oxide (POLO) junctions not only form a highly selective passivated contact that is required for highest efficiencies. They also allow for a spatial separation of the light trapping scheme from the recombination active surface. To demonstrate this, we apply a pigmented diffuse reflector (PDR) on the rear side that consists of Si nanopowder as a scattering pigment embedded in a silicon oxide matrix. Previous reports use particles with a smaller refractive index than Si, like TiO_2 particles, as scatterers. The PDR is applied in a simple spin-coating process and relies on no nanostructuring or vacuum equipment.

We derive an analytical optical model that allows to distinguish between useful absorption in the Si wafer and parasitic absorption in the PDR. By applying the model, we are able to qualify the light trapping scheme from absorptance measurements. We find that on a $300\ \mu\text{m}$ thick absorber, the PDR increases the photogenerated current density by $1.15\ \text{mA}/\text{cm}^2$. Random pyramids on the rear side result in an increase of $2.28\ \text{mA}/\text{cm}^2$. This difference can be attributed to the fact that for random pyramids the scattering takes place in the Si itself while in case of the PDR the light first has to re-enter the Si absorber once it has been scattered within the PDR. The Si nanopowder PDR outperforms previous type-I PDRs that are based on TiO_2 pigments.

We apply the PDR on solar cell precursor samples with POLO junctions and find that the inferior optical performance of the PDR versus random pyramids is compensated by a smaller recombination rate. Overall, this results in a quality factor of the PDR light trapping scheme that exceeds the sample with no light trapping scheme by $(2.7 \pm 0.7)\ \%_{\text{rel}}$. For the pyramidal light trapping scheme, this value amounts to $(1.2 \pm 0.8)\ \%_{\text{rel}}$. The usefulness of the PDR, however, critically depends on the advantage of POLO junctions in passivating (100) surfaces over (111) surfaces

We eventually validate the performance of the PDR on solar cell level by applying it to the rear side of POLO-IBC cells that have a planar front side. The PDR is active on the unmetallized region only, as we deposit it on the finished cell. We find that the gain in short-circuit current density correlates well with the value we expected from the absorptance measurements on the test samples. The PDR even increases the fill factor, which in combination with the short-circuit current density leads to an improvement of the efficiency by $2.9\ \%_{\text{rel}}$ for an unmetallized fraction of $56\ \%$. The best cell efficiency with a PDR is $22.2\ \%$. The positive effect of the PDR on the fill factor may thus even result in an efficiency gain for cells with POLO junctions that already have a light trapping scheme, e.g. a textured front side.

Part 3: Chapter 8

In the last part of the thesis we re-calculate the limiting efficiency of silicon solar cells with Lambertian light trapping by using the accurate expression for the absorptance. This leads to an increase by $0.13\%_{\text{abs}}$ of the previously valid limit to the new limit of 29.56% for an intrinsic Si wafer of thickness $98.1\ \mu\text{m}$.

Appendix A

Clear sky insolation on a collecting surface

The formulas in this appendix can be found in Chapter 7 of Ref. [148]. The aim is to give a general expression for the direct beam insolation on a collecting surface, e.g. a solar cell. This expression is used for the calculation of the data in Fig. 6.9.

A.1 Sun's position

We start with the description of the sun's position at the sky at any time of the day, which is described by the hour angle H , for any day of the year, which alters the declination angle δ , and for an observer at any latitude L on the Earth.

Figure A.1 a) defines the altitude of the sun at noon β_N for an observer at a latitude L . The altitude is the angle between the sun and the local horizon. At noon, the altitude relates to the latitude of the observer on earth and the declination angle by

$$\beta_N = 90^\circ - (L - \delta) \quad . \quad (\text{A.1})$$

The declination δ is defined as the angle formed between the equator plane and a line drawn from the center of the earth and the sun. However, as the radius of the earth is small compared to the distance to the sun, we take the angle between the equator plane and the line between the center of the sun and position of the observer on the earth's surface as δ . The declination varies between the extremes of $\pm 23.45^\circ$ and can be written as

$$\delta = 23.45^\circ \sin \left(\frac{360}{365} (n - 1) \right), \quad (\text{A.2})$$

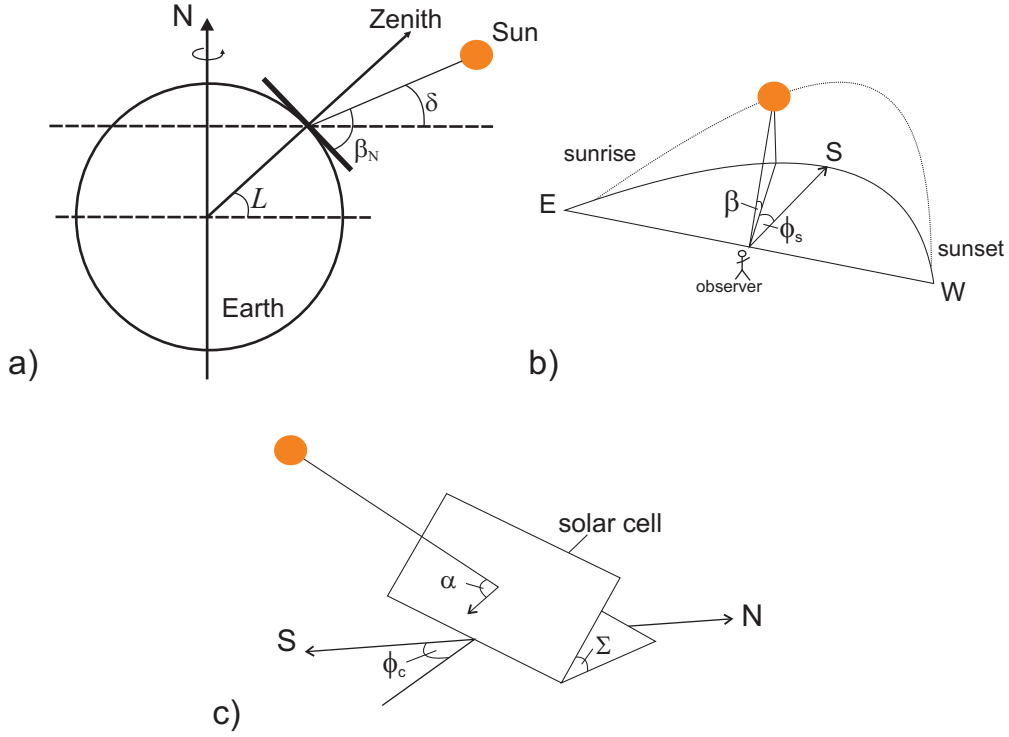


Figure A.1: The figure defines a) the angles to determine the sun's altitude at noon β_N for an observer at latitude L , accounting for the declination δ of the earth's axis, b) the angles ϕ_s and β that determine the sun's position for an observer during the day, and c) the angles for light that is incident under an angle α on a solar cell that is tilted by Σ with respect to the earth's surface and by ϕ_c with respect to the North-South axis.

where n symbolizes the day of the year and thus varies between 1 and 365.

Figure A.1 b) defines the sun's position during the day by the azimuth angle ϕ_s and the altitude angle $\beta \leq \beta_N$. They depend on the latitude, the day number and on the time of day. We account for the time of day by the hour angle H which is defined as

$$H = \left(\frac{15^\circ}{\text{hour}} \right) (\text{hours before solar noon}) \quad . \quad (\text{A.3})$$

At 11 a.m., the hour angle is thus $H = +15^\circ$ and at 2 p.m. $H = -30^\circ$. The sun's position angles are given by

$$\sin \beta = \cos L \cos \delta \cos H + \sin L \sin \delta \quad (\text{A.4})$$

$$\sin \phi_s = \frac{\cos \delta \cos H}{\cos \beta} \quad (\text{A.5})$$

Figure A.2 b) illustrates the azimuth ϕ_s and the altitude β above the horizon, for Hamelin at a latitude L of 52.1° N. The sun is above the horizon for positive values of β .

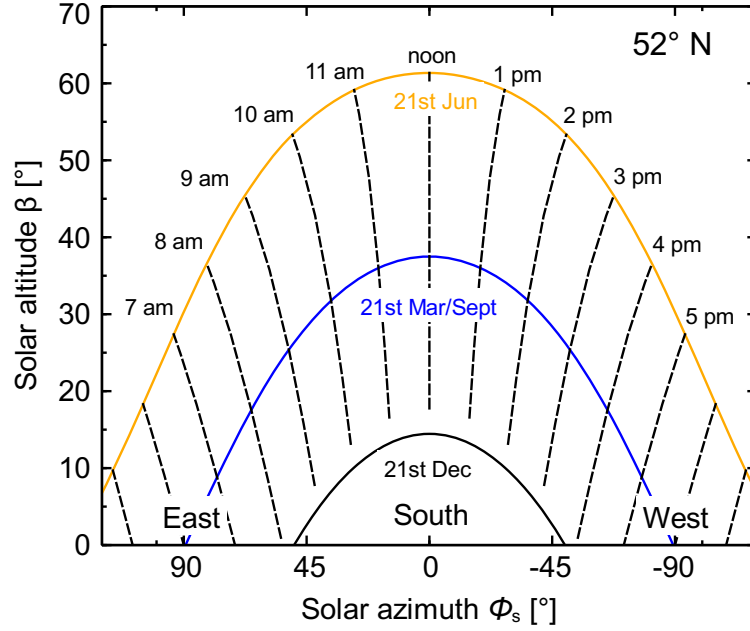


Figure A.2: The figure shows the sun's position in Hamelin ($L = 52^\circ$ N) at different times during the day and year.

A.2 Insolation in dependence of air mass and tilt of solar cell

The clear sky direct beam radiation onto the solar cell in Fig. A.1 c) that is tilted by an angle Σ and forms an azimuth angle of ϕ_c with the south-north axis can be written as

$$I_{BC} = I_B \cos \alpha \quad , \quad (\text{A.6})$$

where I_B is the insolation in W/m^2 normally incident on the earth's surface and α is the angle of incidence on the solar cell. α can be calculated by

$$\cos \alpha = \cos \beta \cos (\phi_s - \phi_c) \sin \Sigma + \sin \beta \cos \Sigma \quad . \quad (\text{A.7})$$

We account for the air mass ratio $m = 1/\sin \beta$ that attenuates the insolation according to

$$I_B = A \exp(-km) \quad . \quad (\text{A.8})$$

A symbolizes the apparent extraterrestrial insolation and k is a dimensionless factor. Empirical expressions for both are

$$A = 1160 + 75 \sin \left(\frac{360}{365} (n - 275) \right) \quad (\text{A.9})$$

$$k = 0.174 + 0.035 \sin \left(\frac{360}{365} (n - 100) \right) \quad (\text{A.10})$$

with n again being the number of the day.

Appendix B

Etching parameters for macropore samples

Table B.1 lists the etching parameters of the macropore samples in Chs. 2, 4 and 5. We use shiny-etched *n*-type Czochralski (Cz) Si wafers that have a resistivity of $(1.5 \pm 0.3) \Omega\text{cm}$ and a thickness of $(305 \pm 5) \mu\text{m}$. For the blind hole samples in Ch. 6 we use a different material. This is both side polished *n*-type float-zone (FZ) Si wafers that have a resistivity of $(3 \pm 2) \Omega\text{cm}$ and a thickness of $(280 \pm 20) \mu\text{m}$. However, the samples from Ch. 6 are described therein. All samples have a phosphorous diffusion at the rear side with a sheet resistance of 10Ω and are etched with the etching setup ELYPOR-3 described in Ch. 3. The etch modes are abbreviated: "curr.", "volt." and "illu." stand for current, voltage and illumination mode, respectively. The electrolyte, in addition to HF, contains 7.5 vol.% acetic acid for all samples. The samples have a planar front side, if the pitch is not specified (–). The illumination intensity rises linearly with the voltage applied to the LED array. A calibration via a photodiode yields that 1 V corresponds to an illumination intensity of $8.6 \text{ mW}/\text{cm}^2$.

Table B.1: The table shows a list of the porosified samples in Chs. 2, 4 and 5.

sample	etch mode	HF conc. [wt%]	temp. [°C]	pitch [μm]	Current $J(t)$ [$\text{mA}/\text{cm}^2(\text{min})$]	Voltage $U(t)$ [V(min)]	Illumination $I(t)$ [V(min)]
Fig. 2.15							
1	curr.	1.5	20	–		-1 to 4 (0.5)	0 (0.5)
2	curr.	1.5	20	–		-1 to 4 (0.5)	1 (0.5)
3	curr.	1.5	20	–		-1 to 4 (0.5)	5 (0.5)
4	curr.	1.5	20	–		-1 to 4 (0.5)	8 (0.5)
Tab. 4.1							
5	curr.	1	10.9	–			-1 to 1.5 to -1 (1)
			12.0				
			14.0				
			16.0				
			18.0				
5 (1)							

			20.1				
			21.9				
			24.1				
			18.0				
			18.9				
			20.1				
6	curr.	2	21.1	–		-1 to 1.5 to -1 (1)	5 (1)
			22.0				
			23.0				
			24.0				
			11.6				
			12.1				
			14.0				
			16.1				
7	curr.	3	18.1	–		-1 to 1.5 to -1 (1)	5 (1)
			20.0				
			22.0				
			24.0				
			14.2				
			15.0				
			14.0				
			16.0				
8	curr.	3.5	17.0	–		-1 to 1.5 to -1 (1)	8 (1)
			18.0				
			19.0				
			20.0				
			10.1				
			12.0				
			16.2				
9	curr.	4	18.0	–		-1 to 1.5 to -1 (1)	5 (1)
							8 (1)
Fig. 4.1							
10	illu.	3.5	20	–	8 (45)	0.5 (45)	
Fig. 4.2							
11	illu.	3.5	20	5	8 (45)	0.5 (45)	
12	illu.	3.5	20	6	8 (60)	0.5 (60)	
13	illu.	3.5	20	9	8 (60)	0.5 (60)	
14	illu.	3.5	20	11	8 (60)	0.5 (60)	
Figs. 4.3, 4.4 and 4.5							
15	illu.	3.5	20	6	4 (40)	0.7 (40)	
16	illu.	3.5	20	7	6 (40)	0.7 (40)	
17	illu.	3.5	20	6	8 (40)	0.7 (40)	
18	illu.	3.5	20	7	10 (40)	0.7 (40)	
19	illu.	3.5	20	6	12 (40)	0.7 (40)	
20	illu.	3.5	20	6	16 (40)	0.85 (40)	
Fig. 4.5							
21	illu.	3.5	20	6	0.5 (120)	0.5 (120)	
22	illu.	3.5	20	6	2 (30)	0.5 (30)	
23	illu.	3.5	20	6	7 (30)	0.5 (30)	
24	illu.	3.5	20	6	9 (30)	1 (30)	
25	illu.	3.5	20	6	14 (30)	2 (30)	
26	illu.	3.5	20	6	18.6 (30)	2 (30)	
Fig. 4.7							
27	volt.	3	20	7	8 (45)		3 (45)
28	illu.	3	20	7	8 (45)	-0.2 (45)	
29	illu.	3	20	7	8 (45)	0.0 (45)	

30	illu.	3	20	7	8 (45)	0.5 (45)	
31	illu.	3	20	7	8 (45)	1 (45)	
Fig. 4.8							
32	illu.	3	20	7	: 8 (5) 15(0.25)	0.38 (5) 0.38 (0.25) :	
repeated 100×							
Fig. 5.3							
33	illu.	3	20	8	8 (30) 8-20 (10) 20 (2) 20-8 (3) 8 (10)	0.5 (30) 0.5-1.2 (10) 1.2 (2) 1.2-0.5 (3) 0.5 (10)	
Fig. 5.4							
34	illu. volt. volt.	3	20	8	8 (40) 8-16 (5) 16 (5)	0.4 (40)	3.5 (10)
35	illu. volt. volt. volt.	3	20	8	8 (40) 8-16 (5) 16 (8) 16-8 (5)	0.4 (40)	3.5 (18)
36	illu. volt. volt. volt. volt.	3	20	8	8 (40) 8-16 (5) 16 (8) 16-8 (5) 8 (10)	0.4 (40)	3.5 (18) 1.2 (10)
Fig. 5.6							
37	illu. volt. volt. volt. volt. illu. volt. volt. volt. volt. illu. volt. volt. volt. volt. illu. volt. volt. volt. volt. volt.	3	20	6	7 (29.5) 7-16.3 (5) 16.3 (7.5) 16.3-7 (5) 0 (0.3) 6.5 (10) 6.5 (22) 6.5-15 (5) 15 (8) 15-6.5 (5) 0 (0.3) 6 (10) 6 (25) 6-13.9 (5) 13.9 (8.7) 13.9-6 (5) 0 (0.3) 5.6 (10) 5.6 (27.5) 5.6-13 (5) 13 (9.4) 13-5.6 (5) 0 (0.3) 5.2 (10)	0.5 (29.5) 0.5 (22) 0.5 (25) 0.5 (27.5)	3.5 (17.5) 0 (0.3) 1.2 (10) 3.5 (18) 0 (0.3) 1.2 (10) 3.5 (18.7) 0 (0.3) 1.2 (10) 3.5 (19.4) 0 (0.3) 1.2 (10)
Fig. 5.8							
38	illu. volt. volt. volt.	3	20	5	6.5 (60) 6.5-16 (3) 16 (8) 16-6.5 (5)	0.6 (60)	3 (16)

volt.				6.5 (10)		0.85 (10)
illu.				6.5 (50)	recondition surface 0.6 (50) commence from step 2	

Bibliography

- [1] Website der Bundesregierung, abgerufen am 21.03.2018.
- [2] Website des Bundeswirtschaftsministeriums, abgerufen am 21.03.2018.
- [3] Fraunhofer ISE, “Energy charts,” abgerufen am 21.03.2018.
- [4] International Technology Roadmap for Photovoltaic ITRPV, “2016 results”, 2016.
- [5] A. Richter, M. Hermle, and S. W. Glunz, “Reassessment of the limiting efficiency for crystalline silicon solar cells,” *IEEE Journal of Photovoltaics*, vol. 3, no. 4, pp. 1184–1191, 2013.
- [6] M. Bruel, B. Aspar, and A.-J. Auberton-Hervé, “Smart-cut: a new silicon on insulator material technology based on hydrogen implantation and wafer bonding,” *Japanese Journal of Applied Physics*, vol. 36, no. 3S, p. 1636, 1997.
- [7] F. Henley, A. Lamm, S. Kang, Z. Liu, and L. Tian, “Direct film transfer (dft) technology for kerf-free silicon wafering.” *Proceedings of the 23rd European Photovoltaic Solar Energy Conference*, pp. 1090–1093, 2008.
- [8] F. Dross, J. Robbelein, B. Vandeveld, E. van Kerschaver, I. Gordon, G. Beaucarne, and J. Poortmans, “Stress-induced large-area lift-off of crystalline Si films,” *Applied Physics A: Materials Science & Processing*, vol. 89, no. 1, 2007.
- [9] J. Hensen, R. Niepelt, S. Kajari-Schröder, and R. Brendel, “Directional heating and cooling for controlled spalling,” *IEEE Journal of Photovoltaics*, vol. 5, no. 1, pp. 195–201, 2015.
- [10] K. J. Weber, A. W. Blakers, M. J. Stocks, and P. J. Verlinden, “Thin silicon cells using novel lase process.” *Proceedings of the 3rd World Conference on Photovoltaic Energy Conversion*, pp. 1262–1264, 2003.
- [11] V. Lehmann, W. Hönlein, R. Stengl, J. Willer, and H. Wendt, “Verfahren zur Herstellung einer Solarzelle aus einer Substratscheibe,” *German patent DE4204455C1*, 1992.

- [12] R. Brendel and M. Ernst, "Macroporous Si as an absorber for thin-film solar cells," *physica status solidi (RRL) - Rapid Research Letters*, vol. 4, no. 1-2, pp. 40–42, 2010.
- [13] M. Ernst and R. Brendel, "Lambertian light trapping in thin crystalline macroporous Si layers," *physica status solidi (RRL)-Rapid Research Letters*, vol. 8, no. 3, pp. 235–238, 2014.
- [14] M. A. Green, Y. Hishikawa, W. Warta, E. D. Dunlop, D. H. Levi, J. Hohl-Ebinger, and A. W. H. Ho-Baillie, "Solar cell efficiency tables (version 50)," *Progress in Photovoltaics: Research and Applications*, vol. 25, no. 7, pp. 668–676, 2017.
- [15] K. Yoshikawa, H. Kawasaki, W. Yoshida, T. Irie, K. Konishi, K. Nakano, T. Uto, D. Adachi, M. Kanematsu, and H. Uzu, "Silicon heterojunction solar cell with interdigitated back contacts for a photoconversion efficiency over 26%," *Nature Energy*, vol. 2, p. 17032, 2017.
- [16] W. Shockley and H. J. Queisser, "Detailed balance limit of efficiency of p–n junction solar cells," *Journal of Applied Physics*, vol. 32, no. 3, pp. 510–519, 1961.
- [17] F. Dimroth, T. Roesener, S. Essig, C. Weuffen, A. Wekkeli, E. Oliva, G. Siefert, K. Volz, T. Hannappel, and D. Häussler, "Comparison of direct growth and wafer bonding for the fabrication of GaInP/GaAs dual-junction solar cells on silicon," *IEEE Journal of Photovoltaics*, vol. 4, no. 2, pp. 620–625, 2014.
- [18] J. P. Mailoa, C. D. Bailie, E. C. Johlin, E. T. Hoke, A. J. Akey, W. H. Nguyen, M. D. McGehee, and T. Buonassisi, "A 2-terminal perovskite/silicon multijunction solar cell enabled by a silicon tunnel junction," *Applied Physics Letters*, vol. 106, no. 12, p. 121105, 2015.
- [19] S. Essig, J. Benick, M. Schachtner, A. Wekkeli, M. Hermle, and F. Dimroth, "Wafer-bonded GaInP/GaAs/Si solar cells with 30% efficiency under concentrated sunlight," *IEEE Journal of Photovoltaics*, vol. 5, no. 3, pp. 977–981, 2015.
- [20] Website des ISFH, "26.1% record efficiency for p-type crystalline Si solar cells.", abgerufen am 05.03.2018.
- [21] International Electrotechnical Commission, "Standard IEC 60904-3: photovoltaic devices," *Part 3: Measurement Principles for Terrestrial Photovoltaic (PV) Solar Devices With Reference Spectral Irradiance Data*, 1987.
- [22] C. Schinke, P. C. Peest, J. Schmidt, R. Brendel, K. Bothe, M. R. Vogt, I. Kröger, S. Winter, A. Schirmacher, and S. Lim, "Uncertainty analysis for the coefficient

- of band-to-band absorption of crystalline silicon,” *AIP Advances*, vol. 5, no. 6, p. 067168, 2015.
- [23] R. Brendel, *Thin-film crystalline silicon solar cells: physics and technology*. John Wiley & Sons, 2011.
- [24] H. Holst, M. Winter, M. R. Vogt, K. Bothe, M. Köntges, R. Brendel, and P. P. Altermatt, “Application of a new ray tracing framework to the analysis of extended regions in Si solar cell modules,” *Energy Procedia*, vol. 38, pp. 86–93, 2013.
- [25] H. K. Raut, V. A. Ganesh, A. S. Nair, and S. Ramakrishna, “Anti-reflective coatings: A critical, in-depth review,” *Energy & Environmental Science*, vol. 4, no. 10, pp. 3779–3804, 2011.
- [26] S. Chattopadhyay, Y. F. Huang, Y.-J. Jen, A. Ganguly, K. H. Chen, and L. C. Chen, “Anti-reflecting and photonic nanostructures,” *Materials Science and Engineering: R: Reports*, vol. 69, no. 1, pp. 1–35, 2010.
- [27] A. Ingenito, S. L. Luxembourg, P. Spinelli, J. Liu, J. C. O. Lizcano, A. W. Weber, O. Isabella, and M. Zeman, “Optimized metal-free back reflectors for high-efficiency open rear c-Si solar cells,” *IEEE Journal of Photovoltaics*, vol. 6, no. 1, pp. 34–40, 2016.
- [28] S.-K. Kim, H.-S. Ee, W. Choi, S.-H. Kwon, J.-H. Kang, Y.-H. Kim, H. Kwon, and H.-G. Park, “Surface-plasmon-induced light absorption on a rough silver surface,” *Applied Physics Letters*, vol. 98, no. 1, p. 011109, 2011.
- [29] H. A. Atwater and A. Polman, “Plasmonics for improved photovoltaic devices,” *Nature materials*, vol. 9, no. 3, pp. 205–213, 2010.
- [30] E. Hecht, “Optics,” *4th Edition, Addison Wesley Longman Inc, 1998*, 1998.
- [31] D. Kray, M. Hermle, and S. W. Glunz, “Theory and experiments on the back side reflectance of silicon wafer solar cells,” *Progress in Photovoltaics: Research and Applications*, vol. 16, no. 1, pp. 1–15, 2008.
- [32] K. O. Davis, K. Jiang, C. Demberger, H. Zunft, H. Haverkamp, D. Habermann, and W. V. Schoenfeld, “Investigation of the internal back reflectance of rear-side dielectric stacks for c-Si solar cells,” *IEEE Journal of Photovoltaics*, vol. 3, no. 2, pp. 641–648, 2013.
- [33] H. Cui, P. R. Campbell, and M. A. Green, “Optimisation of the back surface reflector for textured polycrystalline Si thin film solar cells,” *PV Asia Pacific Conference 2012*, vol. 33, pp. 118–128, 2013.

- [34] S. C. Baker-Finch, K. R. McIntosh, Di Yan, K. C. Fong, and T. C. Kho, "Near-infrared free carrier absorption in heavily doped silicon," *Journal of Applied Physics*, vol. 116, no. 6, p. 063106, 2014.
- [35] D.-H. Neuhaus and A. Münzer, "Industrial silicon wafer solar cells," *Advances in OptoElectronics*, vol. 2007, 2008.
- [36] J. Zhao, A. Wang, P. Altermatt, and M. A. Green, "Twenty-four percent efficient silicon solar cells with double layer antireflection coatings and reduced resistance loss," *Applied Physics Letters*, vol. 66, no. 26, pp. 3636–3638, 1995.
- [37] X. G. Zhang, *Electrochemistry of Silicon and Its Oxide*. Boston, MA: Kluwer Academic Publishers, 2004.
- [38] K. R. McIntosh, T. C. Kho, K. C. Fong, S. C. Baker-Finch, Y. Wan, N. Zin, E. T. Franklin, D. Wang, M. D. Abbott, and N. E. Grant, "Quantifying the optical losses in back-contact solar cells." *Proceedings of the 40th Photovoltaic Specialist Conference*, pp. 115–123, 2014.
- [39] R. Brendel, "Sunrays: a versatile ray tracing program for the photovoltaic community," *Proceedings of the 12th European Photovoltaic Solar Energy Conference*, pp. 1339–1342, 1994.
- [40] F. Pfeffer, J. Eisenlohr, A. Basch, M. Hermle, B. G. Lee, and J. C. Goldschmidt, "Systematic analysis of diffuse rear reflectors for enhanced light trapping in silicon solar cells," *Solar Energy Materials and Solar Cells*, vol. 152, pp. 80–86, 2016.
- [41] M. A. Green, *Solar cells: operating principles, technology, and system applications*. Univ. New South Wales, 1992.
- [42] H. A. Macleod, *Thin-film optical filters*. CRC press, 2017.
- [43] R. Brendel and D. Scholten, "Modeling light trapping and electronic transport of waffle-shaped crystalline thin-film Si solar cells," *Applied Physics A*, vol. 69, no. 2, pp. 201–213, 1999.
- [44] J. H. Lambert, "Photometria sive de mensura et gradibus luminis, colorum et umbrae: Augsburg, 1760. anding e, lamberts photometry," *Klassiker der exakten Wissenschaften. Leipzig, Germany: Verlag Wilhelm Engelman*, pp. 31–33, 1892.
- [45] A. Goetzberger, "Optical confinement in thin Si-solar cells by diffuse back reflectors," *Proceedings of the 15th Photovoltaic Specialists Conference*, pp. 867–870, 1981.

- [46] E. Yablonovitch and G. Cody, "Intensity enhancement in textured optical sheets for solar cells," *IEEE Transactions on Electron Devices*, vol. 29, no. 2, pp. 300–305, 1982.
- [47] E. Yablonovitch, "Statistical ray optics," *JOSA*, vol. 72, no. 7, pp. 899–907, 1982.
- [48] A. Luque and G. L. Araújo, *Solar cells and optics for photovoltaic concentration*. Bristol: Adam Hilger, 1989.
- [49] R. Brendel, "Review of layer transfer processes for crystalline thin film silicon solar cells," *Japanese Journal of Applied Physics*, vol. 40, pp. 4431–4439, 2001.
- [50] M. A. Green, "Lambertian light trapping in textured solar cells and light-emitting diodes: analytical solutions," *Progress in Photovoltaics: Research and Applications*, vol. 10, no. 4, pp. 235–241, 2002.
- [51] M. Abramowitz and I. A. Stegun, *Handbook of mathematical functions*. New York: Dover Publications, 1970.
- [52] P. Campbell and M. A. Green, "Light trapping properties of pyramidally textured surfaces," *Journal of Applied Physics*, vol. 62, no. 1, pp. 243–249, 1987.
- [53] J. C. Miñano, "Optical confinement in photovoltaics," in *Physical Limitations to Photovoltaic Energy Conversion*, Adam Hilger, Bristol, 1990, pp. 50–83.
- [54] A. Höpe and K.-O. Hauer, "Three-dimensional appearance characterization of diffuse standard reflection materials," *Metrologia*, vol. 47, no. 3, p. 295, 2010.
- [55] C. Battaglia, C.-M. Hsu, K. Söderström, J. Escarré, F.-J. Haug, M. Charrière, M. Boccard, M. Despeisse, D. T. L. Alexander, M. Cantoni, Y. Cui, and C. Ballif, "Light trapping in solar cells: Can periodic beat random?," *ACS Nano*, vol. 6, no. 3, pp. 2790–2797, 2012.
- [56] P. Campbell and M. A. Green, "The limiting efficiency of silicon solar cells under concentrated sunlight," *IEEE Transactions on Electron Devices*, vol. 33, no. 2, pp. 234–239, 1986.
- [57] R. Winston and W. T. Welford, "The optics of non-imaging concentrators," 1978.
- [58] A. Luque and G. L. Araújo, eds., *Physical Limitations to Photovoltaic Energy Conversion*. Bristol: Adam Hilger, 1990.
- [59] M. Winter, H. Holst, Vogt, and P. P. Altermatt, "Impact of realistic illumination on optical losses in si solar cell modules compared to standard testing conditions," *Proceedings of the 31st European Photovoltaic Solar Energy Conference*, pp. 1869–1874, 2015.

- [60] S. Mokkaapati and K. R. Catchpole, “Nanophotonic light trapping in solar cells,” *Journal of Applied Physics*, vol. 112, no. 10, p. 101101, 2012.
- [61] Z. Yu, A. Raman, and S. Fan, “Fundamental limit of light trapping in grating structures,” *Optics Express*, vol. 18, no. 103, pp. A366–A380, 2010.
- [62] P. Wang and I. M. Peters, “Impact of structure symmetry on light trapping properties of periodic nanostructures: A systematic discussion and quantification,” *Journal of Applied Physics*, vol. 119, no. 8, p. 083101, 2016.
- [63] S. Eyderman, S. John, M. Hafez, S. S. Al-Ameer, T. S. Al-Harby, Y. Al-Hadeethi, and D. M. Bouwes, “Light-trapping optimization in wet-etched silicon photonic crystal solar cells,” *Journal of Applied Physics*, vol. 118, no. 2, p. 023103, 2015.
- [64] R. A. Sinton and A. Cuevas, “Contactless determination of current–voltage characteristics and minority–carrier lifetimes in semiconductors from quasi–steady–state photoconductance data,” *Applied Physics Letters*, vol. 69, no. 17, pp. 2510–2512, 1996.
- [65] M. A. Green, “Accuracy of analytical expressions for solar cell fill factors,” *Solar cells*, vol. 7, no. 3, pp. 337–340, 1982.
- [66] M. A. Green and M. J. Keevers, “Optical properties of intrinsic silicon at 300 K,” *Progress in Photovoltaics: Research and Applications*, vol. 3, no. 3, pp. 189–192, 1995.
- [67] K. S. W. Sing, “Reporting physisorption data for gas/solid systems with special reference to the determination of surface area and porosity (recommendations 1984),” *Pure and applied chemistry*, vol. 57, no. 4, pp. 603–619, 1985.
- [68] V. Lehmann, “Electrochemistry of silicon: instrumentation, science, materials and applications,” *Electrochemistry of Silicon: Instrumentation, Science, Materials and Applications*, Wiley-VCH, 2002.
- [69] H. Föll, M. Christophersen, J. Carstensen, and G. Hasse, “Formation and application of porous silicon,” *Materials Science and Engineering: R: Reports*, vol. 39, no. 4, pp. 93–141, 2002.
- [70] H. Föll, M. Leisner, A. Cojocar, and J. Carstensen, “Macroporous semiconductors,” *Materials*, vol. 3, no. 5, pp. 3006–3076, 2010.
- [71] V. Lehmann and U. Gösele, “Porous silicon formation: A quantum wire effect,” *Applied Physics Letters*, vol. 58, no. 8, pp. 856–858.

- [72] V. Kochergin and H. Föll, *Porous Semiconductors: Optical Properties and Applications*. Engineering Materials and Processes, London: Springer London, 2009.
- [73] V. Lehmann, “The physics of macropore formation in low doped n-type silicon,” *Journal of The Electrochemical Society*, vol. 140, no. 10, pp. 2836–2843, 1993.
- [74] R. L. Smith and S. D. Collins, “Porous silicon formation mechanisms,” *Journal of Applied Physics*, vol. 71, no. 8, pp. R1–R22, 1991.
- [75] H. Gerischer, “Charge transfer processes at semiconductor-electrolyte interfaces in connection with problems of catalysis,” *Surface Science*, vol. 18, no. 1, pp. 97–122, 1969.
- [76] H. Gerischer, “The impact of semiconductors on the concepts of electrochemistry,” *Electrochimica Acta*, vol. 35, no. 11-12, pp. 1677–1699, 1990.
- [77] V. Bertagna, C. Plougonven, F. Rouelle, and M. Chemla, “p-and n-type silicon electrochemical properties in dilute hydrofluoric acid solutions,” *Journal of The Electrochemical Society*, vol. 143, no. 11, pp. 3532–3538, 1996.
- [78] R. L. Smith and S. D. Collins, “Porous silicon formation mechanisms,” *Journal of Applied Physics*, vol. 71, no. 8, pp. R1–R22, 1992.
- [79] I. Ronga, A. Bsiesy, F. Gaspard, R. Herino, M. Ligeon, F. Muller, and A. Hali-maoui, “Electrical characterization of the silicon-electrolyte interface in the conditions of porous silicon formation,” *Journal of The Electrochemical Society*, vol. 138, no. 5, pp. 1403–1407, 1991.
- [80] V. Lehmann and H. Föll, “Formation mechanism and properties of electrochemically etched trenches in n-type silicon,” *Journal of The Electrochemical Society*, vol. 137, no. 2, pp. 653–659, 1990.
- [81] S. Ottow, G. S. Popkurov, and H. Föll, “Determination of flat-band potentials of silicon electrodes in HF by means of AC resistance measurements,” *Journal of Electroanalytical Chemistry*, vol. 455, no. 1–2, pp. 29–37, 1998/9/15.
- [82] M. H. Al Rifai, M. Christophersen, S. Ottow, J. Carstensen, and H. Föll, “Dependence of macropore formation in n-Si on potential, temperature, and doping,” *Journal of The Electrochemical Society*, vol. 147, no. 2, pp. 627–635, 2000.
- [83] V. Lehmann and S. Ronnebeck, “The physics of macropore formation in low-doped p-type silicon,” *Journal of The Electrochemical Society*, vol. 146, no. 8, pp. 2968–2975, 1999.

- [84] X. G. Zhang, "Mechanism of pore formation on n-type silicon," *Journal of The Electrochemical Society*, vol. 138, no. 12, p. 3750, 1991.
- [85] R. Memming and G. Schwandt, "Anodic dissolution of silicon in hydrofluoric acid solutions," *Surface Science*, vol. 4, no. 2, pp. 109–124, 1966/3.
- [86] M. J. Eddowes, "Anodic dissolution of p- and n-type silicon: Kinetic study of the chemical mechanism," *Journal of Electroanalytical Chemistry and Interfacial Electrochemistry*, vol. 280, no. 2, pp. 297–311, 1990/3/9.
- [87] G. Barillaro and F. Pieri, "A self-consistent theoretical model for macropore growth in n-type silicon," *Journal of Applied Physics*, vol. 97, no. 11, p. 116105, 2005.
- [88] R. Penndorf, "Tables of the refractive index for standard air and the rayleigh scattering coefficient for the spectral region between 0.2 and 20.0 μm and their application to atmospheric optics," *JOSA*, vol. 47, no. 2, pp. 176–182, 1957.
- [89] C. Peest, C. Schinke, R. Brendel, J. Schmidt, and K. Bothe, "Instrumentation-related uncertainty of reflectance and transmittance measurements with a two-channel spectrophotometer," *Review of Scientific Instruments*, vol. 88, no. 1, p. 015105, 2017.
- [90] P. Würfel, *Physics of solar cells: from principles to new concepts*. John Wiley & Sons, 2008.
- [91] A. Richter, S. W. Glunz, F. Werner, J. Schmidt, and A. Cuevas, "Improved quantitative description of Auger recombination in crystalline silicon," *Physical Review B*, vol. 86, no. 16, p. 165202, 2012.
- [92] W. Shockley and W. T. Read Jr, "Statistics of the recombinations of holes and electrons," *Physical review*, vol. 87, no. 5, p. 835, 1952.
- [93] R. N. Hall, "Electron-hole recombination in germanium," *Physical review*, vol. 87, no. 2, p. 387, 1952.
- [94] A. G. Aberle, S. Glunz, and W. Warta, "Impact of illumination level and oxide parameters on Shockley-Read-Hall recombination at the Si-SiO₂ interface," *Journal of Applied Physics*, vol. 71, no. 9, pp. 4422–4431, 1992.
- [95] J. Schmidt and A. G. Aberle, "Accurate method for the determination of bulk minority-carrier lifetimes of mono-and multicrystalline silicon wafers," *Journal of Applied Physics*, vol. 81, no. 9, pp. 6186–6199, 1997.

- [96] K. L. Luke and L.-J. Cheng, "Analysis of the interaction of a laser pulse with a silicon wafer: Determination of bulk lifetime and surface recombination velocity," *Journal of Applied Physics*, vol. 61, no. 6, pp. 2282–2293, 1987.
- [97] A. B. Sproul, "Dimensionless solution of the equation describing the effect of surface recombination on carrier decay in semiconductors," *Journal of Applied Physics*, vol. 76, no. 5, pp. 2851–2854, 1994.
- [98] D. B. Klaassen, "A unified mobility model for device simulation–i. Model equations and concentration dependence," *Solid-State Electronics*, vol. 35, no. 7, pp. 953–959, 1992.
- [99] M. Bail, J. Kentsch, R. Brendel, and M. Schulz, "Lifetime mapping of Si wafers by an infrared camera [for solar cell production]," *Proceedings of the 28th Photovoltaic Specialists Conference*, pp. 99–103, 2000.
- [100] K. Ramspeck, *Characterization techniques for silicon solar cells and material using an infrared-camera based approach*. Der Andere Verlag, 2009.
- [101] K. Ramspeck, K. Bothe, J. Schmidt, and R. Brendel, "Combined dynamic and steady-state infrared camera based carrier lifetime imaging of silicon wafers," *Journal of Applied Physics*, vol. 106, no. 11, p. 114506, 2009.
- [102] K. Ramspeck, S. Reißerweber, J. Schmidt, K. Bothe, and R. Brendel, "Dynamic carrier lifetime imaging of silicon wafers using an infrared-camera-based approach," *Applied Physics Letters*, vol. 93, no. 10, p. 102104, 2008.
- [103] K. Bothe, *Oxygen-related trapping and recombination centres in boron-doped crystalline silicon*. Dissertation, Leibniz Universität Hannover, Hannover, 2006.
- [104] J. S. Swirhun, R. A. Sinton, M. K. Forsyth, and T. Mankad, "Contactless measurement of minority carrier lifetime in silicon ingots and bricks," *Progress in Photovoltaics: Research and Applications*, vol. 19, no. 3, pp. 313–319, 2011.
- [105] P. P. Altermatt, J. Schmidt, M. Kerr, G. Heiser, and A. G. Aberle, "Exciton-enhanced Auger recombination in crystalline silicon under intermediate and high injection conditions," *Proceedings of the 16th European Photovoltaic Solar Energy Conference*, pp. 243–246, 2000.
- [106] M. Ernst, *Macroporous silicon for crystalline thin-film solar cells*. Dissertation, Leibniz Universität Hannover, Hannover, Dezember 2013.
- [107] W. Kern, "The evolution of silicon wafer cleaning technology," *Journal of The Electrochemical Society*, vol. 137, no. 6, pp. 1887–1892, 1990.

- [108] A. S. Glassner, *An introduction to ray tracing*. Elsevier, 1989.
- [109] J. E. A. M. van den Meerakker, R. J. G. Elfrink, F. Roozeboom, and J. F. C. M. Verhoeven, “Etching of deep macropores in 6 in. Si wafers,” *Journal of The Electrochemical Society*, vol. 147, no. 7, p. 2757, 2000.
- [110] A. E. Gershinskii and L. V. Mironova, “Behavior of silicon in aqueous HF solutions,” *Soviet Electrochemistry*, vol. 25, no. 10, pp. 1224–1230, 1989.
- [111] C. Serre. Dissertation, Universite Joseph Fourier, Grenoble, 1992.
- [112] J. E. A. M. van den Meerakker and M. R. L. Mellier, “Kinetic and diffusional aspects of the dissolution of Si in HF solutions,” *Journal of The Electrochemical Society*, vol. 148, no. 3, p. G166, 2001.
- [113] D. J. Monk, “Hydrofluoric acid etching of silicon dioxide sacrificial layers,” *Journal of The Electrochemical Society*, vol. 141, no. 1, p. 264, 1994.
- [114] M. Ernst and R. Brendel, “Macroporous silicon solar cells with an epitaxial emitter,” *IEEE Journal of Photovoltaics*, vol. 3, no. 2, pp. 723–729, 2013.
- [115] M. Ernst, H. Schulte-Huxel, R. Niepelt, S. Kajari-Schröder, and R. Brendel, “Thin crystalline macroporous silicon solar cells with ion implanted emitter,” *Energy Procedia*, vol. 38, pp. 910–918, 2013.
- [116] S. Schäfer, M. Ernst, S. Kajari-Schröder, and R. Brendel, “Multilayer etching for kerf-free solar cells from macroporous silicon,” *Energy Procedia*, vol. 38, pp. 933–941, 2013.
- [117] T. Geppert, S. Schweizer, U. Gösele, and R. Wehrspohn, “Deep trench etching in macroporous silicon,” *Applied Physics A*, vol. 84, no. 3, pp. 237–242, 2006.
- [118] V. Lehmann and U. Grüning, “The limits of macropore array fabrication,” *Thin Solid Films*, vol. 297, no. 1-2, pp. 13–17, 1997.
- [119] S. Matthias, F. Müller, J. Schilling, and U. Gösele, “Pushing the limits of macroporous silicon etching,” *Applied Physics A*, vol. 80, no. 7, pp. 1391–1396, 2005.
- [120] D. Hernandez, T. Trifonov, M. Garin, and R. Alcubilla, “Silicon millefeuille: From a silicon wafer to multiple thin crystalline films in a single step,” *Applied Physics Letters*, vol. 102, no. 17, pp. 172102–172102–4, 2013.
- [121] T. Trifonov, M. Garín, A. Rodríguez, L. F. Marsal, and R. Alcubilla, “Tuning the shape of macroporous silicon,” *physica status solidi (a)*, vol. 204, no. 10, pp. 3237–3242, 2007.

- [122] E. Quiroga-González, E. Ossei-Wusu, J. Carstensen, and H. Föll, “How to make optimized arrays of Si wires suitable as superior anode for Li-ion batteries,” *Journal of The Electrochemical Society*, vol. 158, no. 11, pp. E119–E123, 2011.
- [123] M. Garin, D. Hernandez, T. Trifonov, D. Cardador, and R. Alcubilla, “Single-step multiple-layers wafer slicing from macroporous silicon,” *Proceedings of the 28th European Photovoltaic Solar Energy Conference*, pp. 933–936, 2013.
- [124] R. Brendel, T. Dullweber, R. Gogolin, H. Hannebauer, N. P. Harder, J. Hensen, S. Kajari-Schroeder, R. Peibst, J. H. Petermann, and U. Römer, “Recent progress and options for future crystalline silicon solar cells,” in *Proceedings of the 28th European Photovoltaic Solar Energy Conference*, pp. 676–690, 2013.
- [125] P. Papet, O. Nichiporuk, A. Kaminski, Y. Rozier, J. Kraiem, J.-F. Lelievre, A. Chaumartin, A. Fave, and M. Lemiti, “Pyramidal texturing of silicon solar cell with TMAH chemical anisotropic etching,” *Solar Energy Materials and Solar Cells*, vol. 90, no. 15, pp. 2319–2328, 2006.
- [126] S. Dutttagupta, F. Ma, B. Hoex, T. Mueller, and A. G. Aberle, “Optimised antireflection coatings using silicon nitride on textured silicon surfaces based on measurements and multidimensional modelling,” *Energy Procedia*, vol. 15, pp. 78–83, 2012.
- [127] S. C. Baker-Finch and K. R. McIntosh, “Reflection distributions of textured monocrystalline silicon: implications for silicon solar cells,” *Progress in Photovoltaics: Research and Applications*, vol. 21, no. 5, pp. 960–971, 2013.
- [128] X. Liu, P. R. Coxon, M. Peters, B. Hoex, J. M. Cole, and D. J. Fray, “Black silicon: fabrication methods, properties and solar energy applications,” *Energy & Environmental Science*, vol. 7, no. 10, pp. 3223–3263, 2014.
- [129] M. Otto, M. Algasinger, H. Branz, B. Gesemann, T. Gimpel, K. Fuchsler, T. Käsebier, S. Kontermann, S. Koynov, and X. Li, “Black silicon photovoltaics,” *Advanced Optical Materials*, vol. 3, no. 2, pp. 147–164, 2015.
- [130] H. Savin, P. Repo, G. von Gastrow, P. Ortega, E. Calle, M. Garín, and R. Alcubilla, “Black silicon solar cells with interdigitated back-contacts achieve 22.1% efficiency,” *Nature nanotechnology*, vol. 10, pp. 624–628, 2015.
- [131] P. Repo, J. Benick, V. Vähänissi, J. Schön, G. von Gastrow, B. Steinhauser, M. C. Schubert, M. Hermle, and H. Savin, “N-type black silicon solar cells,” *Energy Procedia*, vol. 38, pp. 866–871, 2013.

- [132] G. von Gastrow, R. Alcubilla, P. Ortega, M. Yli-Koski, S. Conesa-Boj, A. F. i Morral, and H. Savin, "Analysis of the atomic layer deposited Al_2O_3 field-effect passivation in black silicon," *Solar Energy Materials and Solar Cells*, vol. 142, pp. 29–33, 2015.
- [133] C. Barugkin, T. Allen, T. K. Chong, T. P. White, K. J. Weber, and K. R. Catchpole, "Light trapping efficiency comparison of Si solar cell textures using spectral photoluminescence," *Optics Express*, vol. 23, no. 7, pp. A391–A400, 2015.
- [134] A. Ingenito, O. Isabella, and M. Zeman, "Nano-cones on micro-pyramids: modulated surface textures for maximal spectral response and high-efficiency solar cells," *Progress in Photovoltaics: Research and Applications*, vol. 23, no. 11, pp. 1649–1659, 2015.
- [135] A. Ingenito, O. Isabella, and M. Zeman, "Experimental demonstration of $4n^2$ classical absorption limit in nanotextured ultrathin solar cells with dielectric omnidirectional back reflector," *ACS Photonics*, vol. 1, no. 3, pp. 270–278, 2014.
- [136] X. Ao, X. Tong, D. S. Kim, L. Zhang, M. Knez, F. Müller, S. He, and V. Schmidt, "Black silicon with controllable macropore array for enhanced photoelectrochemical performance," *Applied Physics Letters*, vol. 101, no. 11, p. 111901, 2012.
- [137] W. Huang, Y. Xue, X. Wang, and X. Ao, "Black silicon film with modulated macropores for thin-silicon photovoltaics," *Optical Materials Express*, vol. 5, no. 6, pp. 1482–1487, 2015.
- [138] V. V. Iyengar, B. K. Nayak, and M. C. Gupta, "Optical properties of silicon light trapping structures for photovoltaics," *Solar Energy Materials and Solar Cells*, vol. 94, no. 12, pp. 2251–2257, 2010.
- [139] C. H. Crouch, J. E. Carey, M. Shen, E. Mazur, and F. Y. Genin, "Infrared absorption by sulfur-doped silicon formed by femtosecond laser irradiation," *Applied Physics A*, vol. 79, no. 7, pp. 1635–1641, 2004.
- [140] S. Schaefer and R. Lüdemann, "Low damage reactive ion etching for photovoltaic applications," *Journal of Vacuum Science & Technology A*, vol. 17, no. 3, pp. 749–754, 1999.
- [141] M. Algasinger, J. Paye, F. Werner, J. Schmidt, M. S. Brandt, M. Stutzmann, and S. Koynov, "Improved black silicon for photovoltaic applications," *Advanced Energy Materials*, vol. 3, no. 8, pp. 1068–1074, 2013.
- [142] H. M. Branz, V. E. Yost, S. Ward, K. M. Jones, B. To, and P. Stradins, "Nanostructured black silicon and the optical reflectance of graded-density surfaces," *Applied Physics Letters*, vol. 94, no. 23, pp. –, 2009.

- [143] M. A. Juntunen, J. Heinonen, V. Vähänissi, P. Repo, D. Valluru, and H. Savin, “Near-unity quantum efficiency of broadband black silicon photodiodes with an induced junction,” *Nature Photonics*, vol. 10, no. 12, pp. 777–781, 2016.
- [144] S. Koynov, M. S. Brandt, and M. Stutzmann, “Black nonreflecting silicon surfaces for solar cells,” *Applied Physics Letters*, vol. 88, no. 20, p. 203107, 2006.
- [145] M. Kroll, M. Otto, T. Käsebier, K. Füchsel, R. Wehrspohn, E.-B. Kley, A. Tünnermann, and T. Pertsch, “Black silicon for solar cell applications,” *Proceedings Photonics for Solar Energy Systems IV*, vol. 8438, p. 843817, 2012.
- [146] Hendrik Holst, *Development and application of a modular ray tracing framework to multi-scale simulations in photovoltaics*. Dissertation, Leibniz Universität Hannover, Hannover, 2015.
- [147] A. Chutinan and S. John, “Light trapping and absorption optimization in certain thin-film photonic crystal architectures,” *Physical Review A*, vol. 78, no. 2, p. 023825, 2008.
- [148] G. M. Masters, *Renewable and efficient electric power systems*. John Wiley & Sons, 2013.
- [149] M. R. Vogt, H. Holst, H. Schulte-Huxel, S. Blankemeyer, R. Witteck, D. Hinken, M. Winter, B. Min, C. Schinke, and I. Ahrens, “Optical constants of UV transparent EVA and the impact on the PV module output power under realistic irradiation,” *Energy Procedia*, vol. 92, pp. 523–530, 2016.
- [150] J. Schmidt, F. Werner, B. Veith, D. Zielke, S. Steingrube, P. P. Altermatt, S. Gatz, T. Dullweber, and R. Brendel, “Advances in the surface passivation of silicon solar cells,” *Energy Procedia*, vol. 15, pp. 30–39, 2012.
- [151] J. Schmidt, B. Veith, and R. Brendel, “Effective surface passivation of crystalline silicon using ultrathin Al_2O_3 films and $\text{Al}_2\text{O}_3/\text{SiN}_x$ stacks,” *physica status solidi (RRL)-Rapid Research Letters*, vol. 3, no. 9, pp. 287–289, 2009.
- [152] B. Veith, T. Ohrdes, F. Werner, R. Brendel, P. P. Altermatt, N.-P. Harder, and J. Schmidt, “Injection dependence of the effective lifetime of n-type Si passivated by Al_2O_3 : An edge effect?,” *Solar Energy Materials and Solar Cells*, vol. 120, pp. 436–440, 2014.
- [153] B. A. Veith-Wolf and J. Schmidt, “Unexpectedly high minority-carrier lifetimes exceeding 20 ms measured on $1.4\text{-}\Omega\text{ cm}$ n-type silicon wafers,” *physica status solidi (RRL)-Rapid Research Letters*, vol. 11, no. 11, 2017.

- [154] P. Repo, A. Haarahiltunen, L. Sainiemi, M. Yli-Koski, H. Talvitie, M. C. Schubert, and H. Savin, "Effective passivation of black silicon surfaces by atomic layer deposition," *IEEE Journal of Photovoltaics*, vol. 3, no. 1, pp. 90–94, 2013.
- [155] A. D. Mallorquí, E. Alarcón-Lladó, I. C. Mundet, A. Kiani, B. Demaurex, S. de Wolf, A. Menzel, M. Zacharias, and A. F. i Morral, "Field-effect passivation on silicon nanowire solar cells," *Nano Research*, vol. 8, no. 2, pp. 673–681, 2015.
- [156] K. Xiong, S. Lu, D. Jiang, J. Dong, and H. Yang, "Effective recombination velocity of textured surfaces," *Applied Physics Letters*, vol. 96, no. 19, p. 193107, 2010.
- [157] B. Hoex, J. J. Gielis, M. C. van de Sanden, and W. M. Kessels, "On the c-Si surface passivation mechanism by the negative-charge-dielectric Al_2O_3 ," *Journal of Applied Physics*, vol. 104, no. 11, p. 113703, 2008.
- [158] F. Werner, B. Veith, D. Zielke, L. Kühnemund, C. Tegenkamp, M. Seibt, R. Brendel, and J. Schmidt, "Electronic and chemical properties of the c-Si/ Al_2O_3 interface," *Journal of Applied Physics*, vol. 109, no. 11, p. 113701, 2011.
- [159] P. A. Basore and D. A. Clugston, "PC1D version 5.9," *University of New South Wales*, 2003.
- [160] K. R. McIntosh and L. E. Black, "On effective surface recombination parameters," *Journal of Applied Physics*, vol. 116, no. 1, p. 014503, 2014.
- [161] F. Werner, *Atomic layer deposition of aluminum oxide on crystalline silicon: Fundamental interface properties and application to solar cells*. Dissertation, Leibniz Universität Hannover, 2013.
- [162] S. M. Sze and K. K. Ng, *Physics of semiconductor devices*. John Wiley & Sons, 2006.
- [163] P. Ortega, E. Calle, G. Gastrow, P. Repo, D. Carrió, H. Savin, and R. Alcubilla, "High-efficiency black silicon interdigitated back contacted solar cells on p-type and n-type c-Si substrates," *Progress in Photovoltaics: Research and Applications*, vol. 23, no. 11, pp. 1448–1457, 2015.
- [164] R. Peibst, Y. Larionova, S. Reiter, M. Turcu, R. Brendel, D. Tetzlaff, J. Krügener, T. Wietler, U. Höhne, and J. D. Kähler, "Implementation of n^+ and p^+ poly junctions on front and rear side of double-side contacted industrial silicon solar cells," *Proceedings of the 32nd European Photovoltaic Solar Energy Conference*, pp. 323–327, 2016.

- [165] J.-Y. Gan and R. M. Swanson, "Polysilicon emitters for silicon concentrator solar cells," *Proceedings of the 21st Photovoltaic Specialists Conference*, pp. 245–250, 1990.
- [166] R. Peibst, U. Romer, K. R. Hofmann, B. Lim, T. F. Wietler, J. Krügener, N. Harder, and R. Brendel, "A simple model describing the symmetric I-V characteristics of p-polycrystalline Si/n-monocrystalline Si and n-polycrystalline Si/p-monocrystalline Si junctions," *IEEE Journal of Photovoltaics*, vol. 4, no. 3, pp. 841–850, 2014.
- [167] D. Tetzlaff, J. Krügener, Y. Larionova, S. Reiter, M. Turcu, F. Haase, R. Brendel, R. Peibst, U. Höhne, and J.-D. Kähler, "A simple method for pinhole detection in carrier selective polo-junctions for high efficiency silicon solar cells," *Solar Energy Materials and Solar Cells*, 2017.
- [168] M. Rienäcker, M. Bossmeyer, A. Merkle, U. Römer, F. Haase, J. Krügener, R. Brendel, and R. Peibst, "Junction resistivity of carrier-selective polysilicon on oxide junctions and its impact on solar cell performance," *IEEE Journal of Photovoltaics*, vol. 7, no. 1, pp. 11–18, 2017.
- [169] F. Haase, F. Kiefer, S. Schäfer, C. Kruse, J. Krügener, R. Brendel and R. Peibst, "Interdigitated back contact solar cells with polycrystalline silicon on oxide passivating contacts for both polarities," *Japanese Journal of Applied Physics*, vol. 56, no. 8S2, p. 08MB15, 2017.
- [170] F. Haase, C. Klamt, S. Schäfer, A. Merkle, M. Rienäcker, J. Krügener, R. Brendel, and R. Peibst, "Laser contact openings for local poly-Si-metal contacts enabling 26.1 %-efficient POLO-IBC solar cells," submitted to *Solar Energy Materials and Solar Cells*.
- [171] Y. Larionova, M. Turcu, S. Reiter, R. Brendel, D. Tetzlaff, J. Krügener, T. Wietler, U. Höhne, J.-D. Kähler, and R. Peibst, "On the recombination behavior of p^+ -type polysilicon on oxide junctions deposited by different methods on textured and planar surfaces," *physica status solidi (a)*, 2017.
- [172] C. Heine and R. H. Morf, "Submicrometer gratings for solar energy applications," *Applied Optics*, vol. 34, no. 14, pp. 2476–2482, 1995.
- [173] A. Mellor, I. Tobias, A. Marti, and A. Luque, "A numerical study of bi-periodic binary diffraction gratings for solar cell applications," *Solar Energy Materials and Solar Cells*, vol. 95, no. 12, pp. 3527–3535, 2011.
- [174] M. Peters, M. Rüdiger, H. Hauser, M. Hermle, and B. Bläsi, "Diffractive gratings for crystalline silicon solar cells—optimum parameters and loss mechanisms,"

- Progress in Photovoltaics: Research and Applications*, vol. 20, no. 7, pp. 862–873, 2012.
- [175] J. Eisenlohr, N. Tucher, H. Hauser, M. Graf, J. Benick, B. Bläsi, J. C. Goldschmidt, and M. Hermle, “Efficiency increase of crystalline silicon solar cells with nanoimprinted rear side gratings for enhanced light trapping,” *Solar Energy Materials and Solar Cells*, vol. 155, pp. 288–293, 2016.
- [176] H. R. Stuart and D. G. Hall, “Absorption enhancement in silicon–on–insulator waveguides using metal island films,” *Applied Physics Letters*, vol. 69, no. 16, pp. 2327–2329, 1996.
- [177] D. M. Schaadt, B. Feng, and E. T. Yu, “Enhanced semiconductor optical absorption via surface plasmon excitation in metal nanoparticles,” *Applied Physics Letters*, vol. 86, no. 6, p. 063106, 2005.
- [178] S. Pillai, K. R. Catchpole, T. Trupke, and M. A. Green, “Surface plasmon enhanced silicon solar cells,” *Journal of Applied Physics*, vol. 101, no. 9, p. 093105, 2007.
- [179] F. J. Beck, A. Polman, and K. R. Catchpole, “Tunable light trapping for solar cells using localized surface plasmons,” *Journal of Applied Physics*, vol. 105, no. 11, p. 114310, 2009.
- [180] K. R. Catchpole and A. Polman, “Plasmonic solar cells,” *Optics Express*, vol. 16, no. 26, pp. 21793–21800, 2008.
- [181] F. J. Beck, S. Mokkaapati, and K. R. Catchpole, “Plasmonic light-trapping for Si solar cells using self-assembled, Ag nanoparticles,” *Progress in Photovoltaics: Research and Applications*, vol. 18, no. 7, pp. 500–504, 2010.
- [182] G. Mie, “Beiträge zur Optik trüber Medien, speziell kolloidaler Metallösungen,” *Annalen der Physik*, vol. 330, no. 3, pp. 377–445, 1908.
- [183] C. F. Bohren and D. R. Huffman, *Absorption and scattering of light by small particles*. John Wiley & Sons, 2008.
- [184] P. Laven, “Mieplot (a computer program for scattering of light from a sphere using Mie theory & the Debye series),” <http://www.philiplaven.com/mieplot.htm>, 2011.
- [185] H. H. Weber, “Über das optische Verhalten von kugelförmigen, isotropen Teilchen in verschiedenen Medien,” *Colloid & Polymer Science*, vol. 174, no. 1, pp. 66–72, 1961.

- [186] J. E. Cotter, R. B. Hall, M. G. Mauk, and A. M. Barnett, "Light trapping in silicon-film™ solar cells with rear pigmented dielectric reflectors," *Progress in Photovoltaics: Research and Applications*, vol. 7, no. 4, pp. 261–274, 1999.
- [187] O. Berger, D. Inns, and A. G. Aberle, "Commercial white paint as back surface reflector for thin-film solar cells," *Solar Energy Materials and Solar Cells*, vol. 91, no. 13, pp. 1215–1221, 2007.
- [188] J. E. Cotter, "Optical intensity of light in layers of silicon with rear diffuse reflectors," *Journal of Applied Physics*, vol. 84, no. 1, pp. 618–624, 1998.
- [189] B. G. Lee, P. Stradins, D. L. Young, K. Alberi, T.-K. Chuang, J. G. Couillard, and H. M. Branz, "Light trapping by a dielectric nanoparticle back reflector in film silicon solar cells," *Applied Physics Letters*, vol. 99, no. 6, p. 064101, 2011.
- [190] A. Basch, F. Beck, T. Söderström, S. Varlamov, and K. R. Catchpole, "Enhanced light trapping in solar cells using snow globe coating," *Progress in Photovoltaics: Research and Applications*, vol. 20, no. 7, pp. 837–842, 2012.
- [191] B. Lipovšek, J. Krč, O. Isabella, M. Zeman, and M. Topič, "Analysis of thin-film silicon solar cells with white paint back reflectors," *Phys. Status Solidi C*, vol. 7, no. 3-4, pp. 1041–1044, 2010.
- [192] J. Eisenlohr, J. Benick, M. Peters, B. Bläsi, J. C. Goldschmidt, and M. Hermle, "Hexagonal sphere gratings for enhanced light trapping in crystalline silicon solar cells," *Optics Express*, vol. 22, no. 101, pp. A111–A119, 2014.
- [193] J. Eisenlohr, B. G. Lee, J. Benick, F. Feldmann, M. Drießen, N. Milenkovic, B. Bläsi, J. C. Goldschmidt, and M. Hermle, "Rear side sphere gratings for improved light trapping in crystalline silicon single junction and silicon-based tandem solar cells," *Solar Energy Materials and Solar Cells*, vol. 142, pp. 60–65, 2015.
- [194] SkySpring Nanomaterials, www.ssnano.com.
- [195] M. Morita, T. Ohmi, E. Hasegawa, M. Kawakami, and M. Ohwada, "Growth of native oxide on a silicon surface," *Journal of Applied Physics*, vol. 68, no. 3, pp. 1272–1281, 1990.
- [196] B. Veith-Wolf, J. Wang, M. Hannu-Kuure, N. Chen, A. Hadzic, P. Williams, J. Leivo, A. Karkkainen, and J. Schmidt, "Liquid-phase-deposited siloxane-based capping layers for silicon solar cells," *Applied Physics Letters*, vol. 106, no. 5, p. 052104, 2015.
- [197] Desert Silicon, www.desertsilicon.com.

- [198] H. G. J. Moseley, “XCIII. The high-frequency spectra of the elements,” *The London, Edinburgh, and Dublin Philosophical Magazine and Journal of Science*, vol. 26, no. 156, pp. 1024–1034, 1913.
- [199] M. Rüdiger, J. Greulich, A. Richter, and M. Hermle, “Parameterization of free carrier absorption in highly doped silicon for solar cells,” *IEEE Transactions on Electron Devices*, vol. 60, no. 7, pp. 2156–2163, 2013.
- [200] R. Brendel, T. Dullweber, R. Peibst, C. Kranz, A. Merkle, and D. Walter, “Breakdown of the efficiency gap to 29% based on experimental input data and modeling,” *Progress in Photovoltaics: Research and Applications*, vol. 24, no. 12, pp. 1475–1486, 2016.
- [201] www.python.org.
- [202] D. Inns, L. Shi, and A. G. Aberle, “Silica nanospheres as back surface reflectors for crystalline silicon thin-film solar cells,” *Progress in Photovoltaics: Research and Applications*, vol. 16, no. 3, pp. 187–194, 2008.
- [203] N. C. Shaw and J. E. Cotter, “Impact of pigmented diffuse reflector coatings on optical absorption in thin-wafer silicon solar cells,” *Proceedings of Solar Conference*, 2002.
- [204] U. Römer, R. Peibst, T. Ohrdes, B. Lim, J. Krugener, T. Wietler, and R. Brendel, “Ion implantation for poly-Si passivated back-junction back-contacted solar cells,” *IEEE Journal of Photovoltaics*, vol. 5, no. 2, pp. 507–514, 2015.
- [205] R. Peibst, U. Römer, Y. Larionova, M. Rienäcker, A. Merkle, N. Folchert, S. Reiter, M. Turcu, B. Min, and J. Krügener, “Working principle of carrier selective poly-Si/c-Si junctions: Is tunnelling the whole story?,” *Solar Energy Materials and Solar Cells*, vol. 158, pp. 60–67, 2016.
- [206] M. Filipič, P. Löper, B. Niesen, S. de Wolf, J. Krč, C. Ballif, and M. Topič, “CH₃NH₃PbI₃ perovskite/silicon tandem solar cells: characterization based optical simulations,” *Optics Express*, vol. 23, no. 7, pp. A263–A278, 2015.
- [207] S. Reiter, N. Koper, R. Reineke-Koch, Y. Larionova, M. Turcu, J. Krügener, D. Tetzlaff, T. Wietler, U. Höhne, and J.-D. Kähler, “Parasitic absorption in polycrystalline Si-layers for carrier-selective front junctions,” *Energy Procedia*, vol. 92, pp. 199–204, 2016.
- [208] S. Bowden, V. Yelundur, and A. Rohatgi, “Implied- V_{oc} and suns- V_{oc} measurements in multicrystalline solar cells,” *Proceedings of the 29th Photovoltaic Specialists Conference*, pp. 371–374, 2002.

- [209] M. A. Green, *Silicon solar cells: advanced principles & practice*. Centre for photovoltaic devices and systems, University of New South Wales, 1995.
- [210] M. Rienäcker, A. Merkle, U. Römer, H. Kohlenberg, J. Krügener, R. Brendel, and R. Peibst, “Recombination behavior of photolithography-free back junction back contact solar cells with carrier-selective polysilicon on oxide junctions for both polarities,” *Energy Procedia*, vol. 92, pp. 412–418, 2016.
- [211] pv tools, Photovoltaic device analysis, “www.pv-tools.de.”
- [212] S. Schäfer and R. Brendel, “Accurate calculation of the absorptance enhances efficiency limit of crystalline silicon solar cells with lambertian light trapping,” *IEEE Journal of Photovoltaics*, 2018.
- [213] T. Tiedje, E. Yablonovitch, G. D. Cody, and B. G. Brooks, “Limiting efficiency of silicon solar cells,” *IEEE Transactions on Electron Devices*, vol. 31, no. 5, pp. 711–716, 1984.
- [214] M. J. Kerr, A. Cuevas, and P. Campbell, “Limiting efficiency of crystalline silicon solar cells due to coulomb-enhanced Auger recombination,” *Progress in Photovoltaics: Research and Applications*, vol. 11, no. 2, pp. 97–104, 2003.
- [215] P. Würfel, “The chemical potential of radiation,” *Journal of Physics C: Solid State Physics*, vol. 15, no. 18, p. 3967, 1982.
- [216] P. P. Altermatt, F. Geelhaar, T. Trupke, X. Dai, A. Neisser, and E. Daub, “Injection dependence of spontaneous radiative recombination in c-Si: experiment, theoretical analysis, and simulation,” *Proceedings of the 5th International Conference on Numerical Simulation of Optoelectronic Devices*, pp. 47–48, 2005.
- [217] M. A. Green, “Self-consistent optical parameters of intrinsic silicon at 300 K including temperature coefficients,” *Solar Energy Materials and Solar Cells*, vol. 92, no. 11, pp. 1305–1310, 2008.

List of publications

Refereed journal papers

1. S. Schäfer, C. Gemmel, S. Kajari-Schröder, and R. Brendel, “Light trapping and surface passivation of micron-scaled macroporous blind holes,” *IEEE Journal of Photovoltaics*, vol. 6, p. 397, 2016.
2. F. Haase, F. Kiefer, S. Schäfer, C. Kruse, J. Krügener, R. Brendel, and R. Peibst, “Interdigitated back contact solar cells with polycrystalline on oxide passivating contacts for both polarities,” *Japanese Journal of Applied Physics*, vol. 56, p. 08MB15, 2017.
3. S. Schäfer, F. Haase, R. Peibst, and R. Brendel, “Silicon nanopowder as diffuse rear reflector for silicon solar cells,” *Journal of Applied Physics*, vol. 122, p. 053102, 2017.
4. F. Haase, S. Schäfer, C. Klamt, F. Kiefer, J. Krügener, R. Brendel, and R. Peibst, “Perimeter recombination in 25%-efficient IBC solar cells with passivating POLO contacts for both polarities,” *IEEE Journal of Photovoltaics*, vol. 8(1), p. 23, 2018.
5. R. Peibst, Y. Larionova, S. Reiter, T. F. Wietler, N. Orłowski, S. Schäfer, B. Min, M. Stratmann, D. Tetzlaff, J. Krügener, U. Höhne, J.-D. Kähler, H. Mehlich, S. Frigge, R. Brendel, “Building blocks for industrial, screen-printed double-side contacted POLO cells with highly transparent ZnO:Al layers,” *IEEE Journal of Photovoltaics*, vol. 8(3), p. 719, 2018.
6. S. Schäfer and R. Brendel, “Accurate Calculation of the Absorptance Enhances Efficiency Limit of Crystalline Silicon Solar Cells With Lambertian Light Trapping,” *IEEE Journal of Photovoltaics*, 2018.
7. F. Haase, C. Klamt, S. Schäfer, A. Merkle, M. Rienäcker, J. Krügener, R. Brendel, and R. Peibst, “Laser contact openings for local poly-Si-metal contacts enabling

26.1 %-efficient POLO-IBC solar cells,” *submitted to Solar Energy Materials and Solar Cells*, SiliconPV Award Winner, 2018.

8. B. Veith-Wolf, S. Schäfer, R. Brendel, and J. Schmidt, “Reassessment of intrinsic lifetime limit in n-type crystalline silicon and implication on maximum solar cell efficiency,” *submitted to Solar Energy Materials and Solar Cells*, 2018.

International Conferences and Workshops

1. S. Schäfer, M. Ernst, S. Kajari-Schröder, and R. Brendel, “Multilayer Etching for Kerf-free Solar Cells from Macroporous Silicon,” *Energy Procedia*, vol. 38, pp. 933–941, 2013.
2. S. Schäfer, S. Kajari-Schröder, and R. Brendel, “Lithography-free formation of ordered macroporous silicon,” Poster presented at the 9th Porous Semiconductors - Science and Technology (PSST), Benidorm, 2014.
3. S. Schäfer, D. Turkey, C. Gemmel, S. Kajari-Schröder, and R. Brendel, “Macroporous blind holes as surface texture for high efficiency silicon solar cells,” *Proceedings of the 31st European Photovoltaic Solar Energy Conference*, Hamburg, Germany, p. 457, 2015.
4. R. Peibst, Y. Larionova, S. Reiter, N. Orlowski, S. Schäfer, M. Turcu, B. Min, R. Brendel, D. Tetzlaff, J. Krügener, T. Wietler, U. Höhne, J.-D. Kähler, H. Mehlich, S. Frigge, “Industrial, screen-printed double-side contacted POLO cells,” *Proceedings of the 33rd European Photovoltaic Solar Energy Conference*, Amsterdam, Netherlands, p. 451, 2017.
5. S. Schäfer, F. Haase, C. Klamt, C. Kruse, F. Kiefer, J. Krügener, R. Brendel, and R. Peibst, “IBC solar cells with passivating POLO contacts for both polarities—revisiting optical losses,” *presentation at the 8th Workshop on Back Contact Solar Cell and Module Technology*, Freiburg, Germany, 2017.

Danksagung

Zuletzt möchte ich mich bei den Personen bedanken, die zum Gelingen dieser Arbeit beigetragen haben:

Prof. Dr. Rolf Brendel für die sehr gute wissenschaftliche Betreuung, seine Begeisterung und Interesse für Thema und die Möglichkeit, die Arbeit am Institut durchführen zu können,

Prof. Dr. Herbert Pfnür für die Übernahme des Korreferats sowie **Prof. Dr. Klemens Hammerer** für die Übernahme des Prüfungsvorsitzes,

Dr. Moises Garin Escriva und **Prof. Dr. Ramon Alcubilla** von der UPC Barcelona für die Betreuung während des lehrreichen 3-wöchigen Praktikums rund um die Themen Makroporen in Silizium und Photolithografie. Dank hierfür auch an Rolf Brendel für die Ermöglichung des Praktikums,

Deniz Turkey für sein sehr engagiertes Praktikum am ISFH,

Lasse David, Guido Glowatzki und **Oliver Kerker** für die Einweisung in und Unterstützung bei der Reinraumarbeit am LNQE,

Bianca Gehring, Anja Mercker und **Dr. Marco Ernst** für die Einarbeitung in die "Porenätzthematik",

den Projektleitern **Dr. Sarah Kajari-Schröder, Dr. Felix Haase** und **Prof. Dr. Robby Peibst** für ihre Unterstützung und Betreuung,

dem 26plus-Team um **Dr. Felix Haase, Sabine Schmidt, Hilke Fischer, Christina Klamt, Annika Raugewitz** und **Prof. Dr. Robby Peibst** für das Bereitstellen der Zellwafer und die äußerst angenehme Zusammenarbeit,

Dr. Yevgeniya Larionova und dem POLO-Team für das Bereitstellen der POLO-Proben,

den "Laserfuzzis" **David Sylla** und **Tobias Neubert**, für die offenbar kein Prozess unmöglich ist,

Dr. Hendrik Holst für den Raytracer Daidalos und das Erstellen des Simulationsskripts,

Jan Hensen für seine Ideen und Hilfe beim Verlöten der "Streifen-Solarzellen",
der **ISFH-Werkstatt** für das Bauen der Teflonwaferhalterungen,

allen Kolleginnen und Kollegen am Institut, die für die stete Aufrechterhaltung des "Grundzustandes", sei es Wartung der Anlagen, Ausführen von Bestellungen (Kaffebohnen!), das Leeren der Mülleimer, das Füllen des Schokischubers etc., sowie für die entspannte und freundliche Stimmung am Mittagstisch und im Büro sorgen.

Catherin Gemmel, Dr. Dominic Walter und **Dr. Johannes Schurer** für das Korrekturlesen "unter Druck",

bei meiner **Familie** und meinen **Freunden** für die Hilfe, Unterstützung und Ablenkung außerhalb von 634.

Curriculum vitae

Name: Sören Schäfer
Address: Riepenstraße 43, 31789 Hamelin, Germany
Date of birth: 11 December 1986
Place of birth: Korbach, Germany

Education

1993–1997 Primary school, Kellerwaldschule Frankenau
1997–2003 Secondary school, Burgwaldschule Frankenberg
2003–2006 Secondary school, Edertalschule Frankenberg
Abitur 2006
2006–2008 Studies in physics, Philipps-Universität Marburg, Germany
2008–2009 Studies in physics (stay abroad with EU Erasmus programme),
University College Cork, Ireland
2009–2012 Studies in physics, Philipps-Universität Marburg, Germany
Diploma in physics, thesis title: "Zeitaufgelöste Photolumineszenz-
untersuchungen an neuartigen Halbleiternanostrukturen im UV-Bereich"

Working experience

sine 2012 Research associate and doctoral candidate with Prof. Dr. R. Brendel
at the Institute for Solar Energy Research Hamelin (ISFH),
Hamelin, Germany